ANALYSIS

of

THRUSTER EFFECTIVITY

for

DYNAMIC POSITIONING

and

LOW SPEED MANOEUVRING

U. Nienhuis

ANALYSIS of THRUSTER EFFECTIVITY

for

DYNAMIC POSITIONING and LOW SPEED MANOEUVRING

Proefschrift

ter verkrijging van de graad van doctor
aan de Technische Universiteit Delft,
op gezag van de Rector Magnificus,
Prof. Drs. P.A. Schenck,
in het openbaar te verdedigen
ten overstaan van een commissie
door het College van Dekanen daartoe aangewezen,
op vrijdag 30 oktober 1992
te 16.00 uur

door

Ubald Nienhuis

geboren te Jutphaas

scheepsbouwkundig ingenieur

Dit proefschrift is goedgekeurd door de promotor:

Prof. Dr. Ir. J.D. van Manen

Contents

Chapter 1

INTRODUCTION

1.1 Summary

Dynamic positioning, tracking and low-speed manoeuvring have for a long time defied attempts to properly analyse and predict the performance. This is undoubtedly due to the complexity of this dynamic problem where not only hydrodynamic aspects are important but where also control aspects form an integral part of the system.

Traditionally the field of DP or low-speed manoeuvring was analysed by splitting the problem into smaller parts more amenable to analysis. These parts are for example environmental forces (waves, wind and current), control systems and propulsive forces. Each aspect was considered separately and no full coverage of the problem was undertaken.

With the development of time-domain simulation programs more integral analyses were undertaken which, despite their complexity, yielded valuable results pertaining to the design and operability assessment.

Despite this major step forward, many white areas remain in the description of the various components relevant for this topic. One of these components is the force that can be generated by propellers, rudders and thrusters during the low-speed manoeuvers inherent to DP, tracking and harbour manoeuvers.

The large number of parameters involved in this particular problem do not allow an experimental and systematic coverage of the various phenomena. Instead recourse must be taken to a combination of experiments and calculations which together eventually will yield a prediction tool that can be used to further improve the analysis of low-speed manoeuvers.

With CFD codes finding their way in practical applications, such a combined analysis is gradually becoming feasible. Experiments are then used to validate and complement computations. The present work is the first such approach to the particular problem of thruster effectivity during DP, tracking and low-speed manoeuvers.

1.2 General

The concept of dynamic positioning (DP) or dynamic tracking (DT) has become increasingly popular in the last twenty years, both in the offshore industry as well as other areas of seagoing activities.

This change was caused by several factors. In the offshore industry activities were shifting towards increased water depths which in some cases prohibit the use of conventional passive mooring systems. The flexibility and mobility of DP systems led to its (still limited) application for the exploitation of marginal oil fields, with the added advantage that assistance of anchor handling vessels is no longer necessary.

The latter advantage is also beneficial for cable or pipe laying vessels which nowadays may be fitted with dynamic tracking (DT) systems. Indeed there seems to be a trend for oil companies to require the use of actively controlled ships in the vicinity of subsea pipe lines to avoid the risk that these may be damaged by the use of anchors.

In some cases a combination of a passive and an active system will lead to the optimum solution in terms of economy as well as safety. This can be the case for mooring systems where DP is used only for severe weather conditions or where it is used to increase the damping of the system, thus limiting the maximum loads.

In such cases the size of the Single Point Mooring System may be reduced and/or the disconnection operation can be delayed or even omitted. Also the operation of the entire system can be continued in the event that the DP system malfunctions, provided this does not occur during a severe weather period.

DP or DT can also be beneficial in other areas of shipping industry. Examples are dredging vessels (e.g. trenching, stone dumping, beach replenishment) and naval ships (mine hunters in hunting or hovering mode).

Dynamic Positioning is a natural extension of the widely used autopilot which serves to control the course of the ship by means of rudder action. The remainder of the control is performed by the helmsman who will normally adjust the pitch or rpm of the main propeller(s).

Inside a port a more complex manoevring task awaits the ship master or pilot eventually resulting in berthing the ship. The conventional autopilot is useless in that case on account of the low thrust levels of the main propeller(s) and the manoeuvres have to be done manually using the main propellers, rudders and, if present the side thrusters.

For present-day ferries and container ships the complexity of this task becomes enormous due to the large wind areas and the speed with which the manoeuvres, often in severely restricted water, must be carried out. Therefore a joy-stick is often applied which takes care of the translation of the required thrust vector into the propeller and rudder settings.

Whatever mode of control is employed (automatic, manual or a combination) and irrespective of the application (DP, tracking or low-speed manoeuvring), it is essential to know what forces the propellers, thrusters and rudders exert on the ship in the encountered conditions.

This is important for the sizing of the propellers and the power plant, the selection of the thruster arrangement, the design of the control algorithm in case of automatic control, the assessment of the workability and the proper handling of the ship. In short knowledge about these forces is essential for designing and operating a vessel as well as possible.

1.3 Motivation for the Present Work

It is a well-known fact that the total forces necessary to propel a body are usually not equal in magnitude to the forces on the same body experiencing the same motion but now being towed. This difference arises on account of the so-called propeller-hull interaction.

In the normal stationary free-sailing condition of a ship the interaction between the propeller and the hull is commonly described by three factors: the effective wake fraction, the thrust deduction factor and the relative rotative efficiency.

The introduction of the first factor allows the use of an open water diagram to investigate the propulsive behaviour of the ship-propeller system. It reflects the fact that on account of the presence of the hull, the inflow velocity into the propeller differs from the ship's speed.

The second factor, the thrust deduction factor, serves to incorporate the difference between the bare hull resistance force at a given speed and the required thrust to propel the same hull with the same speed. Essentially this difference is a consequence of the changed flow around the ship caused by the propeller operation. In other words: the resistance is changed by the presence of the propeller. Therefore the rarely used 'resistance augmentation factor' is more appropriate compared to the thrust deduction factor.

The operational conditions for DP, tracking and low speed manoeuvring differ widely from the above mentioned free-sailing condition. In the first place instationary conditions are inherent due to the low-frequency motions, the variable thrust vectors as well as the first-order ship motions. Secondly, the low speeds encountered may lead to inflow directions which deviate significantly from the alongship direction. Also the use of azimuthing thrusters or tunnel thrusters leads to thrust directions which do not coincide with this alongship direction. Further it may be expected that other propellers operating in the vicinity of the considered thruster or propeller will not only alter its effective inflow velocity, and hence its thrust, but will also affect the net force which this thruster exerts on the ship. Next, the effect of wind and waves, which more often than not dominates the current, leads to thrust levels of the propellers which are not in balance with the current (or resistance) forces. This is similar to a tug in towing condition. Finally, restricted water (shallow water or the presence of quays) is often encountered, changing the performance of the propulsion devices.

These phenomena all combine to the fact that for a proper design and operation of a vessel operating at low speeds it is not sufficient to know the bollard pull of

each of the propellers. This is similar to the design of a normal cargo vessel which has to meet its trial speed requirement: for this purpose it does not suffice to have the open water diagram of its propeller(s).

For the conditions inherent to dynamic positioning, tracking and low speed manoeuvring, i.e.

- low speed
- drift angle varying from 0 to 360 degrees
- thrust vectors largely uncorrelated with the current force vector
- widely varying propulsion arrangements
- restricted water
- instationary behaviour,

little is known about wake fractions or resistance augmentation factors.

With the increasing importance of DP and low speed manoeuvring the designer as well as the operator must have more information about the propulsive phenomena which occur in the above mentioned situations. This work is aimed at contributing to this knowledge by describing a computational tool that can be used for detailed analyses and by providing insight into the hydrodynamic phenomena. Further it gives access to a rather comprehensive set of experimental data which can be useful for both design as well as operational analysis.

Before proceeding with the the most relevant past work on the propulsive phenomena for low speed manoeuvring, DP or Dynamic Tracking we can now identify the object of the present work, which will be:

1. Establish a theoretical and computational framework for a method that can be used to give detailed qualitative and in many cases also quantitative predictions of the various forms of interaction.

2. Obtain increased insight in the underlying hydrodynamic behaviour, using computational fluid dynamics techniques.

3. Obtain quantitative data which can be used in future analyses of ships fitted with the propulsive devices discussed in this work and which perform low speed manoeuvres.

4. Establish the correlation between calculated and measured results for a limited number of cases, and show some trends which may be expected.

The present work addresses these topics in both a computational as well as an experimental manner and constitutes the first attempt to perform an in-depth analysis of thruster effectivity for conditions typical for DP and low-speed manoeuvring.

A note of caution relates to the fact that the present work is concerned with phenomena on model scale. The application of the present results to full scale is not of concern here although experience indicates that their use leads to an adequate description of the full scale behaviour.

Finally it is remarked that all reported work refers to stationary conditions in still water. Effects of ship motions, (low-frequency or wave-frequency) are not considered.

1.4 Summary of Previous Work

The study of the performance of conventional propellers in off-design conditions is by no means new: Troost [1] already pointed to the behaviour of the thrust deduction factor for bollard pull conditions.

Harvald [2] presented model test results for the wake (w) and thrust (t) deduction factors in non-equilibrium conditions, i.e. conditions where the sum of the ship resistance force (allowing for resistance augmentation effects) and the thrust do not equal zero. Harvald however restricted his attention to ship speeds in the direction of the longitudinal ship axis ($\beta = 0, 180$) and to single propeller cases.

Large variations with advance ratio of t and w were found which were partly attributed to their definition. The variation appeared to depend on whether the speed or the rpm were kept constant. Harvald further concluded that w and t for overload conditions could be derived from the freely running ship values using his measured results.

The above referenced work was valid for inflow directions parallel to the longitudinal ship axis. It is well known that oblique inflow alters the characteristics of open or nozzled propellers, see e.g. Dyne [3], Taniguchi etal [4], Shields [5], Moberg etal [6], Gutsche [7], Bussemaker etal [8], Van Leest etal [9], Binek etal [10], Van der Made etal [11] and Oosterveld etal [12]. The work of Dyne, Taniguchi etal, Shields and Moberg etal is limited to small flow inclinations (upto 15 degrees) while the other authors cover also larger inclinations. The systematic experiments of Oosterveld etal [12] are by far the most comprehensive and cover four quadrant measurements for a range of inflow angles and show the significance of the effect. These measurements refer to the the commonly used MARIN 19A and 37 nozzles which were designed at MARIN and are discussed by e.g. Van Manen [13], [14], Van Manen etal [15], and Oosterveld [16], [17].

The mentioned measurements of Oosterveld etal [12] not only cover nozzled propellers as commonly found in DP ships but also open propellers where similar effects are observed. Gutsche developed a simple theoretical model to calculate the propeller performance in inclined flow, [7].

If the propellers are mounted on the hull similar effects may be expected although due account has to be taken of the influence of the hull on the effective inflow speed and direction, see e.g. Yumuro [18], Kose [19] or Inoue [20]. For conditions relevant for normal manoeuvring operations this effect has been studied experimentally.

The above mentioned research is restricted to relatively small drift angles and

to the conventional main propeller(s).

For DP use is often made of compass or azimuthing thrusters which may assume any thrust direction. These thrusters are in some cases located below the keel and are often found in groups. Such arrangements may suffer from thruster-thruster and thruster-hull interactions.

The thrusters may operate in each others slipstream with a consequent loss of thrust according to Wise etal [21], English [22], English etal [23], Van der Made etal [11] and Lehn [24]. Similar findings were reported by Moberg etal [6], Nienhuis [25] and Van den Boom etal [26]. Nienhuis [25] reported a semi-empirical method capable of adequately predicting this thrust degradation starting from the assumption, which was later confirmed, that the slip stream behaves similar to a turbulent jet. A correlation of calculations with this method and model measurements was also reported by Davison etal [27].

Also thruster-hull interaction may occur which is similar to the phenomena accounted for by the previously mentioned thrust deduction factor. The effect can however be more severe because of the location of the thrusters. In some cases the propeller wash may impinge on the hull leading to large thrust degradations, in other cases the slip stream may be deflected by the bilge with similar losses of effectivity, see [28] as well as the work of Norrby etal [29], [30] where indications of the extent of this effect are given. Minsaas etal [31] also gives some results on the thrust degradation. The slip stream deflection can be ascribed to the Coanda effect, see English [22]: on account of the entrainment into the jet a low pressure region arises which causes the jet to deflect towards the body. Experimental results on the velocity distribution in the deflected jet were presented by Nienhuis [32].

Wise etal [21] and English etal [23] also gave some experimental results for the effective force generated by the thrusters in a 3 knot current. Significant thruster-hull interactions were found for some cases, the exact magnitude of which could not be assessed since the thrust of the individual propellers was not measured. English etal [23] gave pressure distributions around the hull for one thrust condition, showing quite large low pressure areas caused by the thruster operation.

For a semi-submersible considerable additional thrust losses may be observed if the slipstream of a thruster located on one pontoon hits the other floater, see Moberg etal [6]. Note that similar phenomena may also occur for a towed object where the net towing force is reduced because of the tug propeller wash impinging on the towed structure, see Brix [33].

As discussed before, the characteristics of propellers change with changing angle of incidence of the inflow. Tunnel thrusters can be regarded as ducted propellers with a ship-shaped body acting as the duct. Therefore a similar change of propulsive characteristics may be expected.

English etal [34] investigated the side force induced by a tunnel thruster at forward speed. They found a reduced side force compared to the bollard pull value which deteriorated with increasing forward speed upto a certain speed after which a gradual improvement was observed. Their results were similar to those found previously during the investigation of VTOL aircraft, see Gregory etal [35], [36] and

Jordinson [37].

The reduction of the side force was attributed to the change of the pressure distribution caused by the deflection of the propeller slip stream. This effect was confirmed by pressure measurements in the vicinity of the tunnel exit area.

Comparing the results for a large flat plate with those for a ship hull, English etal found a smaller reduction of the side force for the latter case, which was thought to be due to the location of the tunnel close to the keel, thus limiting the area of low pressures. Cooper [38] performed a simple theoretical analysis of the side force reduction valid for an infinitely extending flat plate at zero drift angle and confirmed the cause of this reduction as well as the order of magnitude.

Other authors have also investigated the force reduction, see e.g. Stuntz etal [39], Norrby [40], Ridley [41] and Chislett etal [42]. A disadvantage of these investigations was the fact that it was not possible to measure both the thrust at the vertical drive as well as the total force on the ship. Chislett etal [42] however concluded from their research that the major part of the speed dependence was indeed due to the changed pressure distribution on the ship's hull and not to a changed impeller thrust.

They also found that the turning moment behaves similar to the side force for relatively low ship speeds. For higher ship speeds however the side force stays approximately constant whereas the turning moment increases significantly, indicating a large shift in the point of application of the suction force.

Beveridge [43] investigated these effects for a submarine-shaped hull and found similar results. He concluded from his data that the bow thruster inflow did not play a major role, that the relative duct size was important and that the effect could be diminished by extending the duct beyond the hull.

Another means of reducing the suction force was put forward by Brix [44], [45] who investigated the use of an anti-suction tunnel, a small tunnel located aft of the bow thruster which serves as a pressure equalization duct and thus reduces the suction force.

Brix [44], [45], [46], [47], [48], [49] has presented many experimental results on tunnel thruster effectivity which all showed similar tendencies as discussed before and which also confirmed that the side force reduction is less for astern speeds, an observation which was already made before by Ridley [41].

All analyses were restricted to forward or astern speed excluding other incidence angles which are normal for dynamic positioning or tracking. Kijima [50] theoretically investigated the influence of a small drift angle on the tunnel thruster side force. His results showed that the side force and especially the turning moment were rather insensitive to the drift angle for small values of the angle. For somewhat larger values his calculations predicted larger influences. For large angles his method is not applicable.

English etal [34] suspected a significant influence of the presence of a quay on the side thruster force. This effect was observed for the similar situation of a VTOL aircraft during take-off and landing, [51].

Taniguchi etal [52] have investigated this effect in more detail showing influences of distance to the quay, heading relative to the quay, water depth and ship shape.

Other authors have investigated the thrust degradation of tunnel thrusters in waves, see Karlsen etal [53], Nienhuis [32] and Minsaas etal [31].

Stern thrusters may be expected to behave similar to bow thrusters. However some complications may be expected since the operation of the main propeller(s) and the rudders will affect the performance of these thrusters, see Pronk etal [54] who indicates a strong influence. Also the presence of propeller shafts in case of a twin propeller ship may lead to further thrust degradations. Scarce information about these effects is available in the literature, consisting mainly of the work published by Van Hooren etal [55] and Jonk [56] on the crabbing performance of ships. Jonk adds some results which indicate the importance of quay proximity. Brix [33] shows some measured hull pressure distributions due to two oppositely operating main propellers.

Although useful in obtaining some, if limited, insight in the importance of the various forms of interaction, most of the work in this field is restricted to showing some overall results. It does not provide substantial insight in the phenomena involved and hardly any trends can be isolated. Therefore its application to other situations or ships is rendered impossible.

1.5 Summary of Present Work

Chapter 2 deals with the theoretical and experimental tools which have been used during the investigations. It will discuss the calculation models developed in the course of the present investigation, the measurement techniques and equipment used for the experiments, the ship models tested as well as the propulsive devices which were used.

The theoretical analysis employs a method aimed at solving the three-dimensional time-averaged Reynolds equations for a turbulent flow employing a finite difference method.

The computational tool developed in the course of this work is based on methods reported in the literature. It is aimed at being able to cover most of the forms of interaction between propellers and hulls relevant for DP and low speed manoeuvring.

The numerical model incorporates the commonly employed Hybrid scheme for calculating the convected quantities. It also includes the Quadratic Upstream Interpolation Convective Kinematics (QUICK) scheme which introduces less numerical viscosity compared to this Hybrid scheme. The method is designed to calculate the flow induced by a number of thrusters with or without the presence of a simply shaped hull form. This form is restricted to an arbitrary arrangement of rectangular flat plates allowing the use of a Carthesian coordinate system.

In the present study the object of this tool is primarily to allow an increased insight into the phenomena which play a role for the thruster effectivity, see Chapter 3. However it is found that the numerical model, although demanding considerable CPU power, is sufficiently refined to also give quantitatively meaningful results and can therefore be used to calculate the net force generated by the thrusters and pro-

pellers for many cases. Therefore for a few cases the correlation with measurements is discussed. The agreement is seen to be moderate which in view of the restricted representation of the body geometry is all one could hope for.

In future work trends it will be possible to establish trends based on theoretical calculations carried out with this computational tool. These can then be combined or calibrated with experimental results to obtain a rather general mathematical model for the calculation of the thruster-interaction effects. This in turn can then be used for e.g. real-time simulation purposes or quick preliminary design studies.

Chapter 3 is the main part of the work and concentrates on the various aspects of thruster effectivity. An important part of the discussion is devoted to the thruster slip stream which plays an important role in the various forms of interaction. Measurements of the velocity field in the slipstream are reported for a variety of conditions.

The measurements refer mainly to the bollard pull condition for which the following cases were investigated:

- Ka-4-70 propeller with both MARIN 19A and MARIN 37 nozzle
- Ka-4-70 propeller with nozzle above flat plate
- Ka-4-70 propeller with nozzle under a floater with various bilge shapes

Next to the bollard pull conditions also some low speed situations were considered with the Ka-4-70 propeller and nozzle in open water. Two advance ratios for axial inflow direction and two oblique inflow conditions for one advance ratio were tested.

The aforementioned quantities were measured with a Laser Doppler Anemometer for a series of vertical planes behind the propeller, giving detailed information about the development of the propeller jet.

An attempt to calculate the propeller jet for some of the measured conditions is made subsequently in Chapter 3. The correlation between calculations and measurements is seen to be qualitatively satisfactory.

Chapter 3 continues with the measurements and calculations of thruster-thruster interaction as it occurs for azimuthing thrusters in open water condition and in the vicinity of an infinitely extending flat wall.

Measured thrust and torque values are presented for a set of two thrusters which operate close to each other. The relative position and azimuth angles of both thrusters is varied and the speed of the flat bottom barge to which they are mounted is varied.

A quantitative analysis is made with the theoretical method of Chapter 2 and the correlation with the measurements is found to be good.

Subsequently the focus of the investigations shifts towards thruster/hull interaction of azimuthing thrusters and more complicated geometries are considered.

Measurements are presented of the thrust degradation of a thruster due to the presence of the hull which is related to the Coanda effect.

Finally the net thrust of a thruster mounted under a semi-submersible is investigated experimentally. The thrust degradation due to the impingement of the

thruster wash on the second floater is identified and severe thrust losses are observed. The thrust losses are related to the velocity distribution in the thruster slip stream at the second floater and a clear interdependence is found. The existence of this relation points to the possibility to calculate this form of thruster-hull interaction by first analysing the slip stream of the thruster and subsequently applying a resistance coefficient technique to determine the thrust loss.

Chapter 3 then continues the thruster/hull interaction topic but focusses on another type of propulsive device: the conventional tunnel thruster with the straight duct. Alternative devices such as the Y-, T- or omega- thruster are not discussed since they are uncommon. The static (bollard pull) force of the propeller thrust in unrestricted water is assumed to be known.

First a two-dimensional analysis is carried out using the developed computational techniques. This analysis focusses on the pressure distribution change induced by a two-dimensional propeller located in the flat plate. Effects of propeller loading and inflow direction are investigated indicating the effects that can be expected for three-dimensional realistic cases.

A limited qualitative analysis of the observed interaction phenomena with the 3-D calculation method is subsequently carried out for a simple plate-shaped hull with a center tunnel thruster. This case is similar to a tested configuration and some conclusions are drawn with respect to the phenomena that occur. The correlation between the measurements and the calculations is found to be qualitative only.

Another case refers to bow thruster operation in forward speed for which again calculations are shown. The well-known reason for the thrust degradation is confirmed and a qualitative agreement with measurements is established. As a side step the influence of the Anti-Suction Tunnel is investigated and the calculations confirm the working principle of the AST on the thrust degradation. Also the required position of the AST immediately downstream of the thruster tunnel is confirmed.

The chapter continues with a comprehensive set of model test data concerning bow thruster effectivity in arbitrary inflow. These data together with the theoretical analysis supply insight in the behaviour of the thrusters. It also gives quantitative information which can be used for design and analysis purposes. The model tests cover thrust, torque and force measurements for several ships in arbitrary current conditions and deep water.

The chapter is concluded by covering the more complicated case of shallow water. Again quantitative measured information is presented.

With the investigations for the azimuthing and tunnel thrusters reported in this work an important range of aspects is covered. A remaining and important propulsive arrangement is the main propeller/ stern tunnel thruster/ rudder combination. This arrangement is not covered in this study although the developed computational model is equally well suited for this arrangement.

In Chapter 4 the main topics are summarized and the most important conclusions are listed. Indications for the direction of future developments are given.

Chapter 2

TOOLS AND MODELS

2.1 Introduction

Having set the scope of the covered topics in this work, we now proceed with the discussion of the means by which these topics will be investigated. These means consist of computer programs for the theoretical analyses, experimental equipment and the subjects of the investigation, the models of the ships and propellers.

The reason that all tools and models are discussed here, is to avoid interrupting the discussion of the investigated phenomena in the subsequent chapters as much as possible.

2.2 Coordinate Systems and Sign Conventions

Three co-ordinate systems are used:

1. space-fixed coordinates denoted by X, Y, Z (or by X_1, X_2, X_3), see Figure 2.1a.
2. ship-fixed coordinates denoted by x, y, z (or by x_1, x_2, x_3) with the origin located in the midship section on the center line and in the keel plane, Figure 2.1a.
3. propeller-fixed coordinates x_p, y_p, z_p with the origin located at the propeller axis in the propeller plane, Figure 2.1b. Cylindrical coordinates x_p, r_p and ϕ_p may also be used for the propeller-fixed coordinates.

Throughout this work the sign conventions shown in Figures 2.2 for water velocities and forces, moments etc. are consistently used.

2.3 3-D Turbulent Flow Model

2.3.1 General

The aim of the present work as stated in Chapter 1 is not to be able to calculate the investigated phenomena quantitatively but to understand them qualitatively and to

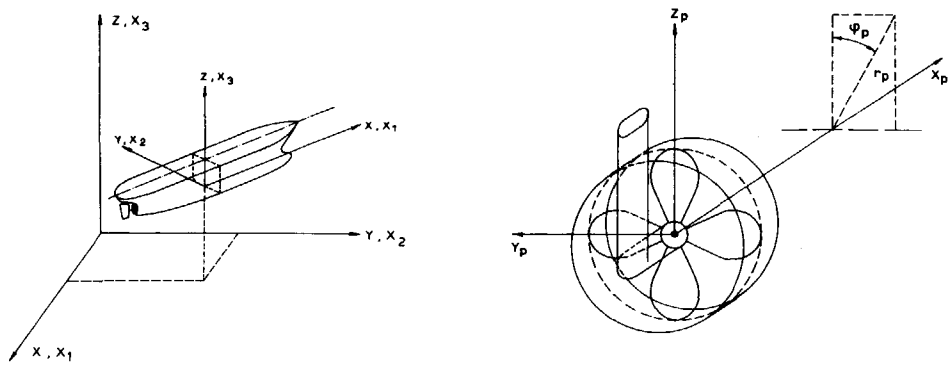

Figure 2.1: space-fixed and ship-fixed coordinate system; propeller-fixed coordinate system

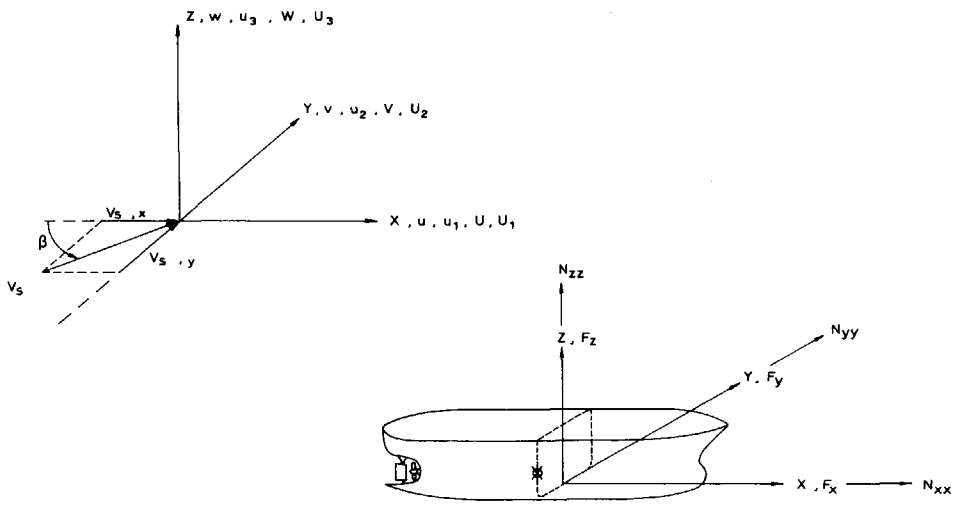

Figure 2.2: sign conventions for water velocities; sign conventions for forces and moments

provide experimental quantitative information relating to these phenomena.

Therefore it was decided to restrict the numerical model to simple geometries where the ship's hull is modeled by an arbitrary number of rectangular flat plates located at $X = c, Y = c$ or $Z = c$. This admits modeling a ship simply by e.g. a single flat plate of zero thickness having the same draft and lateral area as the considered ship. It also enables calculations for e.g. a semi-submersible which can be modeled by a set of rectangular blocks.

This method of modeling bodies limits the complexity of the computational model since in that case Carthesian coordinates can be used. The method has shortcomings as previous work has shown, see Frymier [57]. Computations for a curved body adopting a suitable coordinate system give different results from those for the same body but modeled by a set of straight line segments in a staircase form. However since qualitative rather than quantitative results are aimed for, this approach is thought to be suitable.

In the literature some calculation procedures for a turbulent jet in cross-flow have been published, see e.g. Patankar etal [58], Rodi etal [59] and Demuren [60].

Since the behaviour of a jet in a cross-flow is known to have similarities with the topics that are of concern here, see e.g. Nienhuis [32] and English [22], and since rather good results were obtained with these procedures, a similar solution technique was used in the present case.

2.3.2 Mathematical model

The equations that are of concern here are the time- averaged partial differential equations governing the steady uniform-density three-dimensional flow of a viscous fluid:

$$\frac{\partial(U\phi)}{\partial x} + \frac{\partial(V\phi)}{\partial y} + \frac{\partial(W\phi)}{\partial z} = -\frac{\partial(\overline{u\phi})}{\partial x} - \frac{\partial(\overline{v\phi})}{\partial y} - \frac{\partial(\overline{w\phi})}{\partial z} + \frac{S_\phi}{\rho} \tag{2.1}$$

where ϕ may stand for any of the relevant quantities U, V, W, k and ϵ.

The continuity equation also has to be satisfied:

$$\frac{\partial U}{\partial x} + \frac{\partial V}{\partial y} + \frac{\partial W}{\partial z} = 0 \tag{2.2}$$

The Reynolds stresses which appear in the three momentum equations are modelled the usual way:

$$-\overline{u_i u_j} = \nu_t \left(\frac{\partial U_i}{\partial x_j} + \frac{\partial U_j}{\partial x_i} \right) - \frac{2}{3} k \delta_{ij} \tag{2.3}$$

where $i, j = 1, 2, 3$ and the usual tensor notation is adopted.

The turbulent diffusion flux of the turbulent kinetic energy k and turbulence dissipation ϵ may be expressed by:

$$-\overline{u_i \phi} = \frac{\nu_t}{\sigma_\phi} \frac{\partial \phi}{\partial x_i} \tag{2.4}$$

with $i = 1, 2, 3$ and ϕ denotes either k or ϵ.

The eddy viscosity ν_t which appears in the above equations is related to the turbulent quantities by:

$$\nu_t = c_\mu \frac{k^2}{\epsilon} \tag{2.5}$$

Table 2.1 describes the relations which represent the source terms S_ϕ which occur in the above equations.

Quantity ϕ	Expression
U	$-\frac{1}{\rho}\frac{\partial p}{\partial x}$
V	$-\frac{1}{\rho}\frac{\partial p}{\partial y}$
W	$-\frac{1}{\rho}\frac{\partial p}{\partial z}$
k	$\nu_t G - \epsilon$
ϵ	$\frac{\nu_t c_1 \epsilon G}{k} - c_2 \frac{\epsilon^2}{k}$

Table 2.1: definition of the source terms S_ϕ

It may be noted that in this table G represents the rate of production of turbulent kinetic energy and is given by:

$$\begin{aligned} G &= 2\left[\left(\frac{\partial U}{\partial x}\right)^2 + \left(\frac{\partial V}{\partial y}\right)^2 + \left(\frac{\partial W}{\partial z}\right)^2\right] + \left[\left(\frac{\partial U}{\partial y}\right)^2 + \left(\frac{\partial V}{\partial x}\right)^2\right] \\ &+ \left[\left(\frac{\partial U}{\partial z}\right)^2 + \left(\frac{\partial W}{\partial x}\right)^2\right] + \left[\left(\frac{\partial V}{\partial z}\right)^2 + \left(\frac{\partial W}{\partial y}\right)^2\right] \end{aligned} \tag{2.6}$$

The constants which appear in the turbulence model are listed in Table 2.2. They have the values which were found to give good results for a great many applications, see Launder etal [61].

Note that the above equations refer to the high-Reynolds number case and that the laminar viscosity is neglected.

2.3.3 Finite difference equations

The finite difference equations are obtained by integrating Equation 2.1 over a control volume CV. By applying the mean value theorem and by dividing all terms by the volume of CV ($V_{CV} = \Delta x \Delta y \Delta z$), the following general equation for ϕ is

Quantity	Value
c_1	1.44
c_2	1.92
c_μ	0.09
σ_k	1.0
σ_ϵ	1.3

Table 2.2: turbulence model constants

obtained:

$$
\begin{aligned}
& \frac{\overline{U}_{i+1/2}\overline{\phi}_{i+1/2}-\overline{U}_{i-1/2}\overline{\phi}_{i-1/2}}{\Delta x} \\
+ & \frac{\overline{V}_{j+1/2}\overline{\phi}_{j+1/2}-\overline{V}_{j-1/2}\overline{\phi}_{j-1/2}}{\Delta y} \\
+ & \frac{\overline{W}_{k+1/2}\overline{\phi}_{k+1/2}-\overline{W}_{k-1/2}\overline{\phi}_{k-1/2}}{\Delta z} \\
- & \frac{1}{\Delta x}\left[\frac{\overline{\nu}_{t,i+1/2}}{\sigma_\phi}\left(\frac{\overline{\partial\phi}}{\partial x}\right)_{i+1/2}-\frac{\overline{\nu}_{t,i-1/2}}{\sigma_\phi}\left(\frac{\overline{\partial\phi}}{\partial x}\right)_{i-1/2}\right] \\
- & \frac{1}{\Delta y}\left[\frac{\overline{\nu}_{t,j+1/2}}{\sigma_\phi}\left(\frac{\overline{\partial\phi}}{\partial y}\right)_{j+1/2}-\frac{\overline{\nu}_{t,j-1/2}}{\sigma_\phi}\left(\frac{\overline{\partial\phi}}{\partial y}\right)_{j-1/2}\right] \\
- & \frac{1}{\Delta z}\left[\frac{\overline{\nu}_{t,k+1/2}}{\sigma_\phi}\left(\frac{\overline{\partial\phi}}{\partial z}\right)_{k+1/2}-\frac{\overline{\nu}_{t,k-1/2}}{\sigma_\phi}\left(\frac{\overline{\partial\phi}}{\partial z}\right)_{k-1/2}\right]-\frac{S_\phi}{\rho}=0
\end{aligned}
\tag{2.7}
$$

The overbar on the various variables denote average values over the faces of the control volume. The indices $i+1/2, i-1/2, j+1/2, j-1/2, k+1/2, k-1/2$ indicate the six faces of that control volume, see Figure 2.3.

The grid on which the above equations are solved uses staggered locations for the velocities, Patankar etal [62]. The velocity nodes for U are staggered in x-direction which means that in this direction they lie midway between two consecutive p-nodes. Similar staggering is applied for V and W-nodes. Figure 2.4 shows this grid for a two-dimensional situation. It may be noted that the program is designed for an arbitrary non- uniform Carthesian grid. The quantities which occur in the above finite difference equations have to be related to node values of the unknown quantity ϕ.

Linear interpolation is used for the convecting face velocities

$$
\begin{array}{cc}
\overline{U}_{i+1/2} & \overline{U}_{i-1/2} \\
\overline{V}_{j+1/2} & \overline{V}_{j-1/2} \\
\overline{W}_{k+1/2} & \overline{W}_{k-1/2}
\end{array}
$$

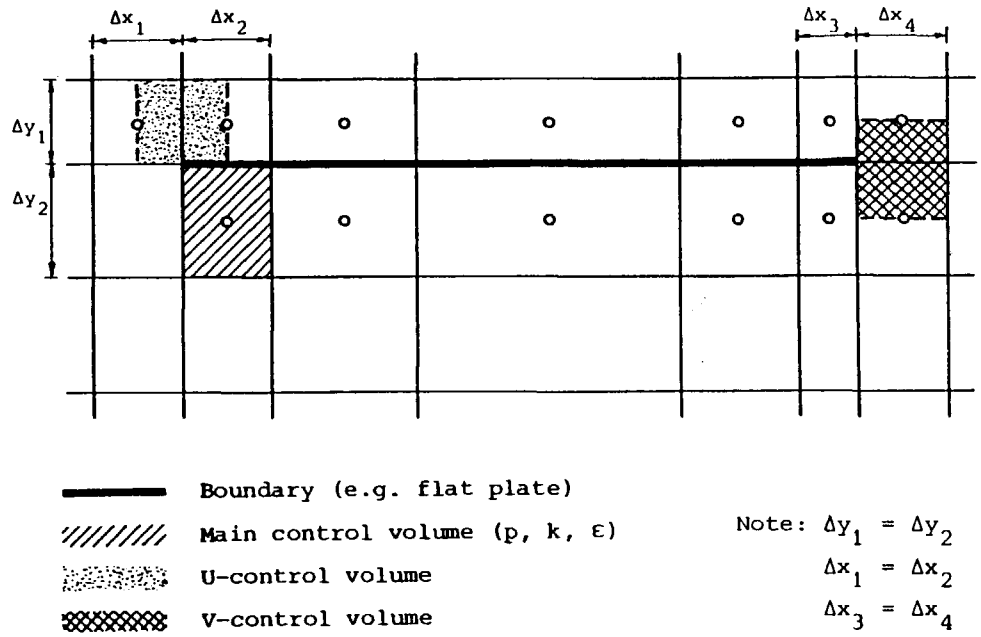

Figure 2.3: faces for control volume

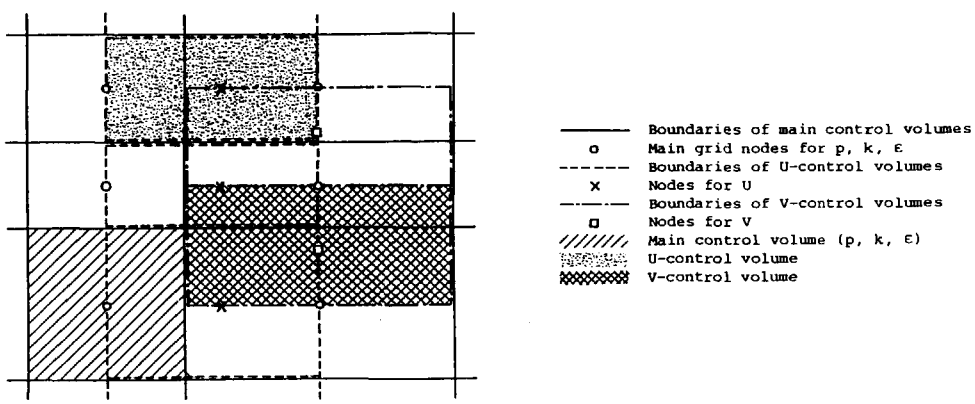

Figure 2.4: staggered grid definition

as well as for the gradients

$$\left(\overline{\frac{\partial\phi}{\partial x}}\right)_{i+1/2} \quad \left(\overline{\frac{\partial\phi}{\partial x}}\right)_{i-1/2}$$
$$\left(\overline{\frac{\partial\phi}{\partial y}}\right)_{j+1/2} \quad \left(\overline{\frac{\partial\phi}{\partial y}}\right)_{j-1/2}$$
$$\left(\overline{\frac{\partial\phi}{\partial z}}\right)_{k+1/2} \quad \left(\overline{\frac{\partial\phi}{\partial z}}\right)_{k-1/2}$$

Linear interpolation is also used for the turbulent viscosities. For the gradients which occur in the source terms S_ϕ, both linear and quadratic interpolations are used.

Patankar etal [62] use a Hybrid (Central/Upwind) interpolation scheme for the convected quantity ϕ. However it was shown that this scheme introduces significant amounts of numerical diffusion, e.g. De Vahl Davis [63].

Leonard [64] has introduced a higher order scheme which suffers to a lesser extent from this diffusion, The Quadratic Upstream Interpolation scheme (QUICK).

This scheme was successfully applied by amongst others Leschziner etal [65], [66] and Demuren [60].

Figure 2.5 shows the node points which are used for the interpolation of the convected face values of ϕ depending on the direction of the convecting flow. The figure also shows the procedure for the Hybrid scheme which is also incorporated in the program. The Hybrid procedure depends on the value of the local grid Peclet number P_l for the face l which is defined as:

$$P_l = \frac{\overline{U}_l \delta x}{\overline{\nu}_{t,l}} \tag{2.8}$$

with δx the distance between the two U-nodes surrounding the face.

2.3.4 Boundary conditions

The incoming flow is always in the horizontal (x, y) plane. It may however have an arbitrary angle with respect to the x-axis to accommodate the required variation of the drift angle β that is of interest for the present investigations.

The boundary conditions relate to six planes, each of one of the following types: inlet, outlet, symmetry plane or solid wall.

At the symmetry plane the normal gradients are prescribed as zero. At the exit plane(s) the condition $\partial p/\partial t = 0$ or $\partial^2 p/\partial t^2 = 0$ was applied since the outlet plane was positioned far enough downstream to assume that the sole influence of the calculation was caused by the pressure. t denotes the direction of the ambient flow: the outlet plane is also assumed to be located far enough downstream so that the outlet flow direction coincides with that ot the ambient flow. For the case this assumption turns out to be too restrictive, an option was included to set t equal to the local outflow direction. Conditions at the outlet plane are also required for the other variables (U, V, W, k, ϵ). In all computed cases the outlet boundary was

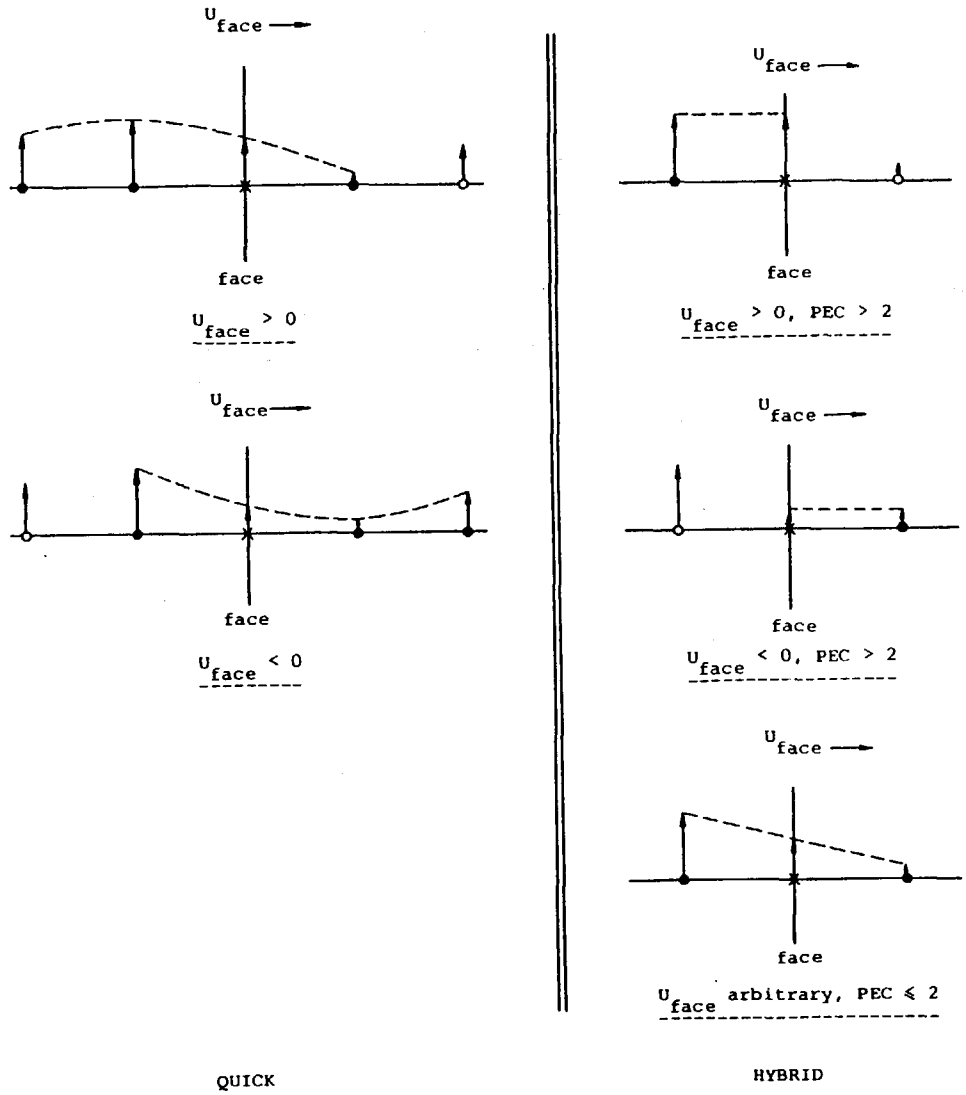

Figure 2.5: interpolation nodes for convected face values of ϕ

assumed to be situated sufficiently far downstream to be able to set the normal gradients of these variables equal to zero.

At the inlet plane suitable conditions for U, V, W, k and ϵ are imposed. The condition for p follows naturally in that case.

At the solid walls, including the flat plates which may be located inside the calculation domain, the turbulence is assumed to be in a state of local equilibrium. Thus the law of the wall approach can be used as described by Launder etal [61].

It is assumed that the law of the wall applies to the entire solid walls and that there is no laminar or transition region.

Following the suggestion of Durst etal [67] the finite difference equations were modified for the region close to the edges of the plate. This was done to allow for the fact that the control volumes for the staggered velocities at the edges have only a partial overlap with the plate, see Figure 2.3. As stated by Durst etal this was found to have a significant effect on the convergence behaviour of the calculations.

2.3.5 Solution algorithm

Most algorithms for the solution of the above given equations employ the SIMPLE algorithm of Patankar etal [62]. However Patankar [68] states that the use of an adapted algorithm using a more accurate pressure equation may lead to faster convergence. This procedure, SIMPLER, is used in the present program.

In this procedure the pressure equation is not, contrary to the SIMPLE approach, an approximate equation, but is derived by substituting the momentum equations into the continuity equation without omitting any terms.

In the SIMPLER algorithm the following steps are carried out:

1. Start with an initial (guessed) velocity field
2. Solve the pressure equation derived from the three momentum equations and the continuity equation
3. Solve the three momentum equations
4. Solve the pressure correction (p_{cor}) equation to reduce errors in the mass balance (similar to SIMPLE algorithm).
5. Correct the velocity field with the pressure correction field but do not correct the pressure field.
6. Calculate the turbulence quantities
7. Check convergence and if convergence is not attained repeat the process starting from step 2.

2.3.6 Computational details

Since the numerical model is merely a tool for the present investigations it is not the aim to describe the numerical model in great detail. This paragraph is restricted to give some observations.

The method described here is only useful if proper convergence is obtained after a certain number of iterations. An exact solution for the cases considered here is never available and it must be established in some way if the method leads to an acceptable solution, both in terms of satisfaction of the balance equations as well as in terms of accuracy of the solution compared to the unknown exact solution.

The satisfaction of the balance equations can be ascertained by investigating the error in the continuity equation since the discretized version of this equation is used to determine the required velocity corrections. If continuity is satisfied the velocity corrections will be zero and the solution field is found. On account of numerical errors and to limit the number of iterations, the calculations are stopped when the error in mass balance becomes smaller than a prescribed value.

The following familiar criterion was formulated for the mass balance error:

$$\epsilon_{err} = \frac{\Phi_{CV}}{\Phi_{tot}} \tag{2.9}$$

which relates the local error in continuity for the particular control volume Φ_{CV} to the overall volume flow Φ_{tot} through the computational domain which is defined as:

$$\Phi_{tot} = \left| \int_{A_{CD}} \vec{V}.\vec{n}\, d\, A_{CD} \right| \tag{2.10}$$

with A_{CD} the area enclosing the computational domain and $\vec{n}$ the outward normal vector of unit length.

A normal stop criterion for the iterations was:

$$\epsilon_{err} = 0.00001 \tag{2.11}$$

which was in many cases found to give a sufficiently converged solution in terms of velocity and pressure distribution as well as integrated forces on any plates in the domain.

To ascertain that the imposed accuracy on the mass balance error leads to sufficient convergence, a check was always performed to check if the variations in e.g. overall forces between consecutive iterations were acceptably small.

For a closed fluid domain the above error criterion ceases to be meaningful and instead the convergence is assessed mainly by observing the required velocity corrections and the evolution of velocities and forces with consecutive iterations.

If following this procedure a converged solution is found it must still be established if this solution resembles the exact solution to a sufficient degree. Failing the exact solution, this was investigated by subsequent grid refinements and observing the local changes in the flow field. This exercise was not performed for each computational case covered in this work, but was done for a simplified two-dimensional case only as described in the next section.

It has been reported in the literature that seemingly stable solutions became suddenly unstable after a large number of iterations. The present method did not give such instabilities and subsequent divergence for the computational case of a flat plate subjected to a perpendicular inflow. The solution remained stable upto 12,500 iterations after which the calculation was stopped.

The method used for the present investigations was found to be very robust; in many cases the initial estimate of the flow field was taken as a uniform flow over the entire fluid domain. Despite this and the presence of actuators and flat plates in the fluid domain, the method did converge in most cases without many problems. However it was necessary to give the relaxation factors small values (in the order of 0.03) throughout the entire calculation as opposed to the factors reported by other authors, e.g. Patankar [68] which are an order of magnitude larger.

In many cases it is necessary to restrict the outflow angles at the exit boundaries somewhat to ensure convergence. At a later stage in the calculations this restriction could then be dropped.

Finally divergence is often observed if actuator forces are introduced in the flow field without relaxation. Usually to have the forces grow to the proper value in some 20 iterations was sufficient to avoid that divergence.

It was found that proper implementation of the edges of any flat plate is important to ensure convergence. This was also reported by Durst etal, [67]. It is however observed that the results are not significantly affected by this aspect.

The solution of each of the equations for $U, V, W, k, \epsilon, p, p_{cor}$ involve the execution of sweeps in the x-, y- or z- direction: the so-called line by line method is employed. Relaxation may be applied after each sweep to ensure convergence. Also to the solution of each equation $(U, V, W, k, \epsilon, p)$ relaxation is applied again to ensure convergence.

Although the QUICK scheme was also implemented, the method was not nearly as stable for this scheme as it is for the Hybrid scheme. Divergence was often encountered unless a significantly smoother grid was employed with expansion ratios in the order of 1.1.

2.3.7 Numerical tests

First the applicability of the method is demonstrated for the same simple two-dimensional case where a flat plate, situated at $y = 0$, -2.65 m $\leq x \leq$ 2.65 m is subjected to a uniform inflow with speed $V_s = 0.319$ m/s. The water inflow is oriented along different angles giving drift angles for the plate varying between 0 $\leq \beta \leq$ 90 degrees.

The grid was kept the same irrespective of drift angle and is shown in Figure 2.6. Only for $\beta = 90$ degrees this grid did not yield a stable solution and a finer grid was adopted. The finer grid gave a stable solution which in terms of pressure distribution on the plate was close to that for the original grid. Note that Figure 2.6 shows the faces of the control volumes for k, ϵ which constitute the main (non-staggered) control volumes.

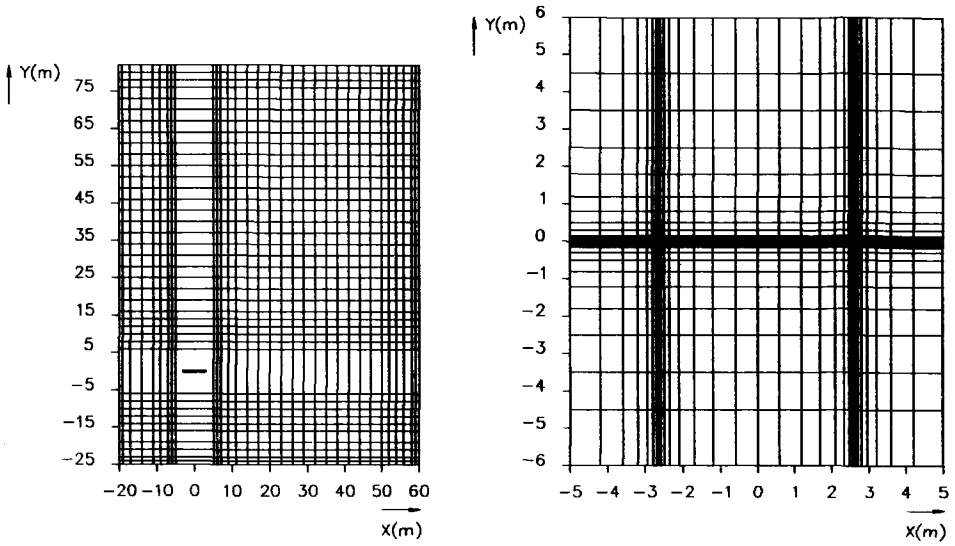

Figure 2.6: grid definition for the calculations with various drift angles

Figure 2.7 shows the vector plots for all considered drift angles whereas Figure 2.8a shows the calculated pressure distributions for all drift angles both on the pressure side as well as the suction side. The pressure distributions are shown in terms of the dimensionless pressure coefficient:

$$C_p = \frac{p - p_0}{\frac{1}{2}\rho {V_s}^2} \tag{2.12}$$

where p_0 is the static pressure which is the pressure far upstream from the plate.

Figure 2.8b summarizes the results for the overall forces and moments on the flat plate. These are expressed in terms of the usual dimensionless coefficients:

$$\begin{aligned} C_y &= \frac{F_y}{\frac{1}{2}\rho {V_s}^2 LT} \\ C_l &= C_y \cos\beta \\ C_{zz} &= \frac{N_{zz}}{\frac{1}{2}\rho {V_s}^2 L^2 T} \\ a_y &= \frac{N_{zz}}{F_y L} \end{aligned} \tag{2.13}$$

Note that the moment coefficient C_{zz} and the point of application a_y are relative to the mid-chord of the plate. This figure includes the measured C_y coefficients of Fage etal, see Hoerner [69].

The vector plots show that recirculation develops for drift (or inflow) angles of between 10 and 15 degrees. Indeed this is confirmed by a small reduction in the

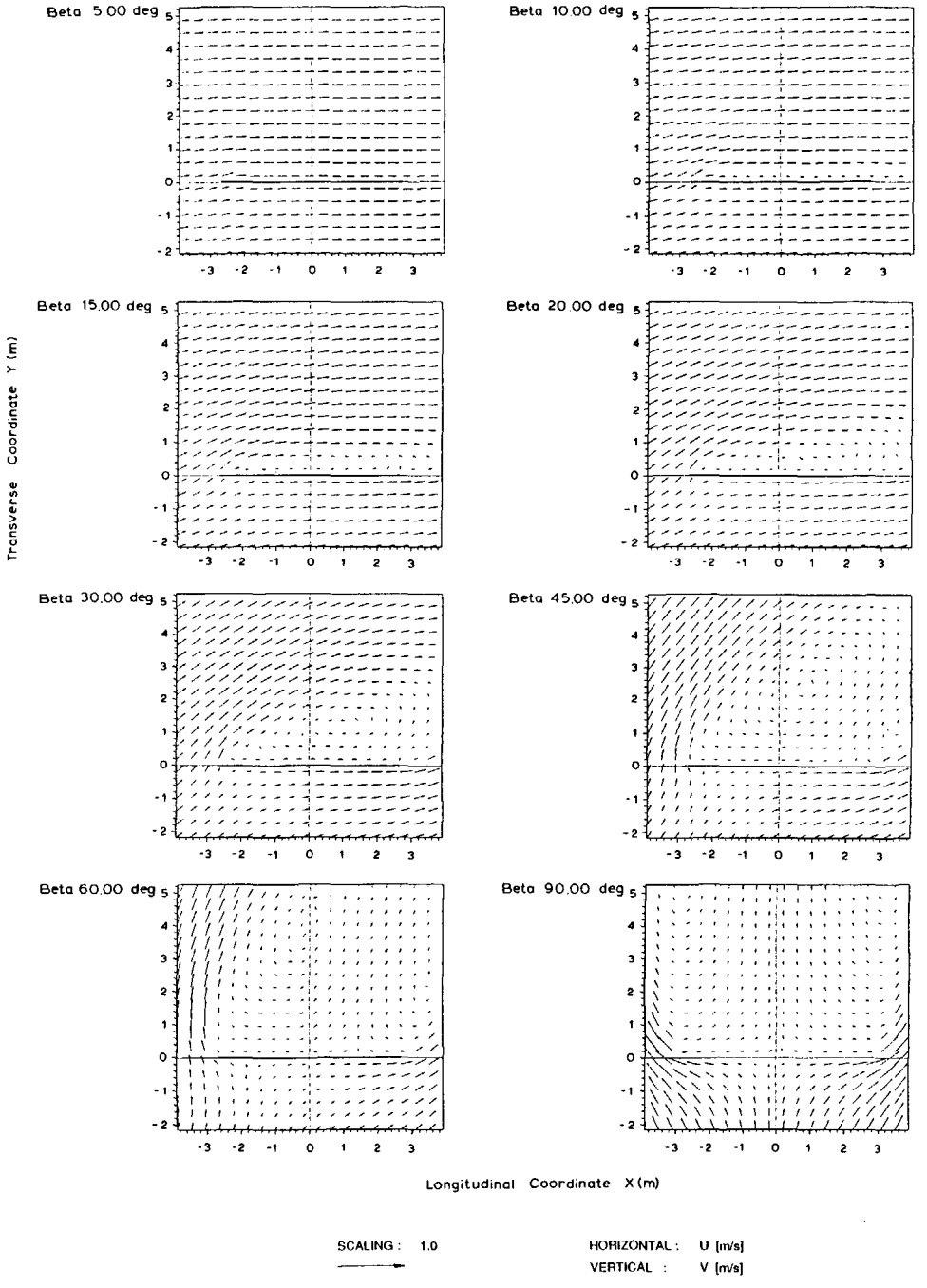

Figure 2.7: vector plots for two-dimensional flow around a flat plate at various drift angles

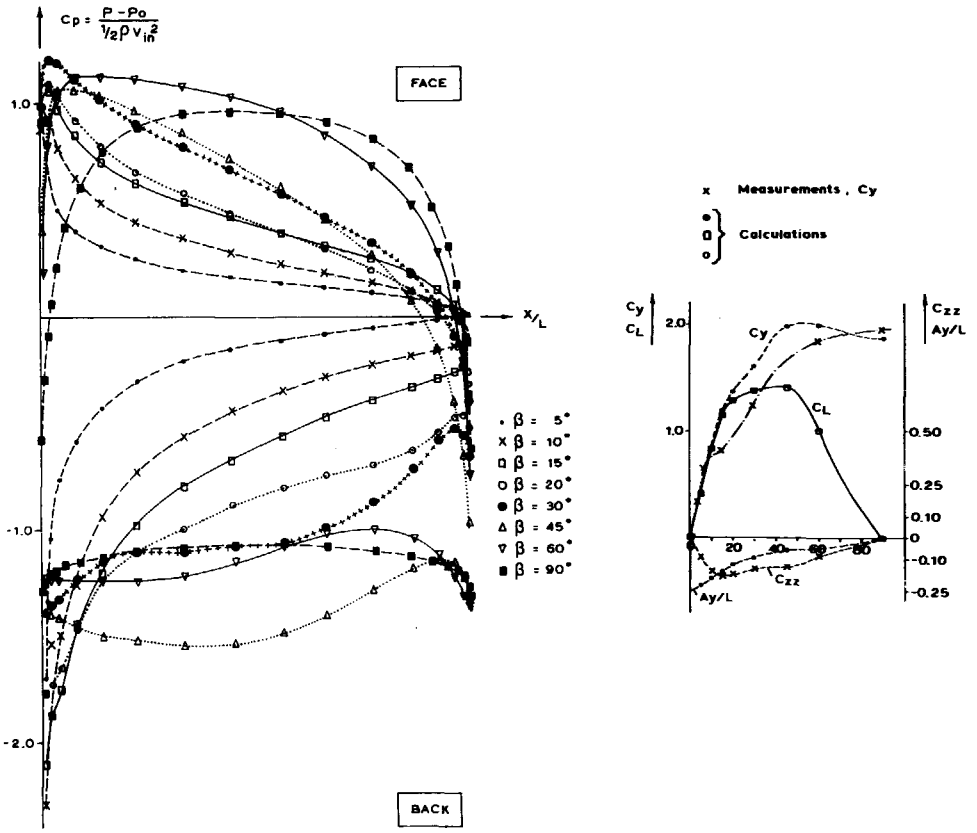

Figure 2.8: a. pressure distributions for two-dimensional flow around a flat plate at various drift angles; b. corresponding force and moment coefficients

tangent to the lift curve, see Figure 2.8a. The separation bubble increases in size with further increase in drift angle. For angles of around 30 degrees and beyond the flow exhibits negative x-velocities in the region close to the leading edge on the face (or starboard) side. This region can be thought of as bounded by the streamline through the stagnation point, i.e. that point close to the wall where the x-velocity is negligible. Similarly on the other side also such a streamline can be identified. Both streamlines move to the mid-chord position as the drift angle increases to 90 degrees.

This behaviour is also borne out by the pressure distributions, see Figure 2.8a, which show pressure peaks shifting away from the leading edge for increasing drift angles.

Comparing the overall side force expressed by C_y with some experimental results found by Fage etal, see Hoerner [69], see Figure 2.8b it is seen that qualitatively the agreement is adequate. The calculations however do not predict the stalling angle adequately and are overestimating the C_y value especially for drift angle between 20 and 70 degrees. The discrepancy can be attributed to several reasons.

For one the grid fineness may be insufficient to obtain correct flow and pressure predictions. However as shown in the subsequent discussion this does not appear to be the case.

Another reason for the inaccuracy in the force prediction may be the numerical scheme that was employed. It is known that this scheme introduces large amounts of numerical viscosity and thereby may lead to wrong predictions. Indeed a calculation for $\beta = 45$ degrees using both the Hybrid as well as the QUICK scheme yields appreciable differences in side force. This can be observed from Figure 2.9 where the pressure distributions are shown for both schemes. It is seen that the pressure distributions are quite different with the QUICK scheme giving a lower side force. This side force is however too low by approximately the same margin as the Hybrid calculations are too high.

An important reason for the remaining discrepancies is probably the employed turbulence model which is known to give erroneous predictions of e.g. the recirculation zone downstream of an obstruction, see e.g. Durst etal [71] and McGuirck etal [72]. Since this effect is related to pressure recovery and thereby also to the total side force this aspect is important. However for the purposes of the present study the observed discrepancies are entirely acceptable in view of the fact that primarily qualitative agreement is sought. Equally important is that the present study is more concerned with differences between flow fields (between cases with and without actuators) rather than with absolute flow fields. Therefore any absolute errors in e.g. force prediction do not jeopardize the conclusions drawn from the work. This is also the reason that calculations with the QUICK scheme were not pursued further.

Nevertheless the presented results demonstrate that the computational method can be expected to give insight in the phenomena of interest here and that it may well be possible to isolate important trends using the numerical model.

To establish the required extent and fineness of the grid for the considered cases a limited study was carried out to determine the influence of varying grid fineness.

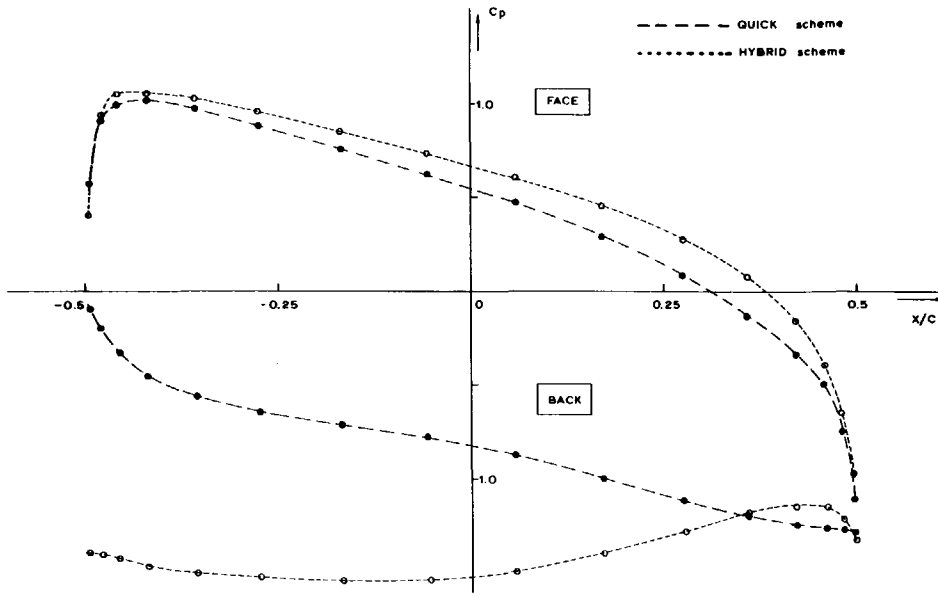

Figure 2.9: comparison of Hybrid and QUICK scheme pressure distributions for two-dimensional flow around a flat plate at 45 degrees drift angle

For the two-dimensional case discussed above the influence of grid fineness was investigated for the $\beta = 45$ degrees case. Figure 2.10 shows the obtained pressure distributions.

It is seen that especially close to the leading edge significant differences in pressure distribution are found. Especially on the suction side (port) large differences are observed. On this side it appears that the pressure distribution approaches a certain limiting distribution as the grid fineness is increased. The coarsest grid is clearly unacceptable compared to the remaining finer grids although it still shows the main features of the pressure distribution. The finest grid shows almost identical results to the one but finest grid.

The difference between the 64×68 and the 77×68 grid results is worth noting; the differences between these grids are confined to the regions away from the plate and constitute only a difference in the x-direction.

The two finest grids show a distinctly different behaviour on the suction side near the leading edge where the pressure initially increases with increasing chordwise coordinate before falling again towards mid-chord. The other coarser grids show a continuous decrease of pressure starting from the leading edge. Note that the results seem to be consistent in that the tangent to the C_p-curve at the leading edge gets steeper for the coarser grids.

Table 2.3 summarizes the corresponding force coefficients for the various grids. It is seen that the differences between the four finest grids are less than 3 % for

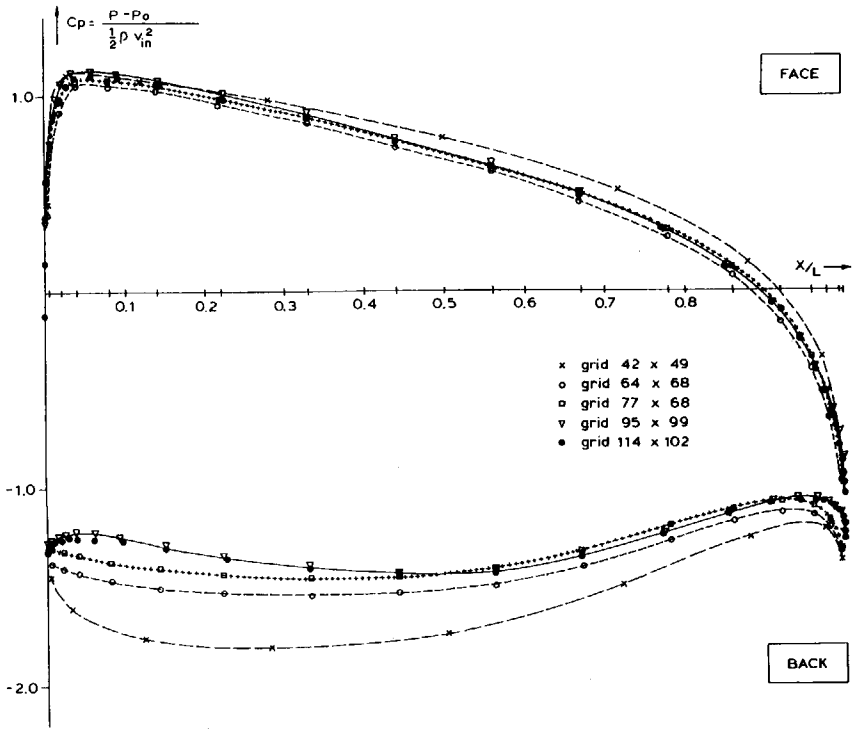

Figure 2.10: pressure distributions for various grids for $\beta = 45$ degrees calculations

the C_y-coefficient and less than 10 % for the C_{zz}-coeficient. For the present purpose such accuracies are amply sufficient and for the computations reported subsequently the adopted grid fineness is usually in the same range.

Grid	C_y	C_l	C_{zz}	a_y
42 × 49	2.28	1.61	-0.149	-0.065
64 × 68	1.97	1.39	-0.144	-0.073
77 × 68	1.93	1.37	-0.139	-0.072
95 × 90	1.92	1.35	-0.131	-0.068
114 × 102	1.91	1.35	-0.132	-0.068

Table 2.3: force coefficients for two-dimensional flow around a flat plate as affected by the grid definition - $\beta = 45$ degrees, $V_s = 0.319$ m/s

Prior to using this computational tool for the present work it was also established if the outflow boundary conditions had any significant influence. Both the type of condition (first order or second order derivative) as well as the location of the outflow boundary was varied. For the two-dimensional case reported here ($\beta = 90$ degrees) this variation did not have significant influence on the obtained pressure distribution: less than 1 % difference was found between the various drag forces.

Also the location of the symmetry boundaries was varied. The effect of blockage was clearly found but for the chosen location of the symmetry plane this effect was insignificant.

Summarizing it can be stated that the computational method appears to give realistic and consistent results for the typical flow problems that are of interest here and that if sufficiently fine grids are employed the results are also numerically accurate enough. For problems such as these a grid of approximately 70 × 70 node points seems adequate. In view of the usually smaller dimensions in vertical direction a number of cells of approximately 35 will usually suffice along the z-coordinate.

2.4 Experimental Tools

2.4.1 Three-component force transducers

Figure 2.11 shows the measuring frame for the horizontal forces. The frame includes three force transducers for the longitudinal force and for the two transverse forces. The frame can be mounted to a rotatable table under the carriage. This allows the model to be towed at various drift angles. The force transducers give the measured forces in ship-fixed coordinates. Hence different measurement ranges can be chosen for each transducer so that the generally much smaller longitudinal force can be measured with the same accuracy as the transverse forces.

The transverse forces forward and aft can be combined to give the turning moment around the reference point as well as the total transverse force.

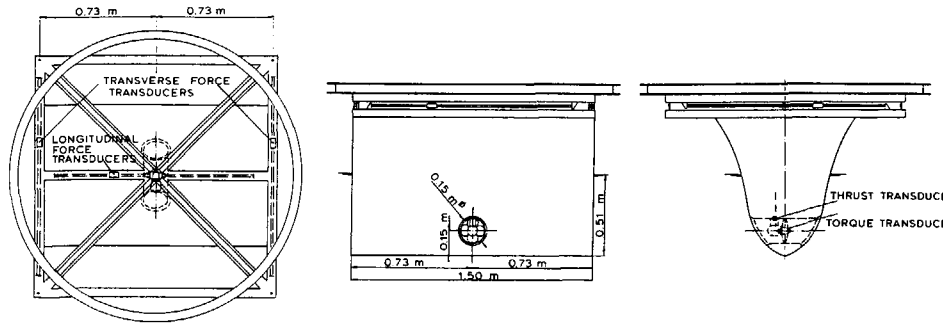

Figure 2.11: three-component force measurement frame

2.4.2 Propeller force measurement device

Figure 2.12 shows one of the rectangular drives used for the model tests. All rectangular drives are fitted with transducers to measure

- the thrust of the duct, T_n,
- the thrust of the propeller at the hub, T_p,
- the thrust of the propeller, hub, and vertical drive combination, i.e. the thrust of the entire unit, T_u,
- the torque of the propeller (at the hub), Q, and
- in some cases the side force of the entire unit, T_y.

2.4.3 2-D laser doppler velocity measurements

Until recently the most common device used to measure the magnitude and direction of the flow velocity at a certain point was the five-hole Pitot tube. Its main disadvantages are well known, i.e. disturbance of the flow by the device itself and a very low frequency response. In the middle of the 1970s a dual beam forward scatter Laser Doppler Velocimetry (LDV) system was introduced at MARIN.

Figure 2.13 shows this velocity measurement equipment, developed by MARIN and used for a part of the model tests described here.

By adjusting the position of the mirrors shown in the figure, a region of 0.4 m $\times$ 0.6 m can be scanned. With this equipment two components of the velocity vector can be measured simultaneously, the velocity in vertical direction and the velocity in horizontal direction. The 2D LDV is of the forward scatter principle and operates in the reference beam mode. The dimensions of its measuring volume are 0.214 mm

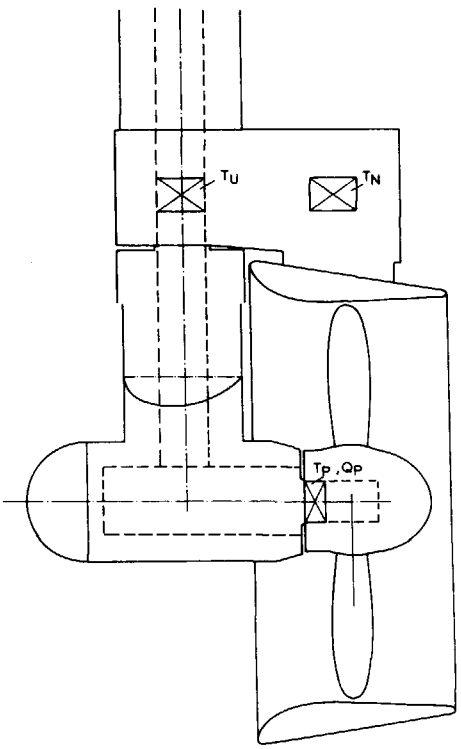

Figure 2.12: thruster rectangular drive with propeller force transducers

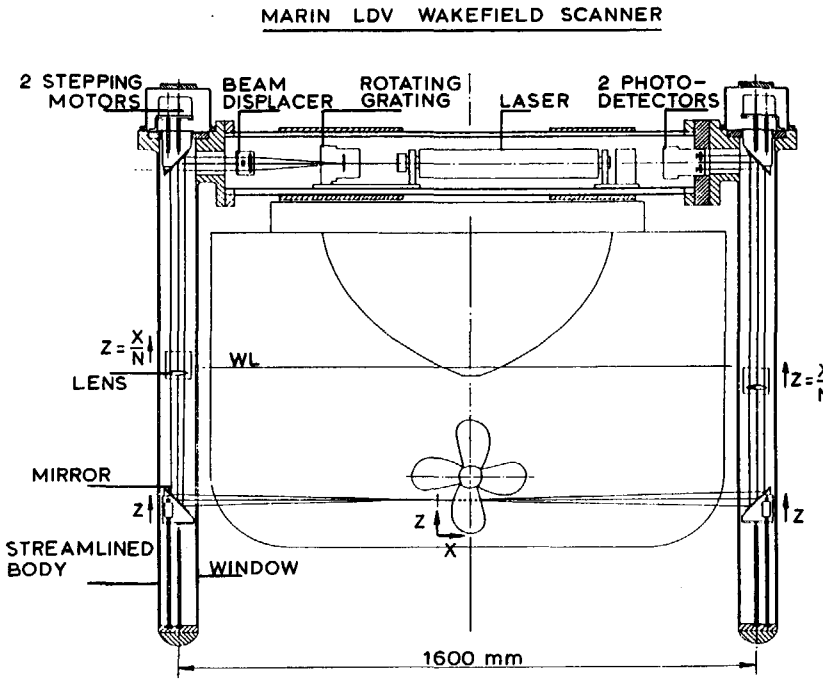

Figure 2.13: 2-D laser doppler anemometer

and 16.34 mm in vertical and horizontal directions respectively. This has a direct consequence for the accuracy of the measurements, the scan in the vertical direction leading to more accurate results.

2.4.4 3-D laser doppler velocity measurements

2.4.4.1 General

The LDV equipment described in the previous Section has the important limitation that only two components can be measured simultaneously. In 1987 a three-component back-scatter LDV system was introduced at MARIN. The following description is adapted from Gottmer etal, [73].

2.4.4.2 Description

The three component LDV system, designed for use in the deep water towing tank as well as the cavitation tunnel, consists of:

- The laser
- The optical components assembled in an underwater body, the optical head
- The traversing systems for the different facilities
- The signal processors
- A computer for control and analysis of the LDV measurements and simultaneous data collection and analysis of other relevant measurements.

In Figure 2.14 a schematic presentation of the system set-up is given.

2.4.4.3 Laser and optical components

The laser light for the LDV system is provided by a 4 Watt argon laser. All transmision and reception optics are arranged in an underwater body, the optical head. The laser light is transmitted to the optical head via a mono-mode fibre. This type of fibre is required to maintain coherence of the laser beam. Phase coherence is a necessary condition to obtain the desired interference fringe patterns in the measurement volume. When using a fibre, there is no need for a rigid mechanical coupling between the laser and the optical head. The latter can be displaced over relatively large distances while the laser is at a fixed location. This has important practical advantages:

- relatively light traversing system
- compact underwater body which results in:
    1. large area of accessible measuring points

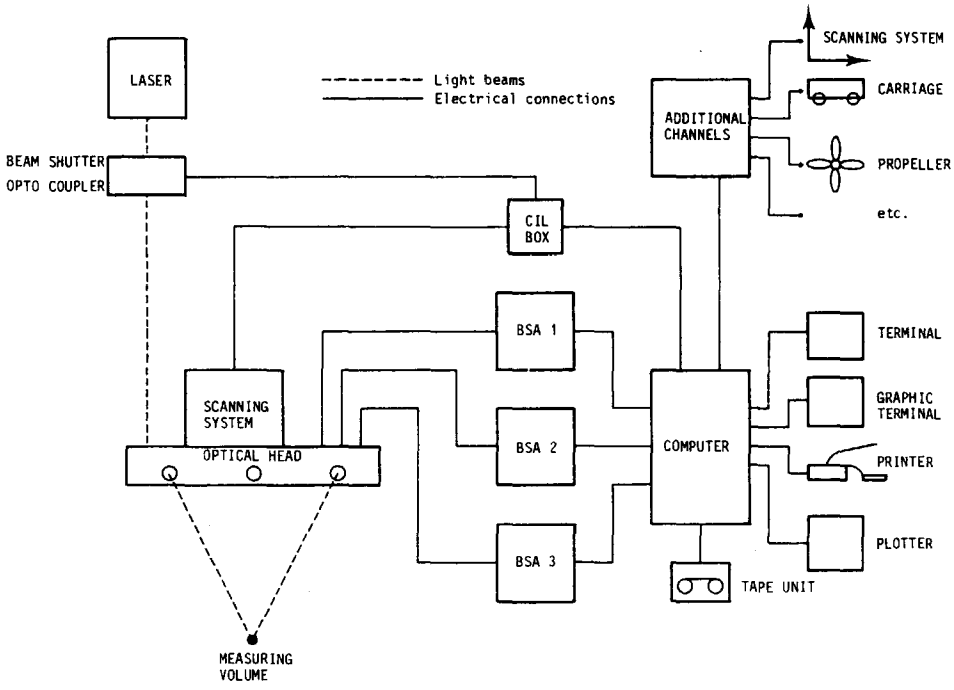

Figure 2.14: 3-D laser doppler anemometer system set-up

2. little disturbance of the flow

- better stability of the outgoing beams.

To obtain mono-mode light transmission the diameter of the transmitting part of the fibre is only 3 microns. This imposes high demands upon the condition of the laser beam: stringent TEM00 mode is required which means that the light intensity distribution at all cross sections along the beam should be Gaussian (for all colours separately).

In the optical head a colour separator and some beam splitters divide the incoming light into two blue beams (λ = 488.0 nm) and three green beams (λ = 514.5 nm). The five beams leaving the optical head are directed to intersect in a common probe volume or measurement volume which defines the measurement location. One horizontal velocity component is determined using the probe volume of the two blue beams. Note that one of the blue beams is frequency-shifted to allow determination of the velocity direction.

The other horizontal component is measured using two green beams. The intersection angle θ_1 between the bisection of the blue and green pairs of beams results in a fixed distance between the measurement volume and the optical unit of about 0.8 m. At this distance and because of the way the optical head is suspended on the strut no appreciable disturbance of the flow in the measurement volume is introduced by the optical head. The intersection angle, θ_1 of 33 degrees is sufficiently large to allow accurate determination of the two orthogonal velocity components (U and V), see Figure 2.15. The third (vertical) velocity component is obtained by the intersection of the unshifted green beam and the third green beam, which is again shifted (by a different amount) in frequency.

Particles in the common probe volume scatter the incoming light. Part of the backward scattered light enters the optical head via the centre window and is detected by one of the two photo multipliers (one for each colour). In the green system the signal contribution related to the vertical velocity component can be separated from the contibution related to the horizontal component by filtering the signal coming from the photo multiplier.

The dimensions of the measurement volume are determined by the beam width, the intersecting angles between the beams and the diameter of the pinhole in front of the photo multipliers. Typical dimensions are 1.3 mm and 0.4 mm.

Due to the finite velocity of the particles as they pass a measurement volume, the frequency of the scattered light is different from the transmitted light. This Doppler effect results in a frequency modulated signal coming from the photo multipliers, called the Doppler burst. The particle velocity, which by assumption defines the fluid velocity in the measurement volume, is proportional to the measured Doppler frequency.

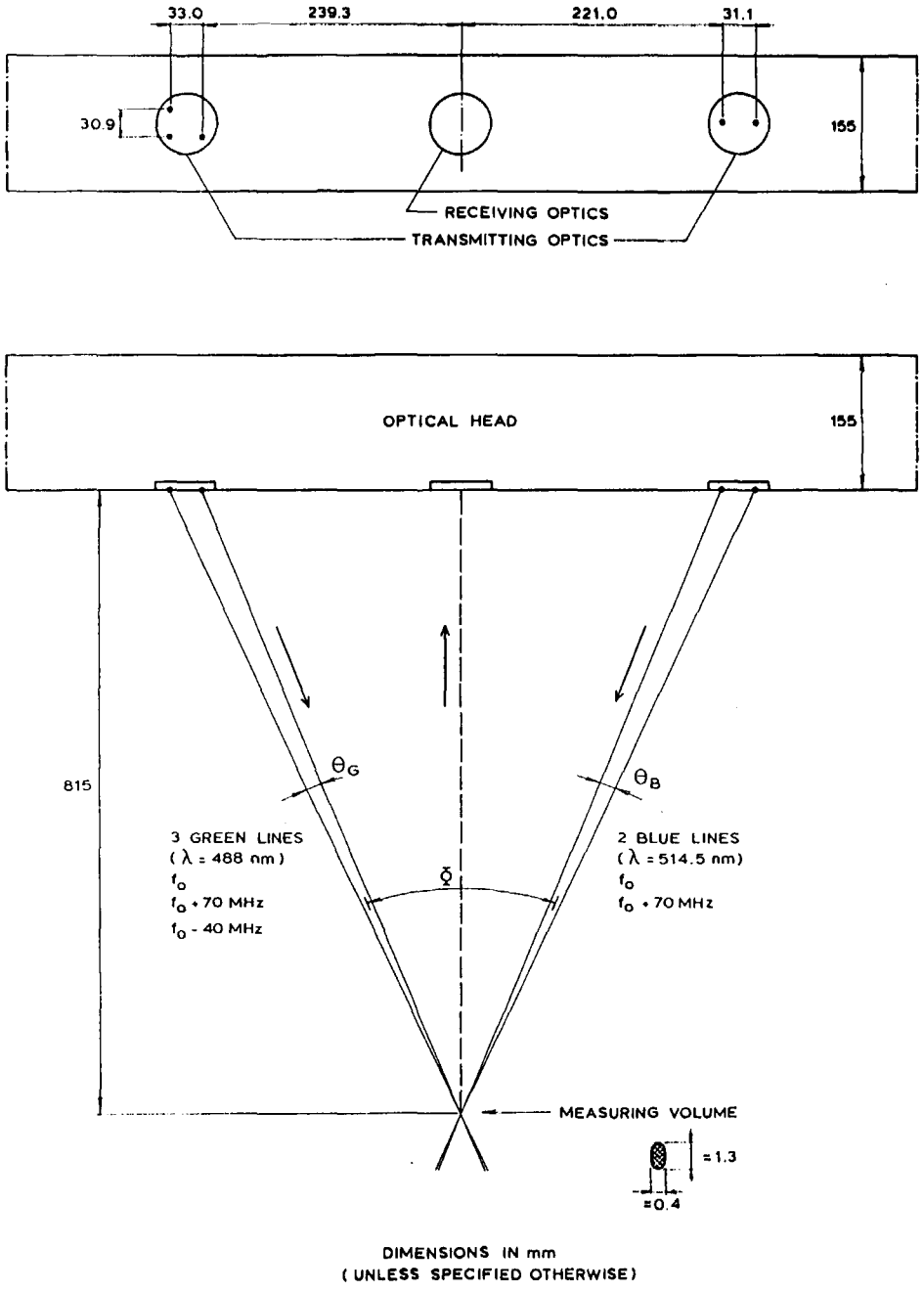

Figure 2.15: optical head and laser beams

2.4.4.4 Traversing system

The optical head is mounted on a faired underwater strut of 0.80 m fitted to a computer-controlled bi-directional traversing system allowing excursions of 1.15 m in the horizontal and 0.85 m in the vertical direction. Traversing in the other direction (parallel to the basin axis) is achieved by displacement of the thruster or ship model.

The accuracy of the traversing system is about 0.2 % of the range of the system. The resolution for the deep water towing tank traversing system is 0.5 mm.

To increase the range of accessible measuring points, the optical head can rotate around its main axis.

2.4.4.5 Signal processor

For the determination of the Doppler frequency from the burst signals a new type of processor called a Burst Spectrum Analyser (BSA) is used. This signal processor is designed and manufactured by DANTEC, Denmark. In total three BSA's are used, one for each velocity component.

As the name already indicates, the basic idea of the BSA is to extract the Doppler frequency from the burst signal by spectral analysis. This analysis is performed by the BSA's on the sampled signal input of the n-th burst coming from the photo multipliers. The power spectrum is calculated from the total burst signal. The Doppler frequency f_d is determined by the peak in the power spectrum. This method is different from that of counter processors which only use the signal information around zero-crossings.

For LDV measurements only the peak in the spectrum of the burst signal is of interest. To determine the position of the peak an interpolation is carried out between the maximum energy line in the spectrum and its two neighbouring local maxima. The position of the maximum of the interpolation is the measured Doppler frequency f_d.

Naturally, the input signal will always contain some disturbant noise which may cause additional maxima in the spectra. Therefore to validate a calculated spectrum, a BSA compares the two largest local maxima in the calculated spectrum. If the ratio between them is greater than 4 the spectrum is judged to be of a good quality and the calculated Doppler frequency is validated.

The BSA is very sensitive and reliable, so that even from bursts with a very poor signal-to-noise ratio, Doppler frequencies can be extracted. Therefore it is possible to obtain relatively high data rates (more than 100 Hz) without artificial seeding of particles in the water. Only the velocities of particles by nature present in the flow (and therefore uniformally distributed) are measured.

2.4.4.6 Analysis of the LDV measurements

The analysis comprises calculation of mean values, maxima, minima, standard deviations, turbulence intensities and Reynolds stresses. The input for the calculation

of these statistical quantities are the individual particle velocities determined from the received reflections in the measurement volume.

As already indicated, the particle velocity is proportional to the measured Doppler frequency. The proportionality constant, or calibration factor, depends only on the laser light wave length λ and the intersecting angle θ_2 between the beams. The intersection angle θ_2 amounts to approximately 2 degrees, see Figure 2.15.

Because of reflections and electronic noise, LDV measurements may contain invalid data despite the validation procedure in the BSAs as mentioned in the previous section. Invalid data can be detected because of their marked disparity from the rest of the measurements. These data should be removed from the signal before further analysis is done. The analysis program contains a procedure that removes data points remote from the mean compared to the standard deviation of the signal or which represent inconceivable accelerations.

The three particle velocity directions are measured independently. For statistical analysis (especially for determination of the Reynolds stresses and transformation to orthogonal components) only those data that are coincident in all three channels are of interest. The analysis program contains a coincidence filtering analysis procedure. If data points are present in all channels during a pre-defined coincidence time window, the mean values of the measurements within this time window are recorded as the measured value in that specific channel. The arrival time of this measurement is defined as the centre of the coincidence window. This centre is defined by the arrival times of all measurements in one pre-defined "coincidence master" channel.

The measured particle velocities are orthogonal to the bisection of the two intersecting beams and not orthogonal to each other. To convert the data and/or statistical quantities to orthogonal components a linear transformation is performed.

2.4.4.7 Accuracy of the LDV measurements

In the process of determining statistical quantities from reflections in the measurement volume, a number of error sources can be distinguished.

The sources are:

- Accuracy of spectral analysis depending on the number of samples and sample frequency of the burst signal
- Noise level in the burst signal arising from various light and electronic sources
- Stability of the beam wave lengths
- Accuracy of the measured intersection angle between the beams
- Accuracy of the applied frequency shifts
- Accuracy of the coordinate transformations depending on the optical configuration and the orientation of the optical head
- Distribution of the particles in the water

- Accuracy of towing carriage speed
- Digitization errors
- Unfavourable filter settings

All factors affect the accuracy of the LDV measurements. The design of the equipment was carefully done to minimize the errors as much as possible.

An idea of the accuracy can be obtained by determining the mean values and standard deviations of the particle velocities in calm water. These measurements are done in the deep water towing tank without a towed model after a long period of rest.

An example of the measured mean velocity components is presented in Table 2.4. Typical values of the standard deviation and the turbulence intensity are given in Table 2.5. All measurements were made with a fixed centre frequency of 500 kHz and bandwidth of 250 kHz for the horizontal channels and 400 kHz and 250 kHz respectively for the vertical channel. The frequency shift was set to 400 kHz for all channels.

Towing speed V_s (m/s)	U/V_s (-)	V/V_s (-)	W/V_s (-)
0.40	1.003	0.012	-0.008
0.80	1.003	0.015	-0.009
1.00	1.004	0.010	-0.009
1.50	1.004	0.012	-0.010

Table 2.4: mean values in an undisturbed flow (normalised for the towing speed)

Towing speed V_s (m/s)	$\sigma U/V_s$ (-)	$\sigma V/V_s$ (-)	$\sigma W/V_s$ (-)	τ (-)
0.40	0.0080	0.0251	0.0163	0.031
0.80	0.0062	0.0179	0.0082	0.021
1.00	0.0054	0.0163	0.0072	0.019
1.50	0.0043	0.0142	0.0067	0.016

Table 2.5: standard deviations and turbulence intensities (normalised for towing speed)

The reproducibility of the mean velocity measurements in Table 2.4 are within 0.3, 0.8 and 0.5 % of the carriage speed, V_s, for U, V and W respectively. An example of the reproducability of measurements in more turbulent flows is given in Figure 2.16. In this vector plot the V and W velocities are plotted in a y - z plane 0.5 m behind a model with running propellers.

Special BSA settings are applied for measurements with a desired carriage speed V_s up to 2 m/s and in flows with a moderate degree of turbulence. Using these

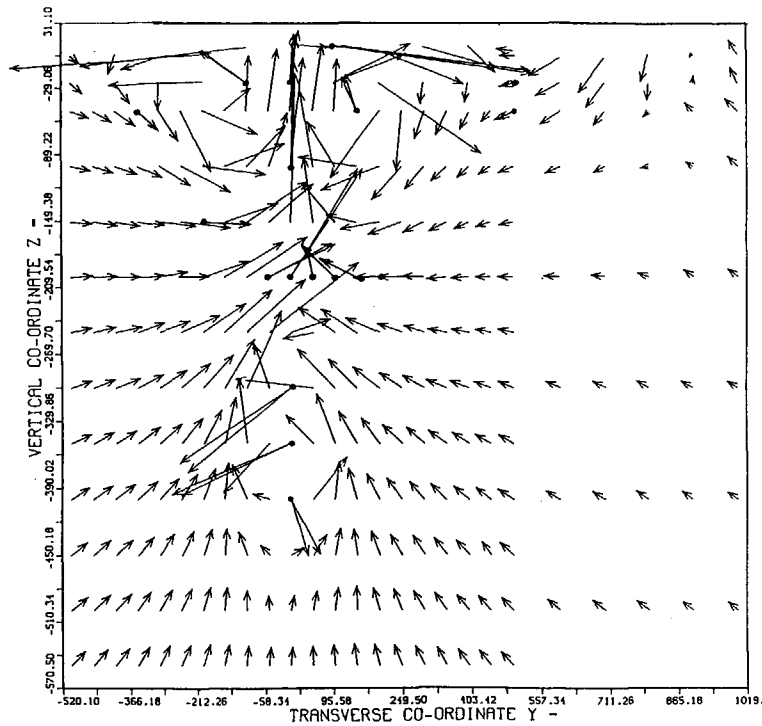

Figure 2.16: example of reproduction of 3-D LDV results

settings and supposing that more than 400 coincident data points are collected within 10 seconds the accuracies listed in Table 2.6 for the calculated normalised statistical quantities apply.

Quantity	Symbols	Accuracy (approx)
Fluid Velocity	U, V, W	0.005 V_s
Standard Deviation	$\sigma_U, \sigma_V, \sigma_W$	5 %
Turbulence Intensity	$\tau, (\tau > 0.02)$	0.0012 V_s
Reynolds stresses	$\overline{uv}, \overline{uw}, \overline{vw}$	5 %

Table 2.6: typical accuracy values for turbulent flow measurements

2.5 Models

2.5.1 Ships

The discussions in Chapter 3 refer to a number of ship models. To interrupt the discussion as little as possible, the relevant models are mentioned in Table 2.7; the details are given in Appendix A.

Model	Code	Model Nr	See Section
Ferry	S-F	5650	A.1
Container vessel	S-CV	5492	A.2
Hopper dredger	S-HD	6779	A.3
Semi-submersible workover vessel	S-SSWV	6306 1	A.4
Wedge-shaped hull	S-W	6236	A.5
Barge with bilges	S-BB	6497	A.6
Rectangular flat barge	S-RFB	-	A.7

Table 2.7: models used for present investigations

2.5.2 Rectangular drives, propellers, nozzles and rudders

For the reported tests and sometimes in conjunction with the just mentioned models, various drives, propellers, nozzles and rudders were used. Table 2.8 lists the various devices which are detailed in Appendix B.

Model	Code	Model Nr	See Section
Rectangular drive	T-AZ14	-	B.1
Rectangular drive	T-AZ21	-	B.2
Propeller	P-4929	4929	B.3
Propeller	P-4944	4944	B.4
Propeller	P-4347	4347	B.5
Nozzle	N-19A	-	B.6
Nozzle	N-37	-	B.7

Table 2.8: drives, propellers, nozzles and rudders used for present investigations

Chapter 3

ANALYSIS OF THRUSTER EFFECTIVITY

Chapter 1 has given an introduction to the present work and a review of past work. Chapter 2 covers all tools (experimental and theoretical) and models used for or during the present investigations. The present chapter forms the core of the work and gives an analysis of thruster effectivity.

After discussing the effectivity in general terms the chapter starts with the discussion of the findings for the slip-stream of the propulsors. It is shown that the thruster slipstream indeed behaves very similar to a turbulent jet and that some similarity in the velocity profiles can be established. Simple relations are given for the thruster slipstream describing the velocity decay and the jet diffusion. Calculations are discussed and sufficient correlation is found to merit the application of such calculations for general cases.

The effect of a flat wall on the slipstream is discussed and again the similarity with an ordinary wall jet is established. Subsequently the jet development for a thruster jet flowing around a ship's bilge is treated and the jet deflection is captured in a simple formula.

Next the effective forces induced by a pair of azimuthing thrusters are discussed both by measurements as well as calculations. The relation with the slipstream development is clearly established.

The effective forces induced by a thruster mounted under a floater of a semi-submersible are covered by presenting measurements. The measurements are analysed and a simple model is derived capable of predicting some of these interactions by using a resistance coefficient type of approach. These predictions are only valid for zero speed and some attention is paid to possible speed effects.

The chapter goes on by presenting calculations for simplified geometries to assess the effectivity of tunnel thrusters in arbitrary inflow. Detailed pressure distributions and flow fields are shown giving insight in the behaviour. Subsequently measurements are presented showing the importance of these effects. The combination of calculations and measurements is found to be a suitable way to address these phe-

nomena and to eventually establish a predictive tool for tunnel thruster effectivity.

Chapter 4 summarizes the main findings of this work.

3.1 Thruster Effectivity - Definition

As discussed in Chapter 1, the total forces necessary to propel a ship are usually not equal to the forces on this ship having the same speed but now being towed. This difference is for the stationary propulsion usually accounted for by the thrust deduction factor t relating the towed resistance R and the thrust T:

$$-R = (1-t)T \tag{3.1}$$

or

$$t = \frac{T+R}{T} \tag{3.2}$$

During stationary propulsion, the resistance of the propelled body equals the thrust:

$$-R_p = T \tag{3.3}$$

which gives:

$$-R_p + R = tT \tag{3.4}$$

which shows the more proper resistance augmentation.

In general operating conditions R_p and T need not be equal and opposite and the vessel may be accelerated and may experience other external forces. The total force on the ship is given by e.g.:

$$F_{tot} = R_p + T + F_{other} \tag{3.5}$$

where F_{other} may be any force such as wind force, wave force etc. This force is not relevant here and is set equal to zero. Substitution then gives:

$$F_{tot} - T - R = tT \tag{3.6}$$

Therefore the general thrust deduction can be defined by:

$$t = \frac{F_{tot} - T - R}{T} \tag{3.7}$$

For the present situation similar factors can be defined substituting the resistance by the current force and defining this factor for all three modes of motion, surge, sway and yaw:

$$C_{F_{Lh}} = \frac{F_L(V,n) - T_{ux}(V,n) - F_L(V,0)}{T_u(V,n)} \tag{3.8}$$

$$C_{F_{Th}} = \frac{F_T(V,n) - T_{uy}(V,n) - F_T(V,0)}{T_u(V,n)} \tag{3.9}$$

$$C_{N_h} = \frac{N(V,n) - T_{uy}(V,n)X_p + T_{ux}(V,n)Y_p - N(V,0)}{T_{uy}(V,n)X_p - T_{ux}(V,n)Y_p} \tag{3.10}$$

where $F_T(V,n)$, $F_L(V,n)$ and $N(V,n)$ are the total forces measured on the ship (assuming no other external disturbances) for inflow speed V and propeller RPM

n, and $F_T(V,0)$, $F_L(V,0)$ and $N(V,0)$ are the corresponding measured forces for non-operating propeller, i.e. the current forces. The thrust is denoted by $T_{ux}(V,n)$, $T_{uy}(V,n)$ being the total thrust of a unit respectively in X,Y-direction, i.e. inclusive of the resistance on e.g. a vertical drive. In these coefficients which are henceforth referred to as thruster effectivity the thrust values of several actuators can be summed. Note that the turning moments are invariably defined around midships.

The numerators of these coefficients can be regarded as induced forces: these are the forces related to a changed pressure distribution on the hull as induced by the working actuators in the vicinity of the hull.

For bollard pull conditions the above coefficients remain meaningful and assume the same meaning as always. For zero-thrust actuator conditions (usually small values of n) the coefficients are ill-defined; this is not serious since these conditions are the least relevant for the judgement of DP performance.

It would be more consistent to express the denominator in terms of the thrust in the direction of the considered mode, i.e. for $C_{F_{Lh}}$ the thrust in x-direction would be used. However for some cases this leads to ill-defined coefficients since a longitudinal force can be induced without the presence of a longitudinal thrust. An example of this behaviour is the lateral tunnel thruster.

Similarly thrust and torque coefficients are formed which give the ratio of the thrust or torque at a certain inflow speed relative to the corresponding values at bollard pull condition:

$$C_{Tu} = PTC = \frac{T_u(V,n)}{T_u(0,n)} \tag{3.11}$$

$$C_Q = PQC = \frac{Q(V,n)}{Q(0,n)} \tag{3.12}$$

The above coefficients address the induced hull force, i.e. the changed pressure build-up due to the working actuator. However it is of equal interest to address the total induced force, i.e. the hull force plus the thrust. In the next sections these coefficients are sometimes used which for a lateral tunnel thruster are:

$$HLC = C_{F_{Lh}} \tag{3.13}$$

$$HDC = C_{F_{Th}} + 1 \tag{3.14}$$

$$HMC = C_{N_h} + 1 \tag{3.15}$$

$$\tag{3.16}$$

The subsequent sections address the thruster effectivity in the above sense. Before doing so the thruster induced flow is investigated which is known to be an important agent of the thruster interaction phenomena observed in many situations. Once the induced flow is covered in some detail, the thruster effectivity is dealt with for a variety of sometimes simplified conditions. The relation between induced flow and induced force, (or interaction) is addressed and is found to be rather straightforward in some cases. For other cases this relation is not so clear and only qualitative results are obtained showing some of the prevailing effects.

3.2 The Induced Flow - Preliminaries

3.2.1 Introduction

The flow field around the propeller has been of interest to many researchers who are engaged in the hydrodynamics of both the marine as well as the aeronautical propeller. Since the Laser Doppler technique was introduced to measure the velocity in a flow field, many surveys of field point velocities were carried out, see e.g. Kotb etal [74], Koyama [75], Min [76], Kobayashi [77] and Schoenberger [78]. The purpose of some of these experiments is to verify the accuracy of and to refine numerical models for calculating propeller hydrodynamics. Other experiments are aimed at a better understanding of propeller/hull interactions. Most of the measurements were performed immediately behind or in front of the propeller, the distance to the propeller never exceeding approximately one diameter. Also the majority of the experiments referred to typical conventional, stationary, free sailing propulsive conditions.

For low speed manoeuvring and position keeping (including dynamic positioning) other conditions arise in terms of propeller loading, advance velocities, advance velocity direction and propeller axis orientation. Also thruster-thruster and thruster-hull interaction phenomena will occur unlike those encountered in ordinary propulsive conditions. These phenomena occur even if the thruster or propeller is located far away from the thruster or hull where the interaction manifests itself.

In 1983 a semi-empirical calculation procedure was developed at MARIN to obtain estimates of thruster-thruster interaction, Nienhuis [25]. The underlying assumption of the model was that the propeller slipstream behaves similar to a swirling turbulent jet.

The good correlation between model test results and calculations were an indication that this assumption was correct. However, a firm conclusion was not possible with this material since the extent of the thruster-thruster interaction is determined largely by two factors, i.e. the decrease of the velocity in the slipstream and the width of the slipstream. These two factors are related by way of the conservation of momentum.

In 1986/1987 the first detailed thruster slipstream measurements were made with the 2D LDV equipment of MARIN, see Section 2.4.3. These measurements referred to a thruster mounted under a simple-shaped barge. Some of the conditions, however, were very similar to a thruster in open-water condition and indicated a jet spread and velocity decay different from that predicted by the simple calculation procedure mentioned above.

The discussion in Sections 3.3 and 3.4 covers these and subsequent propeller slipstream investigations which were carried out using both the 2D LDV as well as the new 3D LDV equipment.

The results of the flow measurements show that the flow behind the ducted propeller behaves similar to a turbulent jet issueing from an orifice. The analysis of the experimental data shows that the velocity profiles in the propeller wake exhibit

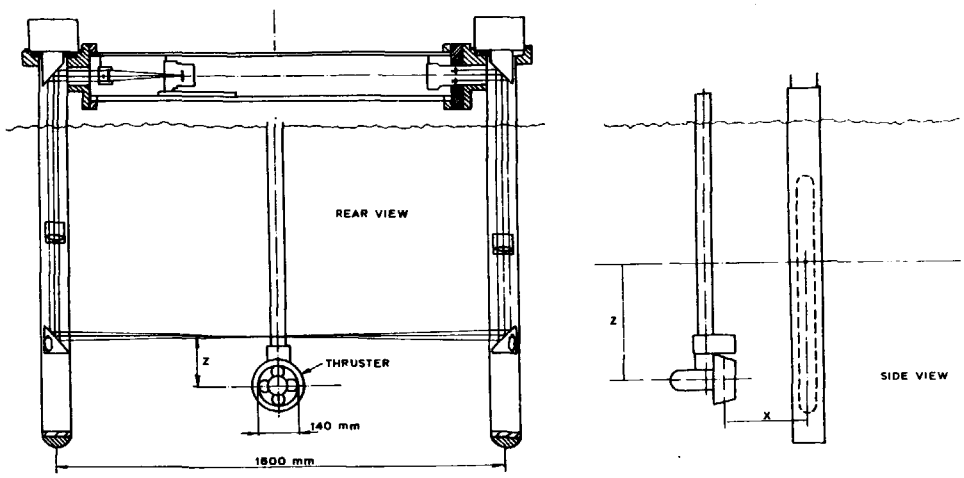

Figure 3.1: test set-up for velocity measurements in the slipstream of a thruster with nozzle 37 in open water

some similarity. The functions expressing the variation of maximum axial velocity and jet width with distance to the propeller plane are given. The effects of advance speed and direction on the wake field are presented and discussed.

Calculations are presented and show a qualitative agreement with the measurements although the jet spread is over-predicted. Nevertheless the computations are sufficiently in agreement to justify the application of the numerical model also for determining the thruster effectivity in various conditions. This is the subject of the subsequent sections, Sections 3.5 and 3.6.

3.2.2 Measurements and calculations

3.2.2.1 Measurements on a thruster with nozzle 37 in open water and above a flat wall

For this case two-component velocity measurements were carried out using the 2D LDV equipment, see Section 2.4.3. The thrust and torque of the thruster were measured, see Section 2.4.2.

The test set-up is shown in Figure 3.1 which shows the arrangement of the thruster, the LDV equipment and the flat plate which was present for part of the tests. The distance of the thruster axis to the plate amounts to $h_p = 0.75D$, which is a commonly encountered value. The propeller axis was located 1025 mm (approximately 7.3 D) under the water surface to eliminate free surface effects.

Table 3.1 gives all details pertaining to the models used for this test series.

The tests were carried out in MARIN's Deep Water Towing Tank. The test con-

Particular	Code	Quantity	Details in Section
Propeller	P-4929	1	B.3
Nozzle	N-37	1	B.7
Rectangular drive	T-AZ14	1	B.1

Table 3.1: models for measurements in the slipstream of a thruster with 37 nozzle in open water and above a flat plate

Advance Velocity V_s (m/s)	Distance to Flat Plate h_p (m)	Distance from Propeller Plane x (m)
0.0	∞	0.080, 0.141, 0.175, 0.247, 0.317, 0.458, 0.600, 0.740 0.881, 1.163, 1.445
0.406	∞	0.080, 0.317, 0.458, 0.600, 0.740, 0.881, 1.163, 1.445
0.811	∞	0.080, 0.175, 0.317, 0.458, 0.600, 0.740, 0.881, 1.163 1.445
0.0	0.105	0.080, 0.175, 0.317, 0.595, 0.881, 1.163, 1.445

Table 3.2: test content for velocity measurements on a thruster with MARIN nozzle 37 in open water

ditions are summarized in Table 3.2; the used models can be identified in Figure 3.1. The pitch setting equals $P_{0.7}/D = 1.1$ for all tests while the propeller rate amounted to 857 per minute. For all cases the thruster angle was set equal to zero, i.e. parallel to the basin axis.

The measurements comprise the two mean (axial and vertical) velocities U, W and the thruster parameters n, Q, T_u and T_n.

Thruster with nozzle 37 below barge-shaped hull. For this case two-component velocity measurements were carried out using the 2D LDV equipment, see Section 2.4.3. The thrust and torque of the thruster were measured, see Section 2.4.2.

The test set-up is shown in Figure 3.2 which shows the variable position of the thruster, the LDV equipment and the barge-shaped hull with variable bilge shapes.

Section A.6 describes all details pertaining to the models used for this test series. The tests were carried out in MARIN's Deep Water Towing Tank. The test conditions are summarized in Table 3.3; the relevant parameters can be identified in Figure 3.2.

Thruster with MARIN nozzle 19A in open water. For this case three-component velocity measurements were carried out using the 3D LDV equipment, see Section 2.4.4. The thrust and torque of the thruster were measured, see Section 2.4.2.

The test set-up is shown in Figure 3.3 which shows the variable position of the thruster and the LDV equipment with the optical head.

Table 3.4 gives all details pertaining to the models used for this test series.

These tests were also carried out in MARIN's Deep Water Towing Tank. The test

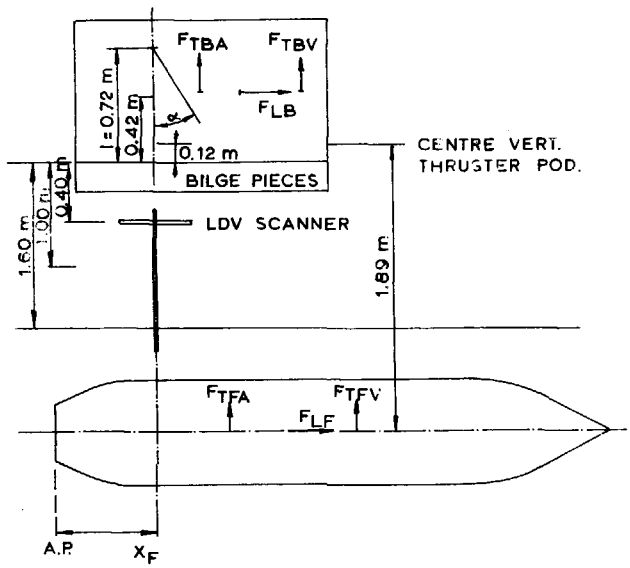

Figure 3.2: test set-up for velocity measurements in the slipstream of a thruster mounted under a barge-shaped hull

Bilge Shape Radius R_b (m)	Thruster Position l_T (m)	LDV Position d_{LDV} (m)
Circular, 0.0	0.120, 0.420, 0.720	0.400, 1.000, 1.600
Circular, 0.050	0.120, 0.420, 0.720	0.400, 1.000, 1.600
Circular, 0.100	0.120, 0.420, 0.720	0.400, 1.000, 1.600
Circular, 0.200	0.120, 0.420, 0.720	0.400, 1.000, 1.600
V-shaped	0.120, 0.420, 0.720	0.400, 1.000, 1.600

Table 3.3: test content for velocity measurements for a thruster with nozzle 37 below a barge-shaped hull

Particular	Code	Quantity	Details in Section
Propeller	P-4929	1	B.3
Nozzle	N-19A	1	B.6
Rectangular drive	T-AZ14	1	B.1

Table 3.4: models for measurements in the slipstream of a thruster in open water

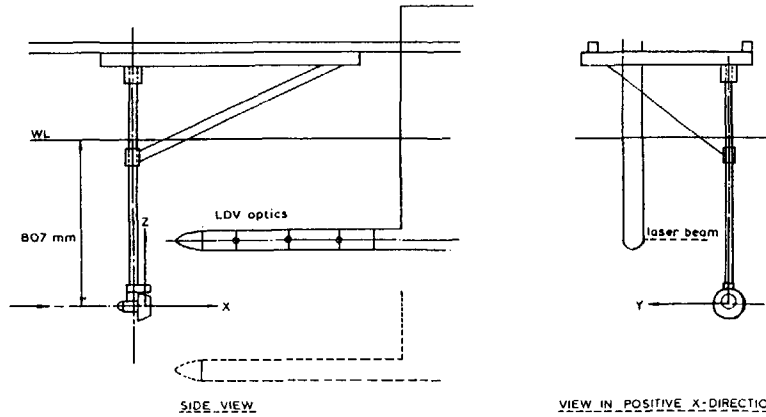

Figure 3.3: test set-up for velocity measurements in the slipstream of a thruster with 19A nozzle in open water

Advance Velocity V_s (m/s)	Thruster Angle α_T (deg)	Distance from Center Propeller Plane x (m)
0.0	0.0	-0.35, -0.15, -0.095, 0.095, 0.14, 0.24, 0.35, 0.49, 0.70, 0.98, 1.40, 2.10
0.406	0.0	-0.15, -0.095, -0.08, 0.08, 0.095, 0.14, 0.35, 0.49, 0.70, 0.98, 1.12, 1.40, 1.68, 2.10
0.406	30.0	0.121, 0.212, 0.424, 0.849, 1.212, 1.818
0.406	60.0	0.123, 0.175, 0.245, 0.35, 0.49, 1.05

Table 3.5: test conditions for velocity measurements for a thruster with 19A nozzle in open water

conditions are summarized in Table 3.5; the relevant parameters can be identified in Figure 3.3. The pitch setting of the propeller equals 1.1 at a propeller rotation rate of $n = 857$. The propeller axis was located 0.807 m below the water surface to eliminate the free surface effects.

The measurements comprise the three mean velocities U, V, W, the six Reynolds stress components $\overline{uu}, \overline{vv}, \overline{ww}, \overline{uv}, \overline{uw}, \overline{vw}$ and the thruster parameters n, Q, T_u and T_n.

3.2.2.2 Slipstream calculations

As the base case the flow induced by a thruster in open water was calculated using the method described in Chapter 2. Several levels of detail for the rectangular drive were considered. The simplest approach was to omit the vertical drive altogether

and to distibute the thrust and torque uniformly over the propeller disk. The grid for this case consisted of 41 × 51 × 46 cells. The fluid domain extends from -1.0 $\leq x \leq$ 15.0, -2.5 $\leq y \leq$ 2.5, -2.5 $\leq z \leq$ 1.5 m which is significantly smaller than the basin dimensions but was considered to be sufficient for the region of interest. The part of the grid close to the propeller is shown in Figure 3.4.

As a next case the force per unit of area for the thrust and torque was taken to vary linearly with the radial coordinate, neglecting again the presence of the hub.

The third computed case includes a single strip in front of the propeller to account for the vertical drive. The strip extends from -0.015 $\leq y \leq$ 0.015, -0.015 $\leq z \leq$ 0.18 and is located at x = -0.065, i.e. 0.065 m in front of the propeller plane. Part of the grid was modified as shown in Figure 3.5. Note that the force field extends down to the propeller axis and that the hub is not represented.

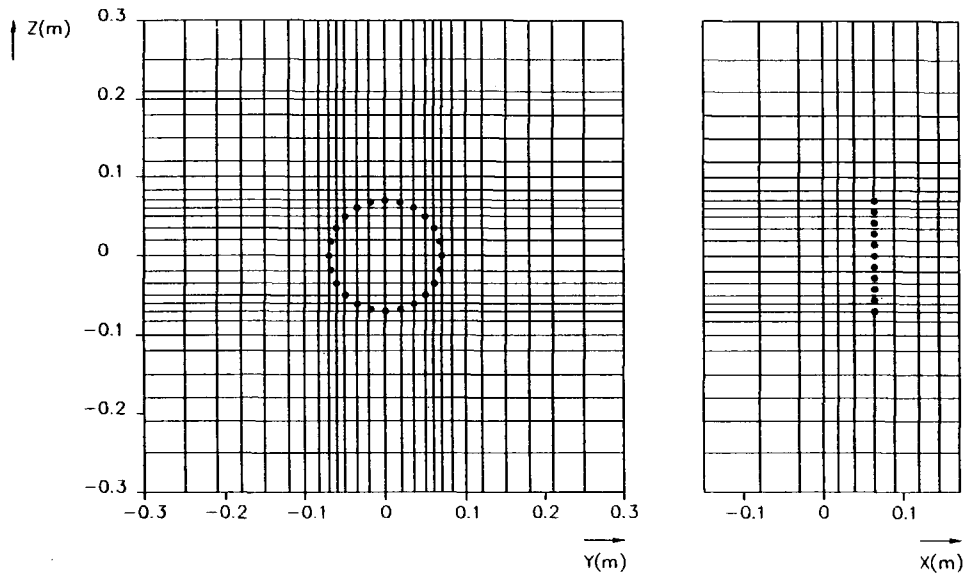

Figure 3.4: grid for the computations without the vertical drive

As a fourth case the vertical drive was modelled in slightly more detail, as shown in Figure 3.6. The arrangement consists of twelve flat plates, two of them representing the forward and aft end plates of the hub box and two of them representing the forward and aft end of the pod. Note that the force field has non-zero values only for radial coordinates $r \geq$ 0.0345, i.e. outside the circle enclosing the square hub plates. For this computation the grid consists of 63 × 53 × 58 cells where the grid is refined close to the vertical drive.

Compared to the open water case the fluid domain was restricted to cover $z \geq$ -0.106 and the grid close to z = -0.106 was adapted.

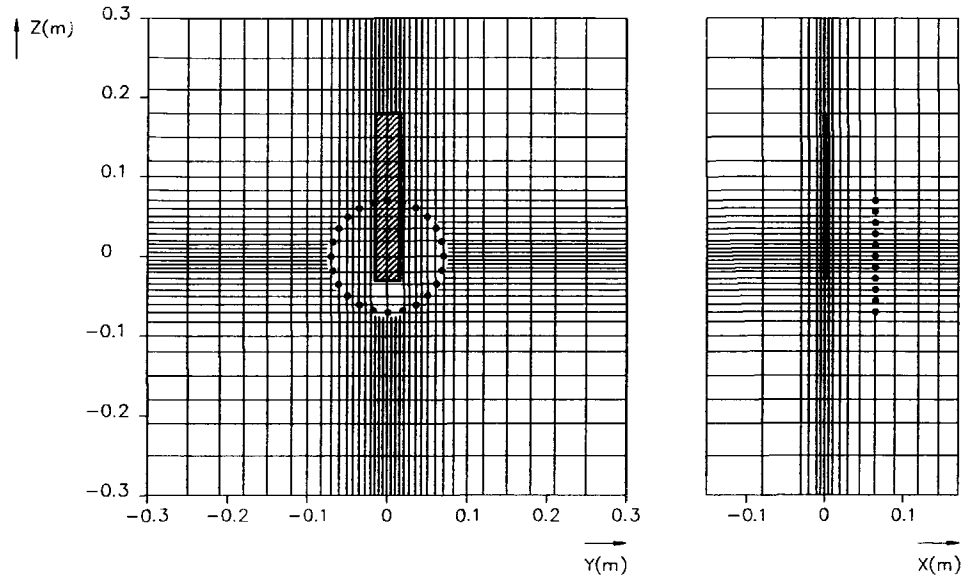

Figure 3.5: grid for the computations with the vertical drive modelled by a single strip

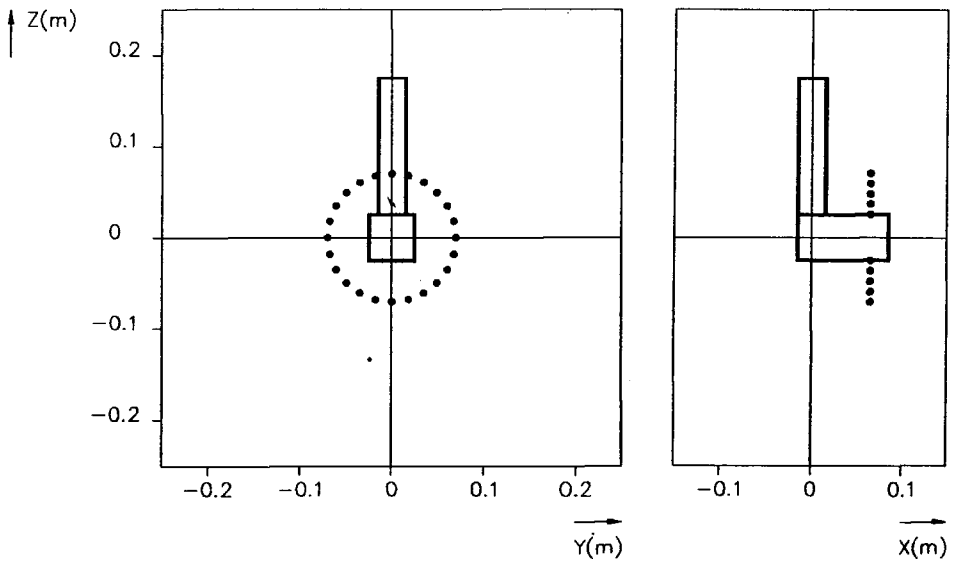

Figure 3.6: modelling of vertical drive

3.3 The Induced Flow for Open Water

3.3.1 Thruster with MARIN 19A nozzle in open water

The thrust and torque levels measured during the tests are given in Table 3.6.

α_T (deg)	V_s (m/s)	T_{tot} (N)	K_{T_p} (-)	K_{T_u} (-)	K_{T_n} (-)	K_Q (-)
0	0	37.43	0.262	0.464	0.202	0.0534
0	0.406	35.88	0.250	0.445	0.195	0.0519
30	0.406	33.94	0.237	0.421	0.184	0.0498
60	0.406	33.55	0.230	0.416	0.186	0.0496

Table 3.6: thrust and torque measurement results for 3D LDV measurements

3.3.1.1 Propeller wake development for axial inflow ($\alpha = 0$) - axial flow component

In this case the inflow velocity, the measured velocity U, the thrust and the propeller axis are all parallel. The mean axial velocities at some of the covered x-stations are shown in Figure 3.7 for the $J = 0$ condition. The results for $J = 0.2$ are depicted in Figure 3.8. These figures show the measured U-velocities as a function of the radial coordinate r.

Drawing from the analogy with normal turbulent jets, the axial profiles are described by five characteristic parameters:

- The maximum velocity U_m
- The velocity on the jet center line U_a
- The radial position of maximum velocity r_m or its normalized value, $R_m = r_m/R$
- The outer half velocity radial position r_{h2} or its normalized value $R_{h2} = r_{h2}/R$ at which the axial velocity $U = 0.5(U_m + V_s)$. Here V_s refers to the ambient velocity i.e. advance speed.
- The inner half velocity radial position r_{h1} or its normalized value $R_{h1} = r_{h1}/R$ at which the axial velocity $U = 0.5(U_m + U_a)$.

The five characteristic parameters for the axial velocity profiles derived with the least-squares analysis are given in Tables 3.7 and 3.8.

Comparing these results it is clear that the propeller wake for $J = 0$ diffuses more rapidly than for $J = 0.2$. As will be shown for the LDV measurements for the thruster with the MARIN 37 nozzle, it may be noted that the velocity field behind the propeller behaves in a manner basically similar to a turbulent jet. This jet model was already adopted in thruster interaction calculations, see Nienhuis [25].

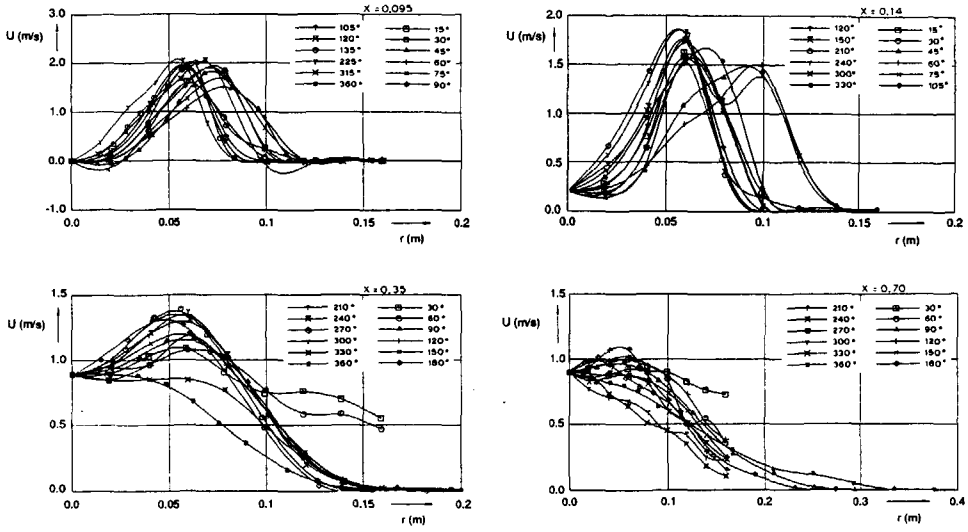

Figure 3.7: axial velocities in the wake of a thruster for $J = 0.0$

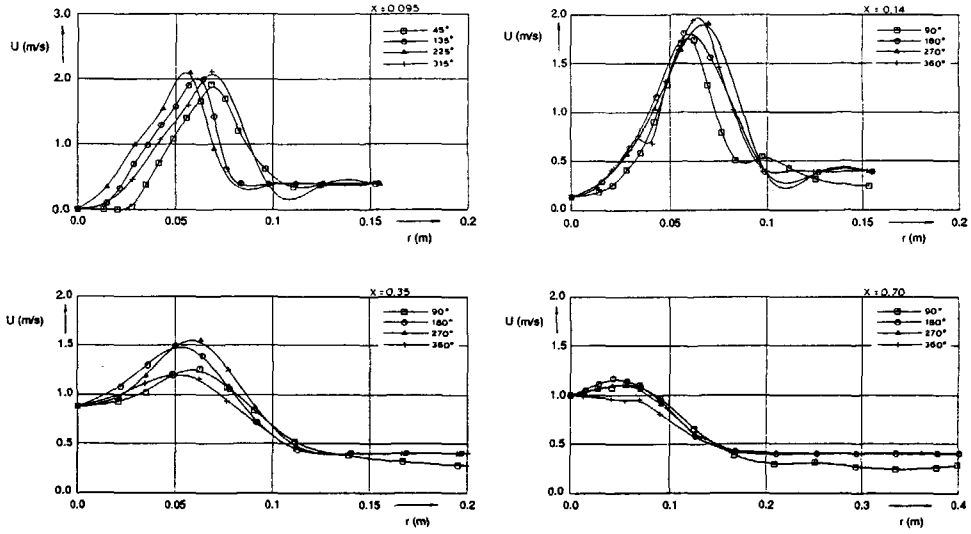

Figure 3.8: axial velocities in the wake of a thruster for $J = 0.2$

x	(m)	0.095	0.14	0.24	0.350	0.49	0.70	0.98	1.40	2.10
U_m	(m/s)	1.951	1.781	1.487	1.335	1.131	0.901	0.862	0.685	0.46
U_a	(m/s)	-0.05	0.201	0.625	0.891	0.931	0.891	0.863	0.685	0.46
R_{h1}	(-)	0.521	0.556	0.495	0.462	0.297	0.125	0.001	0.001	0.001
R_{h2}	(-)	1.025	1.101	1.151	1.313	1.547	1.763	2.271	3.151	5.35
R_m	(-)	0.861	0.823	0.771	0.741	0.671	0.351	0.001	0.001	0.001

Table 3.7: velocity measurements for a thruster with 19A nozzle: change of U_m, R_m, R_{h1}, R_{h2}, U_a with x for $J = 0$

x	(m)	0.095	0.14	0.24	0.35	0.49	0.70	0.98	1.40	2.10
U_m	(m/s)	2.101	1.898	1.681	1.541	1.341	1.135	1.011	0.867	0.77
U_a	(m/s)	-0.101	0.151	0.601	0.881	1.021	1.001	0.991	0.871	0.77
R_{h1}	(-)	0.501	0.615	0.524	0.501	0.331	0.335	0.001	0.001	0.001
R_{h2}	(-)	1.001	1.091	1.091	1.201	1.341	1.541	1.741	2.321	3.401
R_m	(-)	0.901	0.924	0.807	0.801	0.661	0.571	0.001	0.001	0.001

Table 3.8: velocity measurements for a thruster with 19A nozzle: change of U_m, R_m, R_{h1}, R_{h2}, U_a with x for $J = 0.2$

By further analogy with a turbulent jet the velocity field behind a propeller may be divided into two zones:

- The initial developing zone where a core flow with lower axial velocity is surrounded by a progressively thickening turbulent shear layer. The velocity profile in this zone is influenced by propeller geometry (diameter, hub area, pitch), propeller loading and its distribution. The velocity profiles in this zone have a double peak displaced from the center line. The hollow at the center line is caused by the presence of the hub.
- The fully developed zone where the velocity profiles have a single peak at the shaft center line.

The variation of U_m and U_a with x is shown in Figure 3.9. From the figures the following features can be observed. The shape of the axial velocity profiles and the maximum velocity vary with axial distance. At the stations just downstream of the propeller, e.g. $x/D = 0.68$ the axial velocities are almost zero or negative at the inner propeller radii due to the influence of the propeller hub, see Figures 3.7 and 3.9.

The maximum velocity occurs at around $r = 0.8R$. With increasing axial distance, the velocity at the center line U_a increases gradually due to turbulent mixing and the position of maximum velocity position R_m moves from $r/R \approx 0.8$ to the x-axis. The maximum axial velocity decreases with increasing axial distance and can be expressed by the following formula:

$$\frac{U_m}{V_j} = \frac{a}{(\frac{x}{D})^b} \tag{3.17}$$

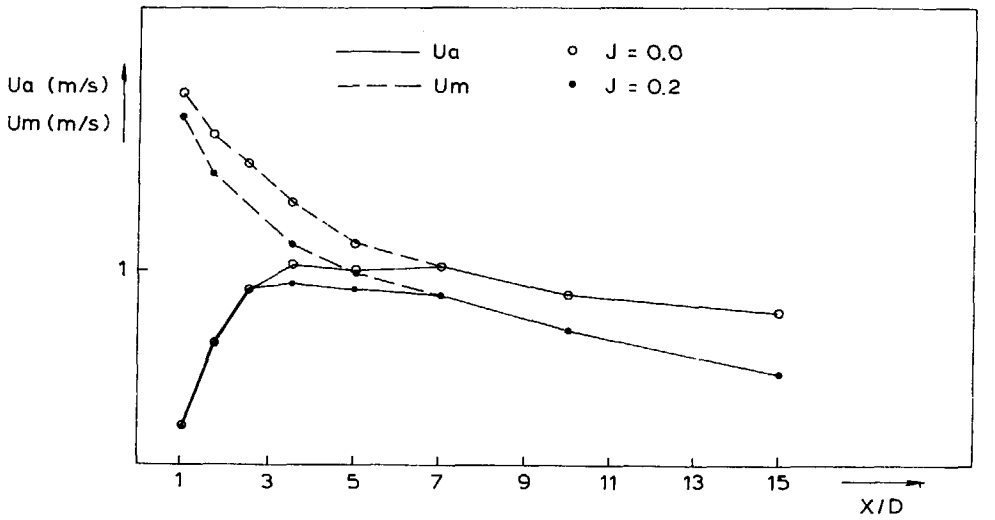

Figure 3.9: measured variation of maximum velocity U_m and center line velocity U_a with distance to the propeller

in which V_j is the average velocity in the propeller race can be calculated on the basis of simple momentum theory, see Gutsche [7]:

$$V_j = (1 - k_m)V_s + k_m\sqrt{V_s^2 + \frac{2T_{tot}}{\rho A}} \tag{3.18}$$

where T_{tot} is the total thrust (propeller and nozzle and vertical drive), A is the propeller disk area and ρ is the density of water. The factor k_m depends on the selected location in the propeller race: $k_m = \frac{1}{2}$ at the propeller plane and $k_m = 1$ far downstream of the propeller plane; usually k_m is close to the value of 1 already at D downstream of the propeller.

The regression analysis gives the approximate values for the coefficients a and b in Equation 3.17 listed in Table 3.9.

J	a	b
0	0.805	0.389
0.2	0.878	0.315

Table 3.9: coefficients for velocity decay in propeller slip stream

The regression coefficients are based on taking the value of V_j far downstream of the propeller, i.e. $k_m = 1$. The result is different from the solution $U_m \sim 1/x$ deduced by e.g. Davis etal [79] from the simplified equations for a free non-swirling jet in the fully developed region. The present result indicates that the axial velocity

decay is decreased by swirl due to an increase in turbulent mixing and entrainment. According to Stern et al. [80], swirling turbulent flows are classified as weak or strong depending on the magnitude of the rotation parameter nD/V_s. It is seen from their investigation that for weak swirl the axial velocity defect follows the $x^{-2/3}$ power law. For strong swirl the velocity defect goes with $x^{-1/3}$. The regression results indicate that for the operational condition of a DP system, i.e low values of J, the swirl is apparently strong and the variation of maximum axial velocity with x follows approximately the $x^{-1/3}$ power law. However the regression result is very sensitive to the use of a virtual origin x_0: if the maximum velocity were defined by $U_m/V_j = a/(x/D - x_0)^b$ the coefficient b assumes a value appropriate for a weak-swirl situation. The fit with the experimental results would then be better. It is doubtful however if so few data allow the use of three fitting coefficients. This matter cannot be resolved with the available information.

The propeller jet width increases with the distance to the propeller. It is difficult to determine the jet width, the edge of the wake being difficult to discern and highly fluctuating. The characteristic parameter R_{h2} may be taken as a representation of the half width of the wake for the fully developed wake zone. For the initial zone, the half width of the wake can be adequately represented by:

$$R_j = R_{h1} + R_{h2} - R_m \tag{3.19}$$

where R_j refers to the non-dimensional half-width of the wake. In the fully developed zone $R_m = 0$, $R_{h1} = 0$ and therefore $R_j = R_{h2}$. Thus the above expression may be used in the entire region of the wake.

The variation of R_{h2}, R_j, R_{h1} and R_m with x are shown in Figure 3.10. For $x/D < 10$, R_{h2} shows approximately a linear dependence on x. The approximations are for R_{h2}:

$$\begin{aligned} R_{h2} &= 0.79 + 0.22(x/D) \qquad J = 0 \\ R_{h2} &= 0.86 + 0.14(x/D) \qquad J = 0.2 \end{aligned} \tag{3.20}$$

and for R_j as a function of x for both $J = 0$ and $J = 0.2$:

$$\begin{aligned} R_j &= 0.45 + 0.26(x/D) \qquad J = 0 \\ R_j &= 0.49 + 0.18(x/D) \qquad J = 0.2 \end{aligned} \tag{3.21}$$

It illustrates that the spread of the wake can be considered to be approximately proportional to x; this result is similar to that for a free jet.

The characteristic parameter R_{h1} or R_m of the axial velocity profile can be used to represent the diffusion in the development region. The variation of R_{h1} and R_m with axial distance x may be approximately expressed by:

$$\begin{aligned} R_{h1} &= 0.58 - 0.076(x/D) \qquad J = 0 \\ R_{h1} &= 0.62 - 0.074(x/D) \qquad J = 0.2 \\ R_m &= 0.91 - 0.11(x/D) \qquad J = 0 \\ R_m &= 0.97 - 0.11(x/D) \qquad J = 0.2 \end{aligned} \tag{3.22}$$

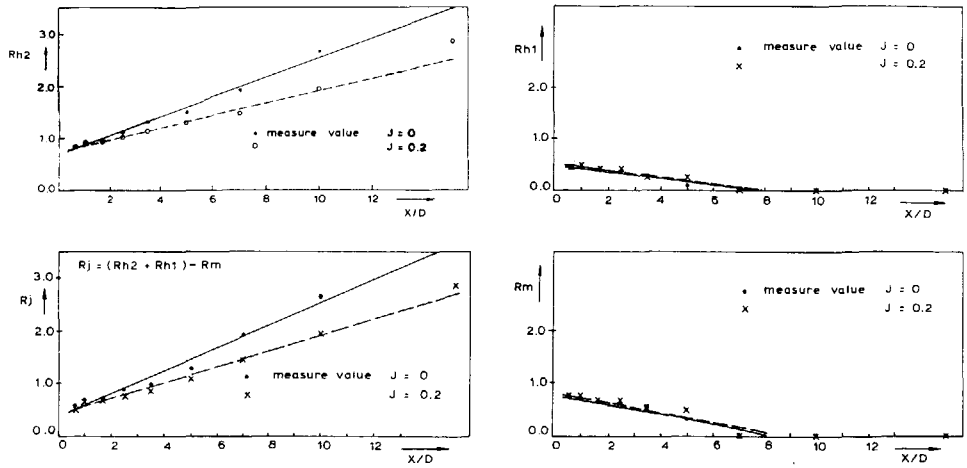

Figure 3.10: characteristic jet width parameters for the wake of a thruster

The axial distance corresponding to $R_m = 0$ represents the length of the initial zone. It extends to approximately $7.5D$ downstream of the propeller. In the initial zone, the region where $r > R_m$ is denominated as outer development zone, with the inner development zone extending from $r = 0$ to $r = R_m$.

In an ordinary turbulent jet, beyond a certain distance from the jet orifice, the velocity profile exhibits similarity. The question is now if this similarity is also found in the propeller wake. Introduce a non-dimensional velocity parameter $\hat{U}$ as follows:

$$\begin{aligned} \hat{U} &= \frac{U-V_s}{U_m-V_s} \qquad r/R > R_m \\ \hat{U} &= \frac{U-U_a}{U_m-U_a} \qquad r/R < R_m \end{aligned} \tag{3.23}$$

and introduce a non-dimensional coordinate $\hat{r}$:

$$\begin{aligned} \hat{r} &= \frac{\frac{r}{R}-R_m}{R_{h2}-R_m} \qquad r/R > R_m \\ \hat{r} &= \frac{R_m-\frac{r}{R}}{R_m-R_{h1}} \qquad r/R < R_m \end{aligned} \tag{3.24}$$

The non-dimensional axial velocity profiles are shown in Figure 3.11 to 3.13 for the fully developed zone, outer and inner development zone respectively. In these figures, the short dotted line refers to the velocity profile due to Schlichting, [81]:

$$\hat{U} = \frac{1}{\left[1+(\sqrt{2}-1)\hat{r}^2\right]^2} \tag{3.25}$$

and the long dotted line represents the exponential velocity profile:

$$\hat{U} = e^{-0.694\hat{r}^2} \tag{3.26}$$

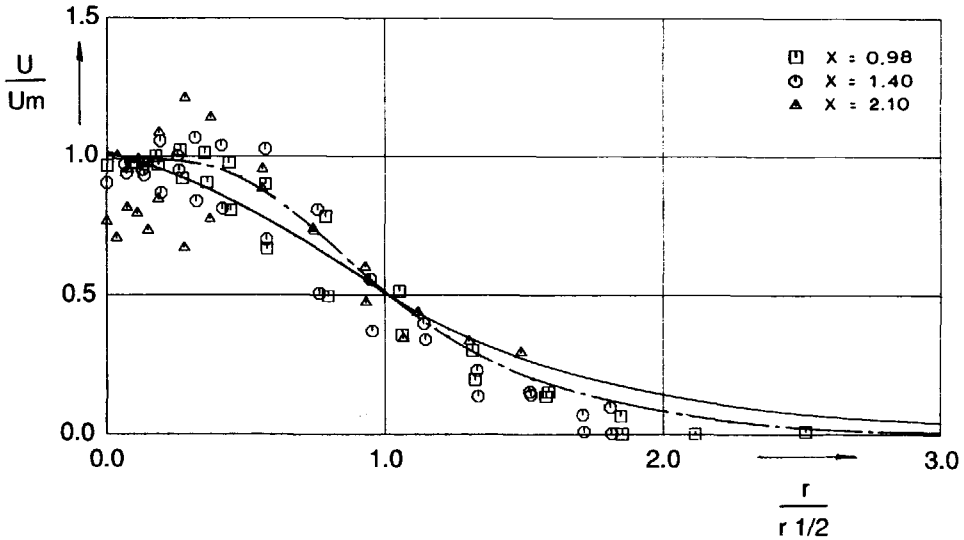

Figure 3.11: dimensionless velocity profiles for fully developed zone

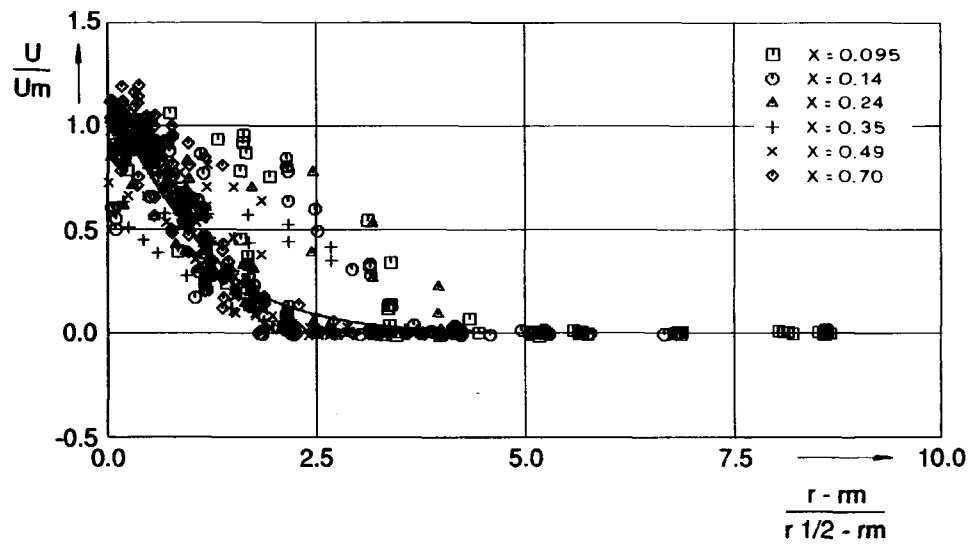

Figure 3.12: dimensionless velocity profiles for outer development zone

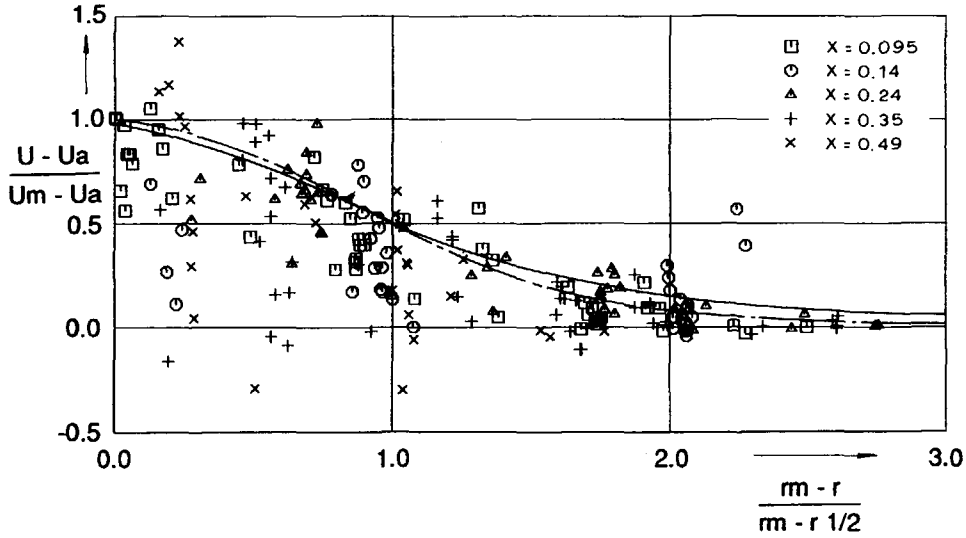

Figure 3.13: dimensionless velocity profiles for inner development zone

It is worth noting from these figures that the axial velocity profile in the propeller wake can be expressed using either the exponential laws or the Schlichting function which approximates the free jet velocity profile. It is not clearly seen which velocity profile is closer to the observed velocity distribution. The velocity profile similarity for the axial velocity is extended to the initial jet zone (for both outer and inner development region). There is considerable scatter in these figures some of it due to the strut influence which will be discussed later.

3.3.1.2 Propeller wake development for axial inflow ($\alpha_T = 0$) - tangential and radial flow components

Three time-averaged velocity components U, V, W in x, y, z direction respectively were recorded by the three-dimensional LDV equipment. The tangential and radial velocity component V_r and V_t can be calculated from V and W.

$$\begin{aligned} V_t = &\quad V\sin(\phi_p) \quad -W\cos(\phi_p) \\ V_r = &\quad V\cos(\phi_p) \quad +W\sin(\phi_p) \end{aligned} \tag{3.27}$$

where the outward pointing radial velocity is taken as positive and the tangential velocity is positive in clockwise (i.e. the propeller rotation) direction.

Figure 3.14 shows the velocity vector (V_t, V_r) diagram for $J = 0$ and $x/D = 1.75$ case as an example. The flow pattern in the y, z plane is clearly observed in this figure. The fluid rotates around the shaft center. The tangential velocity equals zero $(V_t = 0)$ at the centre of propeller rotation (at $r = 0$) and has its maximum value at

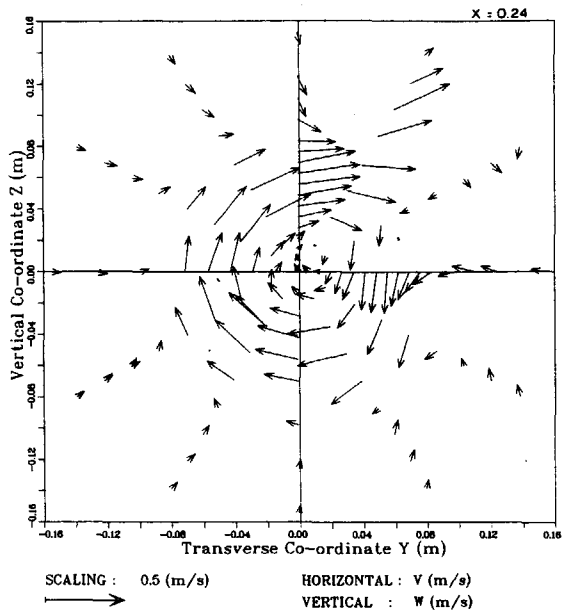

Figure 3.14: radial and tangential velocities in the wake of a thruster, $J = 0$ and $x/D = 1.75$

around $r/R = 0.85$. This value corresponds closely to the value found for free jets, see Chigier etal [82].

The radial velocity generally has a small value. In the wake field, the radial velocities at inner radii have small positive values (outwards and commensurate with the diffusion of the jet), but change their direction near the jet boundary, which implies that the ambient static fluid is entrained into the jet.

3.3.1.3 Propeller wake development for axial inflow ($\alpha_T = 0$) - the strut influence

It can be seen from Figure 3.7 that the velocity field close behind the axisymmetrical propeller is not completely axisymmetrical. The velocities measured in the sector around the positive y-axis ($\phi_p \approx 0$) are apparently lower than those along the other directions. This phenomenon also occurs to some extent at other x-stations and for both advance ratios (see Figure 3.8). With increasing axial distance x, the region with lower velocities changes its angular coordinate. For example, at $x/D = 10$, the velocities measured along $y = 0, z < 0$ ($\phi_p = 270$) become lowest. This phenomenon was also observed during the two-dimensional LDV measurements for the thruster with nozzle 37, as will be discussed subsequently.

In order to determine the basic behaviour of this deviation from axisymmetry, a measurement series was added at the $x/D = 2.5$ station for the $J = 0.2$ condition

where the propeller pitch and turning direction were inverted. By comparing the axial velocity distributions along various angular coordinates, it was established that the non-axisymmetrical behaviour of the velocity field is truly caused by the flow around the thruster, and not by any other influence, such as the presence of the strut of the LDV equipment. Only some relatively insignificant differences in velocity between the various traverses were found which must be attributed to experimental repeatability (on account of the high turbulence levels), measurement accuracy and presence of the LDV equipment. Also the slight asymmetry of the almost lens-shaped blade sections may contribute to this small difference.

The reason for this phenomenon is probably related to the housing and the strut which connect the propeller and duct to the towing carriage (see Figure 3.3).

The axial velocity profile along 12 angular directions and the velocity vector (V_t, V_r) in y, z plane are shown in Figures 3.7 respectively 3.15 for x/D =0.68, 1.0, 1.75, 2.5, 3.5, 5 and $J = 0$. It can be seen from these figures that the strut influence region almost covers a section of 90 degrees and that the angular position of this region moves with increasing x. For example, at $x/D = 1$ station, most of the field point velocity measurements show that the wake edge is located at $r/R = 1.5$. But the measurement along $\phi_p = 75, 60$ and 45 angular directions show significant axial velocities outside the wake edge for values upto $r/R = 2.0$.

For this particular x-station, along the 75 direction the axial velocity profiles have two peaks, one at $r/R \approx 0.8$ and another at $r/R \approx 1.5$ outside the normal wake edge. It is to be noted from the velocity vector diagram that along this angular direction, there are large positive radial velocities at outer radii positions. Usually these velocities should be negative due to the entrainment.

Along the 60 direction, the tangential velocities are relatively smaller at the inner radii and the axial velocities are lower than those along other angular directions. However, at further outward radial positions, the axial velocities are comparatively larger.

Along the 45 direction, the situation is the same as that along the 60 direction for radial and axial velocities, but there are almost no tangential velocities for radii smaller than the propeller radius. This abnormal situation approximately ends at the 30 direction where the radial velocities recover to the normal small negative values, the tangential velocities gradually increase and the axial velocity profile approaches to a normal one.

At the $x/D = 1.75$ station the strut influence section begins at 60 deg and ends at 0 degrees. With increasing x, the strut influence region changes its angular position and grows. For example, it is shown in Figures 3.15 and 3.7 that at the $x/D = 5$ station the influence region reaches $\phi_p = 330$. It appears that the wake produced by the strut resembles a helix with a varying pitch.

The variation of the strut influence region both in terms of extent as well as location is clearly illustrated in the above figures and is summarized in Table 3.10.

The relation between the rotation and forward motion of the strut influence region tends to follow the tangential velocity and can be expressed approximately

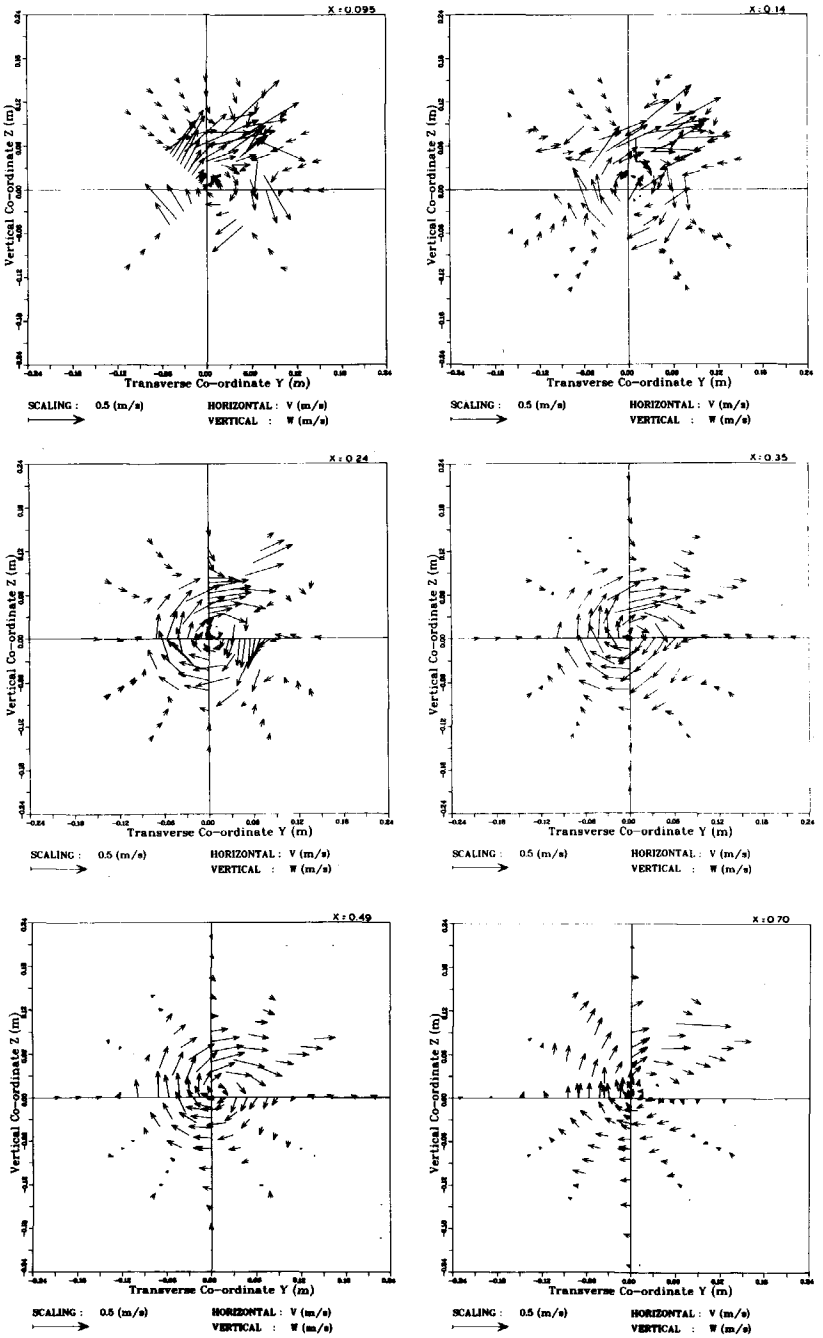

Figure 3.15: velocity vector diagram in the wake of a thruster, J =0.0

x/D	Region angular position	Range of region
1.0	75 deg to 45 deg	$\approx$ 30 deg
1.75	60 deg to 0 deg	$\approx$ 60 deg
2.5	45 deg to 330 deg	$\approx$ 75 deg
3.5	45 deg to 320 deg	$\approx$ 85 deg
5.0	30 deg to 300 deg	$\approx$ 90 deg

Table 3.10: extent and location of strut influence region

as follows:

$$\frac{d\phi_p}{d\left(\frac{x}{D}\right)} = -2arctan\left(\frac{V_{tm}}{U_m}\right) \tag{3.28}$$

The factor 2 is probably partly caused by the increased tangential motion in the strut influence region.

3.3.1.4 Propeller wake development for non-axial inflow ($\alpha_T \neq 0$)

When a thruster is running in an ambient velocity field where the main flow direction is not consistent with the thruster shaft center line direction, the wake will be deflected by the ambient flow and its center line will no longer be parallel to the propeller axis. Figures 3.16 and 3.17 show the variation of the velocity vector (U, V) in the x, y plane. It is observed that for larger distances from the propeller disk, the wake becomes aligned with the ambient flow. The change of the location of the wake center is demonstrated in Figure 3.18. In this figure y_c refers to the coordinate of the jet center in the x, y, z-system. The value of y_c is a function of x, V_s, V_j and α_T.

It is not possible to derive this function with the limited amount of experimental data, but the present measurements illustrate the effect of α_T. If however one were to assume the validity of Margason's relation for the jet deflection, see [83], then for the deflection of the thruster slipstream the following relation gives an indication of the deflection.

$$\frac{x_c}{D} = \frac{1}{4\left(\frac{V_j}{V_s}\right)^2 \sin^2(\alpha_T)}\left(\frac{y_c}{D}\right)^3 + \frac{y_c}{D}\cot(\alpha_T) \tag{3.29}$$

As Figure 3.18 shows, the correlation with Margason's relation is satisfactory. Note that the jet velocity is now taken to be $V_j = \sqrt{T/(\rho A)}$.

3.3.1.5 Calculated propeller wake development

Calculations were also carried out for the thruster slipstream, see Section 3.2.2. These calculations all refer to zero ambient speed and considered variations in the modelling of the vertical drive.

Figure 3.19 shows the axial velocity profiles as calculated for the case without any vertical drive. As expected perfect symmetry is found. Comparing these results with the measured profiles (Figure 3.7) shows that the width of the jet is considerably

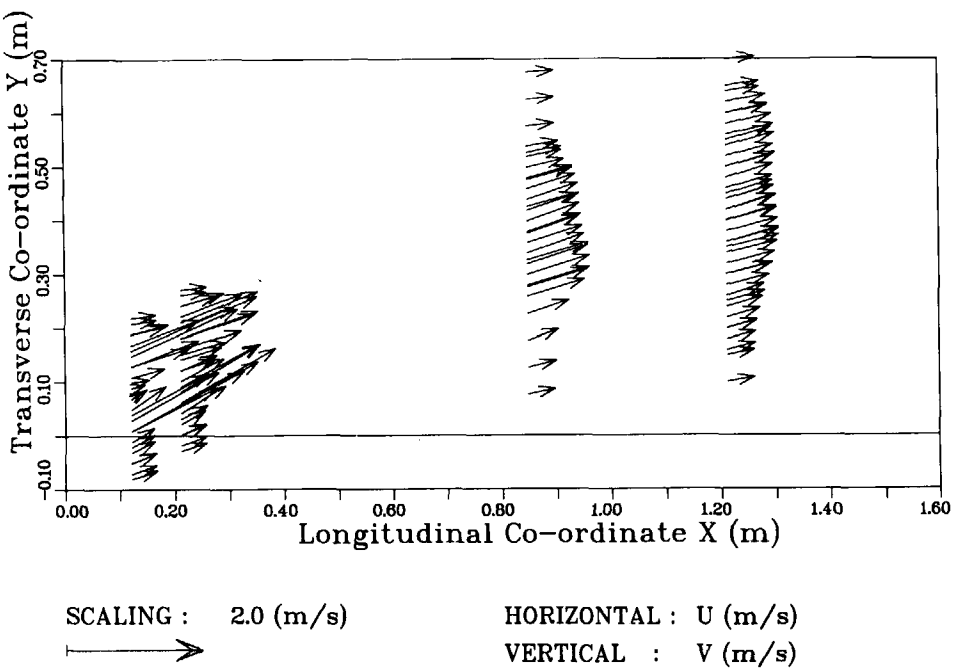

Figure 3.16: velocity vector diagram for the flow in the wake of a thruster in oblique inflow, $\alpha_T = 30$, $J = 0.2$

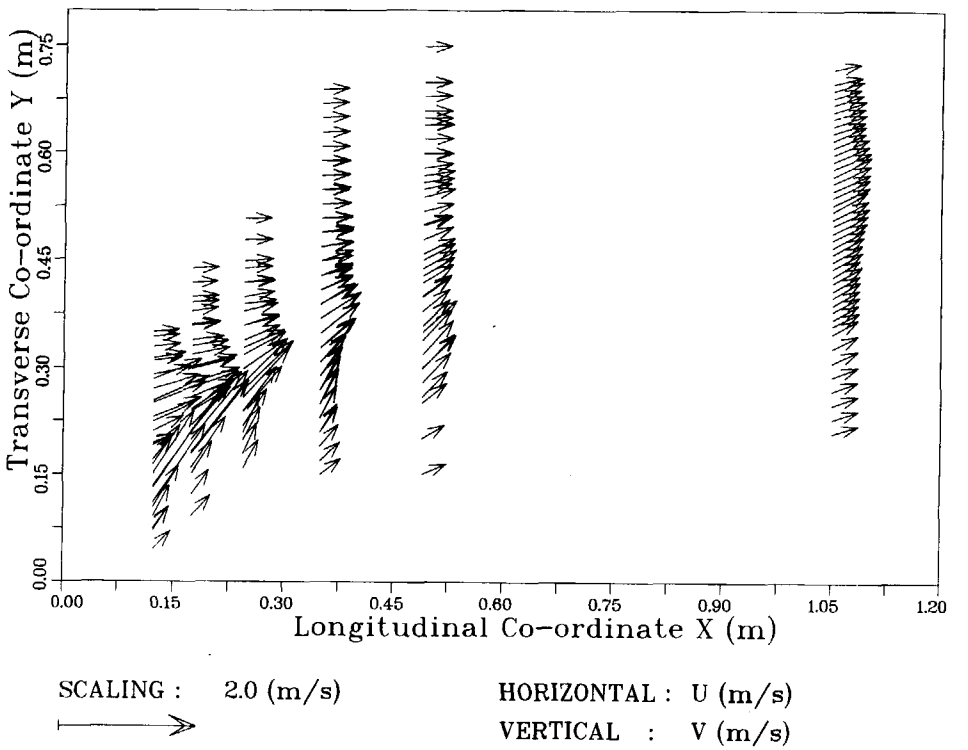

Figure 3.17: velocity vector diagram for the flow in the wake of a thruster in oblique inflow, $\alpha_T = 60$, J =0.2

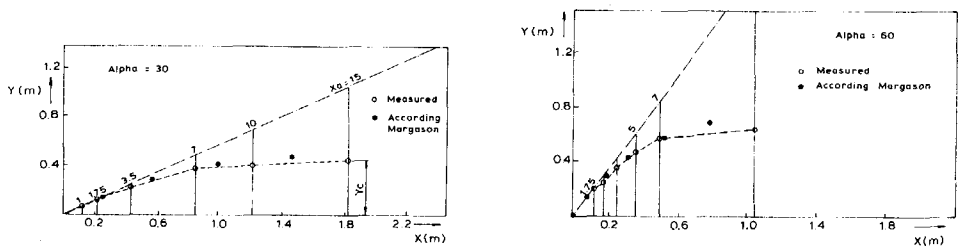

Figure 3.18: propeller slipstream deflection for a thruster in oblique inflow, $J = 0.2$

overpredicted. Especially in the area immediately downstream of the thruster, the jet width is too large. This is partly caused by the presence of the duct which will shift the jet expansion downstream. Also the contraction of the jet is not modelled correctly again leading to an overprediction of the width. Other effects could be the turbulence model and the turbulence production generated by the working propeller which is not correctly modelled. Figure 3.20 shows the value of R_{h2} for some of the calculated cases. The influence of the thrust distribution is seen to be rather small with the exception of the region close to the propeller. Despite the mentioned discrepancies, the predicted jet diffusion can be considered as adequate especially in the far field.

Figure 3.21 shows the calculated velocity decay for all modelled drives. Comparison with the measured data shows that the maximum velocity is underpredicted for all x-coordinates despite the fact that the measured thrust is used for the calculations. Apparently the jet diffusion is overpredicted. However the agreement is qualitatively satisfactory.

An important difference between the calculated and measured velocity distributions occurs immediately downstream of the propeller. Here the measurements show a very low velocity U_a on the propeller axis whereas the calculations cannot show this since the drive and hub are not modelled. Only for the computational case where the hub was modelled, similarly low axial speeds are calculated. Surprisingly the axial speed increases much faster in the calculations than in the measurements. In part this can probably be attributed to the fact that the hub is very crudely modelled and has a very blunt shape; therefore turbulent mixing will be too strong compared to the case where a more streamlined hub is present.

Comparing the various calculated drives one sees that there are only insignificant differences in jet width and velocity decay further downstream. This allows realistic calculations for far-field slip streams without having to model the detailed thruster geometry.

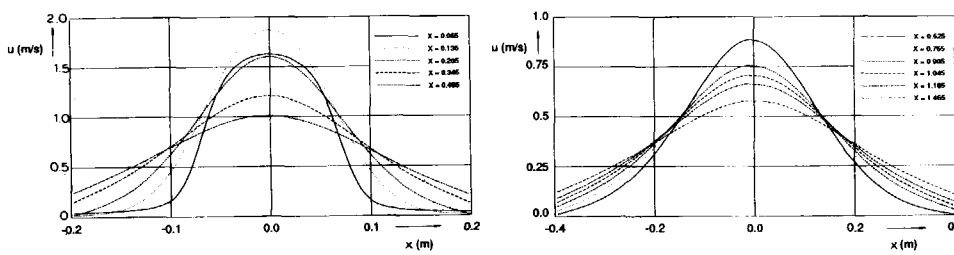

Figure 3.19: calculated axial velocity profiles for a thruster in zero ambient flow - no vertical drive

Figure 3.22 shows the tangential and radial velocities at $x/D = 1.75$. Note

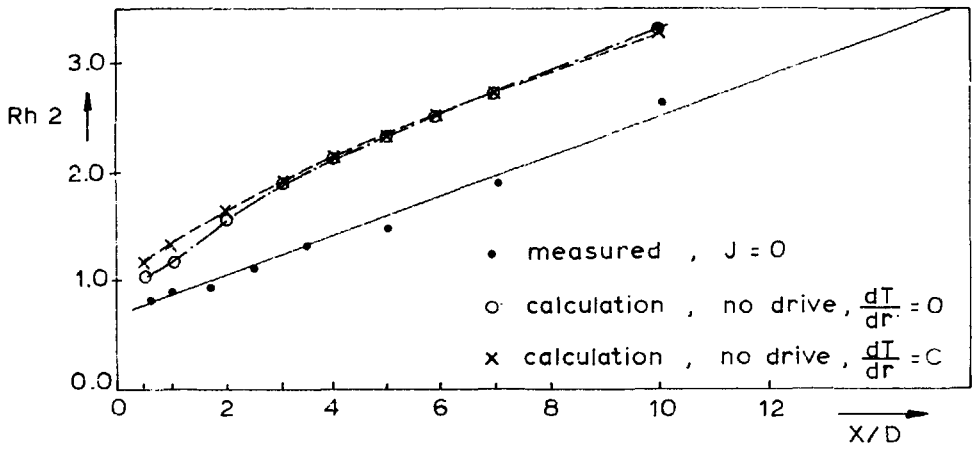

Figure 3.20: calculated jet width for a thruster in zero ambient flow - various vertical drives

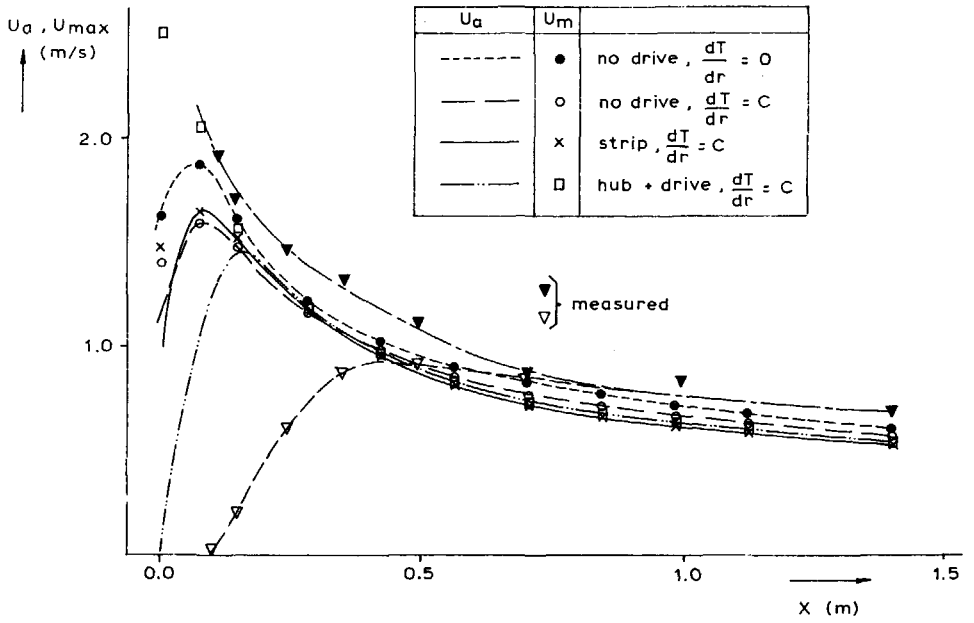

Figure 3.21: calculated jet velocity decay for a thruster in zero ambient flow - various vertical drives

that the propeller turning direction for the calculations was opposite to that for the measurements. Comparison with the measured data depicted in Figure 3.14 shows that the tangential velocity behaves in the same manner. However as shown before the jet width is over-predicted and consequently the maximum tangential velocity is under-estimated. Also the strong an-axisymmetry caused by the thruster housing is not present in the calculations although some asymmetry is observed. The location of this asymmetry is however completely different.

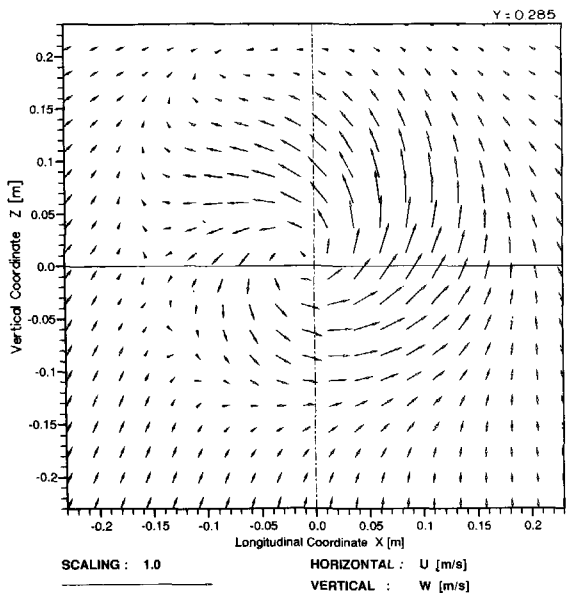

Figure 3.22: calculated tangential and radial velocities for a thruster in zero ambient flow - no vertical drive

On the whole the jet development is adequately predicted with important deviations with respect to the influence of the drive and the hub and quantitative differences in terms of velocity decay and diffusion.

Figure 3.23 shows that the modelled drives do not induce the asymmetrical velocity distributions found in the measurements. This asymmetry therefore is apparently not directly connected with the wake of the drive. As immediately downstream of the drive a non-uniform inflow into the propeller is predicted however, the asymmetry then may be due to the thrust variation of the propeller blades as they pass through the wake of the drive or with the interaction between the nozzle and the pod in the top sector.

3.3.2 Thruster with MARIN 37 nozzle in open water

The thrust and torque levels measured during the tests are given in Table 3.11.

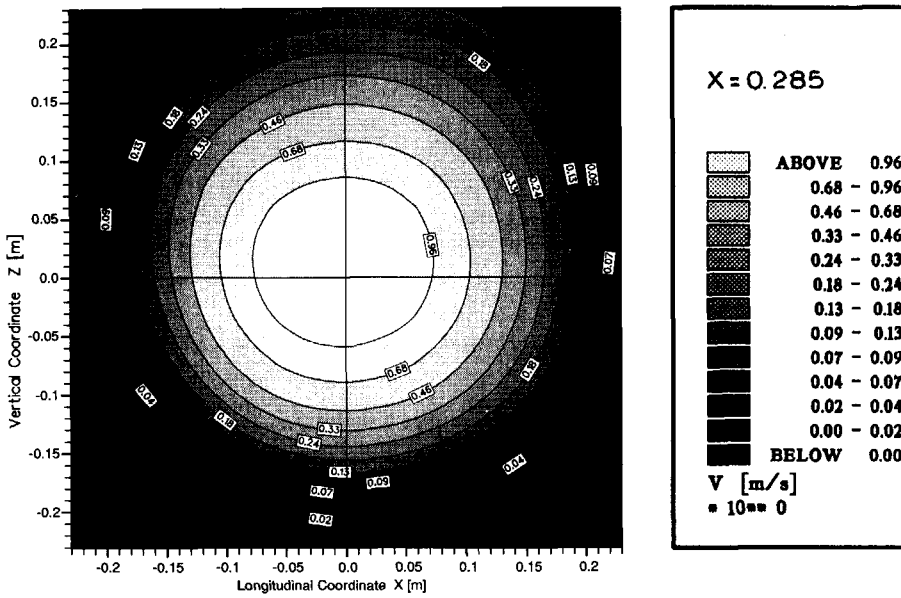

Figure 3.23: calculated axial velocity field for a thruster in zero ambient flow - vertical drive and hub, x/D =1.75

J (-)	V_s (m/s)	T_{tot} (N)	K_{T_p} (-)	K_{T_u} (-)	K_{T_n} (-)	K_Q (-)
0	0	40.86	0.270	0.205	0.296	0.0531
0.1	0.207	35.82	0.265	0.203	0.236	0.0523
0.2	0.411	30.89	0.253	0.194	0.185	0.0507
0.3	0.611	26.22	0.237	0.181	0.141	0.0484
0.4	0.811	21.71	0.216	0.163	0.104	0.0451
0.5	1.016	17.01	0.187	0.138	0.071	0.0409
0.6	1.215	12.27	0.155	0.109	0.041	0.0361

Table 3.11: thrust and torque for a thruster with 37 nozzle in open water

Since the LDV is a two-component system, only the axial or x-component U and the vertical or z-component W were measured.

3.3.2.1 Propeller wake development for $J = 0$ - axial velocity

For the bollard pull open water condition the axial velocity distributions were obtained. Similar results as for the 19A nozzle were found. The axial velocity profile again exhibits basically an axisymmetric behaviour. However as for the measurements with the 19A nozzle, there is considerable scatter especially for r/D-values of approximately 0.45. Especially the velocity for the angular coordinates $\phi_p = 0$ and 45^0 shows a considerable deviation from the results for the other angular coordinates.

At the axial station closest to the propeller, the axial velocities are almost zero at the inner radii due to the influence of the propeller hub. The maximum velocity again occurs around $r/R = 0.8$ and the shape of velocity profile reflects the radial load distribution of propeller.

The experimental results given by Kotb and Schetz [74] and Koyama [75] show an increase of the axial velocity component with increasing axial distance for positions immediately behind the propeller ($x/D < 0.5$). Min [76] showed an increase of the peak of U for $x/D \leq 0.5$ after which a decrease followed. In the present measurement series, the first axial station is located at x/D=0.32 from the duct trailing edge or 0.57 D from the propeller plane. The present test series therefore cannot show such an increase.

Figure 3.24 shows the variation of the position of U_m and the slipstream width with the axial distance x.

The jet width and therefore also the jet half width again present a linear relation with axial distance, see below.

The variation of U_m and V_{tm} with x is shown in Figure 3.25. The figure also indicates the scatter of the data originating in the different values of U_m for the different angular directions.

The average maximum velocity can be expressed by the following expression:

$$\frac{U_m}{V_j} = \frac{0.738}{(x/D)^{0.360}} \tag{3.30}$$

in which V_j is the average velocity far downstream of the propeller plane calculated on the basis of momentum theory, see Eq 3.18. Again the result points to a jet with stromg swirl. The difference with the results for the 19A nozzle is comparatively small indicating that the influence of nozzle type is relatively small. Note that the swirl number for both cases is almost equal.

3.3.2.2 Propeller wake development for $J = 0$ - tangential velocity

The vertical velocity component W on the y-axis is equivalent to the tangential velocity, V_t. The profiles of the tangential velocity components at some x-stations are shown in Figure 3.26. The figure shows that there is some similarity in profile

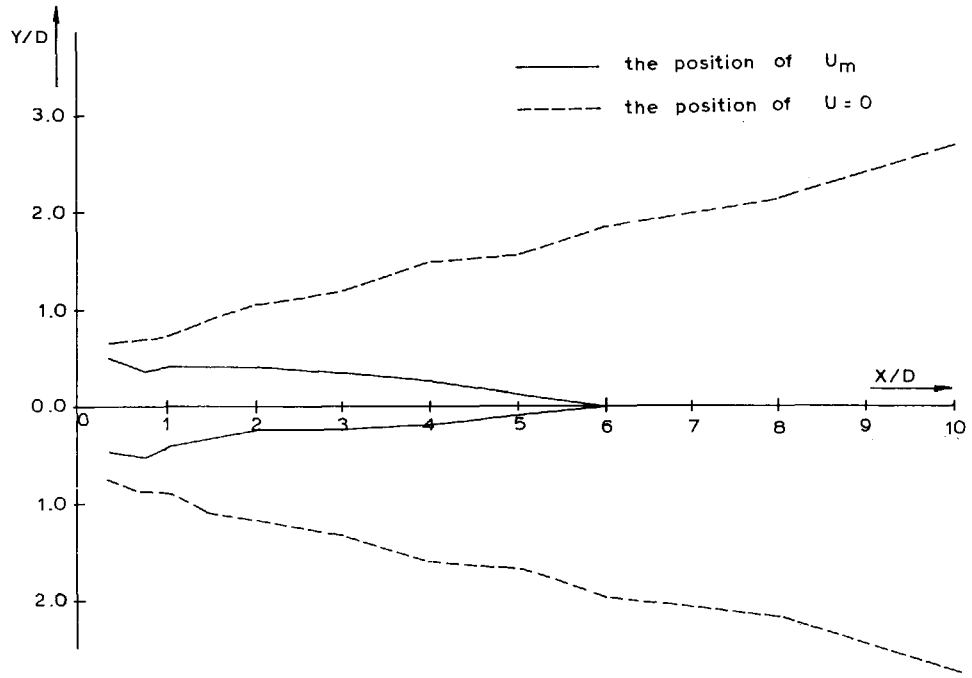

Figure 3.24: maximum velocity location and jet width as a function of distance to the propeller; J =0.0

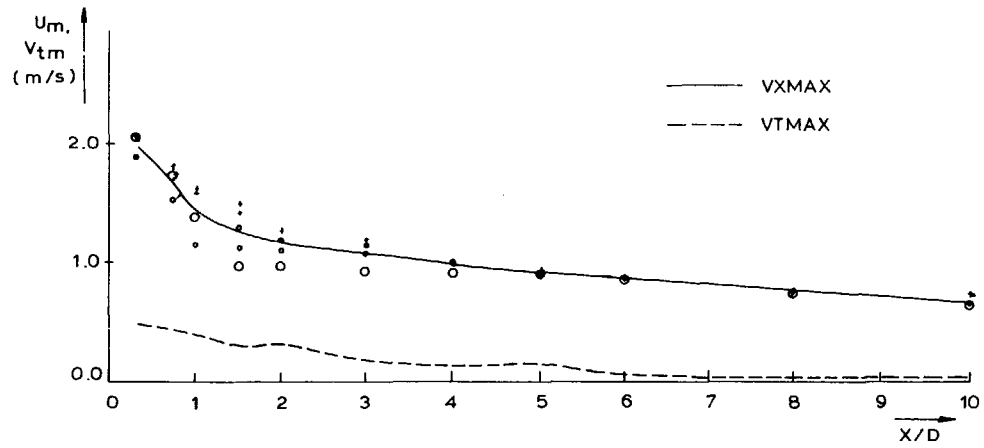

Figure 3.25: maximum axial and tangential velocity as a function of distance to the propeller; J =0.0

shape between the axial velocity profile and the tangential velocity profile at those x-stations which are close to the propeller plane.

With increasing x, the axial velocity at shaft center line increases gradually and the position of U_m moves towards the shaft center line. The axial velocity profile changes its shape with increasing axial distance, but no substantial variation in tangential velocity profile is seen with increasing x, see also Figure 3.15. The tangential velocities at the shaft center line always equal approximately zero and the relative location of maximum tangential velocity remains approximately the same.

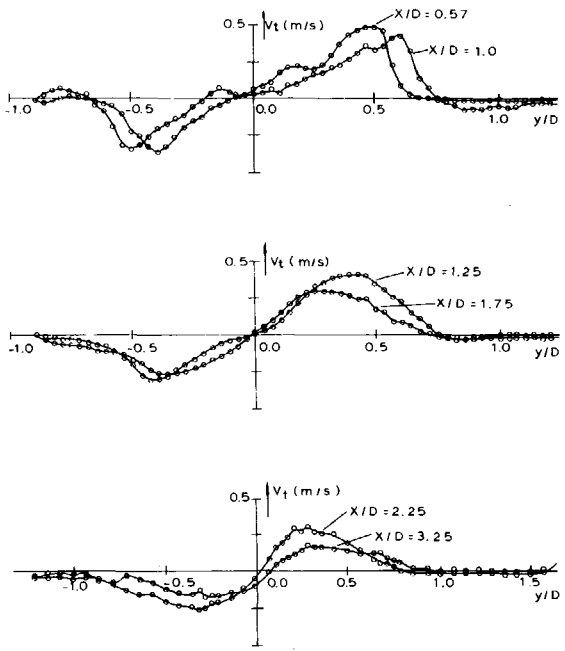

Figure 3.26: radial and tangential velocity component profiles in the wake of a thruster, J =0.0; various x-stations

The variation of V_{tm} with x is included in Figure 3.25. It can be seen that the tangential velocity rapidly reduces to insignificant values. This was also found in the velocity measurements with the 19A nozzle. The variation of the maximum tangential velocity with the x-coordinate follows approximately a power law:

$$V_{tm} = \frac{0.36}{(\frac{x}{D})^{0.65}} \tag{3.31}$$

The found by Chigier etal [82] indicate a still faster decay but as for the axial velocity the exponent depends heavily on the selection of a vertical origin. It is clear however that the decay is much faster than for the axial velocity.

3.3.2.3 Propeller wake development for $J \neq 0$

The experiments were conducted for three J-values with consequently three values of propeller loading as well as ambient speed. Some of the measured axial velocities are shown in Figure 3.27 and 3.28 for $J = 0.2$ and 0.4 respectively.

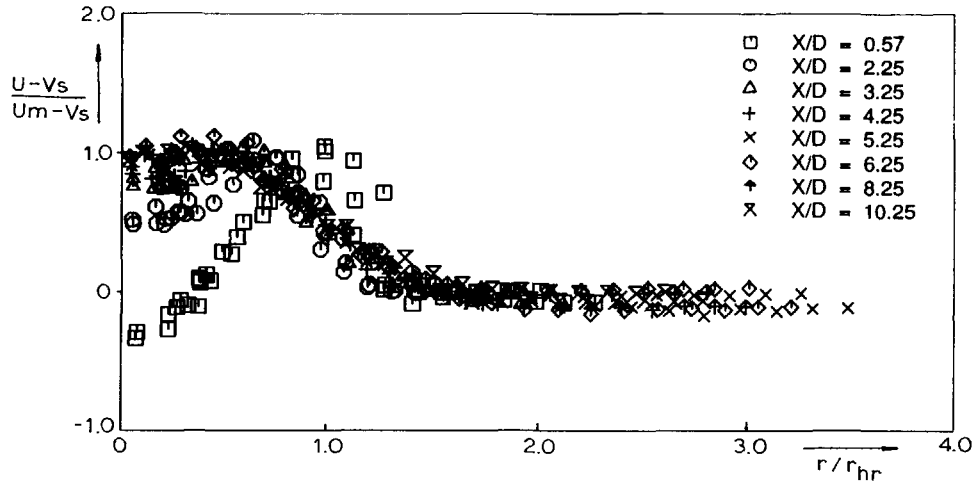

Figure 3.27: axial velocity distributions for $J = 0.2$

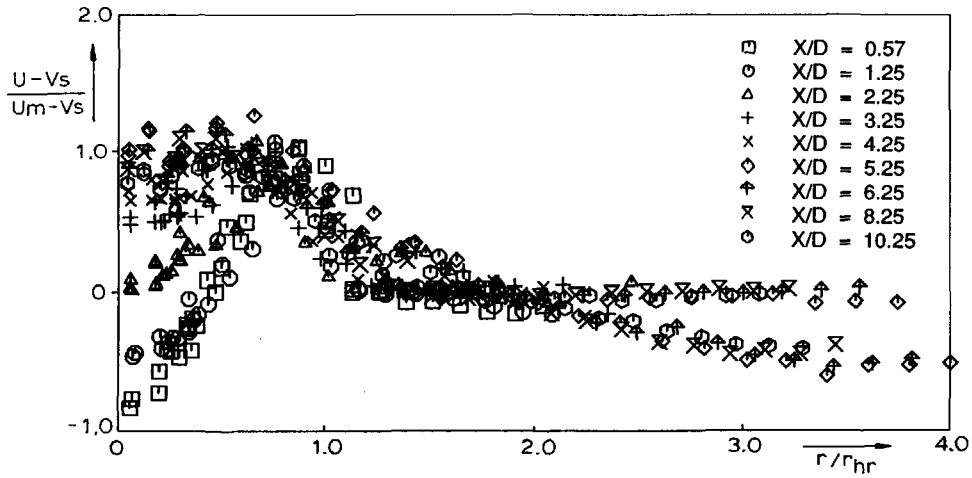

Figure 3.28: axial velocity distributions for $J = 0.4$

The average half width values of the jet for the different J-values are shown in Figure 3.29. It can be seen that the jet half width is reduced with increasing J and

presents a linear dependence on x:

$$R_{h2} = a + b\frac{x}{D} \tag{3.32}$$

The regression coefficients a, b deduced from the experimental data are as indicated in Table 3.12. The agreement with the 19A results is again rather close.

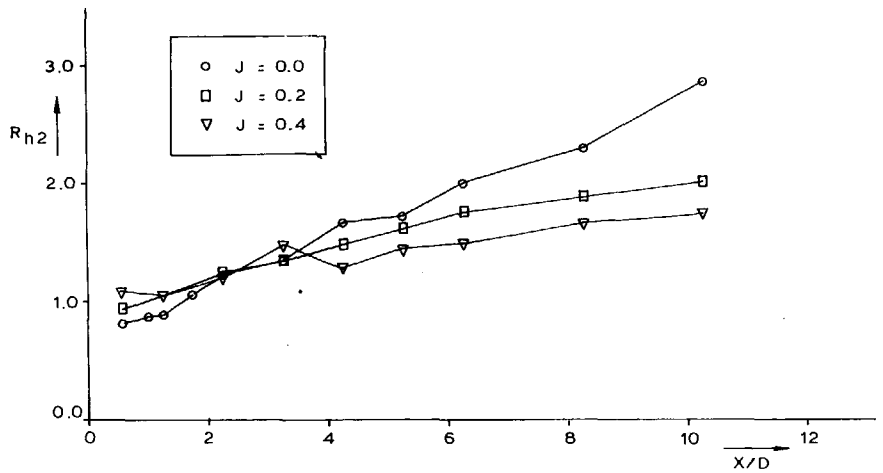

Figure 3.29: average half width values for three advance ratios

J	a	b
0	0.691	0.207
0.2	0.984	0.112
0.4	0.990	0.076

Table 3.12: regression coefficients for jet half width R_{h2}

The length of the development zone, where the position of maximum axial velocity shifts towards the x-axis is slightly increased with increasing advance speed.

The influence of J on U_m is shown in Figure 3.30. The following expression describes the velocity decay:

$$\frac{U_m}{V_j} = \frac{a}{(x/D)^b} \tag{3.33}$$

The regression analysis shows that the coefficients take approximately the values listed in Table 3.13. A distinct trend with advance ratio is found as is to be expected. This trend was also found for the 19A nozzle.

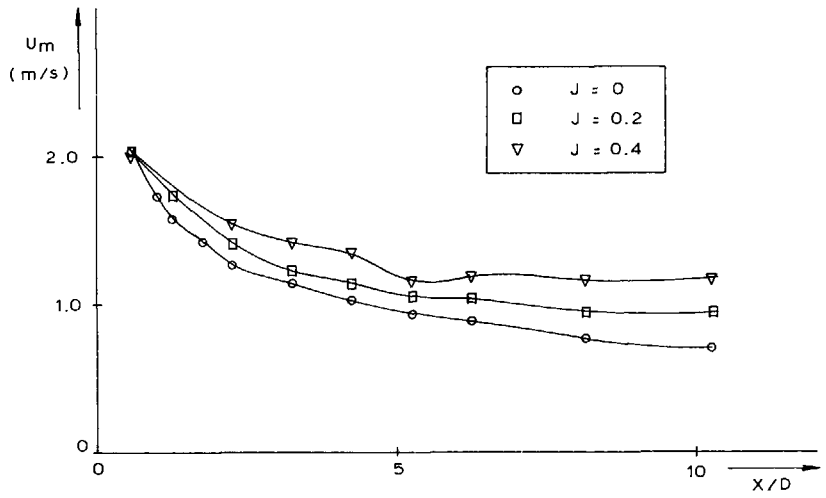

Figure 3.30: maximum velocity as affected by advance speed

J	a	b
0	0.738	0.360
0.2	0.835	0.275
0.4	0.967	0.215

Table 3.13: regression coefficients for jet velocity decay

3.4 The Induced Flow in Behind Condition

3.4.1 Thruster with MARIN 37 nozzle above a flat plate

The thrust and torque levels measured during the tests are given in Table 3.14.

Condition	J (-)	V_s (m/s)	T_{tot} (N)	K_{T_p} (-)	K_{T_u} (-)	K_{T_n} (-)	K_Q (-)
under plate	0	0	40.16	0.269	0.205	0.287	0.0533

Table 3.14: thrust and torque for a thruster with nozzle 37 below a flat plate

3.4.1.1 Propeller wake development for $J = 0$ - influence of a flat plate

The test series considered only one clearance $h_p/D = 0.75$ where h_p denotes the distance from the propeller axis to the flat plate. This clearance is commonly found for thrusters mounted under the ship's keel plating. The plate was parallel to the propeller shaft. The measurements were carried out only for $J = 0$.

Upto a certain distance from the propeller plane, the wake will behave similar as in a free unbounded open water condition. For the axial station $x/D = 0.57$, a comparison of the velocity profile between the open water ($h_p/D = \infty$) and 'behind' ($h_p/D = 0.75$) condition, Figure 3.31, yields almost no differences.

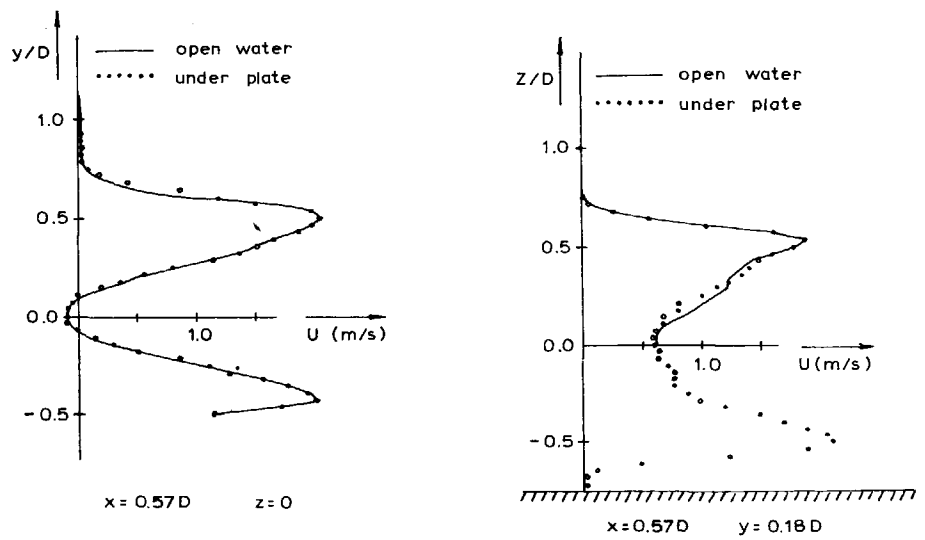

Figure 3.31: comparison of open water and behind condition for $x/D = 0.57$

At a certain distance, which will depend on the clearance, the wake and the plate will start to interact as the jet diffusion becomes sufficient for the jet to hit

the plate. According to Figure 3.24, this interaction will arise around $x/D = 1.0$ for this clearance.

Figure 3.32 shows the velocity profiles for different Z-coordinates for horizontal traverses at the axial stations x/D =4.25, 6.25, 8.25 and 10.25.

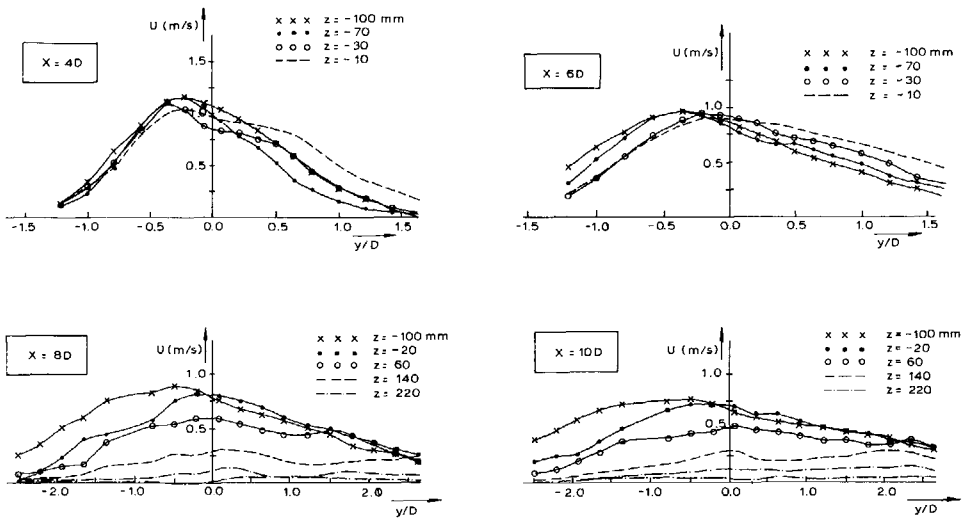

Figure 3.32: axial velocity distributions for a thruster under a flat plate

With increasing x, the presence of the plate increasingly affects the diffusion of the propeller wake. A boundary layer arises which can be inferred from Figure 3.32. This is supported by Figure 3.34 showing the location of maximum axial velocity.

For the fully developed propeller wake region, the velocity profile perpendicular to the plate may be normalized similar as done Davis etal, [79]. In that case for y =0 the same velocity distribution as for the open water case may be used. However in this case the dimensionless vertical coordinate is given by:

$$\hat{z} = \frac{z - z_m}{z_h - z_m} \tag{3.34}$$

in which z is measured perpendicular from the plate. The velocity profile calculated according to this formulation agrees reasonably well with the measured data.

Figure 3.33 shows the comparison between the open water profile and that for the plate condition. It can be seen that the velocity profile for the 'behind' condition for $\hat{z} \geq 0$ is narrowed in the vertical direction by the presence of the plate. This is in agreement with the results of Davis etal [79]. The lateral jet width is larger for this condition compared to the open water case. Also this is in agreement with the results of Davis etal. However the magnitude of this effect is less pronounced for the thruster.

With increasing axial distance x the position of maximum velocity moves towards the plate. Davis etal [79] have shown that for an ordinary turbulent jet the shift

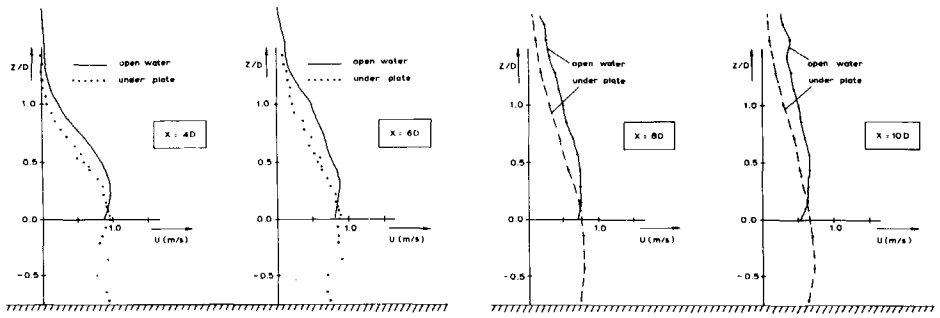

Figure 3.33: axial velocity comparison between open-water and behind condition

depends on the clearance. For the propeller wake and $h_p/D = 0.75$, the variation of the position of maximum velocity U_m is shown in Figure 3.34. This figure also compares U_m as a function of x with the results found for open water. No significant difference is found. This result is supported to some extent by the results of Davis etal [79] who also found little influence of the plate on the maximum velocity decay.

3.4.2 Thruster with nozzle 37 below barge-shaped hull

Table 3.3 shows the conditions for which the velocity measurements were performed. The measurements were subjected to a least-squares analysis assuming a realistic velocity field. The analysis yields the various parameters describing the flow field.

3.4.2.1 Least squares analysis

Let the jet axis be located at the point with coordinates (y_c, z_c) with vertical deflection angle α_j and let α_T be the angle of the jet axis with the horizontal. From the axial, radial and tangential velocities in the slipstream, the velocities in x, y and z-direction may be found:

$$\begin{aligned} U = &\ V_{ax}\cos\alpha_j &&- (V_t\cos\phi_j + V_r\sin\phi_j)\sin\alpha_j \\ V = &\ -V_t\sin\phi_j &&+ V_r\cos\phi_j \\ W = &\ V_{ax}\sin\alpha_j &&+ (V_t\cos\phi_j + V_r\sin\phi_j)\cos\alpha_j \end{aligned} \tag{3.35}$$

For a fully turbulent jet in stationary ambient fluid the following velocity profile can be derived for the axial velocity, see Schlichting, [81]:

$$\frac{V_{ax}}{V_{ax,m}} = \frac{1}{\left[1 + (\sqrt{2}-1)\hat{r}^2\right]^2} \tag{3.36}$$

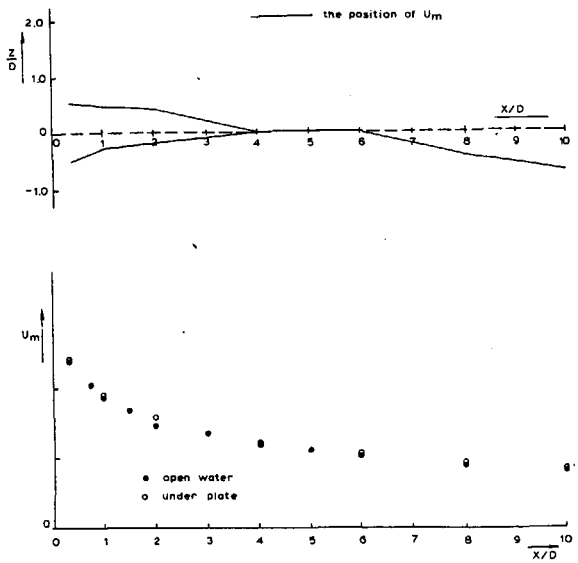

Figure 3.34: magnitude and location of maximum axial velocity in the behind condition

where $V_{ax,m}$ is the maximum axial velocity in the slipstream located on the slipstream center and $\hat{r}$ is the radial coordinate from the center made dimensionless by the jet half-width, r_{h2}. This profile was seen to apply also reasonably well for the thruster slipstream investigated so far.

As the considered propeller slipstream is non-circular due to the deflection originating from the presence of the barge, r_{h2} depends on the direction of the radius considered.

For r_{h2} a 3-term Fourier expansion is used incorporating the assumption of symmetry in the vertical plane going through the propeller axis:

$$r_{h2}(\phi_j) = r_0 + r_1 \sin\phi_j + r_2 \cos 2\phi_j \tag{3.37}$$

The tangential velocity is related to the torque of the propeller. The following representation for V_t is adequate in the case of a swirling jet:

$$V_t = Are^{-Br^2} \tag{3.38}$$

with A, B having constant values depending on the bilge shape and the distance to the propeller. In the above representation of V_t, r is set equal to r_0, i.e. the tangential velocity is thought to be independent of ϕ_j.

The radial velocity is small in all cases and was left out of account.

The equations 3.35 to 3.38 represent the velocity distribution in the propeller jet. The unknowns $V_{ax,m}, \alpha_j, z_c, y_c, r_0, r_1, r_2, A, B$ have to be determined from the measurements for U and W.

Considerations of symmetry lead to $y_c = 0$. Due to the rotation (swirl) of the jet in combination with an upward deflection this assumption may not be entirely valid. Satisfactory results, however, have been obtained with $y_c = 0$.

Conservation of axial momentum leads to a constraint to be satisfied by the velocity distribution:

$$F_{TB} = \int_0^{\infty} \int_0^{2\pi} \rho r U|U| dr d\phi \tag{3.39}$$

Imposing this constraint was found necessary to obtain realistic converged solutions. A similar constraint could have been imposed on the angular momentum but was not necessary.

In order to be able to solve the above integral explicitly some simplifying assumptions have been made. These lead to the following expression:

$$F_{TB} = \int_0^{\infty} \int_0^{2\pi} \rho r {V_{ax}}^2 dr d\phi_j \tag{3.40}$$

Introduction of equations (11) and (15) while taking $r = r_0$ for this constraint leads to:

$$F_{TB} = \frac{\pi \rho \cos^2 \alpha_j V_{ax,m}^2 r_0^2}{3(\sqrt{2}-1)} \tag{3.41}$$

Another constraint between the variables which describe the velocity distribution is imposed by a necessary relation between V_{ax} and V_t. This originates from the fact that the jet radius has to be approximately the same for the axial as well as the tangential velocity. During the tests the thruster force and torque were constant. The swirl number of the jet in this case equals $S = 2Q/(DT_{tot}) = 0.23$ From turbulent jet measurements performed by Chiqier etal, [82] a relation between the jet half width r_h and the location r_{tm} of the maximum tangential velocity V_{tm} may be found: $r_{tm} = 0.775 r_h$. This factor is constant with the distance from the propeller and applies to circular jets. It is also used for the present situation. This condition leads to:

$$B = \frac{0.832}{r_0^2} \tag{3.42}$$

To obtain values for the constants $V_{ax,m}, \alpha_j, z_c, r_0, r_1, r_2, A, B$ the following function is minimized:

$$GX = E_F + 0.1(F_{TB,est} - F_{TB})^2 \tag{3.43}$$

in which: $F_{TB,est}$ denotes the estimated transverse force according to equation 3.41, F_{TB} denotes the measured transverse force and E_F gives the error function denoting the error between the measured and calculated U and W:

$$E_F = \sum_{i=1}^{N} \left[(U_{est} - U)^2 + 50.0(W_{est} - W)^2 \right] \tag{3.44}$$

with N the number of data points for a scan.

The factor 50.0 in Equation 3.44 is added because of the smaller magnitude of W.

3.4.2.2 Discussion

Figures 3.35 to 3.37 show the measured axial velocity profiles in the vertical plane through the propeller axis for three of the covered bilge shapes.

The results of the least-squares analysis of the measured velocity distributions are given in Tables 3.15 to 3.19. Note that to obtain a realistic solution for the least squares analysis, it was necessary in some cases for the largest distance to the barge (d =1.60 m) to set the values of r_1, r_2 to zero. This was necessary for R_b = 0.05, l =0.72; as well as for R_b = 0.10, l = 0.42 and 0.72. Also for R_b = 0.20, l = 0.42 this had to be applied, while for R_b = 0.20, l =0.72 no converged solution could be found with the relations used for the description of the jet.

The measured velocity profiles for the first thruster position (l_T = 2.12 m) in Figures 3.35 to 3.37 confirm that for this thruster position the bilge shape is of no relevance.

Therefore it was allowed to combine the results for all 5 bilge shapes for this thruster position to arrive at a better least-squares solution of the velocity field. These results therefore can be considered to apply to the open-water condition and are entered in Table 3.20.

l (m)	d (m)	V_m (m/s)	z_c/D (-)	α_j (deg)	r_0/D (-)	r_1/D (-)	r_2/D (-)	A (s^{-1})	BD^2 (-)	$V_{r,m}$ (m/s)	$\sqrt{EF/N}$ (-)
0.12	0.4	1.52	0.148	0.4	0.608	-0.184	0.064	-4.99	2.24	-0.202	0.090
0.42	0.4	1.33	0.352	2.2	0.704	-0.196	0.148	-3.13	1.69	-0.148	0.040
0.72	0.4	1.13	0.280	1.8	0.812	-0.120	0.340	-2.17	1.26	-0.117	0.043
0.12	1.0	1.01	0.060	0.4	0.916	0.016	0.152	-1.48	0.99	-0.090	0.034
0.42	1.0	0.87	0.264	2.9	1.072	0.120	0.216	-0.96	0.73	-0.069	0.028
0.72	1.0	0.74	0.244	2.6	1.248	-0.024	0.500	-0.59	0.53	-0.050	0.031
0.12	1.6	0.83	-0.052	1.9	1.120	0.124	0.212	-0.82	0.66	-0.062	0.027
0.42	1.6	0.65	0.264	3.6	1.444	0.280	0.308	-0.38	0.40	-0.036	0.029
0.72	1.6	0.53	-0.072	2.8	1.748	0.376	0.548	-0.22	0.28	-0.026	0.032

Table 3.15: results of least squares analysis of 2D LDV measurements for a thruster mounted to a barge, R_b = 0.0 m

In the least-squares analysis a specific axial velocity distribution was assumed. From the measured profiles in Figures 3.35 to 3.37 it is obvious that this profile is adequate for r/r_h values of up to approximately 2.0. Beyond that the measured profiles fall off more steeply towards the jet boundary compared to Schlichting's profile. Although this does influence the accuracy of the least-squares fit it does not affect the values of the different parameters significantly.

The accuracy of the least-squares fit is also given in Tables 3.15 to 3.19 by the parameter E_F/N. This is the value of the error function mentioned above divided by the number of data points. Generally the fit becomes better for larger distances of the propeller. This is caused by several factors:

- The speed decreases with increasing distance. As E_F is proportional to the square of the speed, E_F tends to decrease as well.

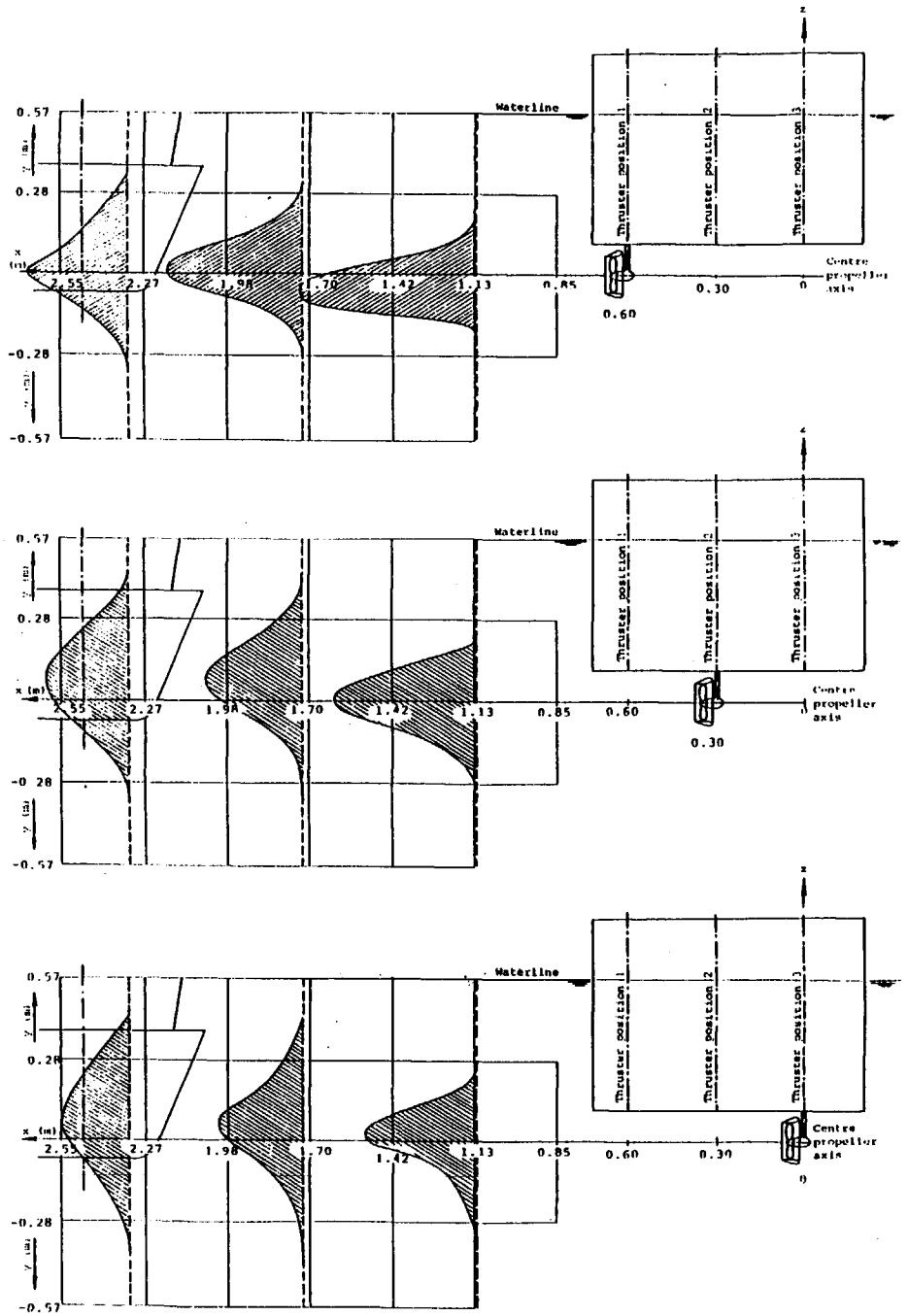

Figure 3.35: axial velocity distribution for a thruster under a barge, $R_b = 0.0$

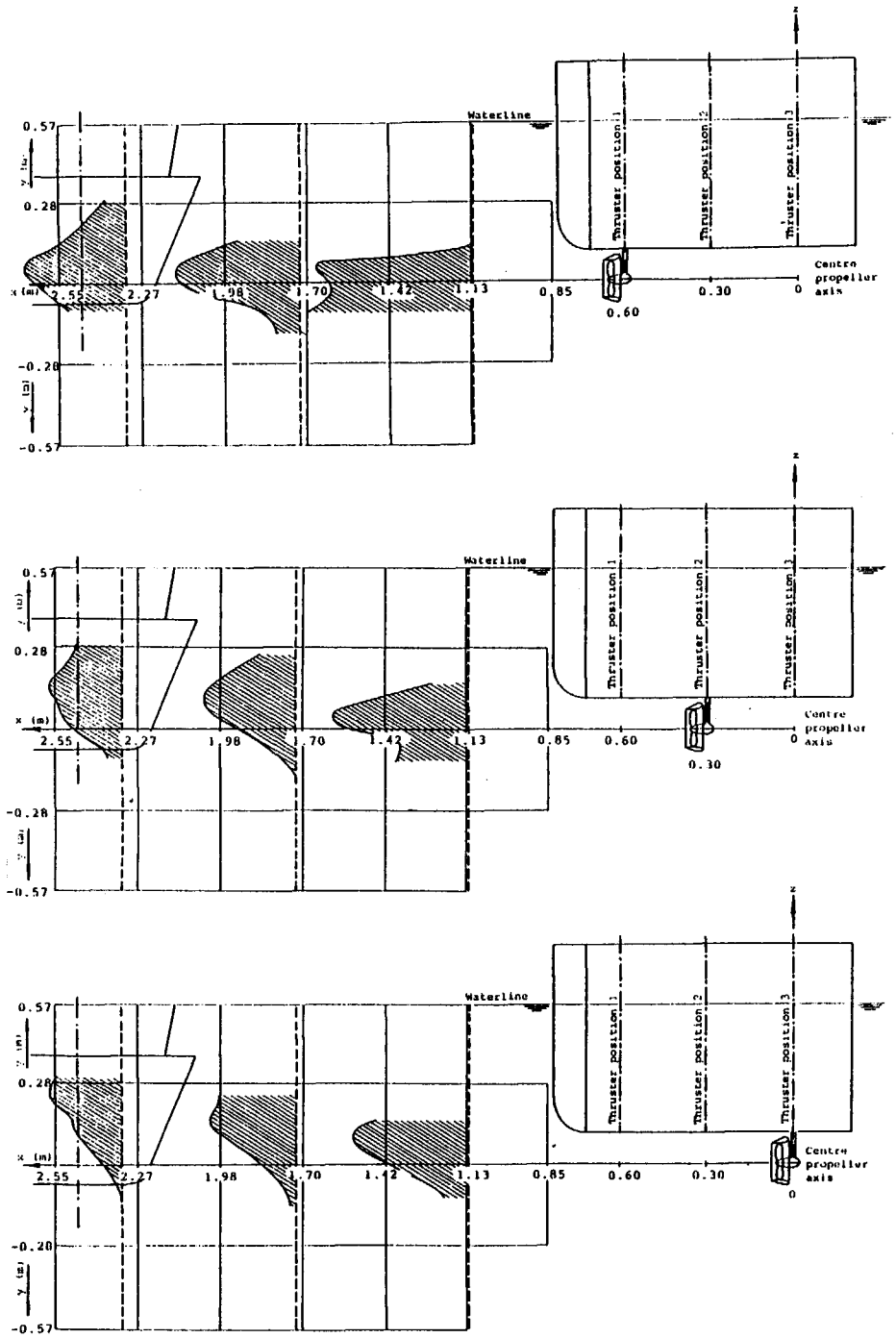

Figure 3.36: axial velocity distribution for a thruster under a barge, $R_b = 1.76$

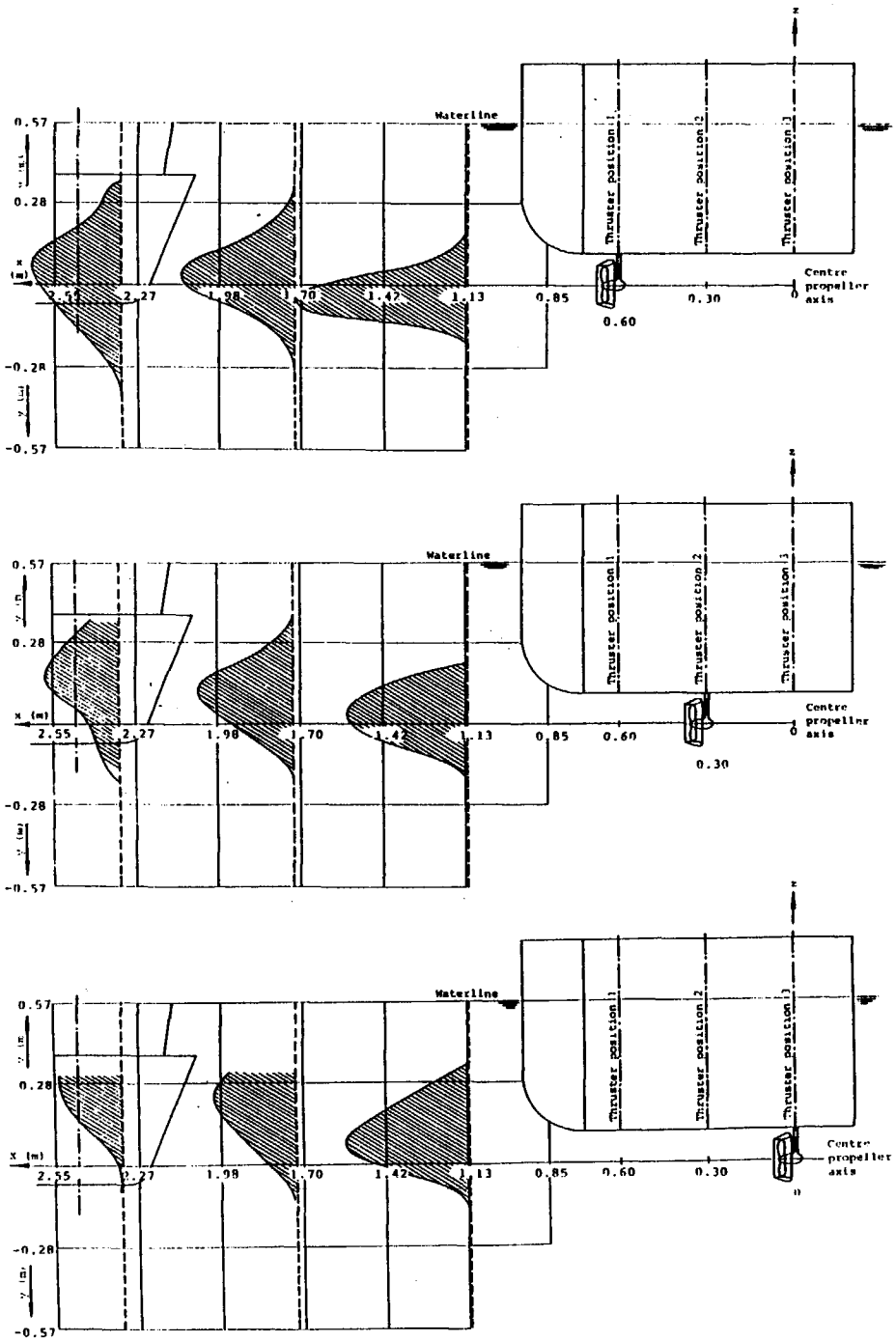

Figure 3.37: axial velocity distribution for a thruster under a barge, $R_b = 3.53$

l (m)	d (m)	V_m (m/s)	z_c/D (-)	α_j (deg)	r_0/D (-)	r_1/D (-)	r_2/D (-)	A (s^{-1})	BD^2 (-)	$V_{r,m}$ (m/s)	$\sqrt{EF/N}$ (-)
0.12	0.4	1.52	0.148	0.4	0.608	-0.184	0.064	-4.99	2.24	-0.202	0.090
0.42	0.4	1.02	0.272	4.2	0.904	-0.032	0.184	-1.55	1.02	-0.093	0.060
0.72	0.4	0.86	0.780	9.6	1.060	-0.164	0.208	-0.96	0.74	-0.067	0.036
0.12	1.0	1.11	-0.072	0.2	0.832	0.132	0.156	-2.01	1.20	-0.111	0.034
0.42	1.0	0.77	0.468	5.6	1.196	0.328	0.164	-0.68	0.58	-0.055	0.037
0.72	1.0	0.55	1.020	8.4	1.652	0.540	-0.032	-0.26	0.31	-0.029	0.028
0.12	1.6	0.82	0.288	2.7	1.132	0.024	0.236	-0.76	0.65	-0.057	0.034
0.42	1.6	0.62	1.108	6.1	1.496	0.008	0.496	-0.35	0.37	-0.036	0.030
0.72	1.6	0.45	1.416	7.0	2.028	0.000	0.000	-0.14	0.20	-0.019	0.028

Table 3.16: results of least squares analysis of 2D LDV measurements for a thruster mounted to a barge, $R_b = 0.05$ m

l (m)	d (m)	V_m (m/s)	z_c/D (-)	α_j (deg)	r_0/D (-)	r_1/D (-)	r_2/D (-)	A (s^{-1})	BD^2 (-)	$V_{r,m}$ (m/s)	$\sqrt{EF/N}$ (-)
0.12	0.4	1.52	0.148	0.4	0.608	-0.184	0.064	-4.99	2.24	-0.202	0.090
0.42	0.4	0.90	0.508	5.8	1.020	-0.256	0.368	-1.07	0.80	-0.074	0.072
0.72	0.4	0.85	0.784	10.3	1.076	-0.272	0.308	-0.92	0.72	-0.067	0.048
0.12	1.0	0.98	-0.032	1.6	0.944	0.184	0.252	-1.33	0.93	-0.083	0.039
0.42	1.0	0.60	0.784	5.8	1.520	-0.024	0.512	-0.33	0.36	-0.033	0.034
0.72	1.0	0.59	1.172	9.9	1.548	0.436	0.120	-0.32	0.35	-0.033	0.027
0.12	1.6	0.66	0.096	-0.1	1.392	-0.064	-0.056	-0.42	0.43	-0.038	0.030
0.42	1.6	0.53	1.004	5.2	1.704	0.076	0.436	-0.24	0.29	-0.029	0.025
0.72	1.6	0.48	1.796	7.3	1.916	0.468	0.184	-0.17	0.23	-0.021	0.020

Table 3.17: results of least squares analysis of 2D LDV measurements for a thruster mounted to a barge, V-shaped bilge

l (m)	d (m)	V_m (m/s)	z_c/D (-)	α_j (deg)	r_0/D (-)	r_1/D (-)	r_2/D (-)	A (s^{-1})	BD^2 (-)	$V_{r,m}$ (m/s)	$\sqrt{EF/N}$ (-)
0.12	0.4	1.52	0.148	0.4	0.608	-0.184	0.064	-4.99	2.24	-0.202	0.090
0.42	0.4	0.88	0.548	6.1	1.056	-0.292	0.424	-0.97	0.75	-0.069	0.079
0.72	0.4	0.90	0.972	11.9	1.012	-0.412	0.336	-1.13	0.81	-0.076	0.047
0.12	1.0	1.04	0.068	2.0	0.531	0.124	0.192	-1.62	1.05	-0.095	0.035
0.42	1.0	0.64	0.680	5.6	1.448	0.192	0.316	-0.39	0.39	-0.038	0.038
0.72	1.0	0.61	1.772	10.6	1.496	-0.556	0.700	-0.36	0.37	-0.036	0.029
0.12	1.6	0.70	-0.043	-0.8	1.320	0.240	0.084	-0.49	0.48	-0.043	0.039
0.42	1.6	0.65	1.136	5.2	1.928	0.000	0.000	-0.16	0.23	-0.021	0.028
0.72	1.6	0.52	2.520	9.4	1.748	0.000	0.000	-0.23	0.28	-0.026	0.019

Table 3.18: results of least squares analysis of 2D LDV measurements for a thruster mounted to a barge, $R_b = 0.10$ m

l (m)	d (m)	V_m (m/s)	z_c/D (-)	α_j (deg)	r_0/D (-)	r_1/D (-)	r_2/D (-)	A (s^{-1})	BD^2 (-)	$V_{r,m}$ (m/s)	$\sqrt{EF/N}$ (-)
0.12	0.4	1.52	0.148	0.4	0.608	-0.184	0.064	-4.99	2.24	-0.202	0.090
0.42	0.4	1.14	0.248	5.8	0.804	0.040	0.164	-2.23	1.29	-0.120	0.052
0.72	0.4	0.87	1.108	15.3	1.048	-0.012	0.060	-1.04	0.76	-0.074	0.035
0.12	1.0	1.01	0.020	1.2	0.920	0.104	0.160	-1.54	0.66	-0.095	0.034
0.42	1.0	0.72	0.908	6.8	1.276	0.088	0.496	-0.56	0.51	-0.048	0.037
0.72	1.0	0.59	2.424	16.1	1.556	0.044	-0.124	-0.32	0.34	-0.033	0.020
0.12	1.6	0.79	-0.072	1.2	1.176	0.160	0.128	-0.72	0.60	-0.057	0.033
0.42	1.6	0.48	1.532	6.5	1.924	0.000	0.000	-0.16	0.23	-0.021	0.029
0.72	1.6	-	-	-	-	-	-	-	-	-	-

Table 3.19: results of least squares analysis of 2D LDV measurements for a thruster mounted to a barge, $R_b = 0.20$ m

l (m)	d (m)	V_m (m/s)	z_c/D (-)	α_j (deg)	r_0/D (-)	r_1/D (-)	r_2/D (-)	A (s^{-1})	BD^2 (-)	$V_{r,m}$ (m/s)	$\sqrt{EF/N}$ (-)
0.12	0.4	1.52	0.148	0.4	0.608	-0.184	0.064	-4.99	2.24	-0.202	0.090
0.12	1.0	1.01	0.008	1.5	0.916	0.128	0.196	-1.51	0.99	-0.093	0.038
0.12	1.6	0.78	-0.072	1.1	1.184	0.252	0.152	-0.70	0.59	-0.055	0.036

Table 3.20: results of least squares analysis of 2D LDV measurements for a thruster mounted to a barge, all bilge shapes combined

- The velocity profile assumed above ideally refers to a fully developed propeller wake; at smaller distances from the propeller this assumption will not be valid with resulting larger values of the error function E_F/N.
- The velocity variations due to turbulence are larger close to the propeller. Therefore the average measured velocities (20-second averages) will fluctuate more in this region. This results in larger errors in the average velocities.

Figures 3.38, 3.39 depict the relations between distance to the propeller respectively bilge radius and the parameters describing the propeller jet.

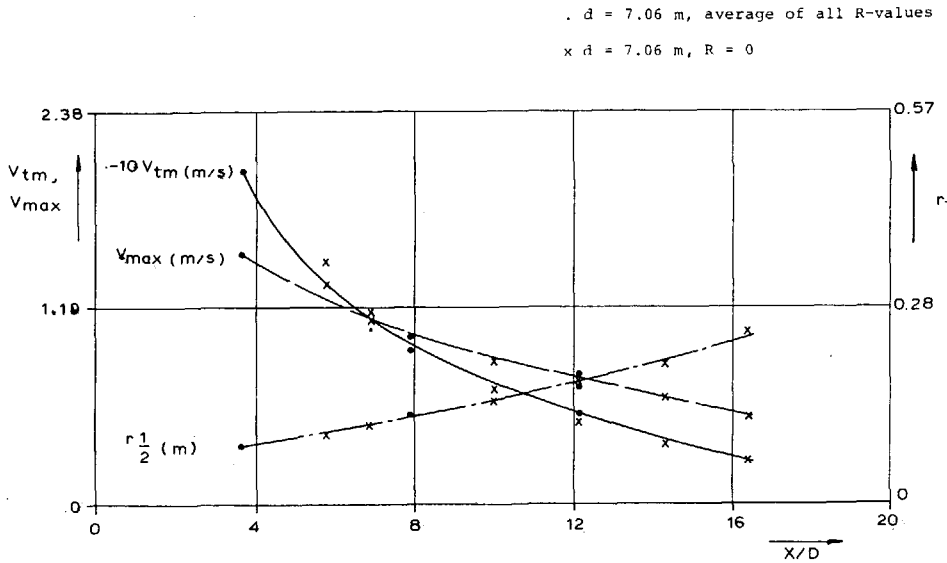

Figure 3.38: jet parameters as a function of distance to the propeller

From Figures 3.35 to 3.37 as well as from Tables 3.15 to 3.19 it is clear that the jet deflection increases with increasing l_T and R_b. This shows both in the values of z_c and the jet angle α_j. For $R_b = 0$ there is hardly any jet deflection to be seen. This agrees with the results of the force measurements discussed in a subsequent section.

Further in accordance with the expectations the maximum velocity decreases and the jet width increases with increasing distance to the propeller.

Comparison between the different tables show that the maximum velocity drops if the bilge radius increases from $R_b = 0$ to $R_b = 0.88$. Beyond that there is no distinct relation between R_b and $V_{ax,m}$. The same remark applies to the value of r_0.

With increasing R_b one would expect asymmetrical velocity distributions to show up. But the values of r_1 and r_2 do not show such a distinct tendency.

Figure 3.39 shows the jet deflection on a basis of the bilge radius. A particle of mass m and velocity V has to experience a force $F = mV^2/r$ to describe a circular

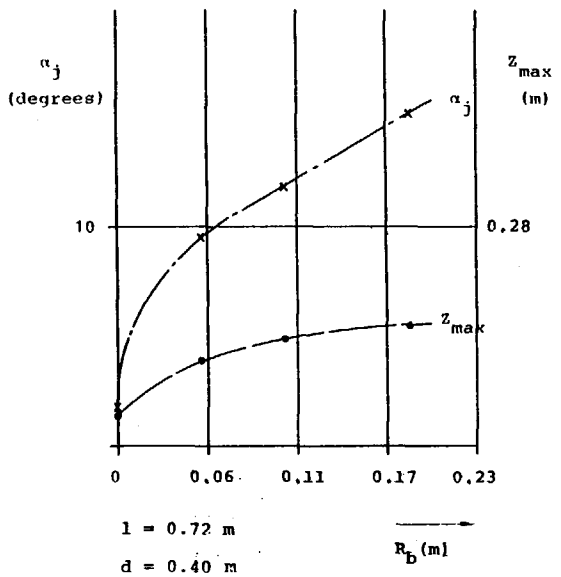

Figure 3.39: jet parameters as a function of bilge radius

arc of radius r. If the suction force per unit mass F/m would be constant with V and bilge radius R_b, a one-to-one relation between the jet deflection α_j and V^2/R_b might be expected. Figure 3.40a shows α_j as a function of V^2/R_b. V is the estimated maximum jet velocity at the axial coordinate which coincides with the start of the bilge. This value is estimated from Figure 3.38 by inserting the appropriate axial coordinate, $x/D = 0.85, 2.96$ and 5.08. It would seem that V^2/R_b has to be replaced by V^2 to obtain a better one-to-one correlation. However, Figure 3.40b shows a bad correlation for smaller V. Figure 3.40c shows the value of $\alpha_j/\sqrt{R_b}$ on a basis of $1/V^2$. In this case the measured data coincide somewhat better.

Therefore a rough estimate of the jet deflection may be given by:

$$\alpha_j = 29\sqrt{\frac{R_b}{D}}\left(\frac{gD}{V^2} - 0.28\right) \tag{3.45}$$

which gives a reasonable fit of the measured results. Note that the use of the propeller diameter in this relation is not supported by any of the measurements. It only serves to non-dimensionalize the formula. Also the non-linearity which is apparent from Figure 3.40c is not covered in the above relation. Further investigations are necessary to determine a more general relation.

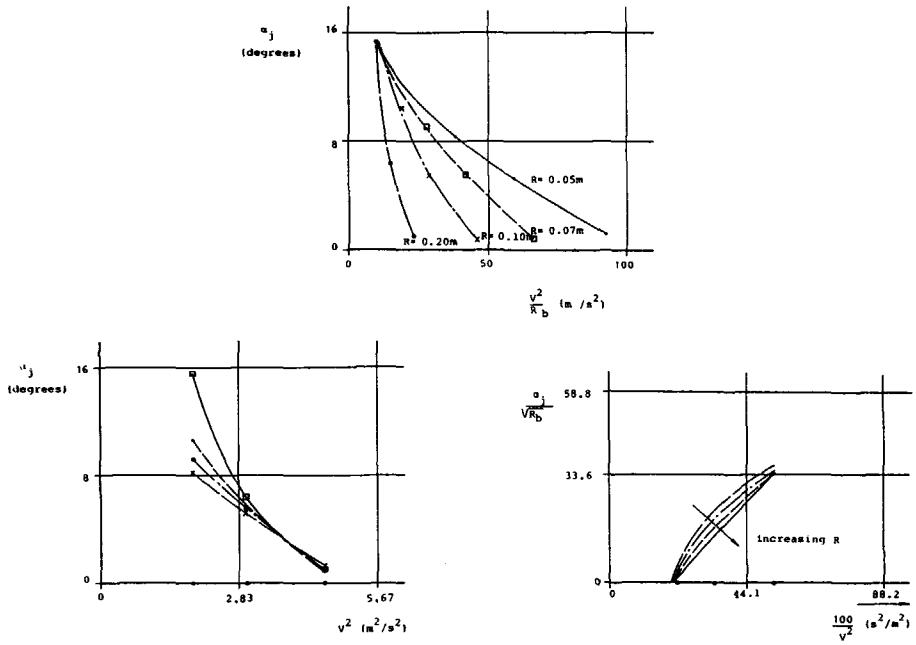

Figure 3.40: jet deflection as a function of bilge radius

3.5 Interaction for Azimuthing Thrusters

3.5.1 Introduction

A common propulsion unit for a dynamically positioned floater is the azimuthing or compass thruster capable of delivering horizontal thrust in an arbitrary direction. These thrusters are frequently fitted with a nozzle of either the NSMB 37 or the NSMB 19A type.

For reasons of size limitations, redundancy and controllability the required thrust is mostly delivered by two or more units rather than by one big unit. These units are often spaced close together giving rise to mutual interaction.

Also the units may be located at almost any place on the hull, rather than at the stern end of the ship. The location of the units close to the hull causes thruster-hull interaction much the same as for conventional propulsion. However the arbitrary thrust direction together with the widely varying hull form in the vicinity of the thruster cause this interaction to be unpredictable at present especially on account of the frequent occurrence of oblique inflow of the thruster.

The picture becomes increasingly complicated if a second body is situated in the presence of the thruster such as occurs for a semi-submersible or in the vicinity of a quay but also for towing of an object. The flow around this object is then altered by the operation of the thruster leading to changed forces on this body. This in turn can cause the flow around the first body to change with corresponding force changes.

The object of the present chapter is to shed some light on these phenomena both by presenting experimental results as well as by carrying out a limited computational study giving insight in the processes involved.

3.5.2 Thruster-thruster interaction

3.5.2.1 Thruster-thruster interaction measurements

Barge with two azimuthing thrusters. These tests were carried out for a large flat bottom barge fitted with two azimuthing thrusters, see Figure 3.41. The two thruster positions were variable as were the azimuth angles. The barge was towed in the longitudinal direction. The details for the tested models are given in Section A.7.

Table 3.21 lists all test conditions for the flat-bottom barge with two azimuthing thrusters. Note that the thruster angles of both thrusters were always equal. The listed relative position of the aft thruster is made dimensionless with the thruster diameter. The pitch of the propellers was equal to $P_{0.7}/D = 0.9$.

3.5.2.2 Thruster-thruster interaction calculations

Open water case One of the cases considered covers the interaction of two azimuthing thrusters in each others vicinity in open water. This situation was covered experimentally by Lehn, [24].

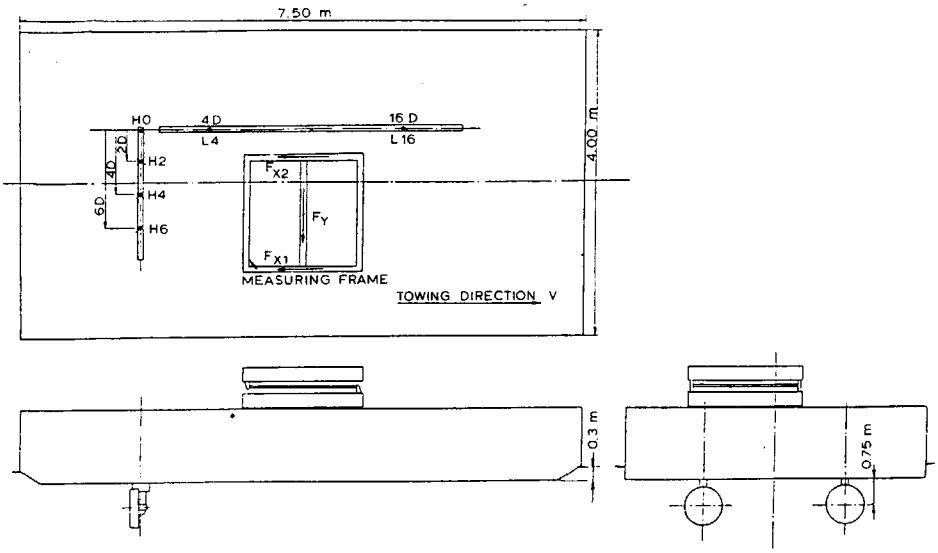

Figure 3.41: test set-up for two azimuthing thrusters under a barge

x/D (-)	y/D (-)	α_T (deg)	V_s (m/s)
2	0	0, 10, 20, 30	-0.14, 0.0, 0.14, 0.28, 0.42, 0.56
2	2	10, 20, 30	-0.14, 0.0, 0.14, 0.28, 0.42, 0.56
4	0	0, 10, 20	-0.14, 0.0, 0.14, 0.28, 0.42, 0.56
4	2	10, 20, 30	-0.14, 0.0, 0.14, 0.28, 0.42, 0.56
4	4	10, 20, 30	-0.14, 0.0, 0.14, 0.28, 0.42, 0.56
8	0	0, 10, 20	-0.14, 0.0, 0.14, 0.28, 0.42, 0.56
8	2	-15, 0, 15, 30	-0.14, 0.0, 0.14, 0.28, 0.42, 0.56
8	4	10, 20, 30	-0.14, 0.0, 0.14, 0.28, 0.42, 0.56
8	6	10, 20, 30	-0.14, 0.0, 0.14, 0.28, 0.42, 0.56
16	0	0, 10, 20	-0.14, 0.0, 0.14, 0.28, 0.42, 0.56
16	2	10, 20, 30	-0.14, 0.0, 0.14, 0.28, 0.42, 0.56
16	4	10, 20, 30	-0.14, 0.0, 0.14, 0.28, 0.42, 0.56
16	6	10, 20, 30	-0.14, 0.0, 0.14, 0.28, 0.42, 0.56

Table 3.21: measurement conditions for thruster-thruster interaction tests with a barge fitted with two azimuthing thrusters

The open-water diagram of the thrusters was not given in [24] for which reason the thrusters were assumed to behave identical to a Ka-4-70 propeller with 19A nozzle adjusted to a pitch of $P_{0.7}/D = 1.0$. The diameter of the propellers equals 0.208 m.

The interaction is determined by calculating the flow induced by one of the two propellers and assuming that the second propeller is not present. Once the flow field is determined, the thrust and torque of the second propeller is calculated by taking the average axial inflow speed to the second propeller and using the open-water diagram. This can be done for any location and orientation of the second propeller assuming the open-water diagram to be valid also for oblique inflow conditions and assuming that the operation of the first propeller is not affected by that of the second propeller.

The last assumption is validated by among others Lehn, [24] who established that the forward propeller (i.e. the thruster that causes the interaction) is not affected by the rear one if the mutual distance exceeds approximately two propeller diameters.

The first assumption is approximately valid if the inflow angle is relatively small or the advance ratio (based on the ambient speed) has a low value, see e.g. Oosterveld etal [12].

The flow induced by the front propeller is calculated in the following fluid domain:

$$\begin{aligned} -1.0 &\leq x \leq 15.0 \\ -4.0 &\leq y \leq 4.0 \\ -4.0 &\leq z \leq 2.5 \end{aligned}$$

with the center of the propeller plane located at (0.055, 0.0, 0.0) and the propeller thrust directed in the negative x-direction.

Only the bollard pull condition is considered by Lehn, [24]. Therefore on all boundary planes a symmetry condition was imposed creating a completely closed fluid domain. The domain was divided in 51 x 41 x 46 control volumes; the control volume faces are located similar as for the slipstream calculations, see Figure 3.4.

The total thrust and torque of the propeller amount to 98.4 N and 1.723 Nm respectively. The propeller turning direction is clockwise looking in the direction of the thrust. The thrust and torque were modeled by a constant force per unit propeller area. The integrated force and moment over the disk equals the mentioned thrust and torque.

Note that the total thrust is spread over the propeller disk; i.e. also the duct thrust is distributed over that area. It is assumed that this simplification does not introduce significant errors in the overall flow field. Further any effects of the hub or vertical drive were neglected both on the force distribution as well as on the open-water characteristics.

3.5.2.3 Discussion of interaction for open water conditions

The only data available for thruster-thruster interaction in open water is that published by Lehn [24] which referred to zero speed conditions only and covered variations in relative thruster position and thruster angles.

Using the calculated velocity field downstream of a simplified thruster, delivering the same thrust as Lehn's thruster and consuming the same power, the interaction was calculated for the cases reported by Lehn. To this end the average inflow velocity over the propeller disk of the second thruster was calculated, and the resulting advance ratio was used in conjunction with the estimated open-water diagram of the thruster used by Lehn [24]. This open-water diagram can be taken to correspond with that of a Ka-4-70 propeller with nozzle 19A.

Figures 3.42 and 3.43 show the measured and calculated data. Figure 3.42 shows the thrust and torque interaction as a fraction of the front thruster's values on the basis of distance between the thrusters. It is seen that the measurements and calculations agree fairly well for the entire range of distances.

Figure 3.43 shows the interaction coefficients for two distances between the two thrusters, respectively 3 and $6D$, and as a function of thruster angle. It is seen that the agreement is again adequate and that for angles around 20 to 30 degrees the interaction disappears. This is of course important for the control system of a DP ship: by rotating both thrusters by some 25 degrees, it is possible to obtain almost the maximum force without serious interaction while keeping the force perpendicular to the line connecting the thrusters zero.

The extent of the interaction can be reduced in case of controllable pitch propellers where the pitch can be adjusted to consume again full power. Thereby the interaction on thrust can be reduced significantly as shown in Figure 3.42.

3.5.2.4 Discussion of interaction for thrusters below a flat plate

For thrusters mounted underneath a ship a different situation occurs since the slipstream of the front thruster will be affected by the presence of the ship's plating. By using the calculated velocity field for a simplified thruster close to a flat plate, it is again possible to calculate the thruster-thruster interaction using the same approach as for the open-water case.

Figure 3.44a shows the obtained interaction as a function of distance between the thrusters both measured and calculated. The agreement is seen to be adequate again. Also it is clear that both for the measurements as well as for the calculations the interaction in open-water persists for larger distances between the thrusters. This is to be ascribed to the increased diffusion of the jet if it is close to a flat plate, see before.

Rotating the front thruster also in this case leads to reduced interaction coefficients, see Figure 3.44b. The agreement between calculation and measurement is again rather good, although the measured interaction falls off more rapidly compared to the calculated one. This is in agreement with the comparison between the measured and calculated velocity distributions in the thruster slipstream.

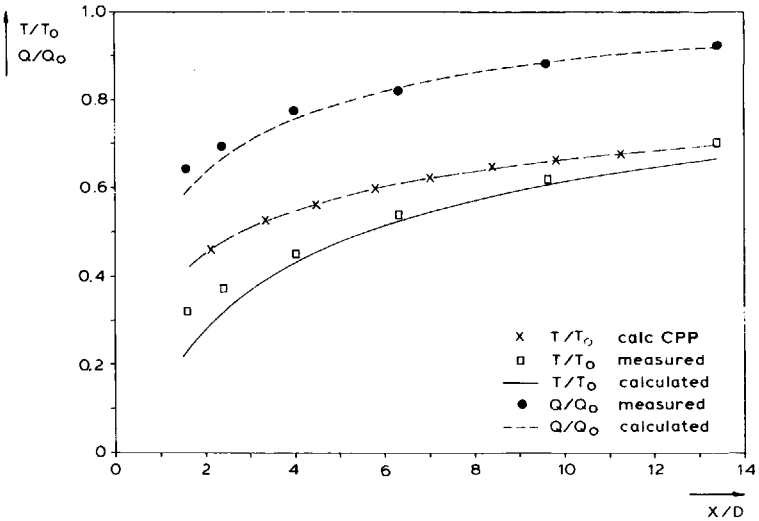

Figure 3.42: thruster-thruster interaction in open water as a function of distance between the two thrusters

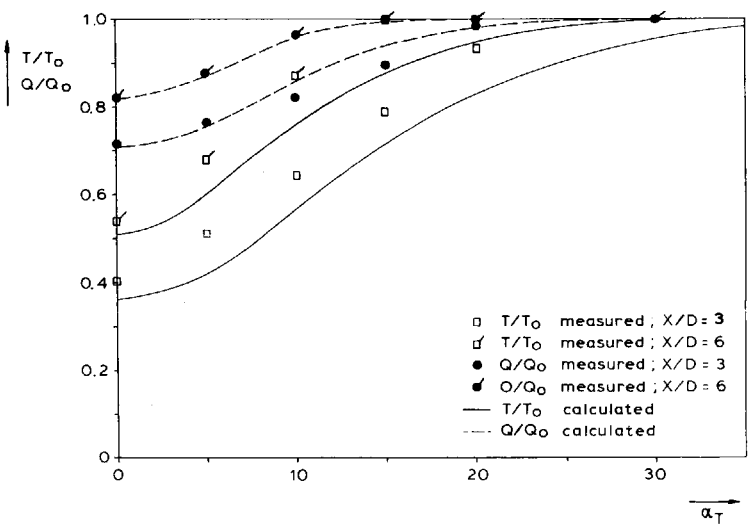

Figure 3.43: thruster-thruster interaction in open water as a function of azimuth angle of the thrusters, $x/D = 3$ and 6

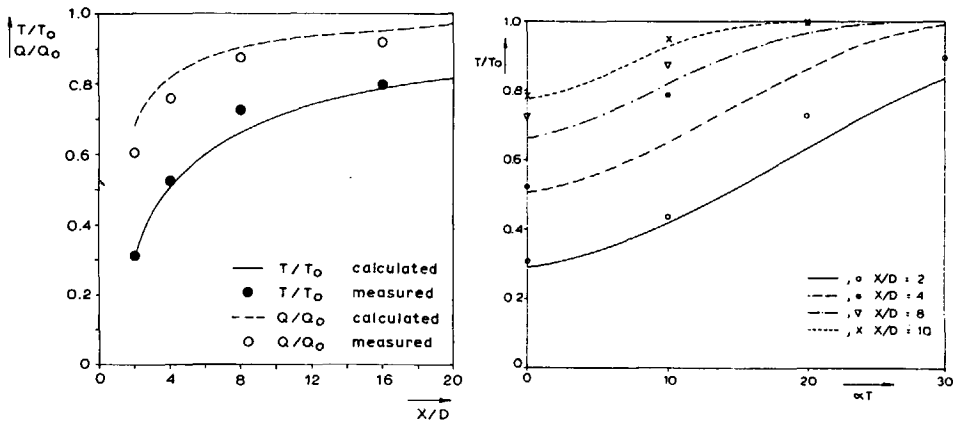

Figure 3.44: thruster-thruster interaction under a flat plate as: a) a function of distance between the two thrusters; b) a function of azimuth angle of the forward thruster

The measurements were also carried out at low speeds. Figure 3.45 shows the influence of speed on the interaction for some of the conditions. It is seen that the effect of speed is rather small in all cases; any effect observed is due to the effect of speed on slipstream decay, which is slower with increasing coflowing ambient speed, and due to the deflection and increased decay of the slipstream in case of oblique flow.

3.5.3 Thruster-hull interaction

3.5.3.1 Thruster-hull interaction measurements

Tests with a flat-bottom barge with various bilge shapes. Force measurements were carried out on the barge fitted with one azimuthing thruster and variable bilge shape. The thrust and torque of the thruster were measured, see Section 2.4.2 as well as the horizontal forces on the barge, see Section 2.4.1.

The test set-up is shown in Figure 3.46 which shows the variable position of the thruster and the barge-shaped hull with variable bilge shapes. Section A.6 gives all details pertaining to the models used for this test series. Table 3.22 gives the test conditions for this case.

Tests for a semi-submersible workover vessel. The same test set-up as described in the previous paragraph was used for measuring the forces on one hull of a semi-submersible as induced by a thruster mounted under a second floater.

The second floater with the thruster was represented by the same barge as described in the previous paragraph. The floater of the semi-sub was realistically

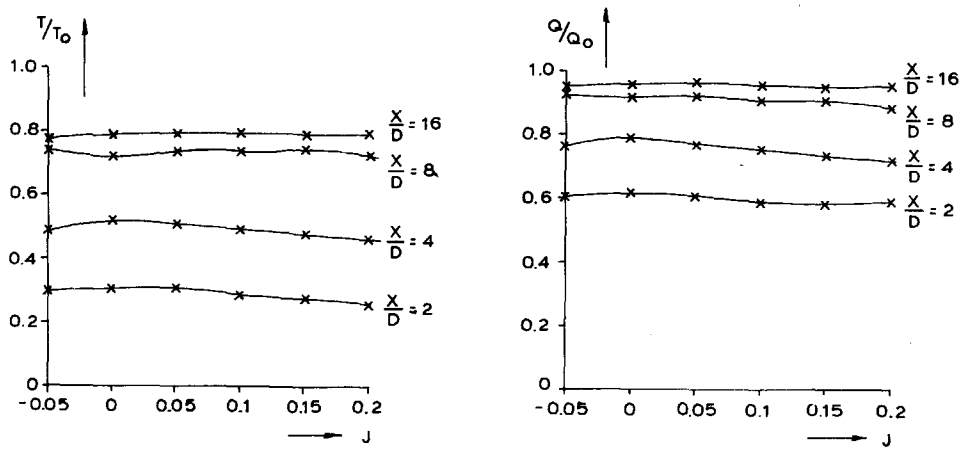

Figure 3.45: thruster-thruster interaction under a flat plate as influenced by ambient speed

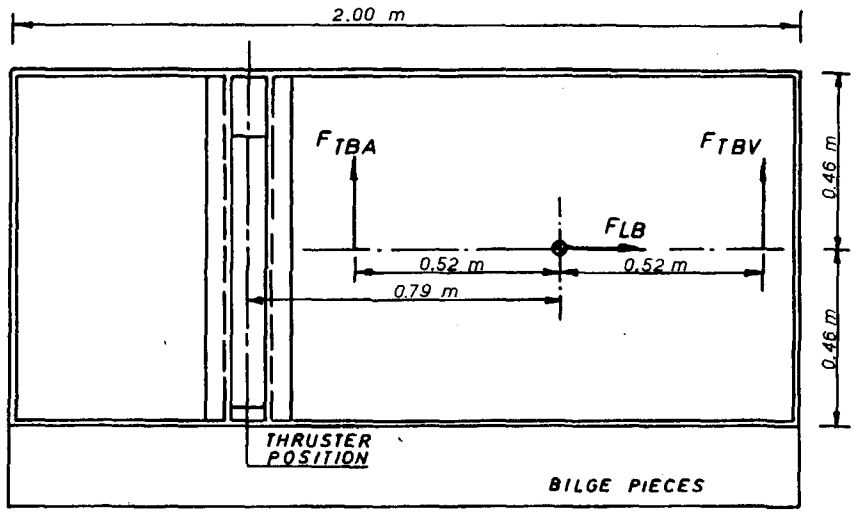

Figure 3.46: test set-up for force measurements on a barge-shaped hull fitted with an azimuthing thruster

Bilge Shape Radius R (m)	Thruster Position l (m)	Thruster Angle (deg)
Circular, 0.0	0.120, 0.420, 0.720	-10, 0, 20, 40
Circular, 0.050	0.120, 0.420, 0.720	-10, 0, 20, 40
Circular, 0.100	0.120, 0.420, 0.720	-10, 0, 20, 40
Circular, 0.200	0.120, 0.420, 0.720	-10, 0, 20, 40
V-shaped	0.120, 0.420, 0.720	-10, 0, 20, 40

Table 3.22: test conditions for force measurements on a flat-bottom barge fitted with an azimuthing thruster

modeled. The test set-up is shown in Figure 3.2. The figure shows the semi-sub floater which could be positioned in various longitudinal positions.

Sections A.4 and A.6 list all details pertaining to the models used for these tests. Table 3.23 gives the test review for the measurements of the forces on a semi-submersible floater induced by an azimuthing thruster mounted under a flat-bottom barge.

Bilge Shape Radius R (m)	Thruster Position l (m)	Thruster Angle (deg)	Floater Position (m)
Circular, 0.0	0.120, 0.420, 0.720	0	0.368, 2.304, 3.344, 3.722
Circular, 0.05	0.120, 0.420, 0.720	0	0.368, 2.304, 3.344, 3.722
Circular, 0.10	0.120, 0.420, 0.720	0	0.368, 2.304, 3.344, 3.722
Circular, 0.20	0.120, 0.420, 0.720	0	0.368, 2.304, 3.344, 3.722
V-shaped	0.120, 0.420, 0.720	0	0.368, 2.304, 3.344, 3.722

Table 3.23: test conditions for force measurements on a semi-submersible floater induced by an azimuthing thruster fitted to a flat-bottom barge

3.5.3.2 Thruster-hull interaction calculations

A very limited number of calculations was undertaken to study the effect of speed on thruster-hull interaction. To this end a two-dimensional plate was subjected to uniform ambient flow and a thruster was positioned upstream and close to the right hand side of the plate. The situation is shown in Figure 3.47 which also shows the grid. The grid covered 58 $\times$ 66 cells and was finely spaced around the thruster and the plate. Calculations were carried out for various thrust levels all creating a thruster wash towards the plate. The location and direction of the thruster was not varied, nor was the ambient speed and the plate size.

3.5.3.3 Discussion of interaction for single-hull floater

Figure 3.48a shows that for the thruster position nearest to the edge of the barge (l = 2.12 m) there is virtually no thrust deduction due the presence of the bilge

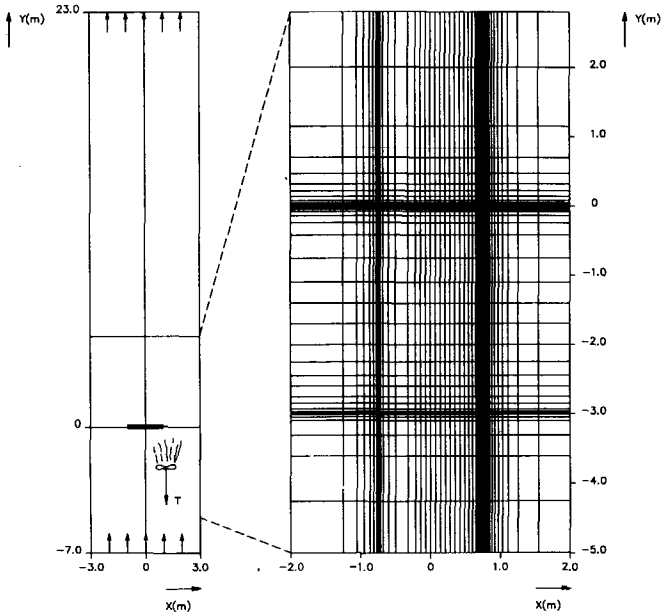

Figure 3.47: situation for two-dimensional jet flow impinging on a flat plate

irrespective of the thruster angle α_T and irrespective of the bilge radius R_b. In view of the conservation of momentum this means that the propeller jet is not changed by the presence of the bilge. As shown in a previous section, this is in line with the results of the velocity measurements which show no appreciable jet deflection.

For larger l-values there is some thrust deduction which increases with l and with the bilge radius. This trend is to be expected since for larger l the velocity in the jet cross-section at the bilge drops. Consequently the flow will remain attached to the bilge for a longer time because the required centripetal force (suction force) for a given deflection will be smaller. As the required acceleration of the flow increases with V^2/R an increase of the bilge radius leads to the same tendency.

From these results it may also be inferred that the thrust deduction will increase with decreasing thrust of the propeller. The present tests covered only high values of the thrust. Still losses of some 15 % are found. Much larger losses will occur for smaller thrust values which occur most often in DP.

Figure 3.48 also shows F_{TB} as a function of α_T for the three thruster positions l =0.12, l =0.42 and l =0.72 m. Some influence of jet-deflection may be seen which as expected is indeed larger for the larger l-values. Percentage-wise the thrust deduction is larger for larger α_T-values. This is to be expected as for larger α_T-values the distance of the thruster to the bilge is larger with a resulting drop in velocity and hence longer attachment of the jet to the bilge. This tendency is clear for both l =0.42 m and l =0.72 m.

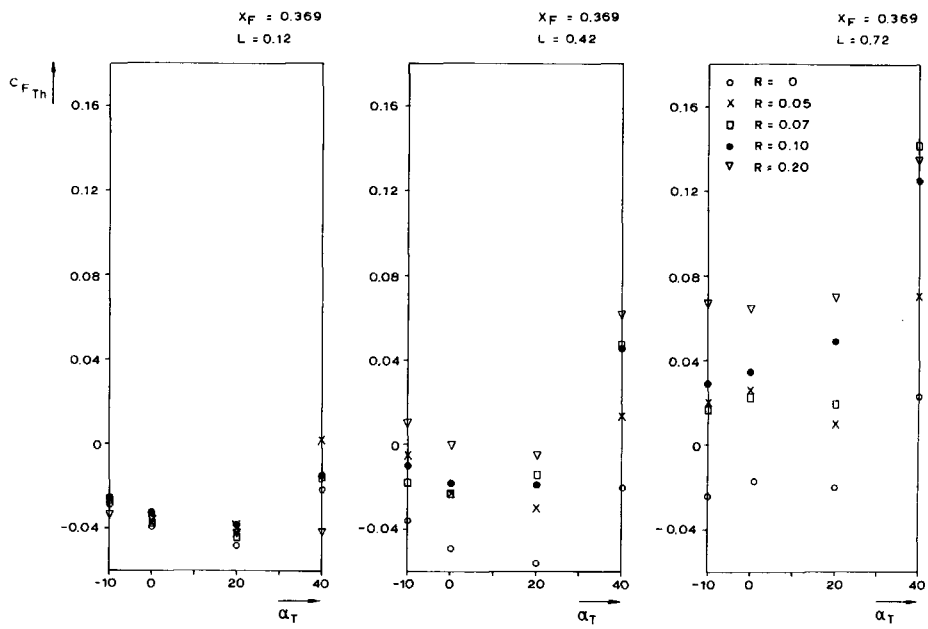

Figure 3.48: transverse barge force as influenced by thruster angle α_T, bilge radius R_b and thruster position l

Figure 3.49 shows the $C_{F_{Lh}}$ coefficient for the longitudinal force on the barge for various thruster angles α_T. The absolute value of $C_{F_{Lh}}$ for α_T =0 increases slightly with larger bilge radius R and thruster distance l. This must be associated with side-ways deflection of the jet flowing around the bilge. The magnitude of this effect is seen to be very small. This shows that the force on the barge associated with jet-deflection acts mainly in the transverse direction for the considered thruster angles. For larger angles close to 90 degrees or for lower jet velocities, the jet will be increasingly deflected towards a direction parallel to the barge and $C_{F_{Lh}}$ will increase. However this increase will be relatively small since the longitudinal force is approximately proportional with the sine of the thruster angle.

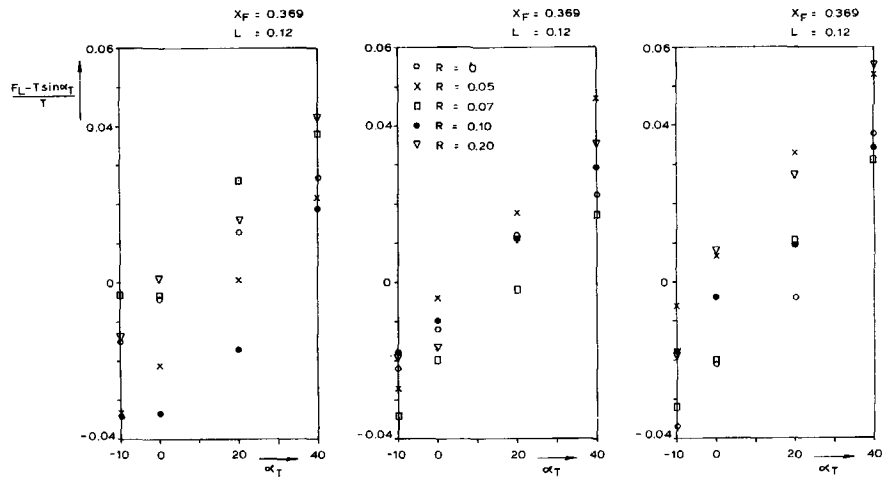

Figure 3.49: longitudinal barge force as influenced by thruster angle α_T, bilge radius R_b and thruster position l

3.5.3.4 Discussion of interaction for a twin-hull floater

Figure 3.50 shows the resistance of the floater to the flow induced by the operating propeller as a percentage of the thrust of the thruster, i.e. the coefficient $C_{F_{Th}}$ introduced in Section 3.1. As this figure shows, losses of between 25 and 45% may be expected for this relative position of floater and barge (X_F =0.368 m) at thruster angle α_T =0.

For the V-shaped frame it appears that the largest thrust deduction occurs for the largest value of l. For a larger bilge radius a further deflection of the jet may lead to reduced deduction factors since then the thruster jet may flow over the submerged floater body. The thrust deduction is seen to be a complicated interplay of the jet deflection, the velocity distribution in the jet and the geometry of the body relative

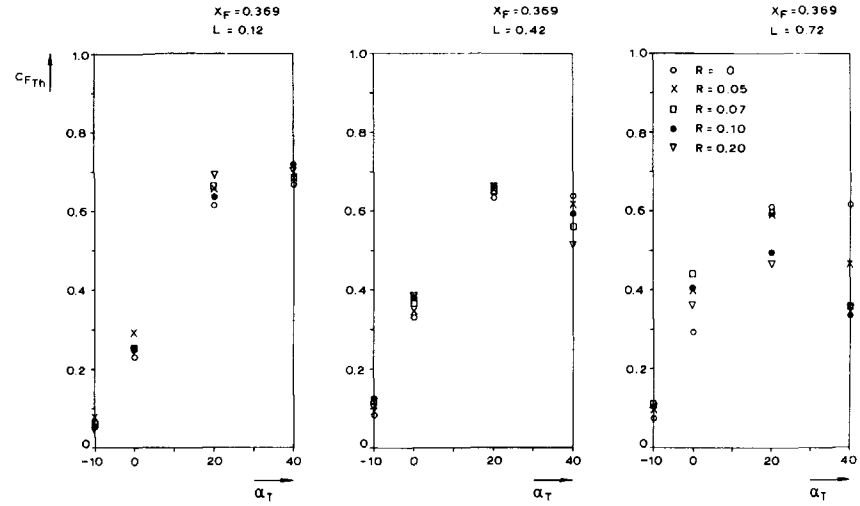

Figure 3.50: transverse floater force as influenced by thruster angle α_T, bilge radius R_b and thruster position l; for X_F =0.368 m

to the jet.

Therefore, it may be possible that a larger thrust deduction on the barge (caused by a larger deflection) may have a favourable influence on the deduction due to the floater. The total resulting net force on the semi-submersible may reach an optimum this way.

This optimum bilge radius obviously also depends on the distance between both floaters (or in this case barge and floater), on the thruster position l, on the dimensions of the floater and on the thrust of the propeller. Further it will depend on the current velocity and current direction, both of which were not considered in these measurements. Therefore it will be impossible to derive an optimum bilge radius for all conditions. However, for the limiting design condition leading to maximum thrust a minimum thrust deduction is required and that aim can be achieved by proper design.

Figure 3.50 shows F_{TF} also as a function of thruster angle α_T. For $X_F = 0.368$ the maximum thrust deduction is found for values of α_T between 20^o and 30^o. For larger α_T the deduction will drop again because of the reduced average transverse velocity in the jet over the floater hull both because of a larger distance to the floater measured along this direction as well as because of the smaller component perpendicular to the floater.

The strong reduction of F_{TF} for thruster positions $l = 0.42$ and 0.72 m for larger α_T could also be ascribed to this sideways deflection, at least partly. As all the aforementioned contributions may be present, the cause of the observed behaviour cannot be firmly established from the presented measurements.

Figure 3.51 shows the point of application of the resistance force on the floater. It may be seen that this point has an almost constant location of approximately 0.2

metres astern of the propeller axis for all values of l and R_b at thruster angle α_T =0. The reason for this value is not clear: with the propeller slipstream located near the aftbody of the floater one would expect positive values for the point of application.

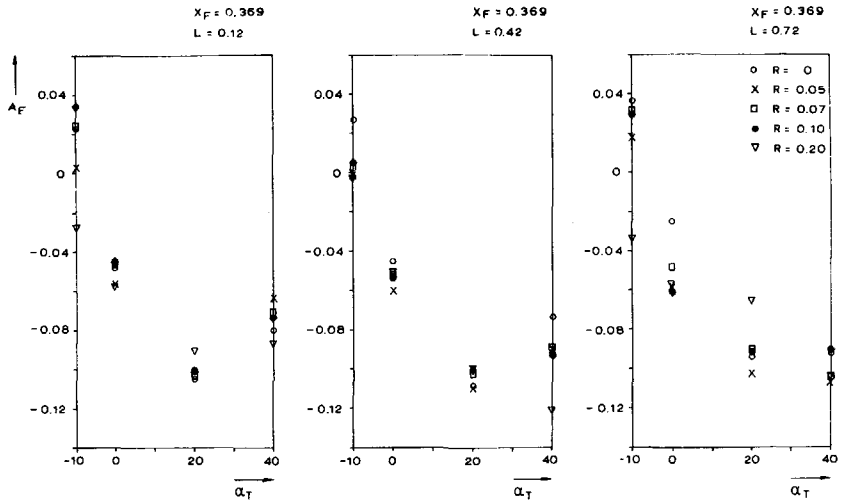

Figure 3.51: point of application of transverse floater force as influenced by thruster angle α_T, bilge radius R_b and thruster position l; for X_F =0.368 m

Figure 3.51 also shows the point of application of the transverse force on the basis of thruster angle. In case the induced flow can be regarded as a local phenomenon this should closely coincide with the value $b \tan \alpha_T$ where b is the distance between thruster and floater. For the case of l =0.12, b = 1.87 m and the results indeed do coincide reasonably well if one starts from a_F = -0.22 m for α_T = 0:

$$a_F = -0.22 + b \tan \alpha_T \tag{3.46}$$

The mentioned figure also includes the point of application for the other two thruster positions l = 0.42 m and l = 0.72 m. Also for these thruster position the linear relationship is adequate. Some of the scatter must be attributed to the fact that if the jet hits a column, the induced floater force can be distributed unevenly across the jet cross-section.

Figure 3.52 shows the transverse floater force as a function of floater position X_F for all values of R_b and l. Considerable thruster force losses of up to 73% due to the presence of the floater are observed. The dependence on l and R_b is obvious from this figure. It is interesting to compare the results for X_F =2.3 with those for X_F =3.35 m. Although the same trends are visible it is apparent that the differences between the 15 combinations of l and R_b-values are smaller. This has to be ascribed to the presence of one of the columns for X_F =3.35 m. This makes the deflection almost irrelevant as a larger deflection will only result in the jet blowing against the column instead of the floater.

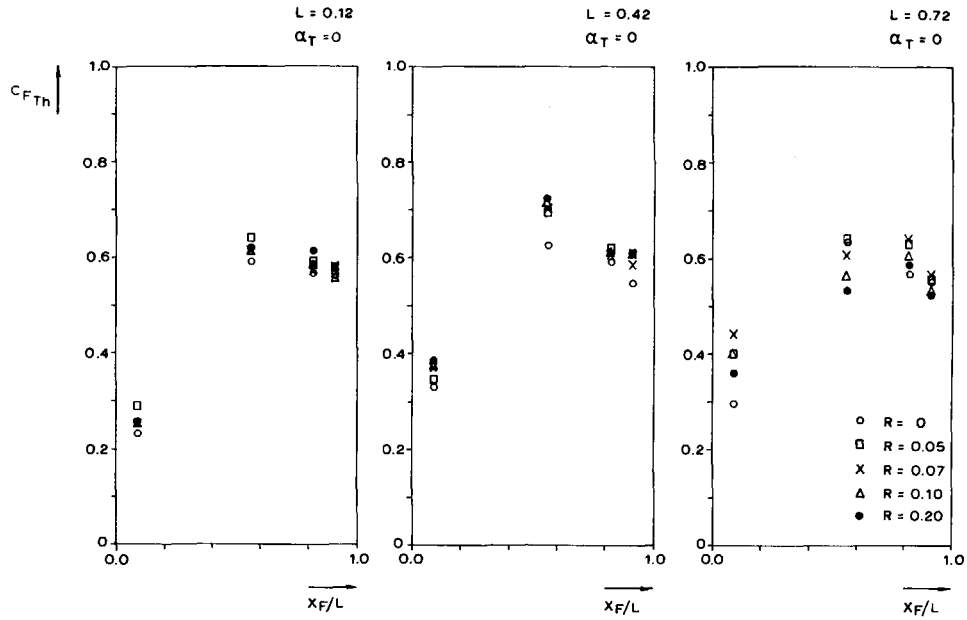

Figure 3.52: transverse floater force as influenced floater position X_F, bilge radius R_b and thruster position l; thruster angle α_T =0

The point of application depicted in Figure 3.53 as a function of X_F, varies in a distinct way around the value of zero. The value $a_F = 0$ agrees with the propeller axis. A shift from negative to positive values of a_F is observed with increasing X_F. This is caused by the asymmetry of the flow conditions due to the presence of the floater. The values of a_F are virtually independent of l or R_b: upward deflection does not change the point of application.

Figure 3.54 shows the longitudinal floater force for different thruster angles at X_F = 0.368m. It may be expected that for $\alpha_T = -20^o F_{LF}$ will be zero as the propeller jet does not interfere with the floater in that case. For $\alpha_T = 40^o$ some 20% of the longitudinal thrust is balanced by floater resistance, $C_{LF} = 0.20$.

Considering the longitudinal floater force F_{LF}, a comparison of the results for l =0.42 and 0.72 m reveals the strange fact that F_{LF} increases with increasing upward jet deflection for $\alpha_T = 20^0$ whereas this trend cannot be observed for $\alpha_T = 40^0$. One possible explanation for this is the sideways deflection of the jet or in other words the bending of the jet into a more longitudinal direction. This could be caused by the suction force at the bilge. The velocity measurements were only carried out for $\alpha_T = 0$ and cannot confirm this explanation. If this were true, however, a shift a maximum F_{LF} towards smaller values of α_T would have to be expected. The increase of F_{LF} for $\alpha_T = 20$ could however also be caused by the presence of the rear column. For $\alpha_T = 20$ and large upward deflection the jet will just hit the forward part of this column. For $\alpha_T = 40$ there would be no such effect which is in

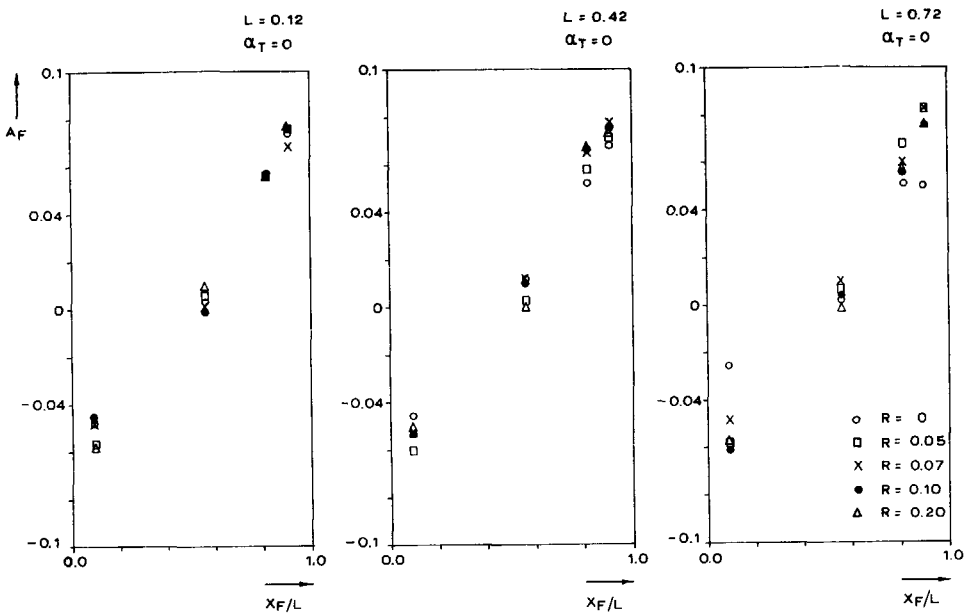

Figure 3.53: transverse floater force point of application on the basis of X_F as influenced by bilge radius and thruster position

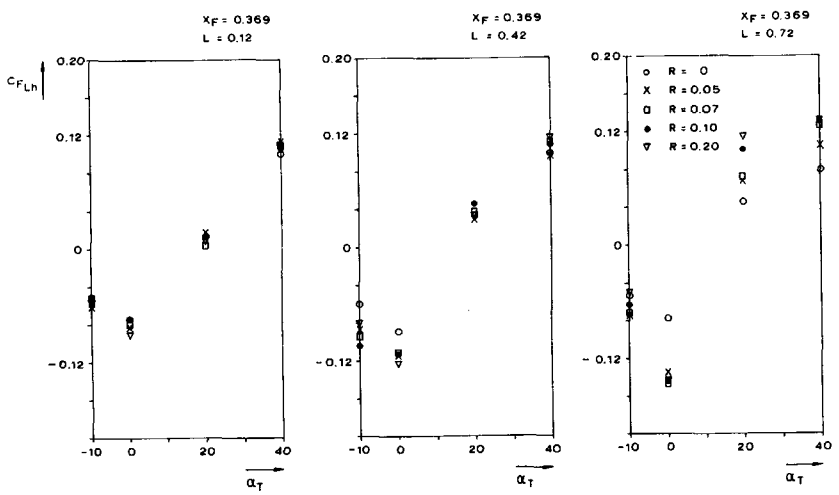

Figure 3.54: longitudinal floater force as influenced by thruster angle α_T, bilge radius R_b and thruster position l

accordance with the measurements.

In this respect it is also interesting to point at the a_F-values for the same thruster positions in Figure 3.51 In case of sideways deflection one would expect an increase in a_F also. The results for l = 0.42 m only mildly exhibit this tendency whereas those for l = 0.72 m does not indicate such a shift of the point of application. It would seem therefore that the sideways shift is mild at most.

Figure 3.55 shows results for the longitudinal floater force for other relative positions of the floater. In the cases of X_F =2.30 m and X_F =3.35 m the longitudinal force is found to be negligible. For X_F =3.72 m a negative longitudinal force is found. In this case the point of impact of the propeller slipstream is located near the bow. This is representative for the case of a forward bow thruster blowing in the direction of the second floater. The resulting force is small, however.

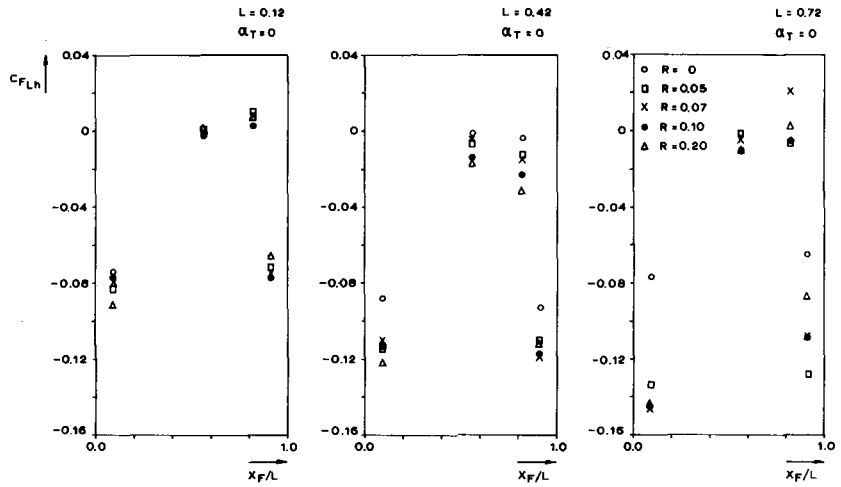

Figure 3.55: longitudinal floater forces for various relative floater positions X_F, bilge radii R_b and thruster positions l; thruster angle α_T =0

An unexplained feature is why all results exhibit negative longitudinal floater forces for both X_F =0.368 m and X_F =3.72 m. One would expect an opposite sign in these two cases. One possibility is that the force is caused by the rotational velocities which would account for the identical sign of the force on both ends of the floater. For intermediate X_F-values all longitudinal forces are indeed almost zero.

3.5.3.5 Interaction resistance coefficients for twin-hull floater

In a previous section, Section 3.4.2, the jet parameters were derived for the jet cross section at the vertical center plane of the second floater. Since also the overall transverse forces on the floater are known it is possible to derive resistance coefficients,

similar to those found for uniform inflow.

However to find meaningful results the resistance coefficient for this analysis is defined by:

$$C_{y,jet} = \frac{F_y}{\frac{1}{2}\rho A_{f,j}\overline{V_{A_{f,j}}}^2} \tag{3.47}$$

where $A_{f,j}$ is the area of the floater lying within the jet cross section which is defined in this case to be the area bounded by the radial coordinate satisfying $r \leq r_j = 3r_{h2}$, see also Figure 3.56. The value of $\overline{V_{A_{f,j}}}$ is the average jet velocity over this area $A_{f,j}$ in the direction of the force F_y.

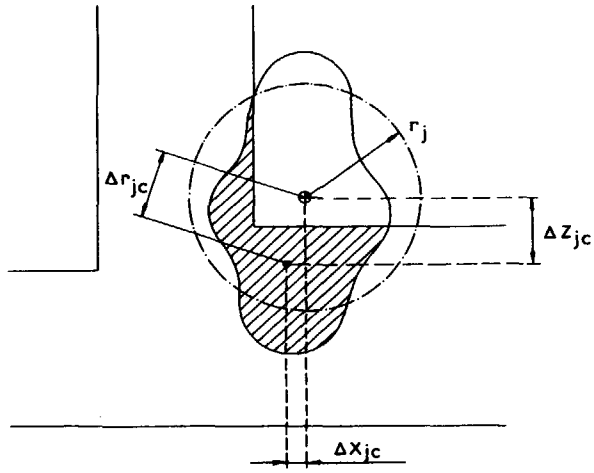

Figure 3.56: area of floater hit by thruster jet

The jet parameters are only known for the thruster angle $\alpha_T = 0$ and the resistance coefficients are only determined for this case. Appreciable scatter of $C_{y,jet}$ was found with values ranging between 1.8 and 3.8. No clear relation with either bilge radius (deflection angle) or floater position (X_F) was observed.

As a next step the fractional area coefficient C_{fa} was determined:

$$C_{fa} = \frac{A_{f,j}}{A_j} \tag{3.48}$$

with A_j the total cross sectional area of the jet again bounded by by the radial coordinate satisfying $r \leq r_j = 3r_{h2}$.

Plotted on the basis of C_{fa} the resistance coefficients are seen to converge with increasing value of C_{fa}, see Figure 3.57a. The scatter is seen to increase with decreasing values of the fractional area coefficient and as the figure shows there is no clear relation with bilge radius. The figure shows that if the jet is blowing

partly past the floater structure the resistance coefficient becomes unpredictable. However if the jet is entirely hitting the floater the value of $C_{y,jet}$ tends to a value of approximately 2.2.

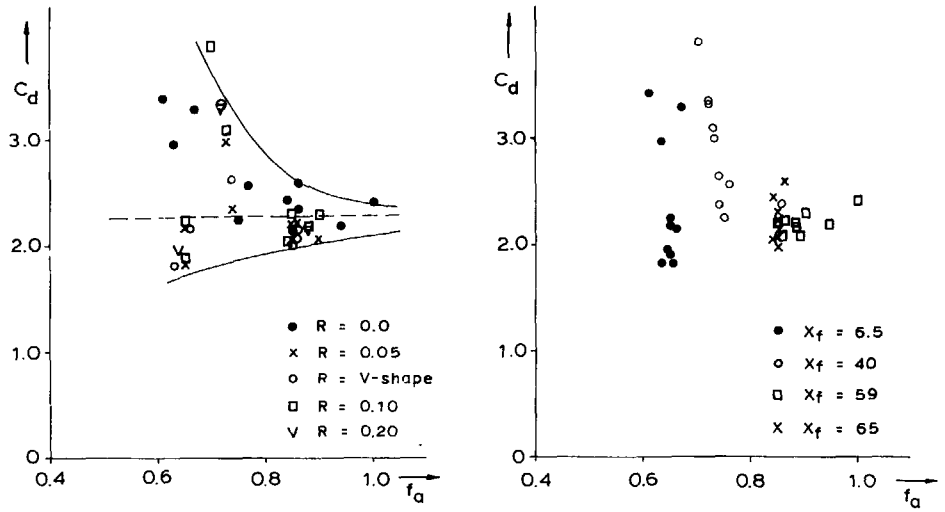

Figure 3.57: floater force resistance coefficients as a function of fractional area coefficient and depending on bilge radius and floater position

If the values of $C_{y,jet}$ are again plotted on the basis of C_{fa} but now indicating the value of X_F for which they are valid, the results fall apart in four groups, see Figure 3.57b.

This figure together with Figure 3.57a indicates that the scatter is not strongly related to either floater position and therefore floater shape or jet deflection. To resolve this matter the center of the floater-jet interaction area $A_{f,j}$ was derived and compared to the jet center. To this end the following two static moments were determined relative to both the x and z-axes, i.e the two axes lying in the floater center plane. These are defined by:

$$\begin{aligned} S_{f,j;x} &= \int_{A_{f,j}} xV dA_{f,j} \\ S_{f,j;z} &= \int_{A_{f,j}} zV dA_{f,j} \\ S_{j;x} &= \int_{A_j} xV dA_j \\ S_{j;x} &= \int_{A_j} zV dA_j \end{aligned} \tag{3.49}$$

From these volume flow static moments the respective centers $x_{f,j}, z_{f,j}, x_j$ and z_j were determined by dividing by the corresponding volume flows across the areas

A_j and $A_{f,j}$ and the distance between the two centers were obtained:

$$\begin{aligned} \Delta x_{jc} &= x_j - x_{f,j} \\ \Delta z_{jc} &= z_j - z_{f,j} \\ \Delta r_{jc} &= \sqrt{(\Delta x_{jc})^2 + (\Delta z_{jc})^2} \end{aligned} \tag{3.50}$$

Figure 3.58 shows the resistance coefficient on the basis of Δz_{jc}. The figure shows the clear change of resistance coefficient with the distance between the jet and jet-floater volume flow centers. The remaining scatter is surprisingly small if one considers the various steps taken to derive the coefficients and the measurement accuracy pertaining to the LDV and force measurements. Indeed the only significant scatter is found for Δz_{jc}-values close to zero.

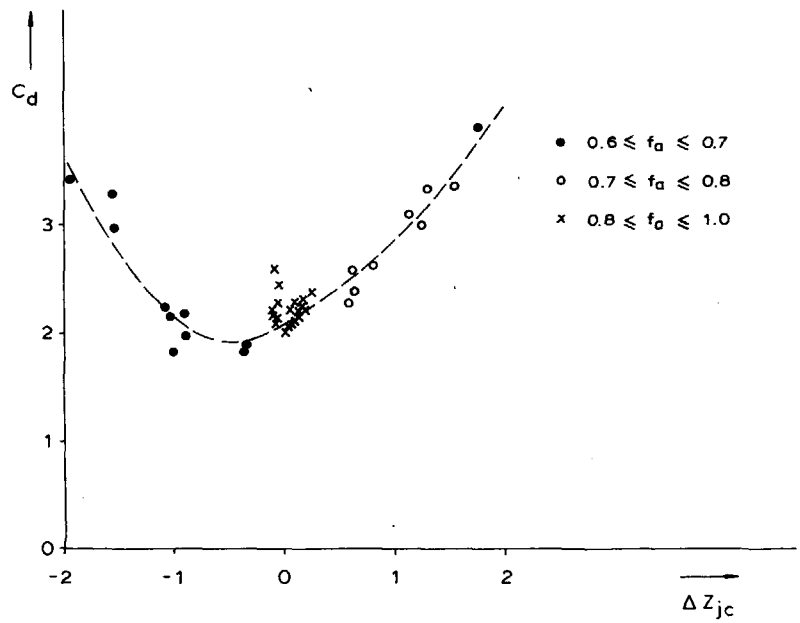

Figure 3.58: floater force resistance coefficients as a function of vertical difference in location of the jet volume flow centers

Also some asymmetry is observed showing that the resistance coefficient differs with the jet flowing around the keel side (showing smaller values of $C_{y,jet}$) or around the upper side (showing larger values of the resistance coefficient).

This can be explained by observing that the cross section of the floater is more rounded on the lower side especially if one considers that the flow is directed somewhat upward on account of the deflection introduced by the bilge. Figure 3.59a illuminates this situation.

At the forward and aft end of the floater similar phenomena will undoubtedly arise; the present measurements however did not cover such floater positions.

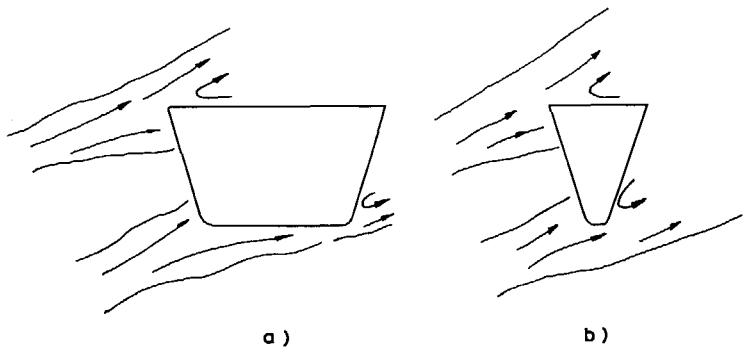

Figure 3.59: explanation of asymmetry in floater force resistance coefficients as caused by vertical differences in the location of the jet volume flow centers

Figure 3.60 shows again the resistance coefficients but now on the basis of the radial distance of the volume flow centers. This distance Δr_{jc} is made dimensionless with the average jet radius $\overline{r_{jc}}$.

The figure again shows two main lines, one for the jet flowing over the floater and one for the jet flowing underneath it. The former exhibits the higher resistance coefficients but for values of $\Delta r_{jc}/\overline{r_{jc}}$ of approximately 0.1 a vague transition region occurs. This is in agreement with the scatter observed in Figure 3.58. Now it must be realized that all the open triangles with larger values of $C_{y,jet}$ in Figure 3.60 relate to the floater position at which the waterlines are running inwards. This means that the cross section is becoming sharper, see Figure 3.59b and the resistance coefficient is increasing. Thus the scatter in this region can be explained again by relating the value of $C_{y,jet}$ to the local shape of the floater.

From the results presented here it is possible to derive a rather accurate general method to determine thruster-hull interaction for a twin-hull situation. Indeed also propeller wash induced forces for e.g. ships towed by tugs can be treated using this material.

The shortcoming still present is the effect of inflow speed on the resistance coefficients which was not covered in the present work.

To that end a limited two-dimensional computational exercise was carried out where the influence of forward speed on the resistance coefficient was studied. The situation refers to a two-dimensional jet in uniform inflow impinging on a flat plate, see Section 3.5.3.

Figure 3.61 shows the velocity distribution and C_p-coefficient for a thrust of 250 N. Despite the strong jet generated by the two-dimensional thruster, the pressure on the flat plate is increased only marginally compared to that of the case without a thruster. The increase of pressure is only local on the right hand side of the plate

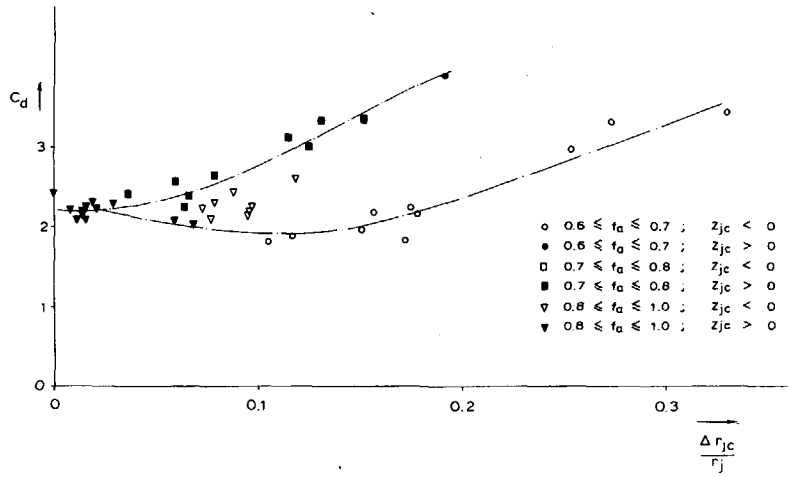

Figure 3.60: floater force resistance coefficients as a function of radial difference in location of the jet volume flow centers

where the jet impinges. The reason for this mild pressure change (and relatively small thrust degradation) is found by considering the flow vectors. These show that the jet is deflected away from the plate by the ambient flow which is curving around the plate. Therefore the thrust degradation is becoming smaller for this particular condition compared to that for zero ambient speed.

The change of pressure coefficient with changing thrust is shown in Figure 3.62 where the C_p-value on both sides of the plate is shown. This figure again confirms that a stronger jet is deflected less by the ambient flow and that the thrust degradation increases. The related induced force on the plate is shown in Figure 3.63 and shows the importance of the ratio between jet velocity and ambient velocity. The figure also shows the point of application of the thruster induced force. It is seen that the induced flow again is a largely local phenomenon not affecting the flow around the remainder of the plate significantly.

It is expected that for a three-dimensional situation the same effects prevail although the deflection of the jet will be probably reduced on account of the possibility for the flow to circumvent the jet.

It can be stated that with the techniques presented, it has become possible to analyse the thrust degradation for these conditions in more detail covering such aspects as jet deflection, ambient flow, simplified geometries and shading effects between 2 parallel floaters.

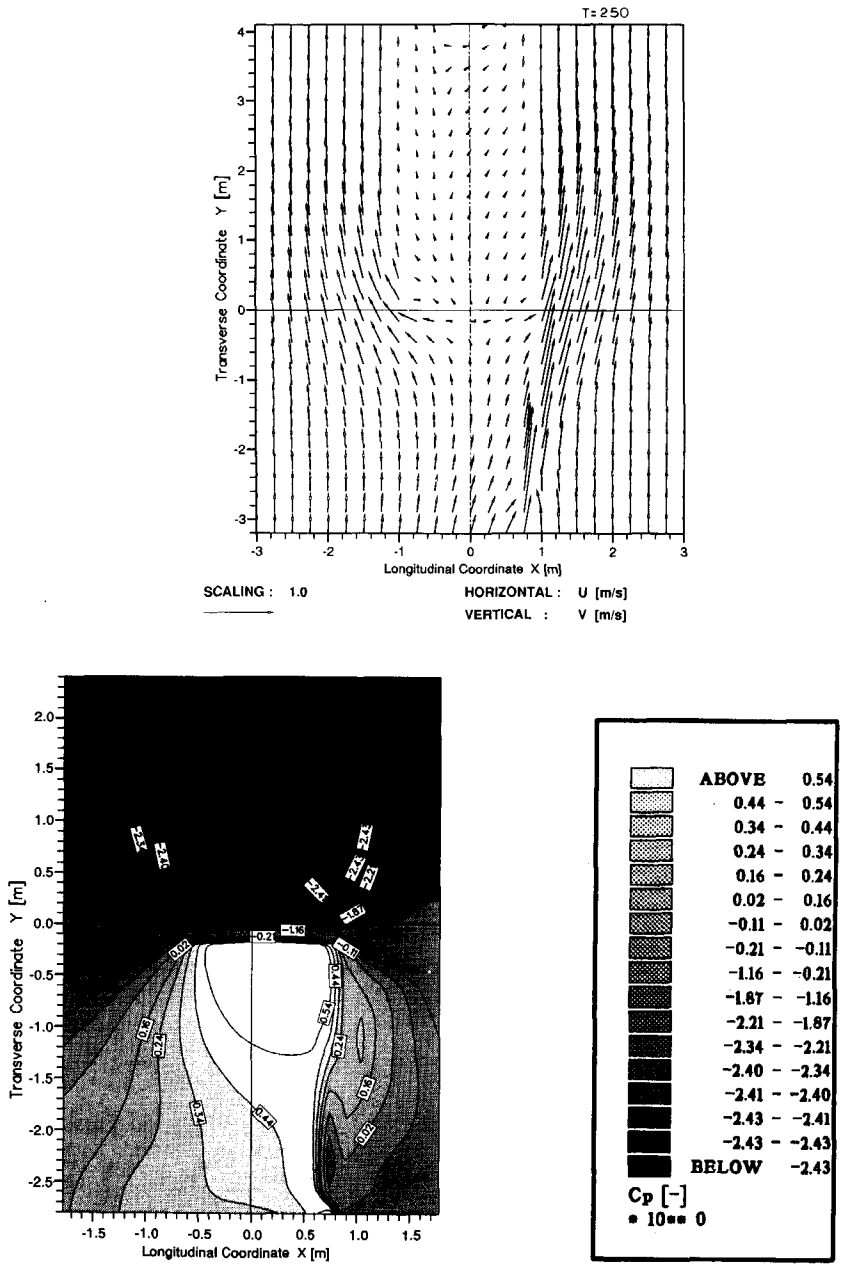

Figure 3.61: flow field for a jet in ambient flow impinging on a flat plate

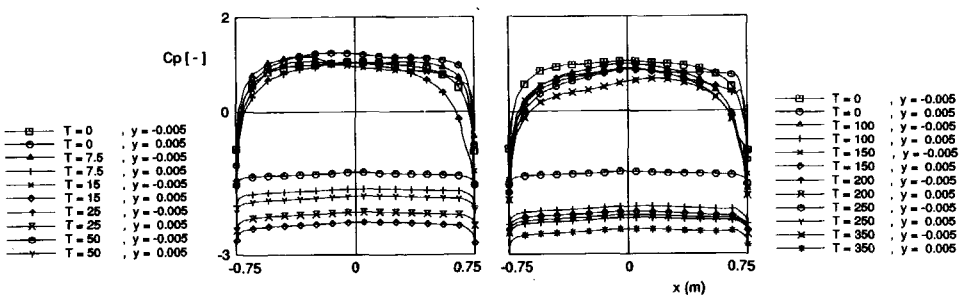

Figure 3.62: pressure coefficient on the flat plate for a jet in ambient flow impinging on a flat plate

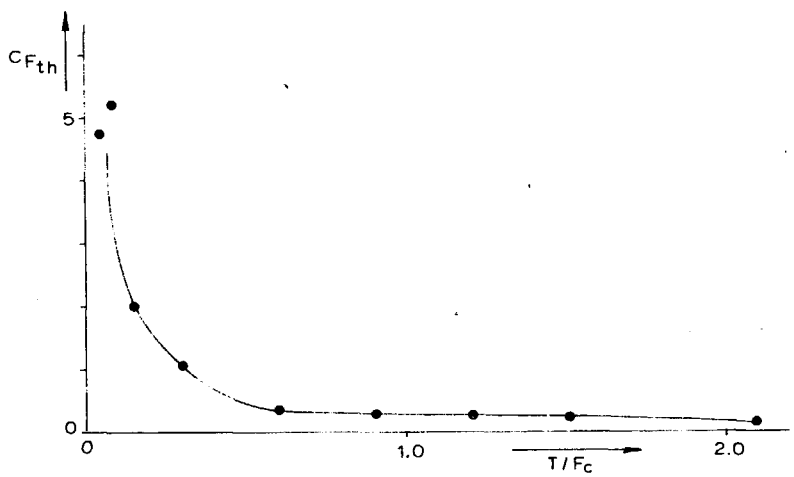

Figure 3.63: thrust degradation factors for a jet in ambient flow impinging on a flat plate

3.6 Interaction for Tunnel Thrusters

3.6.1 Introduction

The previous sections have covered one of the most frequently encountered actuators in some detail. The remaining sections of this chapter treat another important manoeuvring and positioning device, the tunnel thruster.

Past work on this propulsor has identified an important shortcoming of the tunnel thruster, i.e. that its effectivity rapidly decreases with increasing forward speed, see e.g. Chislett etal [42] and Beveridge [43]. The theoretical work concentrated on the forward speed only, see Cooper, [38] with extensions to small drift angles, Kijima [50]. Experimental work focussed on the deep water effectivity of the bow thrusters at forward speed (zero drift angle) mostly disregarding the possible effects of shallow water, large drift angles or presence of quays. Considerable attention was devoted to overcoming the detrimental effect of speed on the tunnel thruster effectivity for which reference may be made to the work of Brix [49], [45] who suggested the application of an anti-suction tunnel to reduce the extent of the low pressure region on the exit side of the thruster jet. This low pressure region is known to be directly related to the reduced side thruster effectivity and is caused by the entrainment into the thruster jet as it is deflected by the inflow (i.e. forward speed) to become increasingly oriented parallel to the ship. This was already found in earlier aerodynamic work, see Jordinson [37].

The following sections form an attempt to shed more light on the phenomena involved in the effectivity of side thrusters in more or less arbitrary inflow conditions. Both calculations for simplified cases as well as measurements are presented and discussed. The calculations are used to obtain more insight in the forces generated by the thruster since they give detailed information on the flow it induces. It is not attempted to carry out a complete correlation study involving the measured as well as calculated forces and moments since the theoretical analysis is aimed to be qualitative. Indeed a full correlation study would also require a detailed modelling of the hull shape which is outside the scope of the computational tool in its present form.

The discussion first deals with the simplified cases for which calculations were carried out. Subsequently the measurements are discussed and reference is made to the relevant results of the calculations.

3.6.2 Calculation of interaction

3.6.2.1 Calculations for a two-dimensional wedge with a tunnel thruster

This computational case refers to a symmetrical situation where a two-dimensional flat plate is subjected to an inflow with a speed of 0.319 m/s. The inflow is directed perpendicular to the plate, i.e. the drift angle equals 90^0. In the center of the plate a tunnel thruster is positioned delivering a certain thrust. The thrust distribution was taken to vary linearly with the distance to the propeller center and a hub was

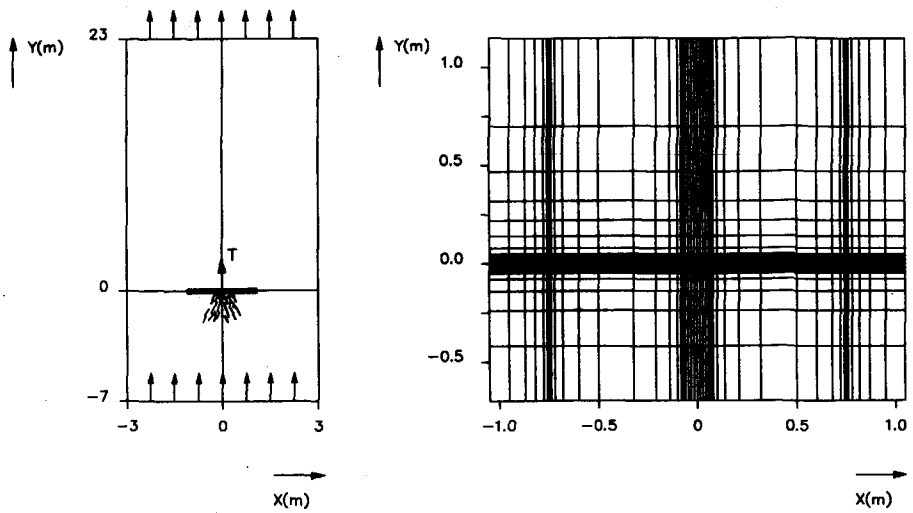

Figure 3.64: two-dimensional plate with a center-line thruster in uniform inflow

not modelled. Figure 3.64 shows the situation and also indicates the extent of the fluid domain which was assumed to be sufficiently large for this study to exclude wall effects. Indeed calculations for a larger domain for one of the cases showed insignificant differences.

Figure 3.64 also shows a part of the grid for these calculations and it is seen that the grid was symmetric with respect to the Y-axis. The grid consists of 53 $\times$ 57 cells. Although the grid is rather coarse compared to the suggested number of cells of approx 70 (see Chapter 2) the present grid is considered to be sufficient since only variations of the flow due to different thrust levels are of interest. Absolute forces or pressure distributions are not of interest here.

3.6.2.2 Calculations for a two-dimensional flat plate with a bow thruster

This case covered a flat plate with dimensions identical to that used for the flow calculations for varying drift angle, see Chapter 2. However in this case a tunnel thruster opening was added at 4.7 % of the length from the leading edge (stern) or trailing edge (bow). The grid was correspondingly modified and is shown in Figure 3.65 for the case of a stern thruster.

The extent of the fluid domain is identical to that used in Chapter 2 and the grid fineness (80 $\times$ 82 cells) is sufficient to obtain reliable two-dimensional results. The tunnel diameter is again 0.14 m with a linearly varying thrust distribution from center to tip.

By varying the drift angle from 0 to 90 degrees and by locating the tunnel both at X = -2.4 and X = 2.4 m as well as considering positive and negative thrust

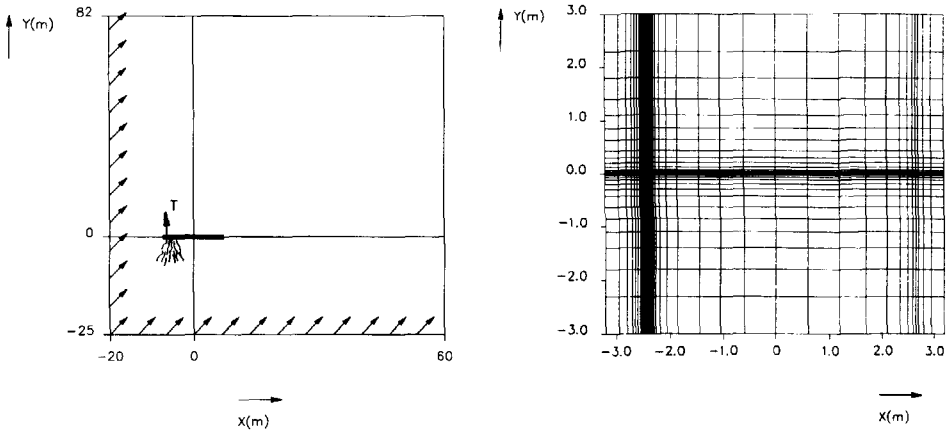

Figure 3.65: grid for two-dimensional plate with a bow thruster

values, the entire drift angle range was covered.

3.6.2.3 Calculations for a three-dimensional wedge with a tunnel thruster

This computational case again refers to a symmetrical situation where a flat plate is subjected to a uniform inflow with speed $V = 0.319$ m/s. As for the two-dimensional case a thruster is located on the center-line of the plate, see Figure 3.66. The thruster opening has a diameter of 0.14 m and the propeller axis is located approximately D from the keel. Again a linear thrust distribution is applied and a hub is not modelled. The torque, for most cases set equal to zero, is also modelled using a linear distribution.

The fluid domain is approximately equal to that in the basin where experiments were performed on a wedge with a tunnel thruster. The calculated and measured conditions were similar with the important exception of the hull shape which was a flat plate for the calculations and a ship-like two-dimensional section for the measurements.

Figure 3.66 shows the grid for the computations which consists of $57 \times 53 \times 37$ cells. The propeller is covered by a total of 58 cells giving a sufficiently fine thrust distribution. Note that the thrust per cell was corrected for the fact that a certain part of the exterior cells is located outside of the propeller radius.

3.6.2.4 Calculations for a three-dimensional flat plate with a bow thruster

This computational case refers to a flat plate of 5.3 m length with a tunnel thruster located at 4.7 % of the length astern of the bow. Figure 3.67 shows both the situation

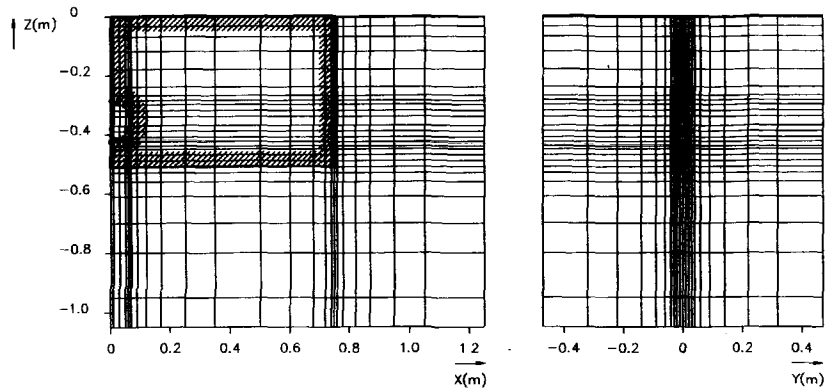

Figure 3.66: three-dimensional plate with a center-line tunnel in uniform inflow

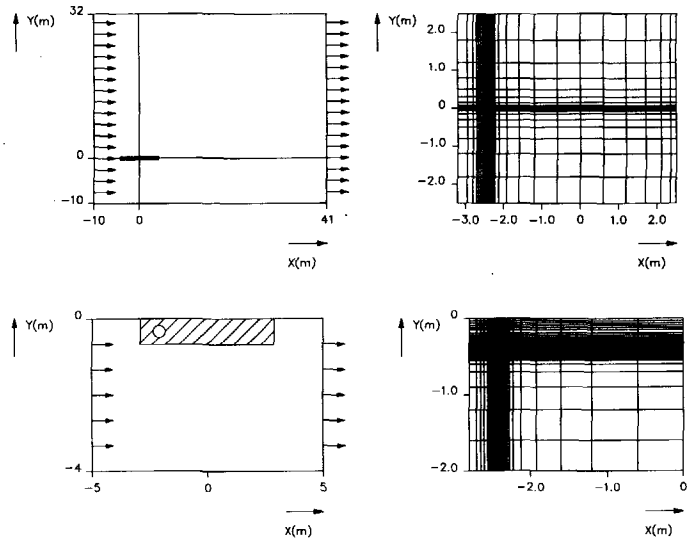

Figure 3.67: three-dimensional plate with a bow thruster in forward speed

as well as the most relevant part of the grid.

Although in principle calculations are possible for arbitrary drift angles attention focussed on forward speed only ($\beta = 180$). Both the thrust as well as the ship speed was varied. Only deep water conditions were considered although again this is not a necessary restriction.

The representation of the propeller thrust and tunnel opening is identical to that for the three-dimensional wedge discussed previously.

To confirm the potential advantage of an anti-suction tunnel a calculation was carried out for the same flat plate but with an additional hole in the vicinity of the tunnel. To this end the local grid was refined to properly define this hole.

3.6.3 Measurement of interaction

3.6.3.1 Tests for a tunnel thruster in a wedge-shaped hull

These tests were performed on a simplified wedge-shaped hull fitted with one tunnel thruster. The wedge has a uniform frame shape similar to a typical ship's frame at the usual location of a bow thruster. The particulars for the tested configuration are given in Section A.5.

Table 3.24 lists the test conditions for the wedge with the tunnel thruster. Note that seven speeds were considered; for each speed seven rpm-values were covered. The velocity direction was parallel to the thruster axis, i.e. perpendicular to the wedge's longitudinal axis (drift angle equal to 90 degrees).

Current Speed (m/s)	Number of Revolutions (1/s)
-0.478, -0.319, -0.159, 0.0, 0.159, 0.319, 0.478	-17.06, -12.79, -8.50, 0.0, 8.50, 12.79, 17.06

Table 3.24: test conditions for tunnel thruster in wedge-shaped hull

During these tests the longitudinal and transverse forces were measured which were translated in the total longitudinal force, F_L, the total transverse force, F_T, and the turning moment N_{zz}.

Also the thrust of the entire unit T_u was measured, i.e. the thrust delivered by the combination of propeller, hub and vertical drive, see Section 2.4.2. Further also the torque in the hub Q was measured.

For the considered inflow angle the longitudinal force and turning moment are not very relevant on account of the symmetry of the hull with respect to the vertical plane through the tunnel center line. They only serve to indicate if a stable asymmetrical flow can exist in certain conditions.

3.6.3.2 Tests for a hopper dredger fitted with a tunnel thruster

Tests were performed on a typical hopper dredger fitted with one bow tunnel thruster unit. The particulars for the tested configuration are given in Section A.3.

Table 3.25 lists the test conditions for the hopper dredger with the tunnel thruster. Note that variations in water depth, current velocity and current direction were covered.

3.6.3.3 Tests for a ferry fitted with a tunnel thruster

Tests were also performed on a typical ferry fitted with one bow tunnel thruster unit. The particulars for the tested configuration are given in Section A.1.

Table 3.26 lists the test conditions for the ferry with the tunnel thruster. Note that variations in thruster RPM, current velocity and current direction were covered. All tests refer to deep water.

Drift Angle (deg)	Current Speed (m/s)	Number of Revs (1/s)	Water Depth/ Draft Ratio (-)
30, 45, 60, 90, 120, 150, 210, 225, 240, 270, 300, 330	0, 0.2, 0.4, 0.6	0, 25.0	∞
0, 15, 180, 195	0, 0.2, 0.7, 1.1, 1.4, 1.7	0, 25.0	∞
30, 45, 60, 90, 120, 150, 195, 210, 225, 240, 270, 300	0, 0.2, 0.4, 0.6	0, 25.0	2.5
0, 15, 180, 330	0, 0.2, 0.7, 1.1	0, 25.0	2.5
15, 30, 45, 60, 90, 120, 150, 195, 210, 225, 240, 270, 300, 330	0, 0.2, 0.4, 0.5	0, 25.0	1.25
0, 180	0, 0.2, 0.7, 1.1	0, 25.0	1.25

Table 3.25: test conditions for tunnel thruster in a hopper dredger

Drift Angle (deg)	Current Speed (m/s)	Number of Revolutions (1/s)
15, 30, 45, 60, 90, 120, 150, 210, 240, 270, 300, 315, 330, 345	0, 0.1, 0.2, 0.3, 0.4, 0.5, 0.6	0, 20, 25
0, 180	0, 0.1, 0.2, 0.3, 0.4, 0.5, 0.6 1.0, 1.4	-25, -20, 0, 20, 25

Table 3.26: test conditions for a ferry and a container vessel with a tunnel thruster

3.6.3.4 Tests for a container vessel fitted with a tunnel thruster

This test series was performed on a typical container vessel fitted with one bow tunnel thruster unit. The particulars for the tested configuration are given in Section A.2.

Table 3.26 lists the test conditions for the container vessel with the tunnel thruster. Note that variations in thruster RPM, current velocity and current direction were covered and that the same test program as for the ferry was performed. All tests again refer to deep water.

3.6.4 Discussion of calculations

3.6.4.1 Calculations for a two-dimensional wedge with a tunnel thruster

For this simple case calculations were performed for one inflow speed (V = 0.319 m/s) and a variety of thrust levels. The imposed thrust levels for the schematized impeller ranged from T_p =320 N to T_p = -320 N which values are approximately twice the current force on the wedge subjected to the same inflow speed but without an operating thruster. Note that the adjusted thrust is different from the normally used total side force value since in the latter also the hull contribution to the force is included. For bollard pull this hull contribution can theoretically be 50 % of the total force, see e.g. Norrby etal [29] and strongly depends on tunnel length, tunnel

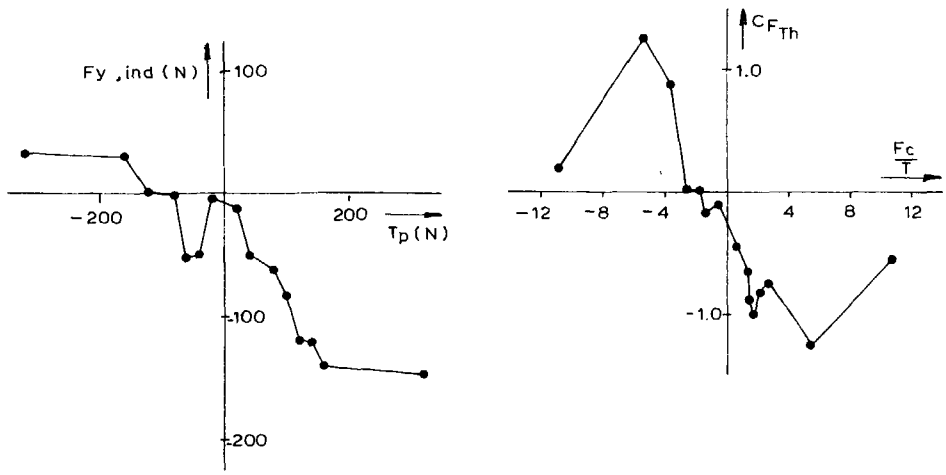

Figure 3.68: a. force on a 2D flat plate induced by tunnel thruster as a function of thrust; b. normalized induced force on a 2D flat plate as a function of normalized thrust

fairing etc, see Taniguchi etal [52]. For the present case the tunnel length is zero, tunnel fairing is absent and the hull contribution to the total bollard pull is less than 10 %.

The reference case is the one with the plate subjected to the inflow and the thruster opening closed. The pressure distribution (in terms of dimensionless C_p coefficient) and velocity vector diagram for this case are very similar to the results reported for the flat plate in Chapter 2.

It can be argued that the reference case is rather formed by the flat plate without a thruster but with the tunnel opening present. However in terms of total side force on the plate the differences are insignificant as can be seen in e.g. Hoerner [69]. This was confirmed by a subsequent calculation with the hole in the plate while setting the thrust at zero. Obviously there is a some change of the pressure distribution in the immediate vicinity of the opening.

Subsequently the thrust was varied from large negative to large positive values. The corresponding side force F_y on the plate was determined by pressure integration. The difference between this force and the current force (i.e. the force at zero thrust) is the force induced on the plate by the action of the thruster, see Section 3.1. Figure 3.68 shows both the calculated total and induced force on a basis of impeller thrust (Figure 3.68a) as well as this induced force as a fraction of the thrust on the basis of the thrust normalized by the current force, Figure 3.68b.

It is common procedure to plot the tunnel thruster side force for a ship with forward speed on the basis of the dimensionless speed, i.e. the ship speed normalized

with the thruster jet speed, see Chislett etal [42]:

$$m = \frac{V_s}{\sqrt{\frac{T}{\rho A_p}}} \tag{3.51}$$

While this is found to result in side force effectivities which lie in a moderately narrow band for the many cases studied for forward speed, it remains to be seen if this is the correct parameter for assessing the effectivity for cases such as considered here. For the forward ship speed problem the induced force is dominated by the jet deflection which is indeed a function of this speed ratio, see e.g Margason [83]. For the present problem deflection can be expected to play a minor role and the induced force may well be related to the influence region of the thruster. On the suction side of the propeller this is probably determined by the thrust whereas on the exit side the jet-flow interaction plays an important role which is largely governed by the ratio of the jet and ambient velocities. This automatically leads to the fact that the propeller diameter is an important factor to consider.

Also since probably the jet influence region is important, the relative size of this region compared to the overall plate or hull size must be considered. For the bow thruster forward speed problem this is irrelevant since the current force is zero anyway. However for larger drift angles, the plate size plays an important role. It is then probably no longer possible to express the thrust degradation only by a single parameter such as the speed ratio m.

The above figures show significant effectivity changes with changing thrust levels. The reason for these changes can be seen if the flow details are considered. Figure 3.69 shows the pressure coefficient and velocity vector diagram for a thrust opposing the current force, T=-160 N, i.e. approximately 90 % of the current force. At this thrust value, where the thruster jet is directed with the inflow, the resistance of the plate increases by some 45 %. In other words in this condition it is significantly more demanding to maintain the position of such an (admittedly unrealistic) ship. As the figures show the flow is strongly affected by the presence of the thruster.

Figure 3.70 shows the C_p-curves for a selected number of negative thrust values. Taking these figures together it is clear that although the pressure is changed at the suction side, i.e. on the face of the plate, the dominant change occurs on the downstream side, i.e. the side where the thruster jet issues in the more or less stagnant flow in the wake of the plate. Apparently the jet reduces the pressure on that side. This will in part be caused by the entrainment into the jet which impairs the recirculation of the flow in the wake of the plate thus preventing some of the pressure recovery to occur. Also the presence of the jet will leave less space for the recirculation region which must therefore restrict itself to a smaller area which furthermore reduces pressure recovery.

The pressure on the upstream side is reduced somewhat which contributes favourably to the thruster-hull interaction. However this minor improvement is more than offset by the large detrimental effect on the downstream side. It is seen that symmetry is preserved very well for these conditions and the solution of the calculations was stable.

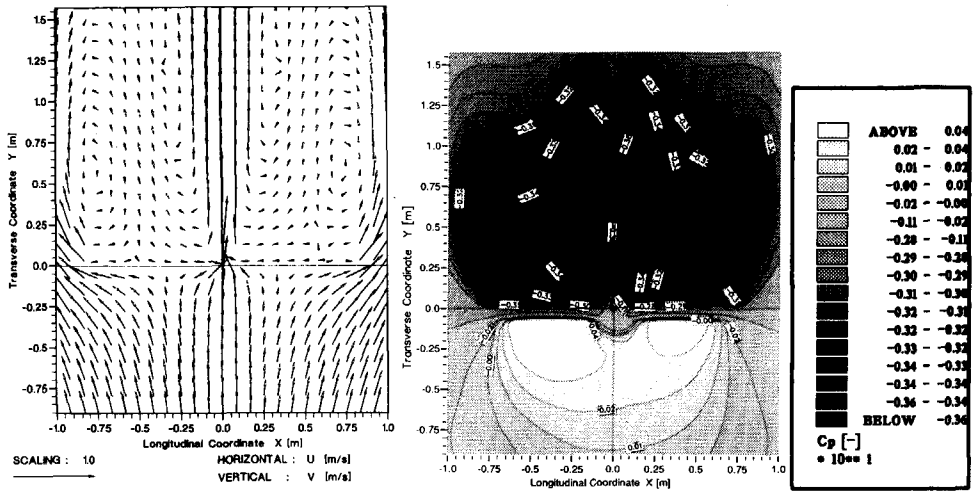

Figure 3.69: pressure coefficient distribution and velocity vector plot for flow around a two-dimensional flat plate - T_p = -160 N

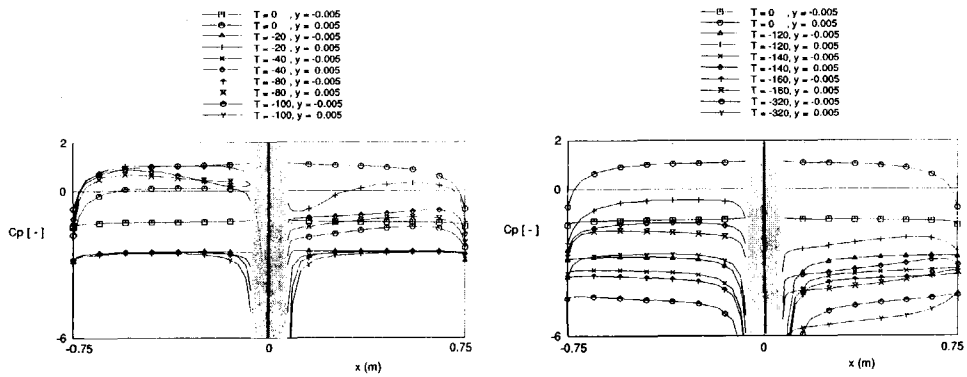

Figure 3.70: pressure coefficient distribution on a flat plate - negative thrust values

An altogether different situation arises if the thruster blows opposite to the inflow, i.e. for positive thrust values. This is similar to an initially stationary ship attempting to move with the current or to a ship in a turn where the vessel drifts such that the ambient flow comes in on the suction side of the thruster. This situation can also occur while station keeping in wind and tidal current where these two are directed opposite to one another and the thrusters are used to counteract the dominant wind force. Nevertheless this situation is of somewhat less relevance for practical situations.

Figure 3.71 shows the main flow particulars for a positive thrust value ($T_p = 160$ N), i.e. a jet opposing the inflow. The velocity vector plot shows that the propeller jet is assuming an unsymmetric pattern despite the symmetry of the inflow and the situation. This is not unexpected since for this two-dimensional situation pressure equalization between the left and right hand side cannot take place and once the jet assumes a small angle with respect to the Y-axis this angle will only increase until a stable flow develops. Indeed the computed flow was found to be stable even for a large number of iterations.

The vector plot already points to the fact that the jet tends to shield the plate from the ambient inflow. This is especially clear from the C_p-distribution shown in the figure which exhibits low pressures on the right hand side and significantly higher pressures on the other side. This means that the force on the plate is decreased by the action of the thruster or conversely a low effectivity of the thruster. Also it is clear that the point of application of the side force will shift towards the left hand side. For a realistic three-dimensional situation it is doubtful if this will arise since then pressure equalization can take place around the jet.

The pressure on the back side of the plate is also affected by the thruster action: the pressure is reduced leading to an increased resistance. As Figure 3.68 already showed the shielding effect prevails over the added pressure reduction on the back side of the plate and the total lateral resistance of the plate diminishes with increasing thrust. Relative to the thrust however the resistance reduction is strongest for thrust values of approximately 50 to 100 % of the plate resistance.

Figure 3.72 shows the corresponding pressure distributions on the plate for the positive thrust values. They confirm the observed behaviour and once again point to a growing shift in the point of application of the side force. This shift is confirmed in Figure 3.73 which shows that the side force point of application moves to approximately 25 % of the plate length showing that one side of the plate is almost completely shielded off by the thruster jet.

3.6.4.2 Calculations for a two-dimensional flat plate with a bow thruster

The previous computational study referred to a flat plate in oblique flow with a center-line thruster. To assess the influence of a drift angle another series of calculations was performed for a plate with a tunnel thruster near the bow subjected to a uniform inflow with variable direction.

Only one speed and one thrust level were considered whereas the inflow direction

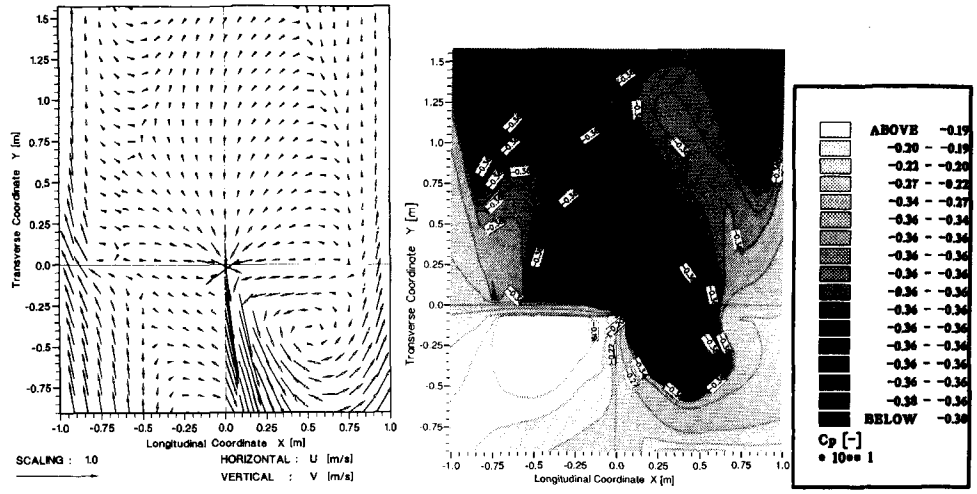

Figure 3.71: pressure coefficient distribution and velocity vector plot for flow around a two-dimensional flat plate - $T_p = 160$ N

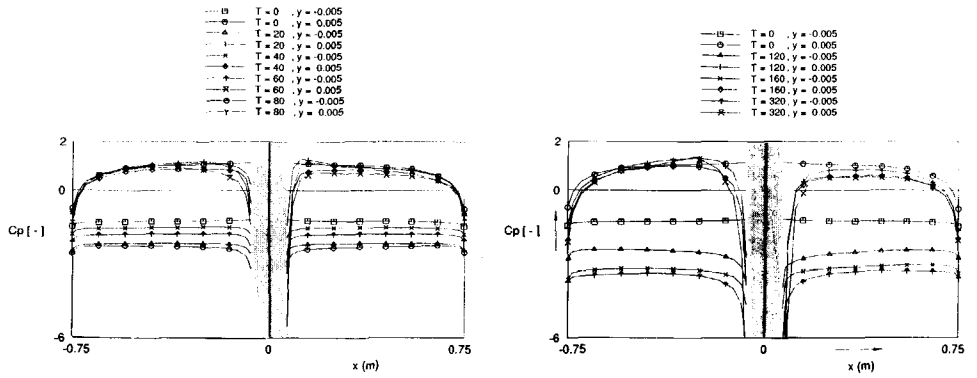

Figure 3.72: pressure coefficient distribution on a flat plate - positive thrust values

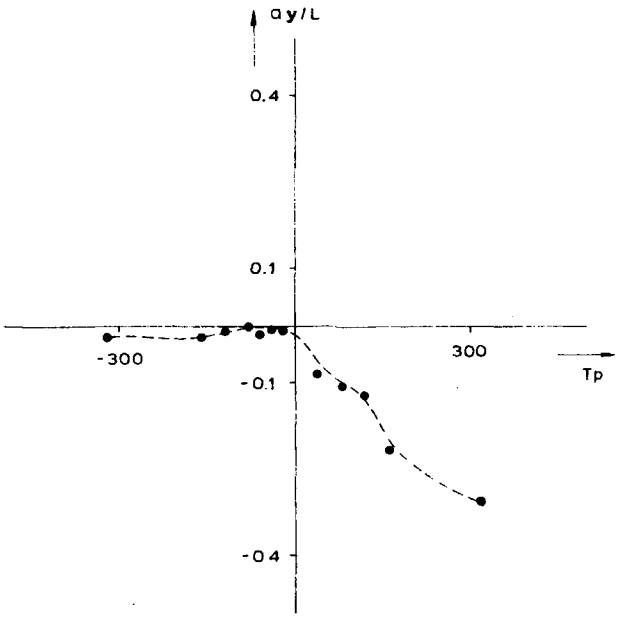

Figure 3.73: point of application of side force for a two-dimensional plate with a center tunnel thruster

was varied to cover all possible directions. The underlying phenomena are similar to those found for the two-dimensional plate with a center-line thruster and can be understood by considering the flow around the plate.

Figure 3.74 shows the local flow (velocity vectors and pressure) induced by the two-dimensional thruster if the inflow is parallel to the plate. The figure shows the deflection of the slipstream and the suction on the tunnel entry side causing the flow just upstream of the plate to be directed at a small incidence angle relative to the plate. A thin recirculation zone is seen to arise in the shadow of the deflected jet.

In conformity with these results the local pressure distribution exhibits high pressure areas upstream of the tunnel exit and downstream of the tunnel entry. Low pressure areas are found downstream of the jet exit and upstream of the jet entry. The low pressure regions are more extensive than the high pressure regions and in total a suction force is found opposite to the thrust. This is in conformity to the usual observation of reduced thruster effectivity for the forward speed condition.

Figure 3.75 shows the same information, i.e. vector diagram and pressure coefficient, for the two-dimensional stern thruster at forward speed or the bow thruster in astern speed. A higher pressure arises now on the upstream side of the jet exit and low pressure regions are observed on the jet entry side and downstream of the jet exit. Compared to the previous case the low pressure area is less extensive with a relatively higher pressure. This leads to a smaller suction force and thereby a reduced thrust degradation compared to the previous case. Again this is in agreement

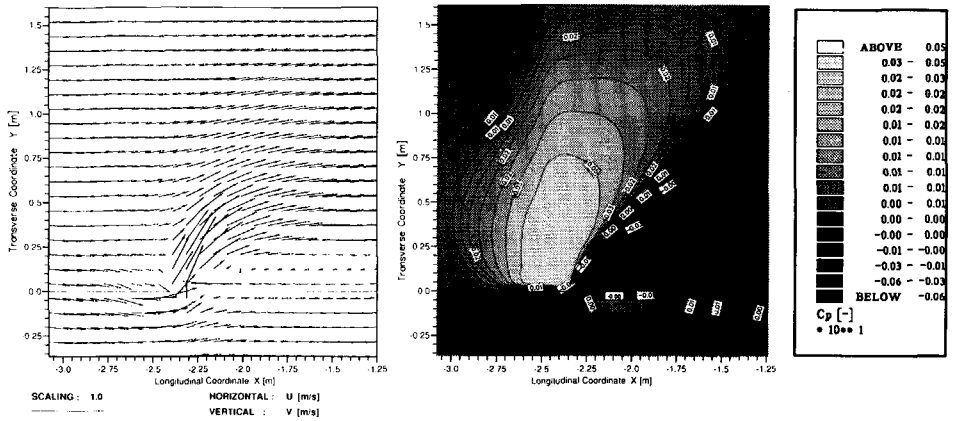

Figure 3.74: flow pattern and pressure coefficient around a flat plate with a bow thruster - $\beta = 0$

with the results found for bow thrusters in astern sailing conditions.

The previous two cases relate to a bow thruster at drift angle $\beta = 0$ respectively $\beta = 180^0$. Calculations were carried out for the entire range of drift angles. The corresponding thruster effectivity is shown in Figure 3.76 as a function of the drift angle. This figure also shows the effectivity of the turning moment as a function of drift angle β.

Figure 3.77 shows the point of application of the total side force (i.e. current force plus induced hull force plus thrust).

It is seen that the turning moment for $\beta = 0$ is considerably reduced by the forward speed of the two-dimensional thin ship. Again looking at the calculated pressure distribution, Figure 3.74 this is not surprising in view of the flow pattern. Percentage-wise the reduction in effectivity is less than that for the side force. This is caused by the changed pressure at the upstream side of the tunnel which gives an increased effectivity and which is more dominant in view of its larger arm.

For $\beta = 180$ the turning moment effectivity is also reduced but, as for the side force, less than for the $\beta = 0$ case. This is again in agreement with the observed behaviour for a real ship.

For a 20 degree drift angle the local flow is shown in Figure 3.78. Results are included for a closed stern tunnel, a stern thruster developing positive thrust, and a stern thruster developing negative thrust. The latter case is the same as a positive thrust at $\beta = 340^0$.

A comparison of the flow vectors shows that the difference between closed tunnel and positive thrust seems small, except locally in the thruster vicinity. The same applies to the negative thrust case. Comparing the pressure distributions shows important differences in the tunnel vicinity and smaller differences elsewhere. It is interesting to note that for $T = 100$ the region with lowest pressure is moved away from the leading edge and away from the plate.

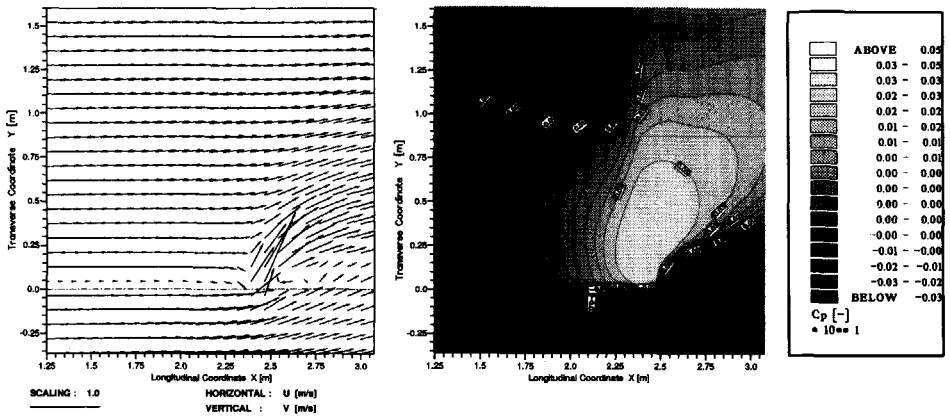

Figure 3.75: flow pattern and local pressure distribution for the flow around a flat plate with a bow thruster - $\beta = 180$

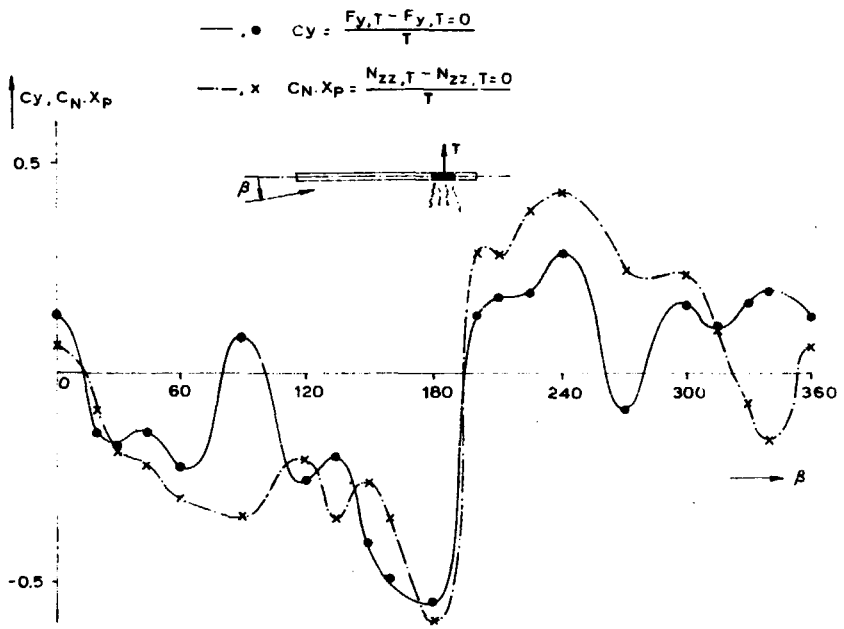

Figure 3.76: thruster force and moment effectivity for a thruster in a flat plate at varying drift angle

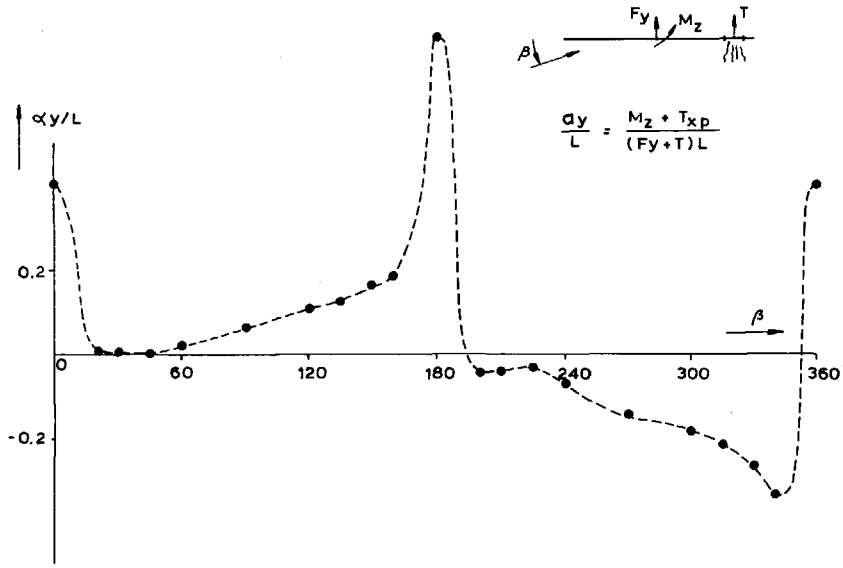

Figure 3.77: point of application of total side force for a thruster in a flat plate at varying drift angle

To get a clearer image the difference in pressure coefficient C_p between closed tunnel and working thruster is shown in Figure 3.79, for all considered cases. This figure shows that invariably the thruster induced pressure is a very local phenomenon.

3.6.4.3 Calculations for a three-dimensional wedge with a tunnel thruster

All previous cases show a simplified two-dimensional flow and although the presented results do show some of the trends that can be expected as well as the underlying reasons, it is useful to cover also some three-dimensional cases.

The first such example is the three-dimensional pendant of the previously covered two-dimensional plate with a center-line thruster. The situation for this case is very similar to that for some of the experiments to be discussed below. Again only one inflow speed was considered and the thrust was varied.

Figure 3.80a shows the part of the hull force induced by the tunnel thruster, i.e. the total hull force reduced with the current force without a thruster operating. As the figure shows a similar behaviour is found as for the two-dimensional case although the force levels are widely different.

Figure 3.80b shows the related effectivity coefficients as a function of the normalized current force F_c/T. The results in this figure may be compared with the case for which measurements are available, see below.

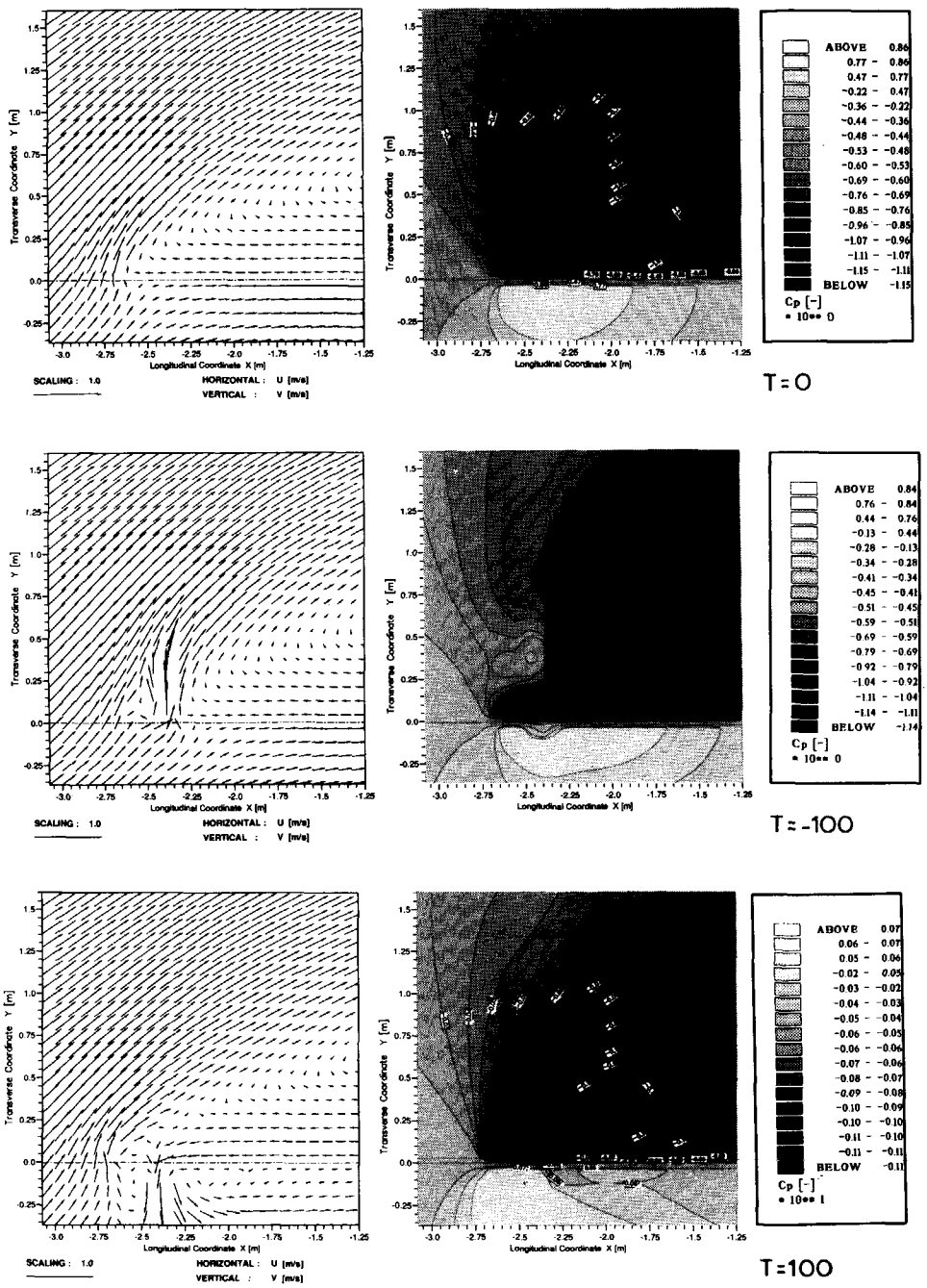

Figure 3.78: flow pattern and local pressure distribution for the flow around a flat plate with a bow thruster - $\beta = 20$

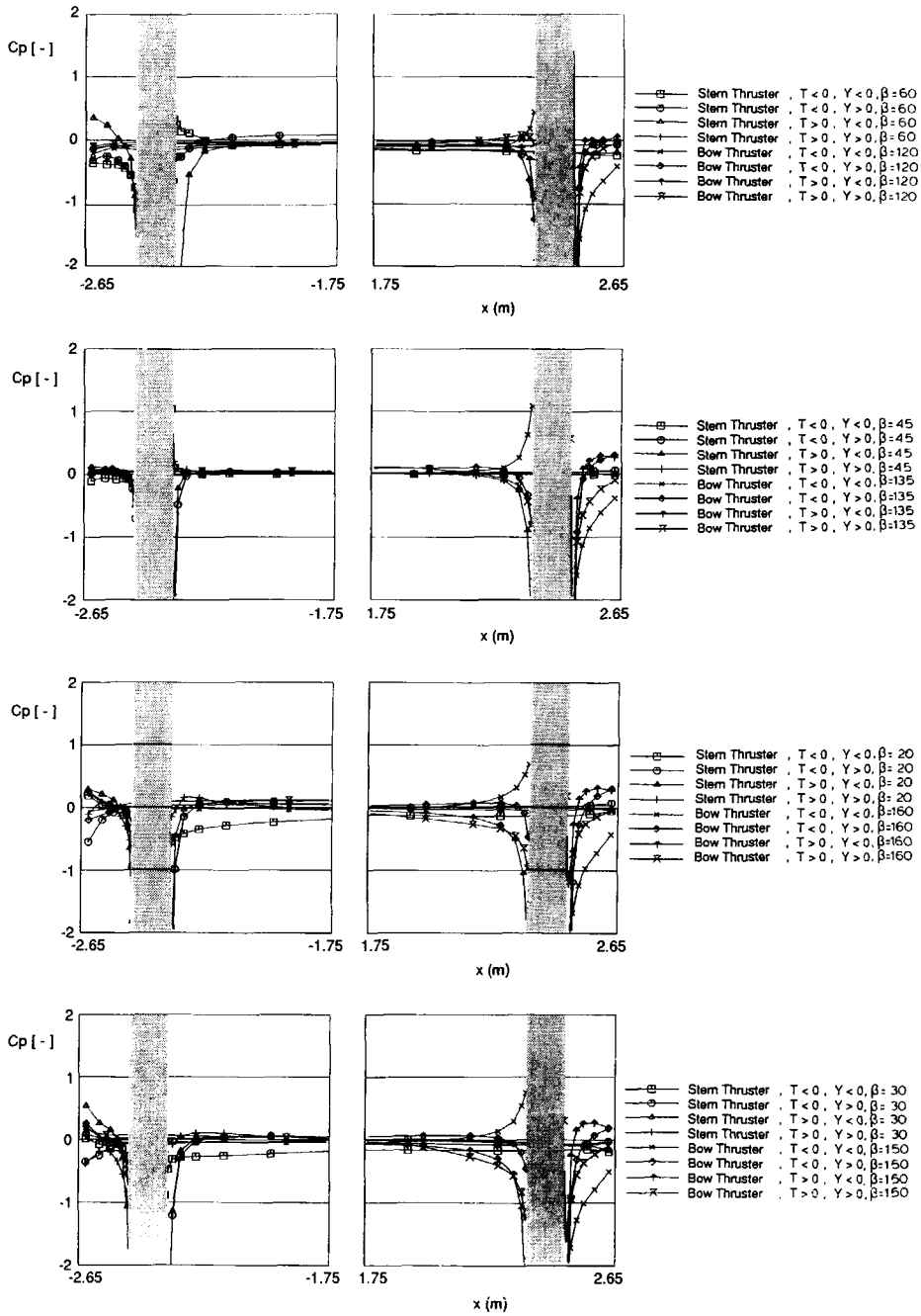

Figure 3.79: difference between the pressure distributions on a flat plate with open and closed bow thruster

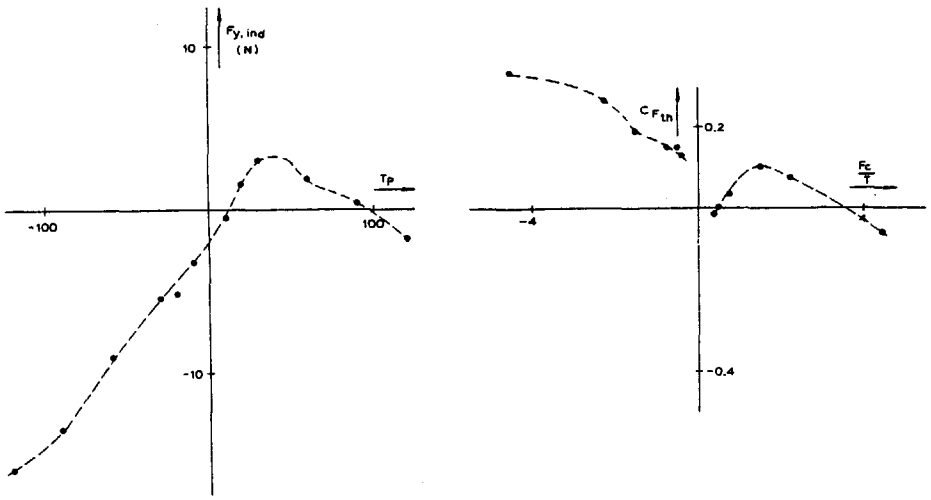

Figure 3.80: induced hull force for a thruster in a three-dimensional flat plate

The reason for this behaviour is similar as for the two-dimensional case as can be seen from the results presented in Figures 3.81 to 3.83 which show the C_p-distributions on both sides of the plate as well as the corresponding velocity fields. The presented results refer to the cases with no thruster, thruster jet opposing the inflow (T_p = 120 N) and thruster jet coflowing with the inflow (T_p = -120 N).

As the vector plots show no appreciable asymmetry is observed even for the counterflowing jet. This is at variance with the two-dimensional case but is not unexpected as explained before.

3.6.4.4 Calculations for a three-dimensional flat plate with a bow thruster

The final computational case refers to the familiar situation of a bow thruster in a ship at forward speed. It is of interest to see if the present computational tools are capable of predicting the side force loss of a thruster in forward speed.

Calculations were performed for several speed-thrust combinations for a suitably sized flat plate in deep unrestricted water. It is of interest also here to visualize the pressure and velocity field. For a speed of 0.319 m/s and a thrust of T_p = 40 N, these are shown in Figure 3.84.

The figure shows the velocity vector plot in the horizontal plane through the propeller axis and clearly indicates the expected jet deflection. Also the induced flow on the entry side of the tunnel can be seen. The penetration depth of the jet into the oncoming flow is seen to be rather small even for this ambient speed.

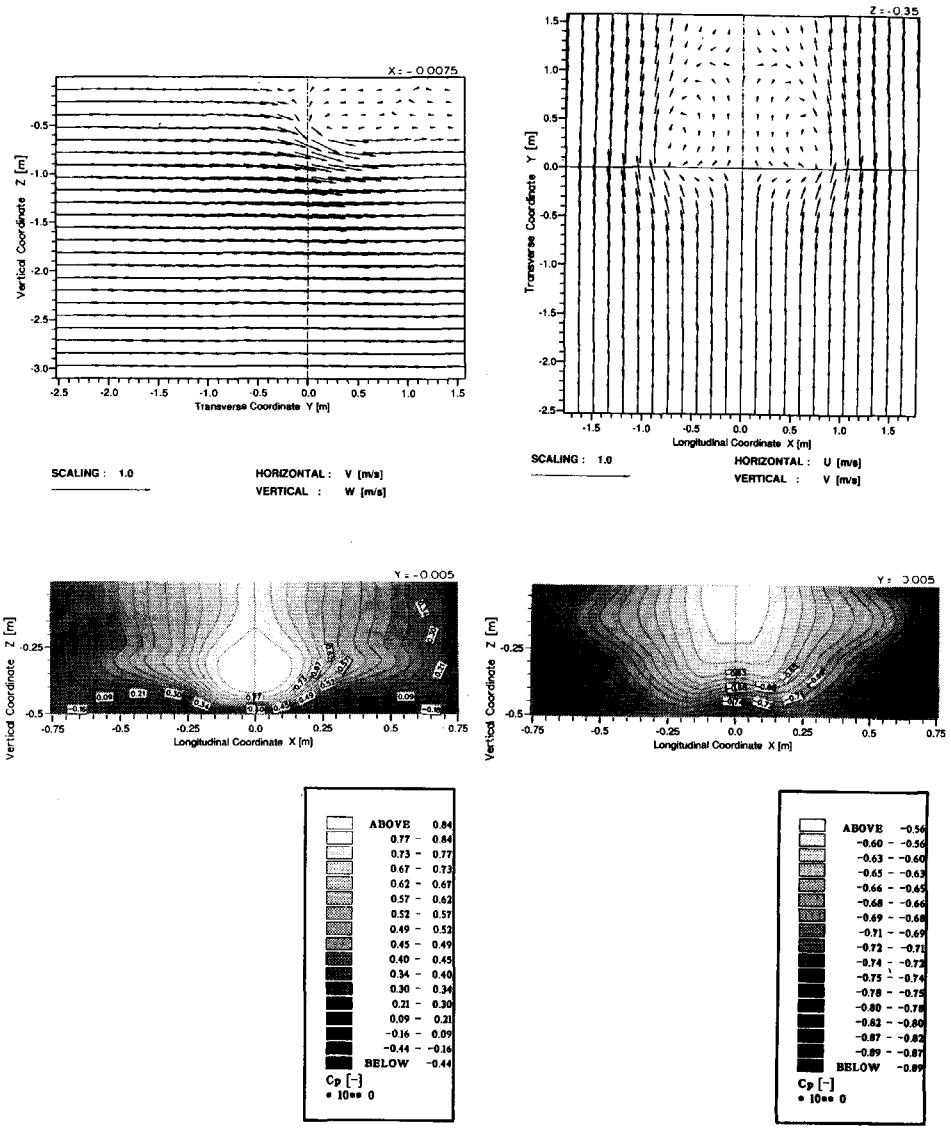

Figure 3.81: flow around a flat plate with a thruster - thruster opening closed

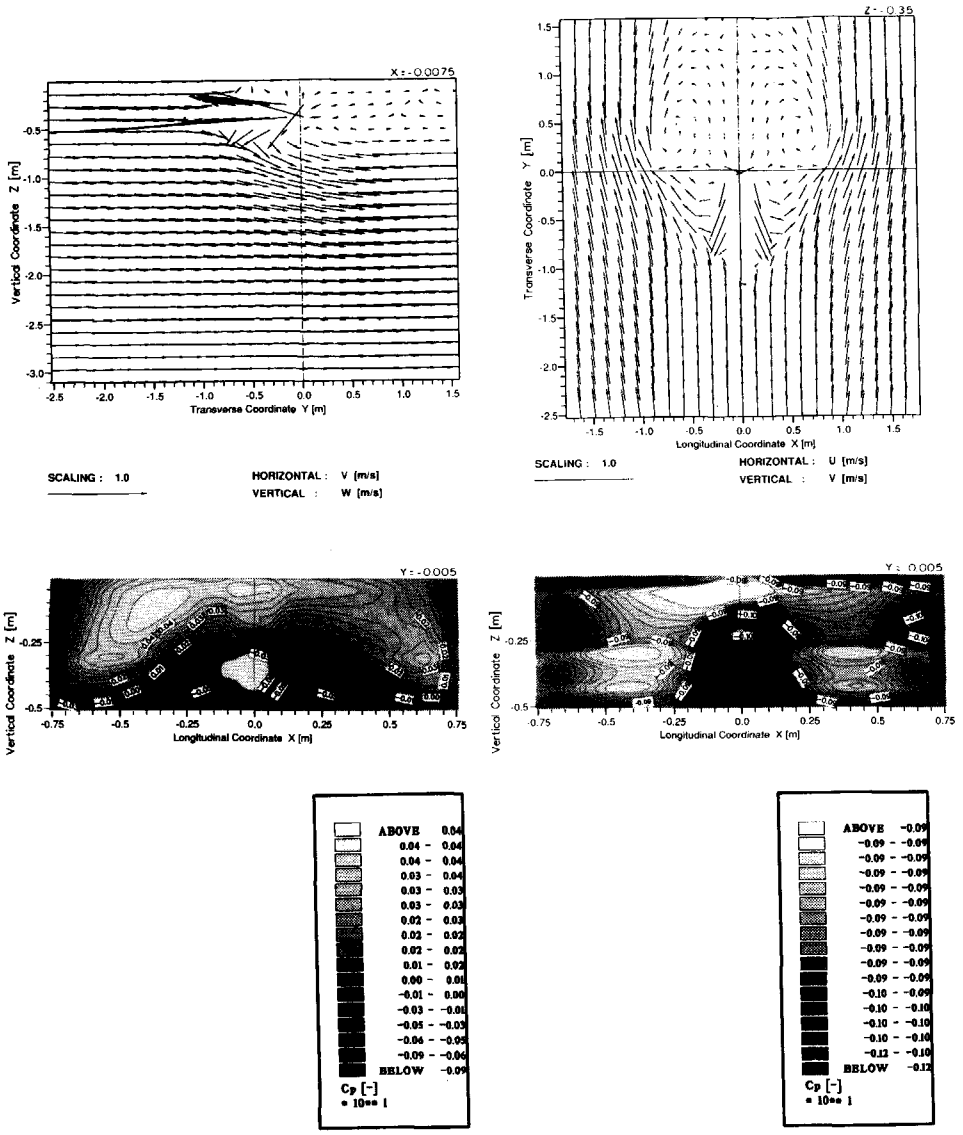

Figure 3.82: flow around a flat plate with a thruster - $T_p = 120$ N

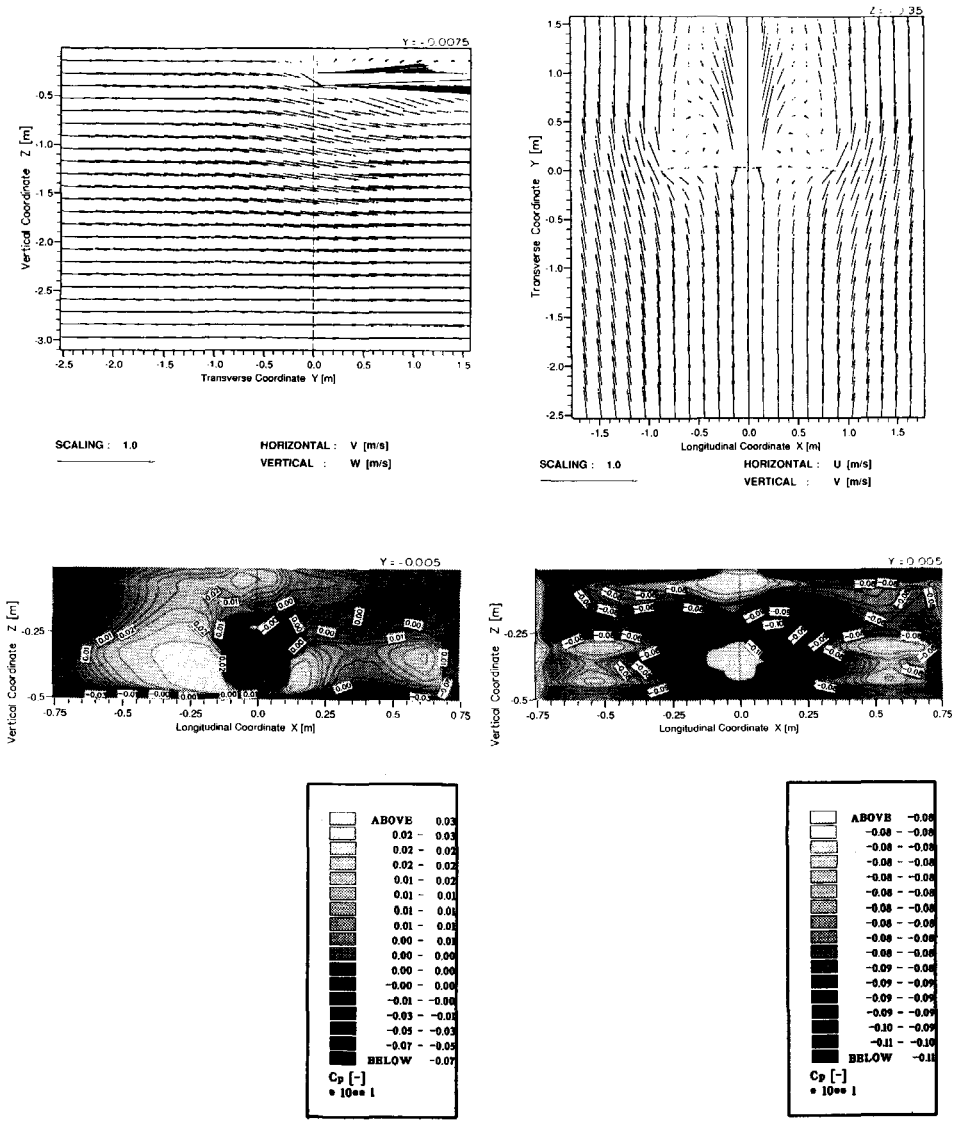

Figure 3.83: flow around a flat plate with a thruster - T_p = -120 N

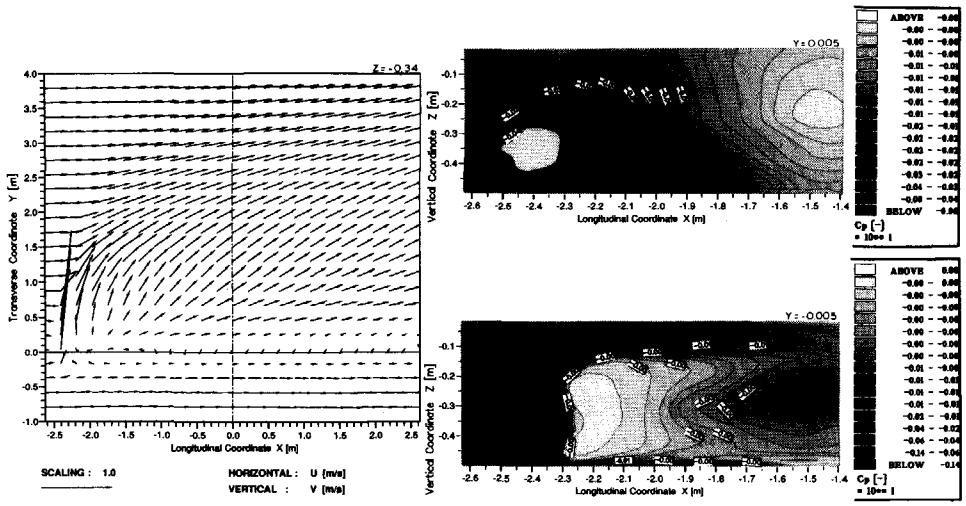

Figure 3.84: velocity vector diagram and pressure coefficient distribution for a ship with bow thruster in forward speed - V = 0.319 m/s, T_p = 40 N

Figure 3.85 shows the corresponding vector plot in a plane downstream of the tunnel perpendicular to the plate. The plane is located at X = -1.76 m. Further away from the plate the jet is observed which is deflecting towards this perpendicular plane. The entrainment into the jet is shown in the vertical velocities towards the jet. Interesting to note is the flow around the lower end of the plate in the positive Y-direction. This is caused by pressure equalization as can be seen in Figure 3.84. This figure shows the pressure fields on the hull both on the tunnel suction side (Y = -0.005 m) and the jet exit side (Y = 0.005 m).

On the suction side a high pressure region is obtained caused by the inward curving flow impinging on the plate just downstream of the tunnel. This higher pressure creates the flow recirculation around the plate's lower edge as remarked before. Comparing the pressure on the suction side with that on the other side, it is clear that the main factor for the thruster effectivity is the jet exit side. As found by many other authors (e.g. English etal [23] and Cooper [38]) a lower pressure region develops on that side mainly downstream of the jet.

An additional calculation was made with the thruster developing a torque and thereby introducing swirl in the thruster jet. No appreciable effect of this torque variation could be found.

The extent of the pressure region also suggests the benificial effect that an anti-suction tunnel may have, see Brix [44] or [45]. To confirm this a calculation was carried out with a suitably sized hole immediately aft of the thruster tunnel opening. The diameter of the AST was set at approx. 0.6 D as suggested by Brix and it was located at approx. 1.55 D downstream of the thruster. The side force effectivity was shown to change only by some 5 % for this particular case and the resultant local pressure and velocity distributions are shown in Figure 3.86. While the side force

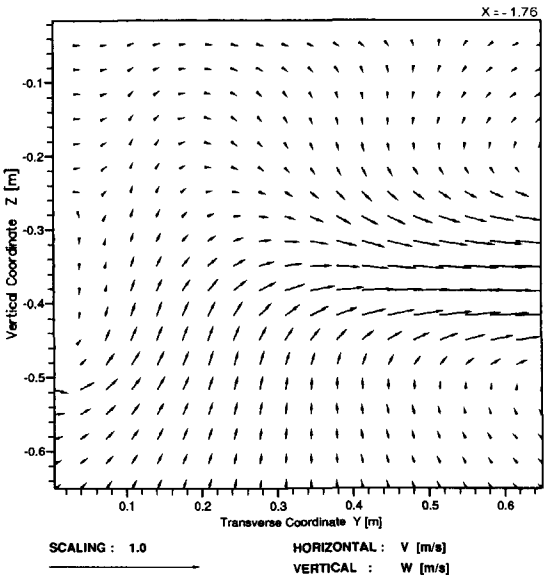

Figure 3.85: lateral velocity field for a ship with bow thruster in forward speed - $V = 0.319$ m/s, $T_p = 40$ N

reduction due to speed is clearly observed the effect of an AST although qualitatively confirmed, is not found to be very effective for the calculated case. This can be explained by the fact that the area where the AST is situated is not the area where the lowest pressures occur. Rather it is located too far downstream to be effective. This is in line with what would be expected from Brix' recommendations.

Figure 3.87 summarizes the effectivity of the thruster as a function of the common speed ratio parameter. It also shows the shift of the point of application of the induced hull side force as a function of the forward speed parameter. As a reference the results of Chislett etal [42] are shown.

As the figure shows the extent of the loss of side force is predicted satisfactorily. However the maximum loss occurs at a higher speed than found in the measurements. Part of the obtained deviations can be attributed to the crudeness of the hull modelling. In a real situation the ambient speed at the thruster openings will be higher compared to that for the flat plate on account of the hull thickness and waterline divergence. This means that the thruster jet will be deflected more rapidly and that the side force will accordingly drop quicker.

3.6.5 Discussion of measurements

3.6.5.1 Tests for a tunnel thruster in a wedge-shaped hull

The tests were performed for a variety of ship speeds and propeller RPM's, see Table 3.24. The tests with zero RPM can be considered as pure current force tests. Strictly speaking this is not correct: also in this condition the thruster delivers a thrust, or rather a resistance. However it is assumed in all cases discussed here that this effect can be neglected. This is substantiated by the fact that the thrust for

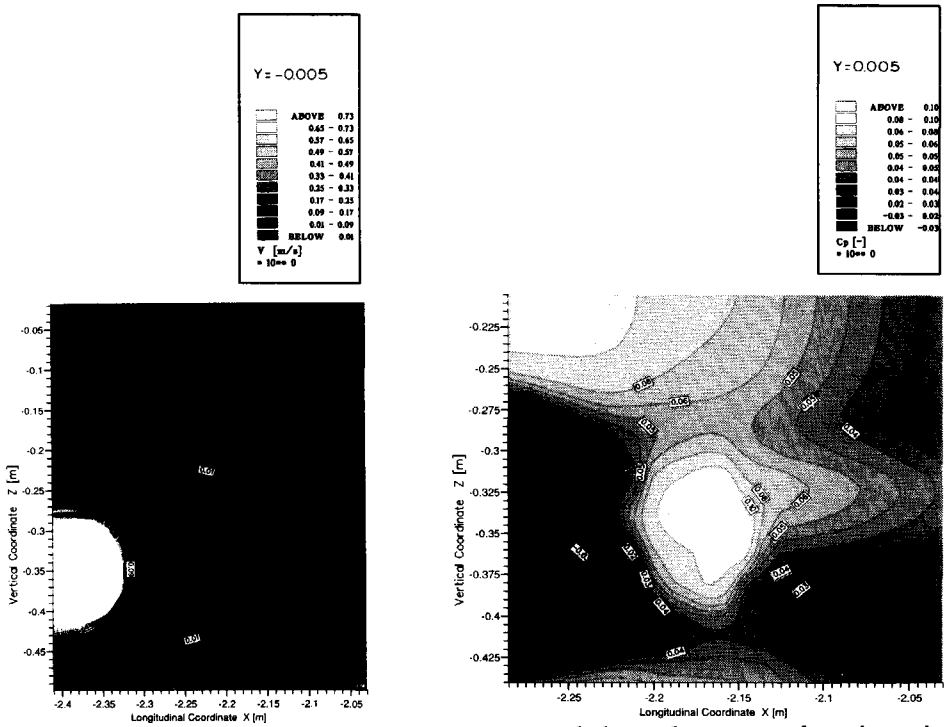

Figure 3.86: local flow parameters for a ship with bow thruster and anti-suction tunnel in forward speed

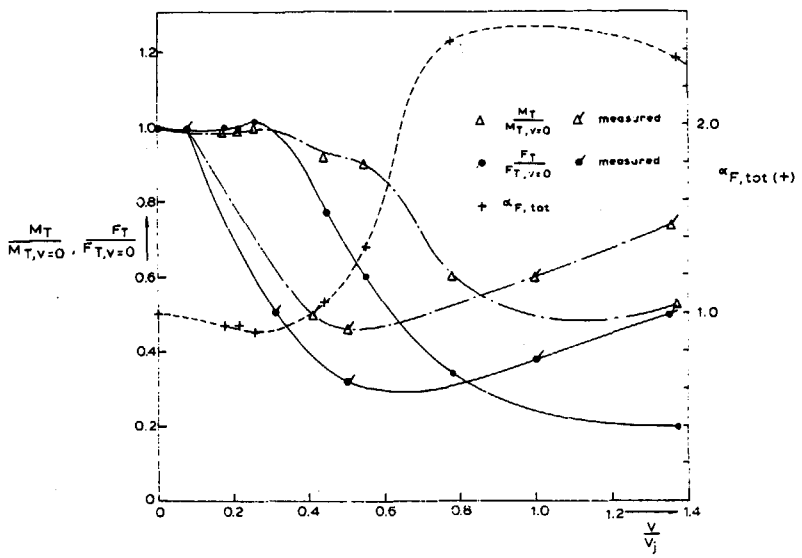

Figure 3.87: side thruster effectivity and side force point of application for a ship with bow thruster in forward speed

these conditions never exceeds roughly 3% of the total force on the hull section.

Figures 3.88 and 3.89 show the effectivity coefficients for the covered range of inflow speed and number of revolutions. The coefficients are defined in Section 3.1.

Figure 3.88 shows that the thrust and torque of the impeller are affected by speed in the usual manner. The influence is however limited on account of the low speeds and do not explain the important loss in side force shown in Figure 3.89.

Figure 3.89 does not show any relation between the various conditions. By replotting the results on a basis of the ratio between bollard thrust and current force, a narrower band is obtained, see Figure 3.90. In these two figures $C_{F_{Th}}$ is plotted along the vertical coordinate. Although appreciable scatter is encountered a clear trend can be discerned.

The agreement with the calculated results for the 3D wedge or the 2D wedge is poor. It is observed that the calculated and measured trends are similar for the cases where the thruster jet issues on the side of the incoming flow. The quantitative differences are important and can be attributed to many reasons one of them being the simplified modelling of the wedge hull form. If the thruster jet issues on the other side in the recirculation region even the trends are not comparable. The trends for 2D and 3D calculations are similar however. This qualitative difference indicates that the flow of a jet in a turbulent recirculating wake is poorly predicted. It is not clear if a more refined modelling of the hull would alleviate this problem or that it is rather related to grid fineness or turbulence modelling.

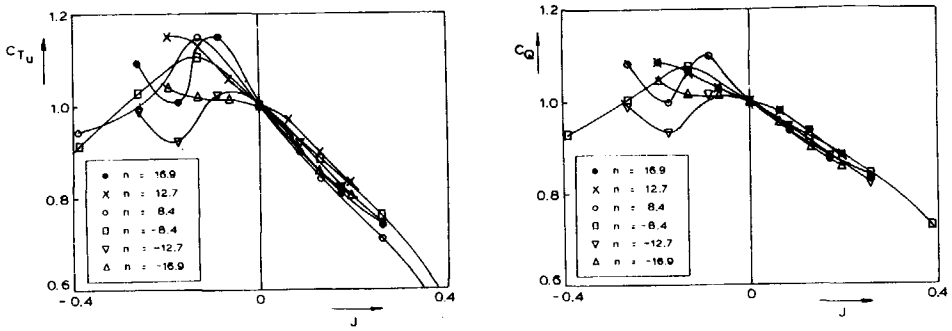

Figure 3.88: results for tunnel thruster effectivity in a wedge-shaped hull; C_{Tu} and C_Q coefficients

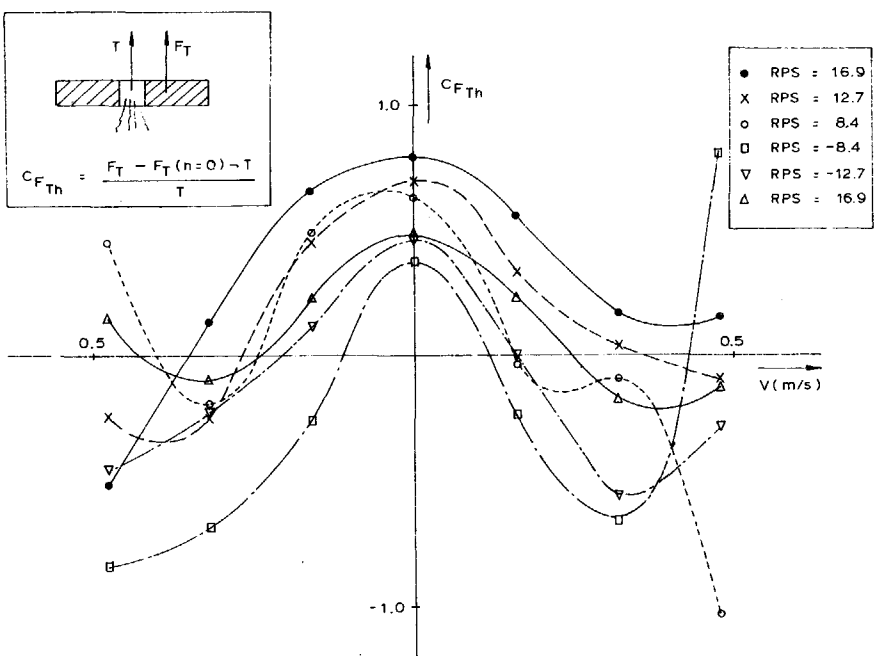

Figure 3.89: results for tunnel thruster effectivity in a wedge-shaped hull; $C_{F_{Th}}$ coefficient

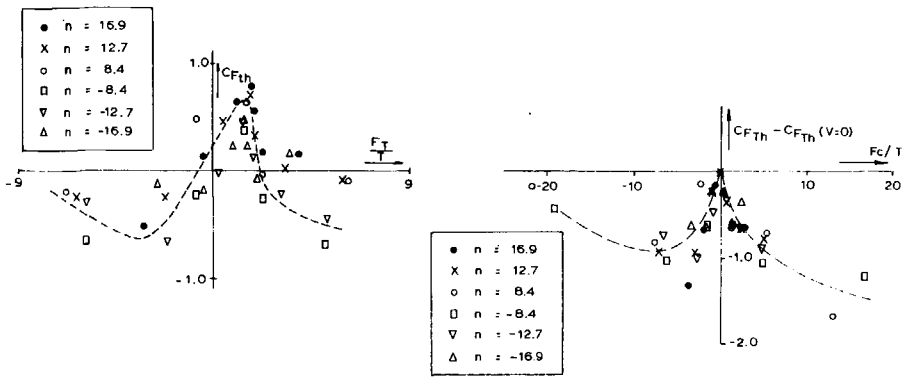

Figure 3.90: results for tunnel thruster effectivity in a wedge-shaped hull

3.6.5.2 Tests for 3 ships fitted with a tunnel thruster

The tests were subjected to the same analysis as the previously mentioned wedge results, see Section 3.1.

Figure 3.91 shows the impeller thrust and torque coefficients for a range of speeds and drift angles. It can be seen that the impeller thrust is not heavily affected by the inflow, especially for currents directed along the ship's axis. For perpendicular flow both the thrust and the torque coefficient are behaving as for normal propellers. It is clear from the presented results that the impeller operation is not the cause of all observed thrust degradation effects, but that the origin of these effects must indeed be found in the flow around the body.

Figure 3.92 shows the longitudinal induced force coefficient for a low RPM value of 20 s^{-1} model value. The figure shows a very crude sinusoidal behaviour with an amplitude depending on the ship speed. For the highest model speed of 0.6 m/s the amplitude is approximately 0.06, i.e. 6% of the bollard thrust is found as an induced longitudinal force in such a way that the ship's resistance is increased by the thruster operation. For this particular case this 6% thrust corresponds to some 40% of the ship resistance at the same speed but without the thruster operation.

Comparing the previous results with those for a higher RPM, i.e. a higher bollard thrust, see also Figure 3.92, seems to suggest that the HLC-coefficient decreases with increasing tunnel thruster thrust. However as a fraction of the corresponding ship resistance the induced force increases with bollard thrust.

Assuming as a reference that HLC varies as follows with the drift angle:

$$HLC = A_{HLC} cos\beta \tag{3.52}$$

and determining the coefficient A_{HLC} by a least squares fit yields the values for A_{HLC} as shown in Figure 3.93 as a function of model speed V and for both values

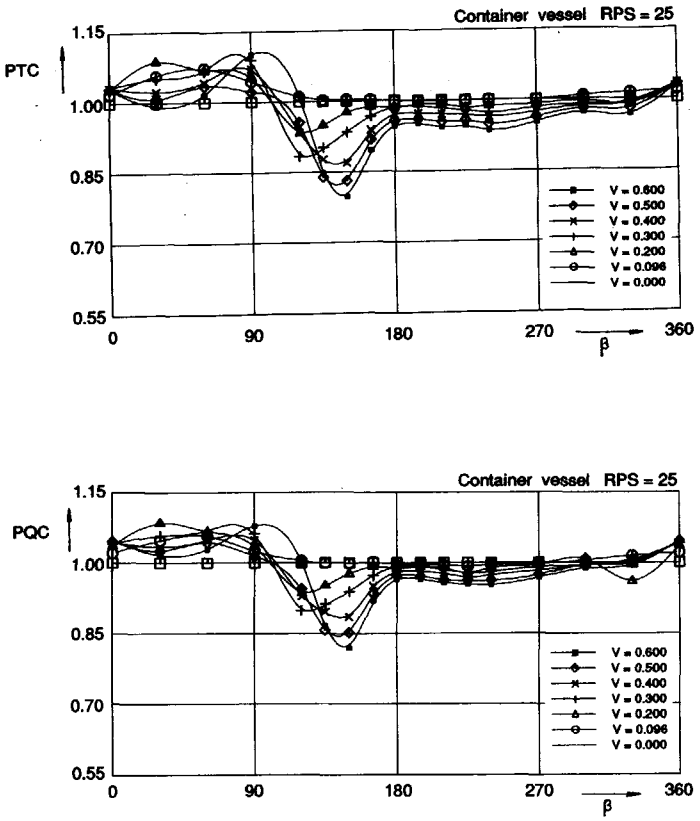

Figure 3.91: results for tunnel thruster effectivity for a container vessel; C_{T_n} and C_Q coefficients

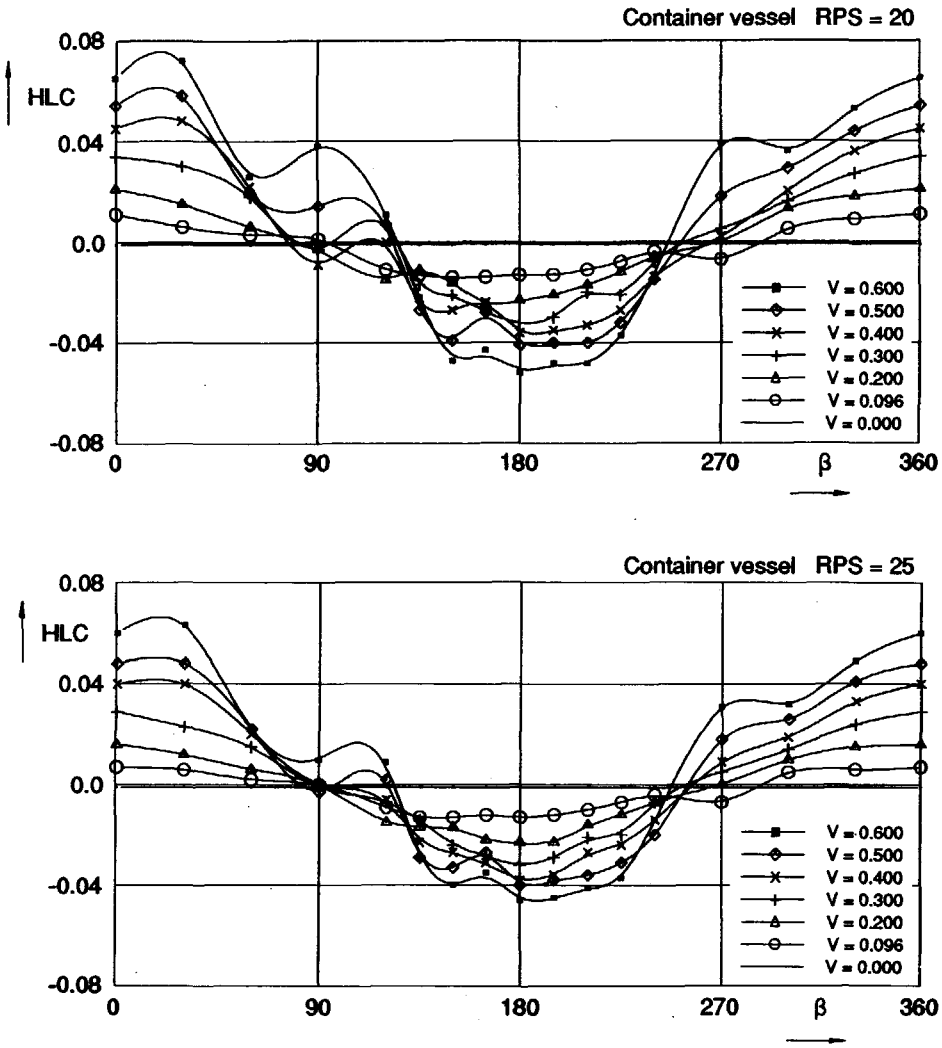

Figure 3.92: results for tunnel thruster effectivity for a container vessel; $C_{F_{Lh}}$ coefficient

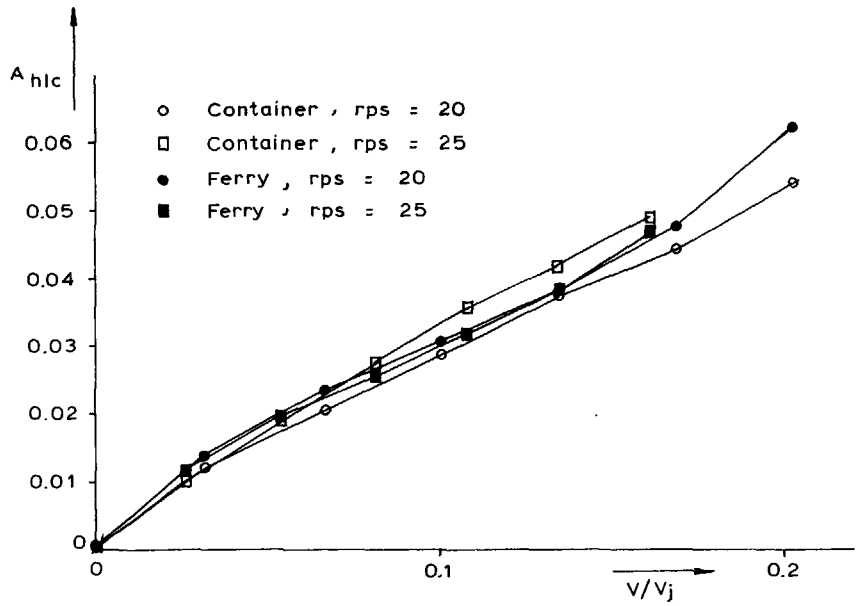

Figure 3.93: value of A_{HLC} as a function of model speed and thrust

of the bollard thrust.

As Figure 3.93 shows the coefficient A_{HLC} is approximately linearly dependent on the model speed and decreases with increasing bollard pull. Plotted on a basis of V/V_j ($V_j = \sqrt{2T/(\rho A)}$) a rather consistent trend is found.

Notable deviations from the sinusoidal behaviour are found in the drift angle regions around $\beta = 90^0$ and 270^0. For both drift angles the bow thruster operation causes the vessel to experience a forward force. The explanation of this forward force must be sought in the induced pressures arising on the hull at the thruster location in accordance with the numerical calculations reported previously. The thruster action and the induced jet will cause a shift in the recirculation zone downstream of the hull. Apparently the changed pressure distribution adds to a forward force component. Since the changes in pressure distribution are rather local, it is expected that a reduced pressure occurs in this case at the forward end of the ship. This is in line with the pressure reduction which can be inferred from the measured interaction on the transverse force.

The trends found for the container ship are confirmed by the results of the ferry, see Figure 3.94. The amplitudes of the sinusoidal fit are included in Figure 3.93 and confirm the previous findings. The similarity between the 2 ships is striking.

The induced side force coefficient HDC is shown in Figure 3.95 for the container vessel with respectively RPM = 20 s^{-1} and 25 s^{-1}.

It is to be noted that on account of the definition of HDC its value at V =0, is larger than 1. This arises since the hull gives a positive contribution to the total

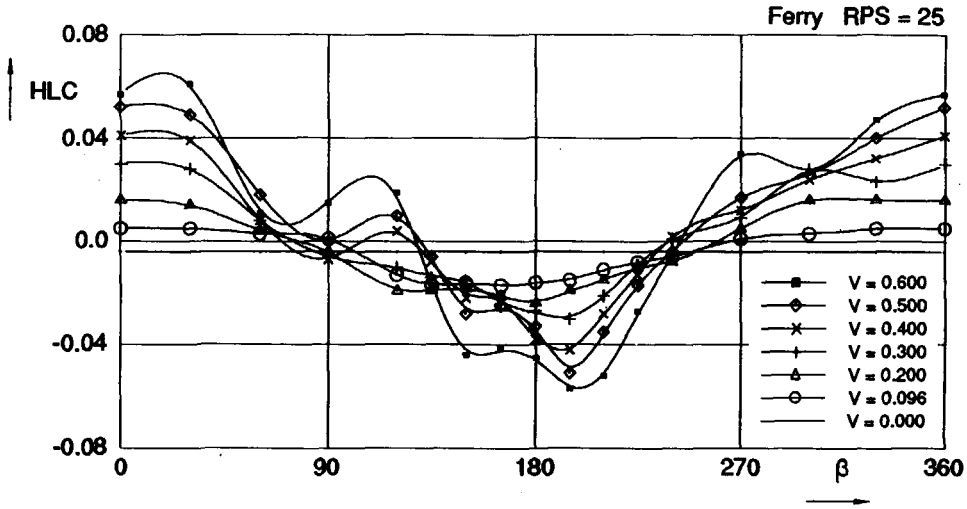

Figure 3.94: results for tunnel thruster effectivity for a ferry; $C_{F_{Lh}}$ coefficient

side force: there is an induced hull force already for V =0.

A somewhat irregular behaviour is found for both bollard pull levels, with a very pronounced peak around $\beta = 135^0$ and less distinct peaks at $\beta = 225^0$ and 270^0. With increasing bollard pull the HDC-values have the tendency to reduce, a fact confirmed by the results for a ferry, see Figure 3.96 The ferry results show similar trends to the container vessel except for an additional peak in the $\beta = 330^0$ range.

Although not valid for every single case, again the clear tendency is observed that the HDC-values increase with increasing model speed. This and the fact that HDC decreases with increasing thrust is in agreement with the well-known results for tunnel thruster effectivity at forward speed. Note that these trends are confirmed for $\beta = 0$ and $\beta = 180^0$ for both vessels.

It is interesting to compare the results with those for the simple 2-D case of a flat plate with a tunnel thruster in arbitrary inflow, see Section 3.6.4. The results show that some qualitative agreement with the measurements is obtained with a rather pronounced peak in the calculated effectivity for angles between 130 and 180 degrees. For drift angles between 180 and 30 degrees mostly positive values of the interaction coefficient were found both in the calculations as well as in the measurements. Quantitatively any agreement is absent but it is seen that the calculations can provide assistance in understanding the phenomena. Even a more quantitative agreement is expected once the hull form is modelled in more detail.

Figure 3.97 shows that the induced turning moment coefficient HMC behaves very similar to HDC. This shows that the point of application does not move in a very erratic way and it supports the idea that the induced forces are a local phenomenon rather that an effect caused by a completely changed flow around the

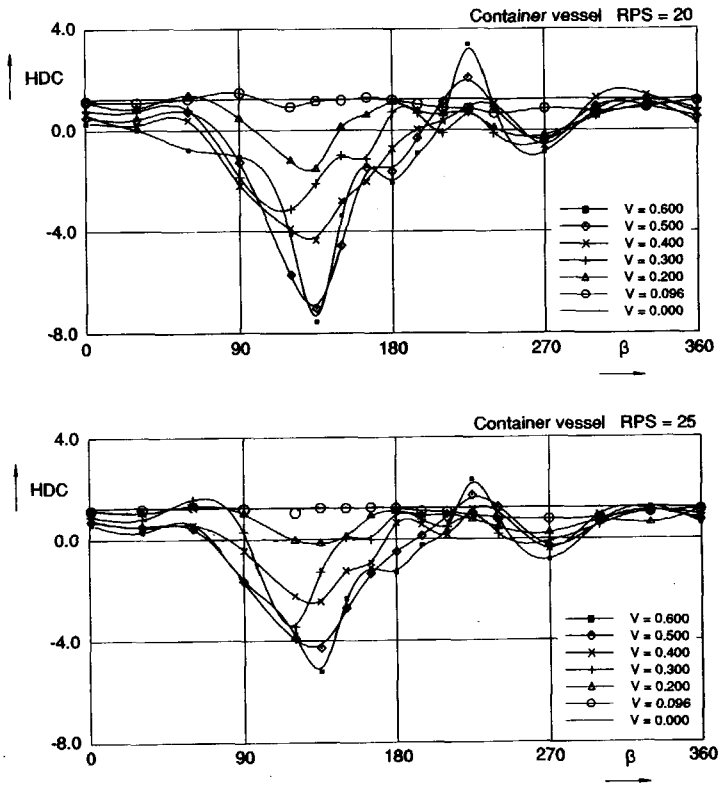

Figure 3.95: results for tunnel thruster effectivity for a container vessel; $C_{F_{Th}}$ coefficient

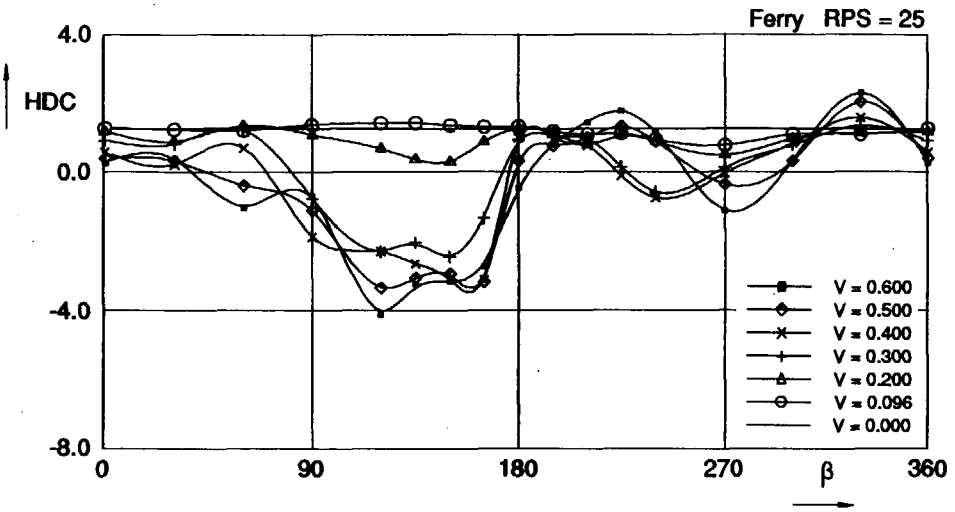

Figure 3.96: results for tunnel thruster effectivity for a ferry; $C_{F_{Th}}$ coefficient

entire body.

The trends with speed and thrust are again similar. Comparing the results with those for the two-dimensional plate with bow thruster lead to similar conclusions as discussed above.

For a typical hopper dredger the effect of water depth was investigated. Figure 3.98a, b and c shows the HDC coefficient for 3 water depths $H/T = \infty$, $H/T = 2.5$ and $H/T = 1.25$. Comparison of the figures clearly shows that the induced forces become significantly larger with decreasing water depth. The peak at $\beta = 135^0$ is deepened roughly by a factor 2. Much more pronounced is the influence of water depth on the values near $\beta = 30^0$ and 330^0. These values are multiplied by a factor 4 to 5 for the $H/T = 1.25$ compared to $H/T = \infty$. The smaller the water depth the more a two-dimensional situation is created. This will lead to a more important contribution of the thruster jet since it becomes progressively more difficult for the ambient flow to circumvent the jet: the jet will become a bigger obstacle having more influence.

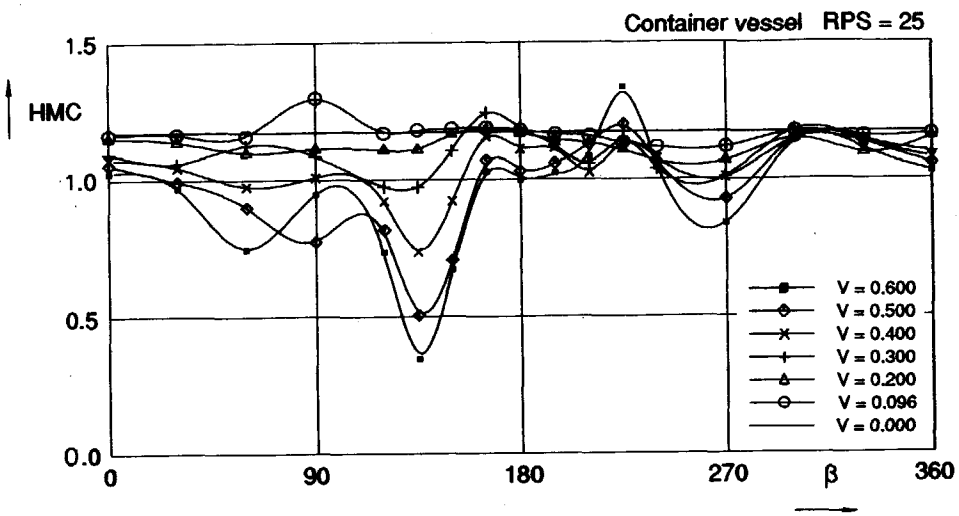

Figure 3.97: results for tunnel thruster effectivity for a container vessel; C_{N_h} coefficient

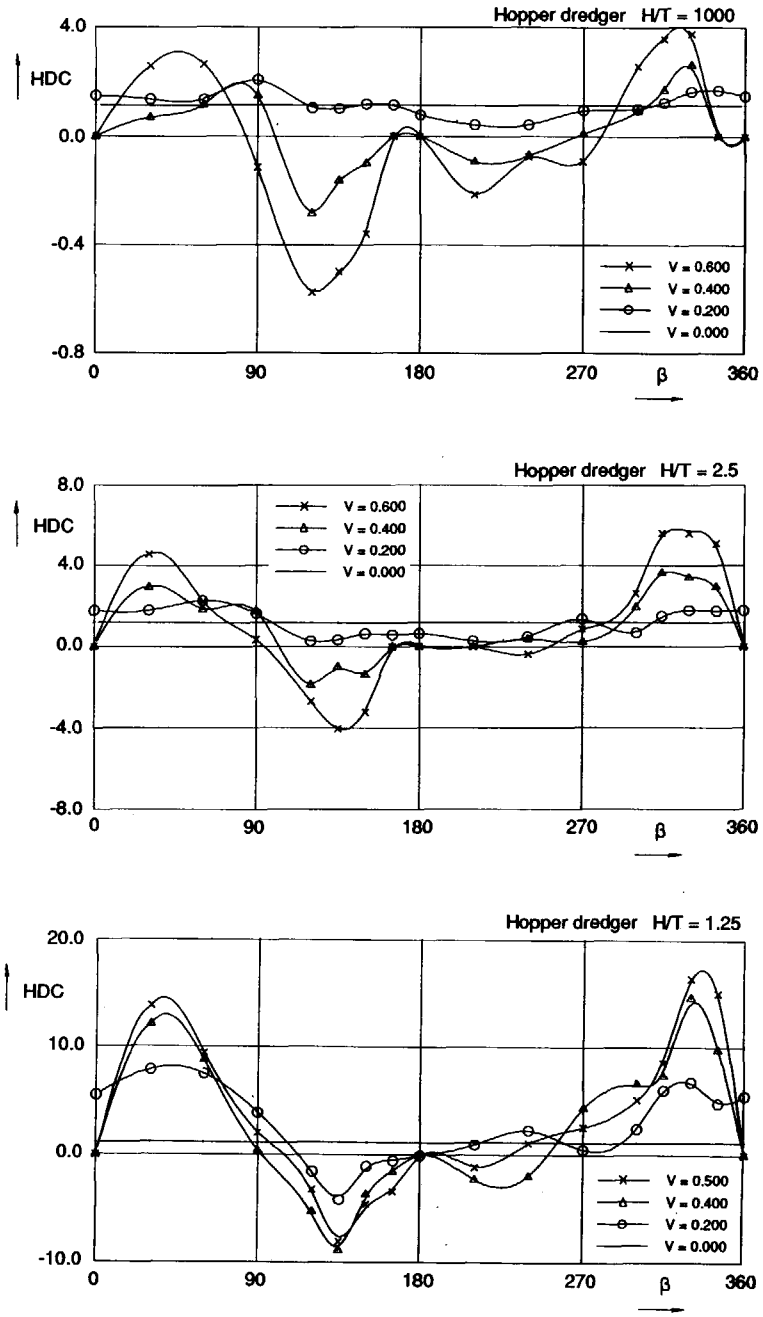

Figure 3.98: results for tunnel thruster effectivity for a hopper dredger; $C_{F_{Th}}$ coefficient

Chapter 4

SUMMARY AND CONCLUSIONS

4.1 Summary

The present work has covered subjects relevant for dynamic positioning and low speed manoeuvring both from a design point of view as well as from the point of view of operations.

The study is aimed at an analysis of thruster effectivity and has covered three main subjects, i.e.

- The development of the slip stream of a thruster;
- The effectivity of azimuthing thrusters; and
- The effectivity of tunnel thrusters.

The analysis was performed both with theoretical (numerical) as well as experimental tools. The computational analysis was carried out with a software package specifically developed for the subjects of interest here. It is aimed at solving the three-dimensional Reynolds equations for turbulent flow employing the k, ϵ turbulence model. The solution procedure follows a finite-difference scheme and two methods of determining the convected quantity are used, one employing the Hybrid scheme and one employing the QUICK scheme.

The software is capable of calculating the detailed flow around an arbitrary number of, possibly adjoining, blocks and actuators, given an arbitrary inflow direction. Therefore it can be used for computations of the flow around single or multi-hulled ships fitted with main propellers, rudders, tunnel thrusters, and azimuthing thrusters provided it is sufficient to model the hull by rectangular blocks and the actuators by means of their force field. Shallow water and quay effects can be incorporated; free-surface effects are left out of account.

The experimental analysis yields both detailed flow information for the thruster slip stream employing state-of-the-art Laser-Doppler techniques as well as overall forces induced by the various actuators.

A detailed study was made of the behaviour of the thruster slip stream as affected by inflow speed, inflow direction and presence of a ship-like body. Both measurements and experiments were presented. These were analysed such that simple expressions were found for the jet spread, velocity decay, jet deflection etc as a function of distance to the propeller.

Subsequently the effectivity of azimuthing thrusters was covered in some detail, both looking into thruster-thruster interaction as well as thruster-hull interaction. The thruster-hull interaction was studied for single-hull as well as twin-hull situations. Insight was provided in the origin of the various interactions and relevant information for design and or operational analysis was given.

Also the effectivity of tunnel thrusters was covered in some detail. This referred to the effects of ship speed and current on the forces developed by a tunnel thruster. Variations in ship shape, tunnel thruster power, water depth, relative current speed and relative current direction were considered. Both measurements and calculations were discussed. These gave both insight in the phenomena as well as relevant information for design and operational analysis.

Based on this work the following conclusions can be formulated. These are divided in the following topics:

- Conclusions for the computational tool developed for the present analysis;
- Conclusions relative to the behaviour of the slip stream of a thruster;
- Conclusions with regard to the effectivity of azimuthing thrusters; and
- Conclusions for the effectivity of tunnel thrusters.

Last but not least this chapter is concluded with suggestions for future work.

4.2 Computational Tool

1. The standard elliptic 3D time-averaged, constant density Navier Stokes equation solver described here is capable of addressing a multitude of aspects related to low speed, stationary manoeuvers of simple-shaped bodies with arbitrary actuators.
2. This computational tool is quite robust but CPU and RAM-demanding.
3. All considered cases reached a steady state solution without exhibiting the tendency to diverge after a great many iterations.
4. The computational tool is shown to be capable of addressing
   - simple bodies
   - thrusters and propellers
   - wall boundaries and other boundaries

- shallow water
- varying speed and drift angle

5. The far-field velocity distribution in the slipstream may be calculated using standard turbulent flow models achieving acceptable qualitative agreement. However, more refined models are needed for a close fit of the measured results.

6. Quantitative agreement could not be obtained because of limitations in the the turbulence model, grid resolution, numerical viscosity and body form description.

7. Two-dimensional calculations already give some insight into the phenomena that can be expected for complex 3D geometries.

8. Qualitative agreement may be obtained with this program for problems dominated by jet/inflow interactions. For topics where the interaction of the jet and a recirculating zone (e.g. a wake) is most important this qualitative agreement is more difficult.

9. The main strongpoint of applying this solver to complex problems such as covered here, is the possibility to obtain increased insight.

4.3 Thruster Slip Stream

Based on the aforegoing results some general conclusions may be formulated regarding the thruster slip stream.

1. The propeller slipstream may be regarded as a modified turbulent jet.

2. Jet deflection around a curved body increases with decreasing velocity in the jet (e.g. due to reduced thrust) and with increasing bilge radius.

3. The velocity field behind a ducted propeller behaves in a manner basically similar to a turbulent jet. The velocity field may be divided into two zones:

   - the initial zone called development zone;
   - the fully developed zone.

4. The velocity field in the propeller wake exhibits a similarity similar to that found for a free turbulent jet. Both the Schlichting and the Gortler function which approximate the free jet axial velocity profile can also be used to represent the axial velocity profile in the propeller wake. The normalized velocity and jet width parameters used in this work allow the velocity similarity to be extended to the potential core zone. Therefore, if U_m, R_m, R_{h1}, R_{h2}, U_a are known as a function of x, then the axial velocity at an arbitrary point in the wake can be determined approximately.

5. The effect of swirl introduced into the flow by the propeller is expected to be one of the causes of the variation of U_m, R_m and R_{h2} with x, which is different from the variations which are found in a free jet. However, also other factors may be the cause for these differences such as the presence of a nozzle, a very high turbulence degree caused by the propeller operation or the radially varying velocity distribution over the propeller disk.

6. The axial velocity profile can be described in terms of four characteristic parameters: U_m, R_m, R_{h1} and R_{h2} which can determine the axial velocity field completely.

   - The variation of maximum axial velocity U_m with x can be expressed as $U_m/V_j = a/x^b$. The measurements show that the change of U_m/V_j with x follows approximately the $x^{-1/3}$ power-law.
   - The position of the maximum axial velocity, R_m, can be approximated by a piece-wise linear function of x.
   - The half width of the propeller wake can be expressed by using the characteristic parameters R_{h1}, R_{h2} and R_m in the following combination $R_j = R_{h1} + R_{h2} - R_m$. R_{h1} and R_m represent the development of the potential core zone. The R_{h1}, R_{h2}, R_m and R_j are approximately proportional to the axial distance x.

7. The differences between the slipstreams of a 19A nozzle propeller and a 37 nozzled propeller are insignificant.

8. The development of a slipstream along a flat wall exhibits the same features as a wall jet. A boundary layer develops, the maximum velocity moves slightly towards the wall, the jet width grows somewhat faster in transverse direction as opposed to the direction perpendicular to the wall.

9. The ambient velocity reduces the wake diffusion (wake width). The direction of ambient velocity will change the propeller wake. The center of the wake will deviate from the shaft center line when the direction of ambient flow is not consistent with the shaft center line.

10. The strut influence is large. There are two kinds of strut influence. The first one occurs only when the ambient velocity is not equal to zero and is caused by that part of the vertical drive that is located outside of the propeller disk. This influence region does not change its angular position with increasing distance to the propeller.

    The second strut influence is related to that part of the vertical drive located within the propeller disk. This influence region resembles a helix with a pitch which is proportional to the tangential velocities.

11. The detailed thruster house geometry has little influence on the far-field development of the thruster slipstream.

trends. With such a module it would become possible to efficiently carry out sensitivity studies or to perform simulations of e.g. low-speed manoeuvres.

To reach this goal additional work is necessary especially to derive the influence on the various interactions of factors such as ship size, thruster size, quay proximity, shallow water etc. While measurement of all these factors would be prohibitive on account of the many variables involved, calculation of these factors would be more feasible since the insight obtained requires fewer calculations to be carried out.

At present the computational effort for each case is still enormous. However by optimizing the code and with the advent of faster and cheaper computers soon these calculations can be feasible even for more complicated cases.

Then it will be possible to investigate complex design areas such as propulsion for DP and low-speed manoeuvring which until recently were not amenable for more detailed analyses.

Chapter 5

LIST OF SYMBOLS

a, b	constants
a_y	point of application of side force
A	propeller disk area
A_{CV}	area of control volume CV
A_j	total cross-sectional area of a jet ($r \leq 3r_{h2}$)
$A_{f,j}$	area of the jet cross section hitting a body
C_{fa}	fractional area coefficient, $C_{fa} = A_{f,j}/A_j$
C_l	dimensionless lift coefficient
C_p	dimensionless pressure coefficient, $C_p = \frac{p-p_0}{1/2\rho V_s^2}$
C_y	dimensionless side force coefficient, $C_y = \frac{F_y}{1/2\rho V_s^2 LT}$
$C_{y,jet}$	dimensionless resistance coefficient for jet hitting a body
C_{zz}	dimensionless turning moment coefficient, $C_{zz} = \frac{N_{zz}}{1/2\rho V_s^2 L^2 T}$
c_1, c_2	turbulence model calibration factors
c_μ	eddy viscosity constant, $\nu_t = c_\mu k^2/\epsilon$
D	propeller diameter
E_F	velocity error function
f_d	Doppler frequency
F	force
F_y	side force
$F_{y,B}$	side force on the barge
G	rate of production of turbulent kinetic energy
GX	total error function
h_p	distance of propeller axis to plate
$i, j, k \pm \frac{1}{2}$	indices of faces of control volume along x, y, z-coordinates
J	advance speed coefficient $J = V_s/nD$
k	turbulent kinetic energy
K_{T_p}	propeller thrust coefficient $K_{T_p} = \frac{T_p}{\frac{1}{2}\rho n^2 D^4}$
K_{T_u}	unit thrust coefficient
K_{T_n}	nozzle thrust coefficient

K_Q	torque coefficient $K_Q = \frac{Q}{\frac{1}{2}\rho n^2 D^5}$
L	chord length of plate, length of ship
N	number of velocity measurement points
N_{zz}	turning moment about the vertical z-axis
n	number of revolutions of propeller
$\vec{n}$	unit outward normal vector
p	pressure
p_{cor}	pressure correction
p_0	undisturbed pressure
$P_{0.7}/D$	pitch ratio
$\overline{q}_l$	average value of quantity q over face l
Q	torque
r	radial coordinate
$\hat{r}$	non-dimensional radial coordinate
r_{h1}	inner half velocity radial coordinate where $U = 0.5(U_m + U_a)$
r_{h2}, r_h	outer half velocity radial coordinate where $U = 0.5(U_m + V_s)$
$\overline{r_{jc}}$	average jet radius
r_m	maximum axial velocity radial coordinate
$r_{rot,m}$	radial coordinate at which $V_t = V_{tm}$
r_0, r_1, r_2	jet radius constants
R	propeller radius $R = 0.5D$
R_b	bilge radius
R_{h1}	non-dimensional inner half velocity radial position
R_{h2}	non-dimensional outer half velocity radial position
R_j	non-dimensional jet radius
R_m	non-dimensional maximum velocity radial position
S	swirl number
$S_{f,j;x}, S_{f,j;z}$	static moments of the jet volume flow hitting a body
$S_{j;x}, S_{j;z}$	static moments of the total jet volume flow
T	span of plate, draft of ship
T_p, T_n, T_u	propeller, duct, unit thrust
T_{tot}	total thrust, $T_{tot} = T_u + T_n$
T_y	side force of thruster unit
S_ϕ	source term for quantity ϕ
U, V, W	mean velocity component in x, y, z-direction
$\hat{U}$	non-dimensional velocity parameter
u, v, w	fluctuating velocity components in x, y, z-direction
$\overline{u_i u_j}$	Reynolds stress for momentum equations
$\overline{u_i \phi}$	stress for quantity ϕ (k, ϵ)
U_a	velocity U at propeller shaft center line
U_{est}, W_{est}	estimated values of U, W
U_m	maximum of U

V	velocity
V_{ax}	velocity parallel to the jet-axis
$V_{ax,m}$	maximum value of V_{ax}
V_{CV}	volume of control volume CV
V_j	initial velocity of propeller jet
V_r, V_t	radial, tangential velocity in jet cross-section
V_s	ambient velocity, advance speed
V_{tm}	maximum tangential velocity
$\vec{V}$	velocity vector, $\vec{V} = (U, V, W)$
x, y, z	Carthesian space-fixed coordinates
x_1, x_2, x_3	Carthesian space-fixed coordinates (identical to x, y, z)
x_{jc}, z_{jc}	coordinates of jet cross-sectional volume flow center
$x_{f,jc}, z_{f,jc}$	coordinates of volume flow center of jet part that hits a second body
x_s, y_s, z_s	Carthesian ship-fixed coordinates
x_p, y_p, z_p	Carthesian propeller-fixed coordinates
x_p, r_p, ϕ_p	cylindrical propeller-fixed coordinates
y_c, z_c	transverse, vertical location of jet center
$\hat{z}$	dimensionless vertical coordinate
z_h	jet half width perpendicular to plate
z_m	z-coordinate of maximum jet velocity location
Z	number of blades
α_j	angle of jet axis with x-axis
α_T	angle between propeller shaft (thrust direction) and x or x_s-direction
β	drift angle
δ_{ij}	Kronecker symbol, $\delta_{ij} = 0$ for $i \neq j$ and $\delta_{ij} = 1$ for $i = j$
$\Delta x, \Delta y, \Delta z$	control volume sizes in x, y, z-direction
$\Delta x_{jc}, \Delta z_{jc}$	difference between jet volume flow centers
Δr_{jc}	radial distance between jet volume flow centers
ϵ	turbulent kinetic energy dissipation
ϵ_{err}	continuity error
θ_1, θ_2	intersection angles between two laser beams
λ	laser beam wave length
ν_t	turbulent viscosity
ρ	density
σ_ϕ	turbulence model calibration factor for quantity ϕ
$\sigma_U, \sigma_V, \sigma_W$	standard deviation of U, V, W
τ	normalized turbulence intensity, $\tau = \sqrt{\overline{uu} + \overline{vv} + \overline{ww}}/U_{ref}$
ϕ	convected quantity
ϕ_j	cylindrical angle in plane perpendicular to jet-axis
Φ_{CV}	volume flow through control volume CV
Φ_{tot}	total volume flow through fluid domain

Bibliography

[1] L. Troost. The propulsive and thrust deduction coefficients of single screw ships. *Schiffstechnik*, 3, 1955.

[2] Sv. Aa. Harvald. *Wake and Thrust Deduction at Extreme Propeller Loadings.* Publication 61, Statens Skeppsprovningsanstalt, 1967.

[3] G. Dyne. Systematic studies of accelerating ducted propellers in axial and inclined flows. In *Symposium on ducted propellers*, The Royal Institution of Naval Architects, 1973.

[4] K. Taniguchi, H. Tanibayashi, and N. Chiba. Investigation into the propeller cavitation in oblique flow. *Journal of Zosen Kiokai*, 121:81–94, 1967.

[5] C.E. Shields. *Open-Water Performance in Inclined Flow.* Test Report 110-H-01, Hydromechanics Laboratory of David Taylor Model Basin, 1965.

[6] S. Moberg and S.A. Hellstrom. Dynamic positioning of a four-column semi-submersible. model tests of interaction forces and a philosophy about optimum strategy when operating the thrusters. In *Second International Symposium on Ocean Engineering and Ship Handling*, Swedish Maritime Research Center SSPA, Gothenburg, 1983.

[7] F. Gutsche. Untersuchung von Schiffsschrauben in schraeger Anstroemung. *Schiffbauforschung*, 1964.

[8] O. Bussemaker and E.C.B. Corlett. Tractor tug family fitted with rudder propellers. In *2nd International Tug Conference*, Ship and Boat International, 1971.

[9] H. van Leest and O. Bussemaker. The performance and characteristics of thrusters. In *Offshore South East Asia Conference*, Singapore, 1976.

[10] H. Binek and E. Mueller. Steuerpropeller. *Schiff und Hafen*, 27:1101–1106, 1975.

[11] A. van der Made and O. Bussemaker. Thrusters for dynamic positioning. In *Offshore Craft Conference*, London, 1976.

[12] M.W.C. Oosterveld and G. van Oortmerssen. Thruster systems for improving the maneuverability and position-keeping capability of floating objects. In *Offshore Technology Conference*, 1972.

[13] J.D. van Manen. Open water test series with propellers in nozzles. *International Shipbuilding Progress*, 1, 1954.

[14] J.D. van Manen. Recent research on propellers in nozzles. *International Shipbuilding Progress*, 4, 1957.

[15] J.D. van Manen and M.W.C. Oosterveld. Analysis of ducted propeller design. *Transactions of the Society of Naval Architects and Marine Engineers*, 74, 1966.

[16] M.W.C. Oosterveld. *Wake Adapted Ducted Propellers.* PhD thesis, Delft University of Technology, Delft, The Netherlands, 1970.

[17] M.W.C. Oosterveld. Ducted propeller characteristics. In *RINA Symposium on Ducted Propellers*, Teddington, UK, 1973.

[18] A. Yumuro. A model experiment on incoming-flow direction to the rudder of a ship sailing obliquely. In *14th International Towing Tank Conference*, 1975.

[19] K. Kose. On a new mathematical model of maneuvring motions of a ship and its applications. *International Shipbuilding Progress*, 29(363), 1982.

[20] S. Inoue, M. Hirano, K. Kijima, and J. Takashina. A practical calculation method of ship maneuvring motion. *International Shipbuilding Progress*, 28(325), 1981.

[21] D.A. Wise and J.W. English. Tank and wind tunnel tests for a drill-ship with dynamic position control. In *Offshore Technology Conference*, 1975.

[22] J.W. English. Propeller/hull interaction. In *14th International Towing Tank Conference*, 1975.

[23] J.W. English and D.A. Wise. Hydrodynamic aspects of dynamic positioning. *Transactions of the North East Coast Institution of Engineers and Shipbuilders*, 1975.

[24] E. Lehn. *Thruster Interaction Effects.* Report R-102.80, The Ship Research Institute of Norway, 1980.

[25] U. Nienhuis. Simulations of low frequency motions of dynamically positioned offshore structures. In *RINA Spring Meeting*, London, 1986.

[26] H.J.J van den Boom and U. Nienhuis. Hydrodynamic analysis of dynamically positioned vessels. In *International Workshop on Ship and Platform Motions*, Berkeley, 1983.

[27] N.J. Davison, N.T. Thomas, U. Nienhuis, and J.A. Pinkster. Application of an alternative concept in dynamic positioning to a tanker floating production system. In *Offshore Technology Conference*, Houston, 1987.

[28] Anonymous. Getting the most out of semisub thrusters promises to save up to 10 percent on fuel. *Shipping News International*, 1986.

[29] R.A. Norrby and D.E. Ridley. Notes on thrusters for ship manoeuvring and dynamic positioning. *Transactions of the Society of Naval Architects and Marine Engineers*, 1980.

[30] R.A. Norrby and D.E. Ridley. Notes on ship thrusters. *Transactions of The Institute of Marine Engineers*, 1981.

[31] K.J Minsaas, H.J. Thon, W. Kauczynski, and S.I. Karlsen. Estimation of required capacity for operation of offshore vessels under severe weather conditions. In *3rd Symposium on Practical Design of Ships and Mobile Units*, MARINTEK, Norway, 1987.

[32] U. Nienhuis. Propulsive aspects of dynamically positioned vessels. In *Conference on Stationing and Stability of Semi-Submersibles*, Glasgow, 1986.

[33] J. Brix. Ship handling under the influence of jet-hull interaction. In *West European Conference on Maritime Technology*, Paris, 1984.

[34] J.W. English and B.N. Steele. *The Performance of Lateral Thrust Units for Ships as Affected by Forward Speed and Proximity of a Wall.* Technical Report SH R28/62, National Physics Laboratory, Ship Division, Feltham, United Kingdom, 1962.

[35] N. Gregory and W.G. Raymer. *Wind Tunnel Tests on the Boulton-Paul Rectangular Wing (Aspect Ratio 2) with Lifting Fan.* Technical Report R and M 20356, Aeronautical Research Council, 1958.

[36] N. Gregory and W.S. Walker. *Measurements of Lift and Ground Interference on a Lifting Fan Wing at Zero Forward Speed.* Technical Report R and M 20006, Aeronautical Research Council, 1958.

[37] R. Jordinson. *Flow in a Jet Directed Normal to the Wind.* Technical Report R and M 3074, Aeronautical Research Council, 1956.

[38] T.C. Cooper. *Theoretical Modeling of Fluid Interactions.* Master's thesis, Naval Postgraduate School, Monterey, California, 1982.

[39] G.R. Stuntz and R.J. Taylor. Some aspects of bow thruster design. *Transactions of the Society of Naval Architects and Marine Engineers*, 72, 1964.

[40] R. Norrby. The effectiveness of a bow thruster at low and medium ship speeds. *International Shipbuilding Progress*, 14, 1967.

[41] D.E. Ridley. Observations of the effect of vessel speed on bow thruster performance. *Marine Technology*, 1971.

[42] M.S. Chislett and O. Bjorheden. *Influence of Ship Speed on the Effectiveness of a Lateral-thrust Unit.* Technical Report Hy-8, Hydro- og Aerodynamisk Laboratorium, Lyngby, 1966.

[43] J.L. Beveridge. Bow-thruster jet flow. *Journal of Ship Research*, 15:177–195, 1971.

[44] J. Brix. Querstrahlsteuer mit Druckausgleichskanaelen A.S.T. *HANSA*, 109:1597–1603, 1972.

[45] J.E. Brix and O. Bussemaker. Lateral thrusters with anti-suction tunnels. In *1st North Americal Tug Convention*, Ship and Boat International, 1973.

[46] J. Brix. Moderne Querstrahlsteuer als Manoevrierhilfen. *Schiff und Hafen*, 1977.

[47] J. Brix. Modellversuche mit der Schottel-Querstrahlanlage S 500 L. *HANSA*, 108:2195–2208, 1971.

[48] J. Brix. Doppelquerstrahlanlagen. *HANSA*, 111:1487–1496, 1974.

[49] J. Brix. Die Querstrahlanlage des 'Railship I'. *HANSA*, 1975.

[50] K. Kijima. The effect of drift angle on side thruster performance. *Transactions of the West-Japan Society of Naval Architecture*, 54, 1976.

[51] Anonymous. *Aerodynamics of a Wing-Fan System. Effect of Ground on the Resultant Thrust Occurring on a Fan Inset in a Rectangular Wing.* Technical Note 3, Boulton - Paul Aircraft Ltd., unknown.

[52] K. Taniguchi, K. Watanabe, and H. Kasai. *Investigations into the Fundamental Characteristics and Operating Performances of Side Thruster.* Mitsubishi Technical Bulletin 35, Mitsubishi Heavy Industries Ltd., 1966.

[53] S. Karlsen, K. Martinussen, and K.J. Minsaas. Towing performance and effectiveness of bow thrusters in waves and current. In *9th International Tug Convention*, Thomas Reed Publications Ltd., London, 1986.

[54] C. Pronk and A.F. Wesselink. Improved manoeuvring with integrated control of propulsion and steering devices. In *Automation for Safety and Shipping and Offshore Petroleum Operations*, 1980.

[55] C.M. van Hooren and J.J. Huisman. Crabbing performance of ferries. In *6th LIPS Propeller Symposium*, Drunen, The Netherlands, 1986.

[56] A. Jonk and A. Rem. Hydrodynamic optimization in ship design. *Schip en Werf*, 1989.

[57] P.D. Frymier, H.A. Hassan, and M.D. Salas. Navier-stokes calculations using cartesian grids: i. laminar flows. *AIAA Journal*, 1988.

[58] S.V. Patankar, D.K. Basu, and S.A. Alpay. Prediction of the three-dimensional velocity field of a deflected turbulent jet. *Transactions of the ASME*, 1977.

[59] W. Rodi and S.K. Srivatsa. A locally elliptic calculation procedure for three-dimensional flows and its application to a jet in cross-flow. *Computer Methods in Applied Mechanics and Engineering*, 1979.

[60] A.O. Demuren. Numerical calculations of steady three-dimensional turbulent jets in cross flow. *Computer Methods in Applied Mechanics and Engineering*, 37:309–328, 1983.

[61] B.E. Launder and Spalding D.B. The numerical computation of turbulent flows. *Computer Methods in Applied Mechanics and Engineering*, 3:269–289, 1974.

[62] S.V. Patankar and D.B. Spalding. A calculation procedure for heat, mass and momentum transfer in three-dimensional parabolic flows. *International Journal of Heat and Mass Transfer*, 15:1787–1805, 1972.

[63] G. De Vahl Davis and G.D. Mallinson. An evaluation of upwind and central difference approximations by a study of recirculating flow. *Computers and Fluids*, 4:29–43, 1976.

[64] B.P. Leonard. A stable and accurate convective modelling procedure based on quadratic upstream interpolation. *Computer Methods in Applied Mechanics and Engineering*, 19:59–98, 1979.

[65] M.A. Leschziner. Practical evaluation of three finite difference schemes for the computation of steady-state recirculating flows. *Computer Methods in Applied Mechanics and Engineering*, 23:293–312, 1980.

[66] M.A. Leschziner and W. Rodi. Calculaton of annular and twin parallel jets using various discretization schemes and turbulence-model variations. *Transactions of the ASME*, 1981.

[67] F. Durst and A.K. Rastogi. Theoretical and experimental investigations of turbulent flows with separation. In *Second International Symposium on Turbulent Shear Flows*, Springer, 1979.

[68] S.V. Patankar. *Numerical Heat Transfer and Fluid Flow. Computational Methods in Mechanics and Thermal Sciences*, Hemisphere Publishing Corporation, 1980.

[69] S.F. Hoerner. *Fluid-Dynamic Drag.* Hoerner Fluid Dynamics, Albuquerque, 1965.

[71] F. Durst and A.K. Rastogi. Turbulent flow over two dimensional fences. In *Second International Symposium on Turbulent Shear Flows*, Springer, 1979.

[72] J.J. McGuirck, A.K.M.P. Taylor, and J.H. Whitelaw. The assessment of numerical diffusion in upwind difference calculations of turbulent recirculating flows. In *Second International Symposium on Turbulent Shear Flows*, Springer, 1979.

[73] M.C. Gottmer, W. de Bruin, and J. van der Kooij. *Three Component Laser-Doppler Velocimetry at MARIN, Technique and Application.* Technical Report X50889-1-RM, Maritime Research Institute Netherlands, Wageningen, The Netherlands, 1988.

[74] M.A. Kotb and J.A. Schetz. Detailed turbulent flow field measurements immediately behind a propeller. In *SNAME Propeller 1984 Symposium, paper 3*, 1984.

[75] K. Koyama, A. Kakugawa, and M. Okamoto. Experimental investigation of flow around a marine propeller and application of panel method to the propeller theory. In *16th Symposium Naval Hydrodynamics*, University of California, 1986.

[76] K.S. Min. *Numerical and experimental methods for the prediction of field point velocities around propeller blades.* Technical Report 7078-12, MIT Department Ocean Engineering, 1978.

[77] S. Kobayashi. Propeller wake survey by laser-doppler velocimeter. In *International Symposium Applicated Laser-Doppler Anemometry of fluid mechanics*, Lisbon, 1982.

[78] R.B. Schoenberger. Improved technique for the experimental determination of propeller field point velocities using laser-doppler anemometry. In *SNAME Propeller '84, Symposium paper 7*, 1984.

[79] M.R. Davis and H. Winarto. Jet diffusion from a circular nozzle above a solid plane. *Journal of Fluid Mechanics*, 101, 1980.

[80] F. Stern, H.T. Kim, V.C. Patel, and H.C. Chen. Viscous-flow computation of propeller hull interaction. In *16th ONR Symposium of Naval Hydrodynamics*, 1986.

[81] H. Schlichting. *Boundary Layer Theory. Mechanical Engineering*, McGraw-Hill, 1979.

[82] N.A. Chigier and A. Chervinsky. Experimental investigation of swirling vortex motion in jets. *Journal of Applied Mechanics*, 1967.

[83] R.J. Margason. *The Path of a Jet Directed at Large Angles to a Subsonic Free Stream.* Technical Report TN D-4919, NASA, 1968.

Appendix A

SHIP MODELS

A.1 Ferry; Code S-F

The body plan of the ship (MARIN Model Nr 5650) is shown in Figure A.1. The main (model) particulars are listed in Table A.1. This table also lists the actuator arrangement. The arrangement of the tunnel thruster in the model is shown in Figure A.2.

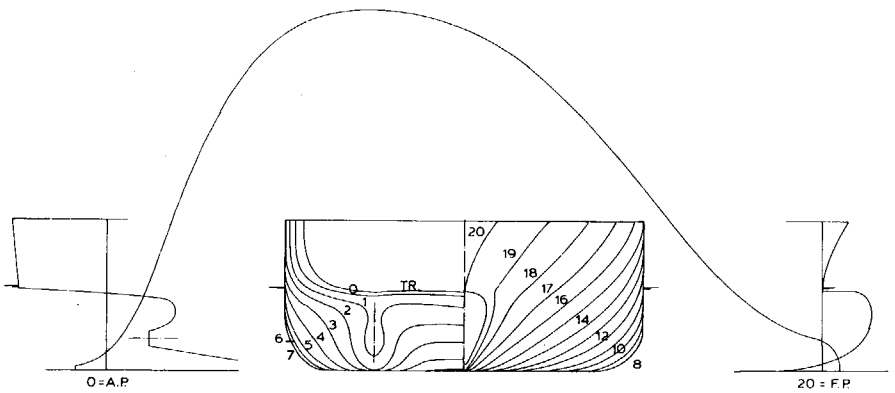

Figure A.1: body plan for ferry S-F

A.2 Container Vessel; Code S-CV

The body plan of the ship (MARIN Model Nr 5492) is shown in Figure A.3. The main (model) particulars are listed in Table A.2. This table also lists the actuator arrangement. The arrangement of the tunnel thruster is shown in Figure A.2.

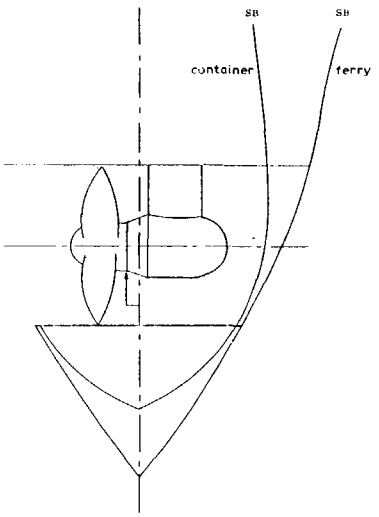

Figure A.2: tunnel thruster arrangement for ferry S-F

Particular	Dimension	Value
Length between pp	(m)	9.835
Beam	(m)	1.811
Draft (forward)	(m)	0.412
Draft (aft)	(m)	0.412
Block coefficient	(-)	0.612

Particular	Code	See Section	Location		
			x	y	z
Bow tunnel thruster	P-4929	B.3	4.342	0.032	0.206
Rectangular drive	T-AZ14	B.1	4.342	-0.033	0.206

Table A.1: main particulars for ferry S-F

Particular	Dimension	Value
Length between pp	(m)	8.182
Beam	(m)	1.465
Draft (forward)	(m)	0.411
Draft (aft)	(m)	0.438
Block coefficient	(-)	0.599

Particular	Code	See Section	Location		
			x	y	z
Bow tunnel thruster	P-4929	B.3	3.586	0.032	0.15
Rectangular drive	T-AZ14	B.1	3.586	-0.033	0.15

Table A.2: main particulars for container vessel S-CV

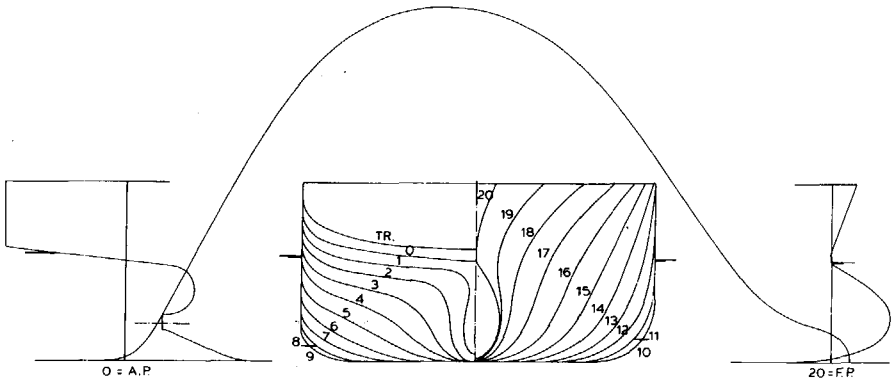

Figure A.3: body plan for container vessel S-CV

A.3 Hopper Dredger; Code S-HD

The body plan of the ship (MARIN Model Nr 6779) is shown in Figure A.4. The main (model) particulars are listed in Table A.3. This table also lists the actuator arrangement. The arrangement of the tunnel thruster for this model is shown in Figure A.5.

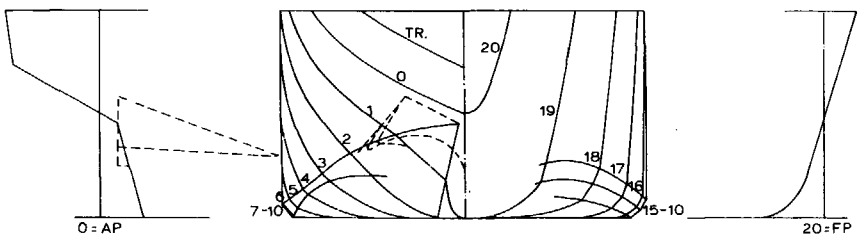

Figure A.4: body plan for hopper dredger S-HD

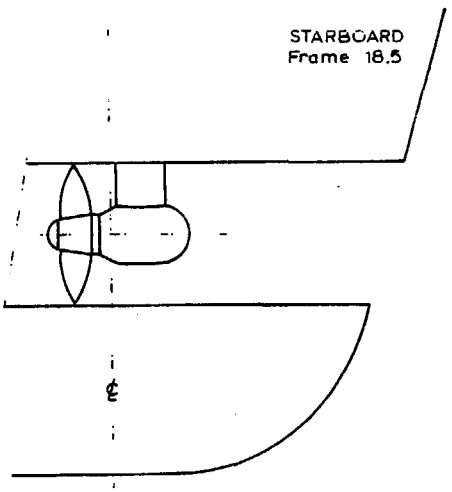

Figure A.5: tunnel thruster arrangement for hopper dredger S-HD

Particular	Dimension	Value
Length between pp	(m)	5.476
Beam	(m)	1.095
Draft (forward)	(m)	0.457
Draft (aft)	(m)	0.457
Block coefficient	(-)	0.848

Particular	Code	See Section	Location		
			x	y	z
Bow tunnel thruster	P-4929	B.3	2.327	0.032	0.218
Rectangular drive	T-AZ14	B.1	2.327	-0.033	0.218

Table A.3: main particulars for hopper dredger S-HD

A.4 Semi-Submersible; Code S-SSWV

The body plan of one of the hulls of the semi is shown in Figure A.6. The main (model) particulars are listed in Table A.4. For the tests reported here the semi-submersible was not fitted with any thruster, propeller or rudder.

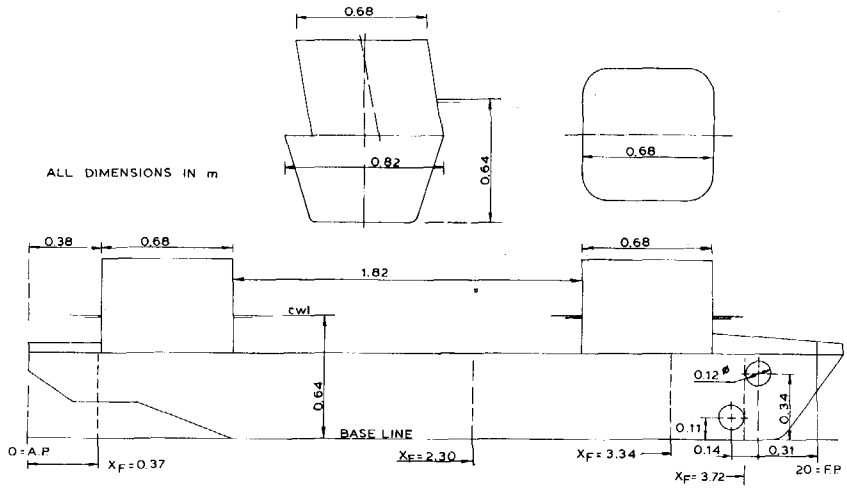

Figure A.6: body plan for semi-submersible workover vessel S-SSWV

Particular	Dimension	Value
Length between pp	(m)	4.104
Beam of each hull	(m)	0.816
Draft (forward)	(m)	0.640
Draft (aft)	(m)	0.640
Block coefficient of each floater	(-)	0.668

Table A.4: main particulars for semi-submersible workover vessel S-SSWV

A.5 Wedge-Shaped Hull; Code S-W

The body plan of this simplified ship hull section (MARIN Model Nr 6236) is shown in Figure A.7. The arrangement of the thruster in the hull is also shown in this figure. The main (model) particulars are listed in Table A.5. This table also lists the actuator arrangement, if any.

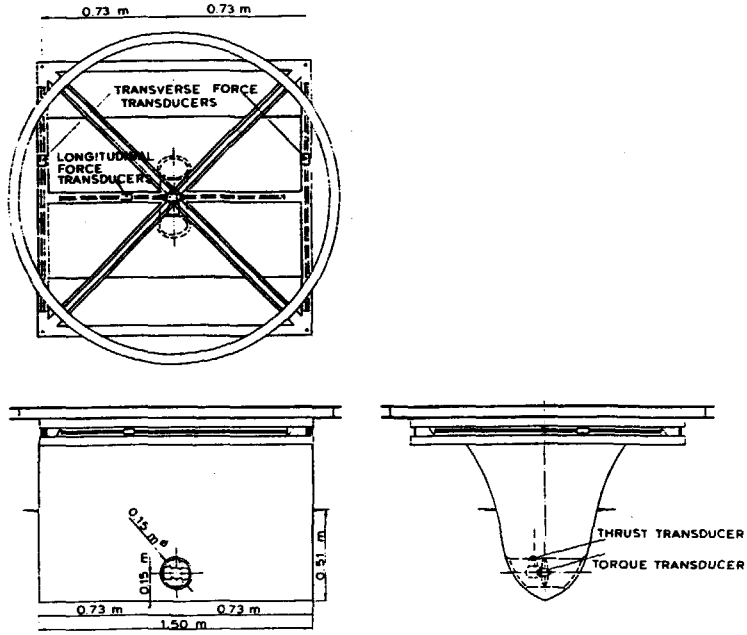

Figure A.7: body plan and thruster arrangement for wedge-shaped hull S-W

Particular	Dimension	Value
Length between pp	(m)	1.5
Beam	(m)	0.546
Draft (forward)	(m)	0.508
Draft (aft)	(m)	0.508
Block coefficient	(-)	0.715

Particular	Code	See Section	Location		
			x	y	z
Tunnel thruster	P-4347	B.5	0.0	0.0	0.152
Rectangular drive	T-AZ14	B.1	0.0	-0.065	0.152

Table A.5: main particulars for wedge-shaped hull S-W

A.6 Barge with Various Bilges; Code S-BB

The body plan of this flat-bottomed barge to which various bilges could be connected (MARIN Model Nr 6497) is shown in Figure A.8. The arrangement of the thrusters under the barge is also shown in this figure. The main (model) particulars are listed in Table A.6. This table also lists the actuator arrangement particulars.

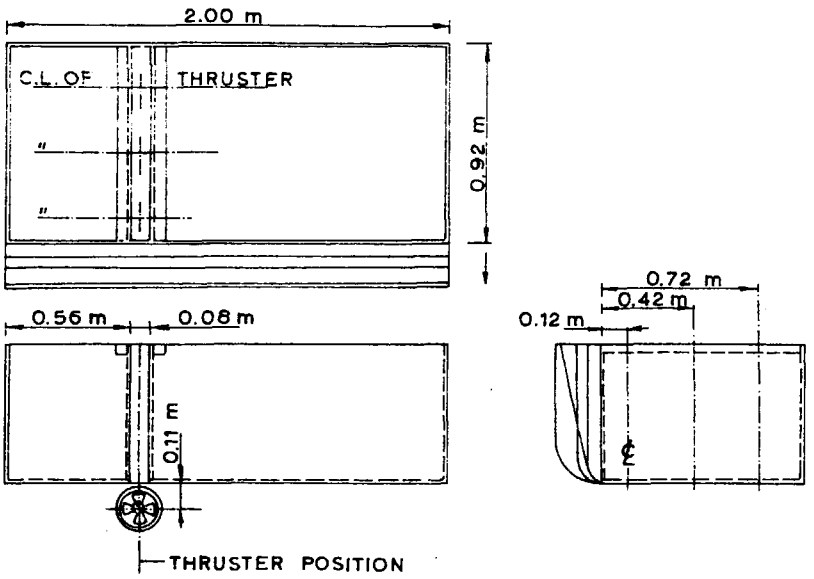

Figure A.8: body plan and thruster arrangement for barge with various bilges S-BB

Particular	Dimension	Value
Length between pp	(m)	2.0
Beam (without bilges)	(m)	0.920
Draft (forward)	(m)	0.450
Draft (aft)	(m)	0.450
Block coefficient (no bilges)	(-)	1.0

Particular	Code	See Section	Location		
			x	y	z
Azimuthing thruster	P-4929	B.3	-0.400	var	-0.110
Nozzle	N-37	B.7	-0.400	var	-0.110
Rectangular drive	T-AZ14	B.1	-0.400	var	-0.110

Table A.6: main particulars for barge with various bilges S-BB

A.7 Rectangular Flat Barge; Code S-RFB

The body plan of this flat-bottomed rectangular barge is shown in Figure A.9. The arrangement of the thrusters under the barge is also shown in this figure. The main (model) particulars are listed in Table A.7. This table also lists the actuator arrangement particulars.

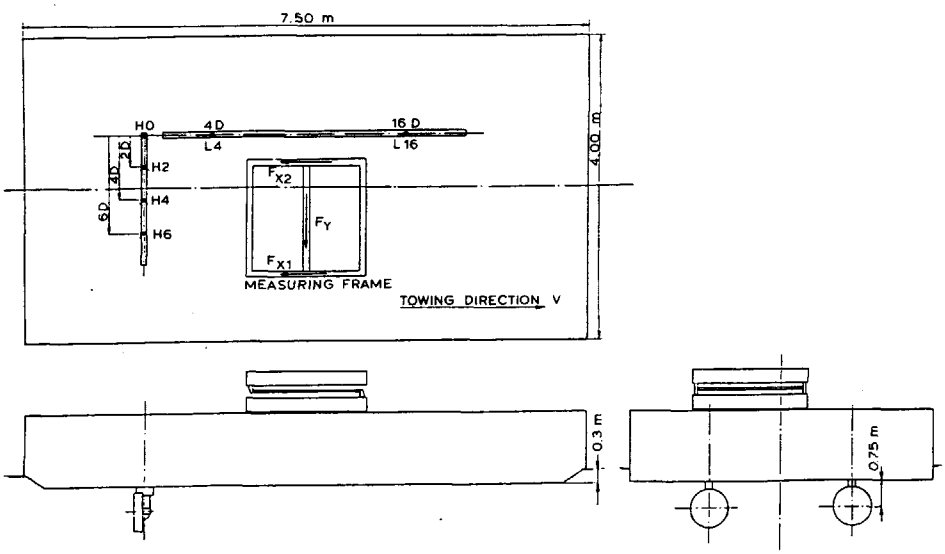

Figure A.9: body plan and thruster arrangement for rectangular flat barge S-RFB

Particular	Dimension	Value
Length between pp	(m)	7.5
Beam	(m)	4.0
Draft (forward)	(m)	0.3
Draft (aft)	(m)	0.3
Block coefficient (no bilges)	(-)	0.931

Particular	Code	See Section	Location		
			x	y	z
Azimuthing thruster	P-4944	B.4	-2.220	var	-0.159
Nozzle	N-37	B.7	-2.220	var	-0.159
Rectangular drive	T-AZ21	B.2	-2.130	var	-0.159
Azimuthing thruster	P-4944	B.4	var	0.690	-0.159
Nozzle	N-37	B.7	var	0.690	-0.159
Rectangular drive	T-AZ21	B.2	var	0.690	-0.159

Table A.7: main particulars for rectangular flat barge S-RFB

Appendix B

DRIVES, PROPELLERS AND RUDDERS

B.1 Rectangular Drive 14 cm; Code T-AZ14

The thruster rectangular drive is shown in Figure B.1. This drive admits the use of various propellers but is used mostly in conjunction with 14 cm propeller and nozzle.

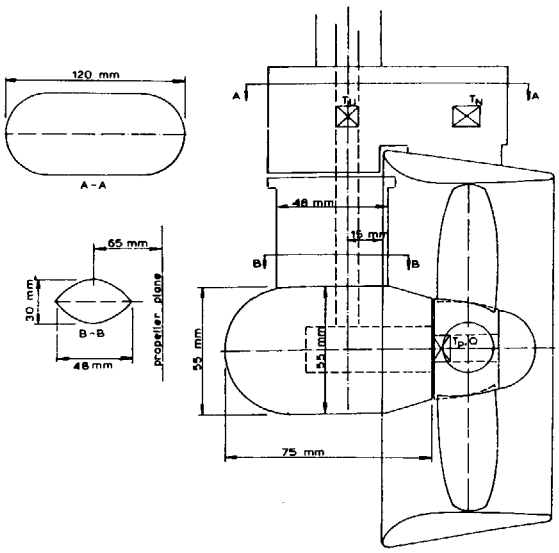

Figure B.1: rectangular drive geometry for azimuthing thruster T-AZ14

B.2 Rectangular Drive 21 cm; Code T-AZ21

This rectangular drive is shown in Figure B.2. It is mostly fitted with propellers and nozzles of approximately 21 cm diameter.

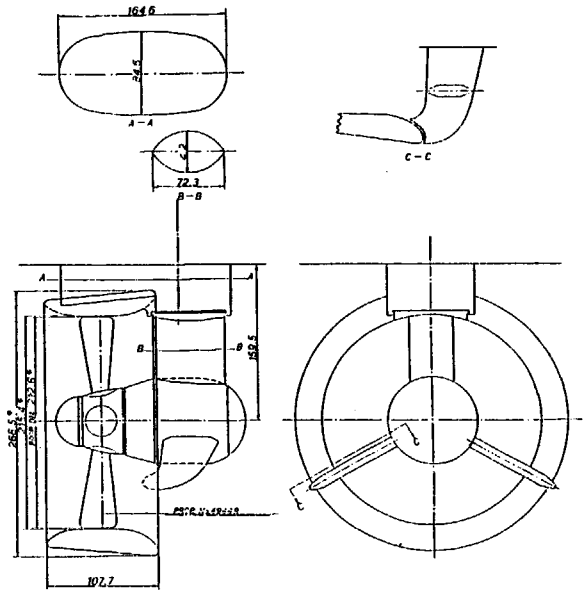

Figure B.2: rectangular drive geometry for azimuthing thruster T-AZ21

B.3 Propeller P-4929

The propeller geometry for this propeller, MARIN Propeller Number 4929, is shown in Figure B.3.

B.4 Propeller P-4944

The propeller geometry for this propeller, MARIN Propeller Number 4944, is shown in Figure B.4.

B.5 Propeller P-4347

The propeller geometry for this propeller, MARIN Propeller Number 4347, is shown in Figure B.5.

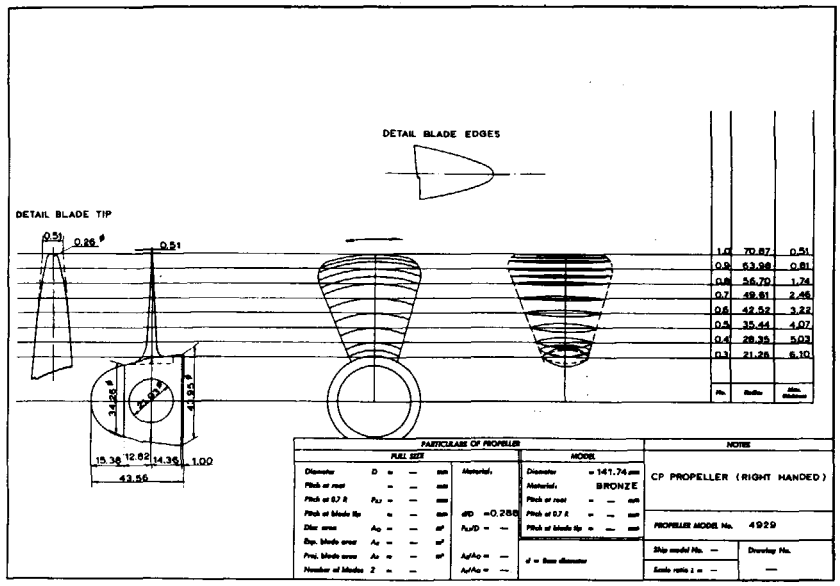

Figure B.3: propeller geometry of propeller P-4929

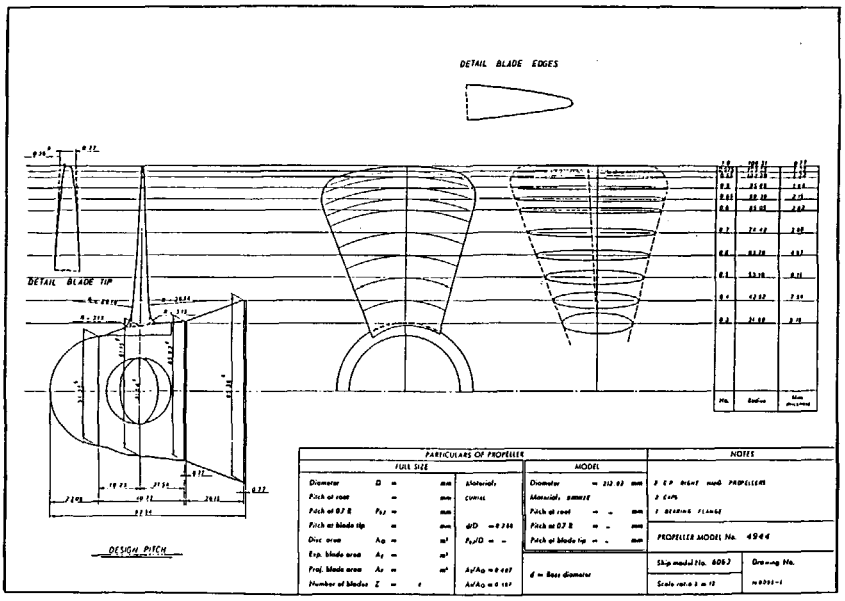

Figure B.4: propeller geometry of propeller P-4944

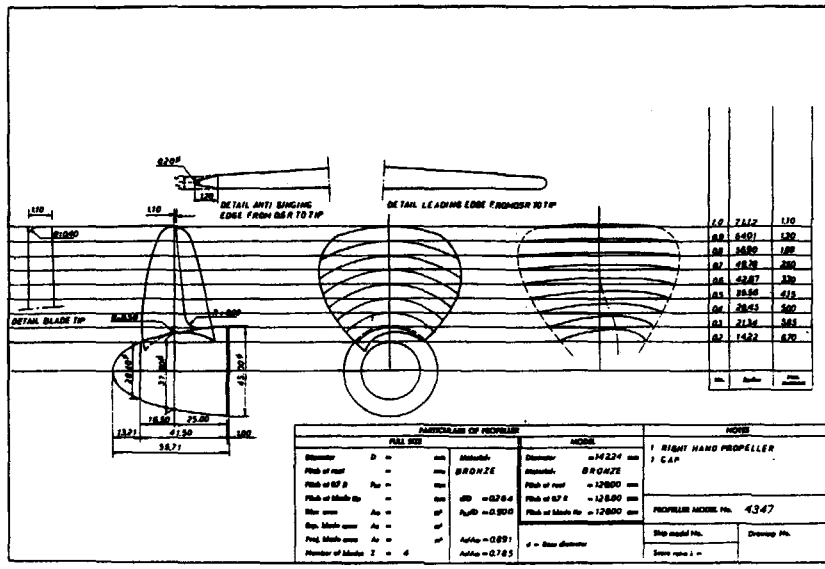

Figure B.5: propeller geometry of propeller P-4347

B.6 Nozzle N-19A

The nozzle geometry of this common MARIN 19A duct is shown in Figure B.6.

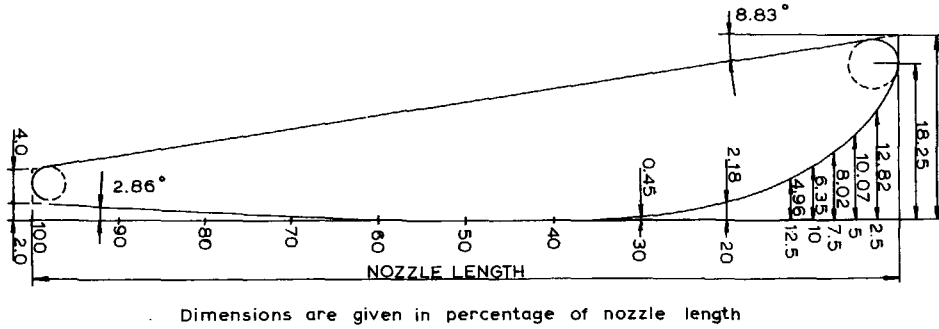

Figure B.6: nozzle geometry of duct N-19A

B.7 Nozzle N-37

The nozzle geometry of this common MARIN 37 duct is shown in Figure B.7.

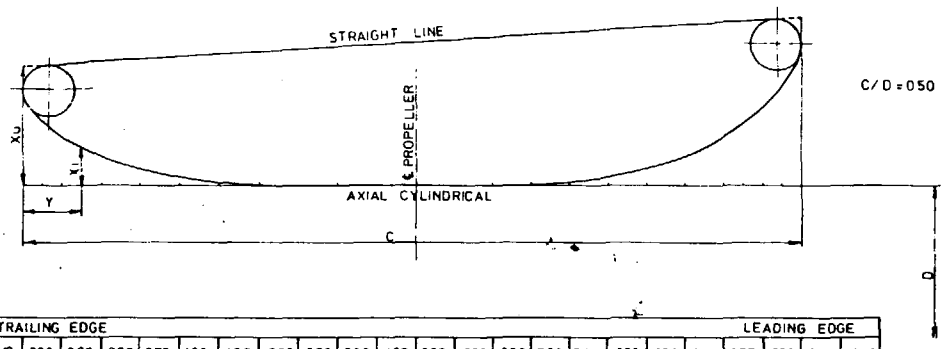

TRAILING EDGE																					LEADING EDGE
Y/C	000	025	050	075	100	150	200	250	300	400	500	600	650	700	750	800	850	900	925	950	975	1.000
Xi/C	1242	0829	0650	0500	0383	0213	0100	0042	0013	CIRCULAR CYLINDRICAL			0008	0033	0108	0213	0383	0629	0792	1004	1283	1833
Xu/C	1538	STRAIGHT LINE																				2154

Figure B.7: nozzle geometry of duct N-37

List of Figures

List of Tables

ABOUT THE AUTHOR

Ubald Nienhuis was born October 1960. After graduating from High School he went to study at Delft University of Technology, Department of Maritime Technology, from which he graduated in May 1983.

He then joined the Maritime Research Institute Netherlands (MARIN) in Wageningen, The Netherlands, as a research engineer and as such worked on the development of time-domain simulation programs for station-keeping.

In 1985 he moved to MARIN's Ocean Engineering Department and was involved in experimental and computational work concerning seakeeping, Single Point Moorings and station-keeping.

In 1989 he changed to the Nautical Department of MARIN working on simulator development and simulator application. The applications consisted of projects covering port-admission policy and port design.

Finally in 1991 he changed again in the MARIN organization to join the Ship Research Department and as such is active in the fields of resistance, propulsion, cavitation, vibration excitation, manoeuvring and seakeeping.

ACKNOWLEDGEMENT

First of all I like to express my gratitude to my promotor Prof. Dr. Ir. J.D. van Manen for his continuous and enthusiastic interest in this work.

Further I like to thank the Maritime Research Institute Netherlands for the permission to publish this research in the form of a thesis and for their assistance in providing the time and facilities to complete this work.

I am also indebted to the Netherlands Foundation for the Coordination of Maritime Research (CMO) for the possibility to use some of the research contracted by CMO to MARIN for this thesis.

The help of my colleagues in performing the experiments, analysing the results, providing computer services is greatly appreciated. Special mention is due to Mr. G. Radstaat who has painstakingly transformed my scribbled notes into proper and legible figures.

Last but not least I want to thank my wife Sylvie for keeping up with me and the time-consuming process of writing this thesis.